P-01

Ground state phase diagram of interacting Dirac electrons in graphene under magnetic field

Tatsuya Higashi

Dept. of Physics, Tohoku U.

Low-energy states of electrons in graphene

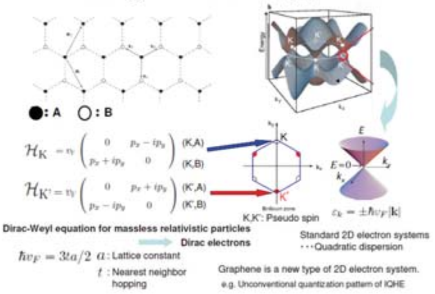

Electronic states of graphene in magnetic fields

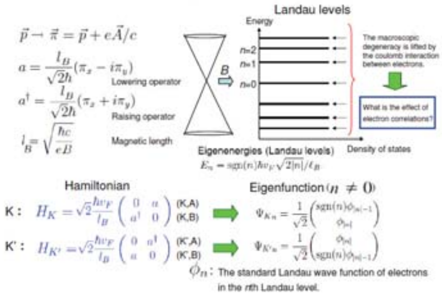

Effective inter-electron interaction of the Nth Landau level

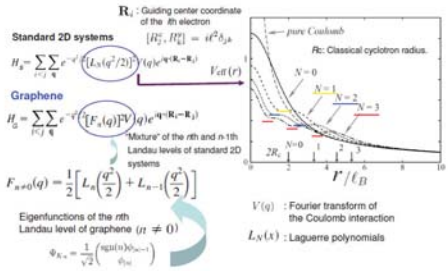

Fractional quantum Hall effects in standard 2D electron systems in the N=0 and 1 Landau levels

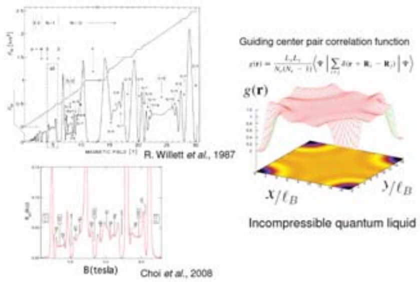

CDW ground states of standard 2D electron systems in high Landau levels

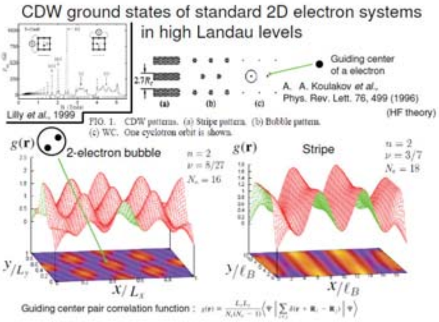

Motivation (N=2 Landau level in graphene)

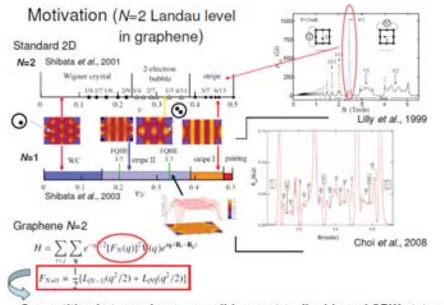

Competition between incompressible quantum liquids and CDW states

Previous theoretical works

- Hatree-Fock theory (C.-H.Zhang *et al*, PRB 75, 245414 (2007))
  - Charge density waves (CDW) called stripes and bubbles realize in the ground state in high Landau levels of graphene.
  - But, quantum fluctuations are neglected in HF theory.
  - Can the CDW ground states survive under quantum fluctuations?
- Exact diagonalization (ED) (H.Wang *et al*, PRL 100, 116802 (2008))
  - The system size treated by ED is quite small.
  - The filling factor studied is limited.

Because of these limitations, such studies cannot determine the phase diagram of the present system.

Purpose of this study

We use the density matrix renormalization (DMRG) method to investigate the ground state at various fillings in the N=2 Landau level of graphene, and determine the ground state phase diagram.

Model

Periodic boundary condition is imposed both in the x and y directions. (Torus geometry)

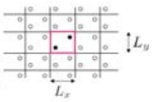

Approximations
- assume spin-polarized ground state
- assume valley-polarized ground state
- neglect Landau level (LL) mixing

Relevant energy scales

LL Separation between 0th and 1th Landau level: $\sqrt{2}\hbar v_F/\ell_B \simeq 400\sqrt{B[T]}[K]$

Typical Coulomb energy between electrons: $e^2/\epsilon\ell_B \simeq 100\sqrt{B[T]}[K]$

Energy difference between i+1th and ith LL

E(1)-E(0) =400 $\sqrt{B}$

E(2)-E(1) =166 $\sqrt{B}$

E(3)-E(2) =128 $\sqrt{B}$

E(4)-E(3) =108 $\sqrt{B}$

We solve inter-electron interaction Hamiltonian for spin and valley-polarized electrons at various filling factors in the N=2 Landau level of graphene.

$$H=\sum_{n_1}\sum_{n_2}\sum_{n_3}\sum_{n_4}A_{n_1n_2n_3n_4}c^\dagger_{n_1}c^\dagger_{n_2}c_{n_3}c_{n_4}$$

Filling factor $\nu^* = 2\pi N_e/L_xL_y = N_e/N_\phi$

N_ϕ: Total number of flux quanta in

DMRG method for quantum 2D electron systems under high magnetic field

The DMRG method was originally developed for 1D lattice models, short range interactions.

Map to a 1D model (N. Shibata *et al*. Phys. Rev. Lett. 86, 5755 (2001))

One-particle states of free electrons in 2D under perpendicular magnetic field: $\Psi_{NX}(x,y)$, $X_n = 2\pi\ell^2 n/L_y$

Two quantum numbers: N: Landau level index, Xn: Guiding center (n : integer)

The ground state is determined only by the electrons in top most Landau level.

We can omit the Landau level index, N.

The quantum number is only Xn, which is a discrete number.

1D lattice model !

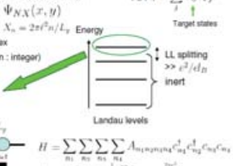

[redacted]

$$H=\sum_{n_1}\sum_{n_2}\sum_{n_3}\sum_{n_4}A_{n_1n_2n_3n_4}c^\dagger_{n_1}c^\dagger_{n_2}c_{n_3}c_{n_4}$$

$1 \leq n_1, n_2, n_3, n_4 \leq N_s$ Long-ranged hopping

Ground state phase diagram of graphene in the N=2 Landau Level

[redacted]

Ground state at low fillings

Guiding center pair correlation function

[redacted]

[redacted]

Ground state at low fillings [redacted]

Guiding center pair correlation function

[redacted]

Comparison with the result of the HF theory

[redacted]

Summary

- By the use of DMRG method, we determined the ground state of Dirac electrons in the N=2 Landau level of grapnene at various filling factors.
- By analyzing the guiding center pair correlation function, we obtained the reliable ground state phase diagram.

[redacted]

Gamma-ray spectroscopy of $^{11}_{\Lambda}$B and $^{12}_{\Lambda}$C

K. Hosomi for KEK-E566 collaboration

Department of Physics, Tohoku University

1. Introduction

■ ΛN interaction

Study of the ΛN interaction is the first step toward the unified understanding of general baryon-baryon interactions beyond the well-known NN interaction. Since ΛN scattering experiments are quite difficult due to the short lifetime (263 ps) of a Λ hyperon, structure of Λ hypernuclei give us almost unique information of the ΛN interaction.

■ Hypernuclear structure

A weak-coupling scheme is a assumed that a hypernucleus consists of two components, a Λ hyperon and the remaining "core" nucleus, and the Λ hyperon does not change the structure of the core nucleus. In this scheme, non-zero-spin states of a core nucleus split into spin-doublet states with Λ inclusion as shown in Fig. 1. The energy spacing of the doublet states is determined only by the spin-dependent part of the ΛN interaction. Because the doublet spacing is typically of the order of 100 keV, a γ-ray spectroscopy method using germanium (Ge) detectors with a few keV resolution is essential to resolve their splitting.

From the previous results of a series of γ-ray spectroscopy experiments, it is proposed that energy shifts of hypernuclear levels due to the coupling between the ΛN and ΣN channels (ΛN-ΣN coupling) are important to generally understand the spin-dependent part of the ΛN interaction in p-shell hypernuclei, which have p-shell core nuclei. Fig. 2 shows the important diagram for ΛNN three-body interaction caused by ΛN-ΣN coupling.

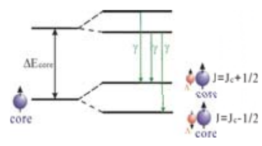

Fig. 1: Low-lying hypernuclear levels.

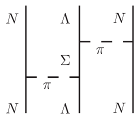

Fig. 2: ΛNN three-body diagram for ΛN-ΣN coupling channel.

■ KEK-E566 experiment

The KEK-E566 experiment was performed at KEK-PS K6 beam line in 2005 in order to investigating the ΛN interaction in p-shell hypernuclei including the effect of ΛN-ΣN coupling. In this experiment, $^{11}_{\Lambda}$B and $^{12}_{\Lambda}$C hypernuclei were produced via the ^{12}C(π^+, K^+) reaction with the beam momentum of 1.05 GeV/c.

2. Experimental Setup

■ K6 beam line and SKS spectrometer

The primary proton beam is accelerated by KEK 12-GeV PS and irradiated on a production target located at the most upstream of the K6 beam line. The produced secondary pion beam is transported to the experimental target. Fig. 3 shows the whole schematic view of the experimental setup.

The pion beam momentum is analyzed by the beam line spectrometer which consists of QQDQQ magnets, tracking chambers and timing counters. The scattered kaons are identified and momentum analyzed by the SKS spectrometer which consists of the SKS magnet, tracking chambers and timing counters.

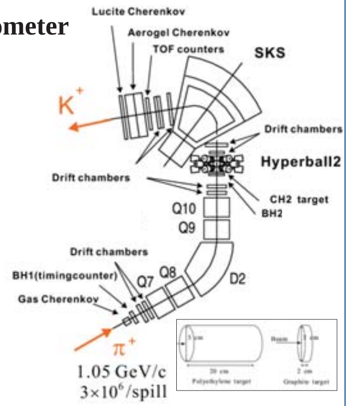

Fig. 3: Schematic view of experimental setup.

■ Hyperball2

γ-rays emitted form produced hypernuclei were detected by using a Ge detector array called Hyperball2, which was installed around the experimental target. As shown in Fig. 4, Hyperball2 has a total of 14 single-type Ge detectors and 6 clover-type Ge detectors, each of which is surrounded by $Bi_4Ge_3O_{12}$ scintillation counters in order to suppress background signals mainly caused by Compton scattering.

The in-beam energy resolution and photo-peak efficiency were 5.4 keV (FWHM) and 2.3 % at 1.33 MeV, respectively.

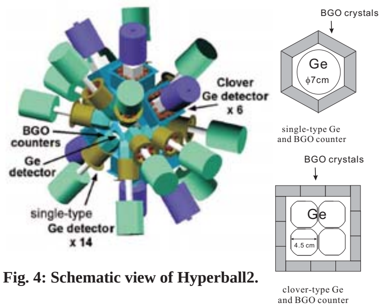

Fig. 4: Schematic view of Hyperball2.

3. Data analysis

■ Missing mass spectrum

$$M_{HY} = \sqrt{(E_\pi + M_{target} - E_K)^2 - (p_\pi^2 + p_K^2 - 2p_\pi p_K \cos\theta_{\pi K})}\ ,$$
$$B_\Lambda \ \ = M_{core} + M_\Lambda - M_{HY}\ .$$

The mass of a produced hypernucleus (M_{HY}) is obtained as a missing mass in the (π^+, K^+) reaction by calculating the above equation in the laboratory frame, where E_π and p_π are the energy and the momentum of the pion, E_K and p_K are those of the kaon, M_{target} is the mass of target nucleus (^{12}C), and $\theta_{\pi K}$ is the reaction angle. Then, the missing mass can be converted to the Λ binding energy (B_Λ) by subtracting the mass of the core nucleus (^{11}C) and a Λ hyperon. Fig. 5 shows the obtained missing mass spectrum.

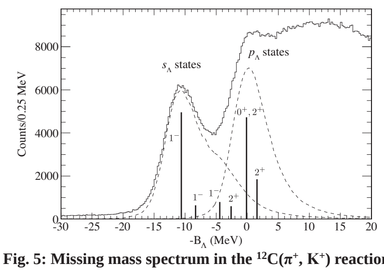

Fig. 5: Missing mass spectrum in the ^{12}C(π^+, K^+) reaction.

■ γ-ray spectrum for $^{11}_{\Lambda}$B

The $^{11}_{\Lambda}$B hypernucleus was populated via the one proton mission from p_Λ states of $^{12}_{\Lambda}$C. By selecting the p_Λ region in the missing mass spectrum, we observed three γ-ray peaks associated to $^{11}_{\Lambda}$B as shown in Fig. 6. In Fig. 6, right figures are the enlarged views of the left figures around 511-keV annihilation peak.

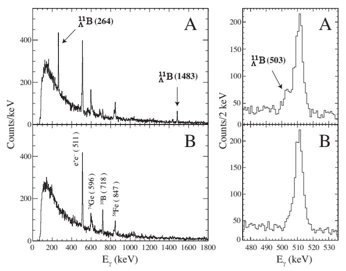

Fig. 6: "A" indicates the γ-ray spectrum for the events of $^{11}_{\Lambda}$B production. The events are corresponding to the p_Λ region in the missing mass, where a Λ hyperon occupies the p orbit.

■ γ-ray spectrum for $^{12}_{\Lambda}$C

Four γ-ray peaks associated to $^{12}_{\Lambda}$C were identified by selecting the s_Λ states region in the missing mass spectrum as shown in Fig. 7. Except for the 161-keV peak, Doppler-shift correction is necessary to observed as a sharp peak. The Doppler correction was applied event-by-event by the following equation

$$E_\gamma^{corrected} = \frac{1}{\sqrt{1-\beta^2}} \cdot (1 - \beta\cos\phi) \cdot E_\gamma^{measured}$$

,where β is the velocity of a recoiling hypernucleus, and φ is the angle between the direction of β and γ-ray emission

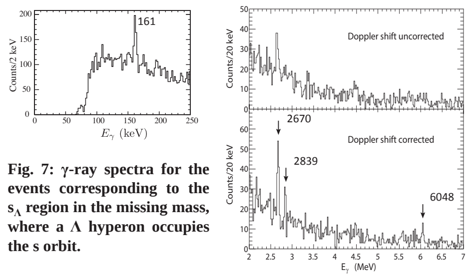

Fig. 7: γ-ray spectra for the events corresponding to the s_Λ region in the missing mass, where a Λ hyperon occupies the s orbit.

4. Results

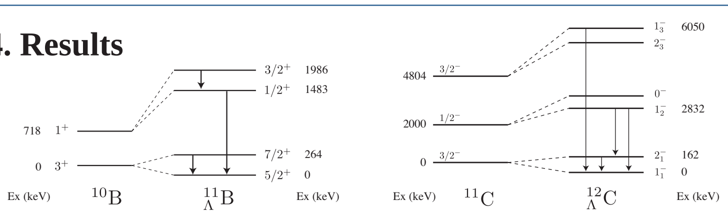

$M1(7/2^+ \to 5/2^+) : E_\gamma = \ \ 263.7 \pm 0.1(\mathrm{stat}) \pm 1.0(\mathrm{syst})$ keV
$M1(3/2^+ \to 1/2^+) : E_\gamma = \ \ 503.0 \pm 0.4(\mathrm{stat}) \pm 1.0(\mathrm{syst})$ keV
$E2(1/2^+ \to 5/2^+) : E_\gamma = 1483.3 \pm 0.3(\mathrm{stat}) \pm 1.0(\mathrm{syst})$ keV

$M1(2_1^- \to 1_1^-) : E_\gamma = \ \ 161.5 \pm 0.3(\mathrm{stat}) \pm 1.0(\mathrm{syst})$ keV
$M1(1_2^- \to 2_1^-) : E_\gamma = 2670.2 \pm 2.9(\mathrm{stat}) \pm 3.6(\mathrm{syst})$ keV
$M1(1_2^- \to 1_1^-) : E_\gamma = 2839.3 \pm 3.6(\mathrm{stat}) \pm 3.2(\mathrm{syst})$ keV
$M1(1_3^- \to 1_1^-) : E_\gamma = 6048.4 \pm 6.8(\mathrm{stat}) \pm 6.7(\mathrm{syst})$ keV

Fig. 8: Low-lying level schemes of $^{11}_{\Lambda}$B and $^{12}_{\Lambda}$C and of their core nuclei. γ-ray transitions observed in the KEK-E566 experiment are indicated by arrows, and determined level energies are also shown.

5. Discussion

$$\Delta = 0.43 \text{ or } 0.33,\quad S_\Lambda = -0.02,\quad S_N = -0.4,\quad T = 0.03\ \ \mathrm{MeV}$$

In the p-shell hypernuclei, the spin-dependent interactions are represented by the four parameters as above, where Δ, S_Λ, S_N and T denote the radial integrals of the effective $s_\Lambda p_N$ interactions for the spin-spin, Λ-spin-dependent spin-orbit, nucleon-spin-dependent spin-orbit and tensor components, respectively. The quoted values are suggested by D. J. Millener based on previous results. The energy spacing of two hypernuclear levels are generally described by linear combinations of these parameters and the strength of ΛN-ΣN coupling. The NSC97f interaction of the Nijmegen models is assumed for estimating the effect of ΛN-ΣN coupling.

The measured spin-doublet spacings of $^{11}_{\Lambda}$B(3/2$^+$, 1/2$^+$), $^{11}_{\Lambda}$B(7/2$^+$, 5/2$^+$) and $^{12}_{\Lambda}$C(2_1^-, 1_1^-) are well explained by these parameters. The present experimental results favors the NSC97f interaction for ΛN-ΣN coupling.

P-03

Λ photoproduction on a deuteron at threshold energies.

B. Beckford for NKS2 collaboration, Dept. of Physics, Tohoku University

Introduction

Strangeness photoproduction

Strangeness production on a nucleon or a nucleus by the electromagnetic interaction provides invaluable information on the strangeness production mechanism and strengths of meson-hadron coupling constant. Kaon photoproduction can be a good probe to find missing resonance states.

NKS2 experiment aims to explore the strangeness photoproduction on the deuteron by measuring neutral kaons and Λ hyperons with tagged photon beams of E_γ = 0.8-1.1 GeV.

We focus on Λ, a elementary particle composed of uds, an up, down and strange quark.

$N(\gamma, K^0)\Lambda$ reaction in the threshold region

$n(\gamma, K^0)\Lambda$ process has unique features in the investigation of kaon production process by electromagnetic interaction as follows,

- no charge in initial and final state
  - → t-channel Born term does not contribute
- isospin symmetry to $p(\gamma, K^+)\Lambda$ process
  - → sign of coupling constant in u-channel is opposite
  - $g(K^0\Sigma^0 n) = -g(K^+\Sigma^0 p)$
- the electromagnetic coupling constants of resonances in the s- and t-channels
  - → different from K^+ process : e.g., $g(N^* n\gamma)$ and $g(K^+K^0\gamma)$

Due to these characteristics, the interference among the diagrams in the K^0 production process is quite different from that in the K^+ process. For the elementary reaction of $\gamma n \to K^0\Lambda$, photon energy dependence and angular distribution at Eg = 1.05 GeV are calculated using Kaon-MAID (KM) model and Saclay Lyon A model (SLA). These two isobar models agree well in their predictions of the $\gamma p \to K^+\Lambda$ process, however they are significantly different for the $\gamma n \to K^0\Lambda$ process.

Total cross section for kaon photo-production

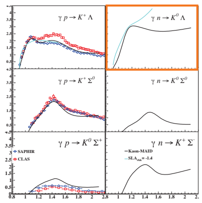

solid lines : Kaon-MAID [T. Mart and C. Bennhold, Phys. Rev. C 61 012201(R) (1999)]
data : SAPHIR(98) [M. Q. Tran et al., Phys. Lett B445, 20 (1998)] [S. Goers et al., Phys. Lett B445, 20 (1998)]
SAPHIR(04) [K. -H. Glander et al., Eur. Phys. J. A 19, 251 (2004)] [R. Lawall et al., Eur. Phys. J. A 24, 275 (2005)]
CLAS [R. Bradford et al.(CLAS Collaboration), Phys. Rev. C 73, 035202 (2006)]

Feynman Diagrams for isobar model

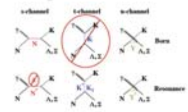

• Kaon-MAID and Saclay Lyon A

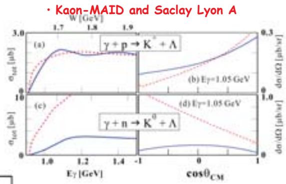

• RPR (Regge Plus Resonance)

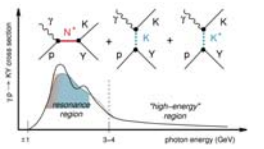

• Photon Energy Dependent Integrated Cross Section
• Kaon-MAID and Saclay Lyon A Isobar Models

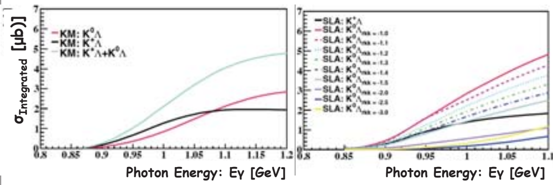

Experimental Apparatus

Tagged photon beam

NKS2+ is installed at the Research Center for Electron Photon Science (ELPH-Tohoku).

The photon beam is generated via bremsstrahlung and the scattered electron's energy is tagged by STB-Tagger system.

• Energy Region	0.8 - 1.1 GeV
$n(\gamma, K^0)\Lambda$ threshold	(915 MeV)
• Energy Resolution	10 MeV
• Beam Intensity	2×10^6 Hz
• Duty Factor	35 - 85 %

Schematic view of the experimental hall

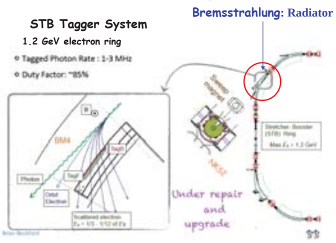

NKS2+ Upgrade Setup

- Liquid D2 or H target:
- Magnetic spectrometer
  - Hodoscopes
    - Time of Fight (TOF)
  - Particle Tracking
    - Pair of Drift Chambers: CDC and VDC
    - Momentum, trajectory, decay vertex

Schematic view of NKS2

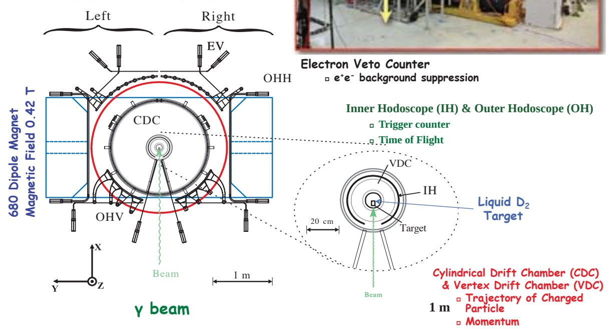

Particle Identification: PID

PID for two charged particle track events with opening angle and vertex in target region

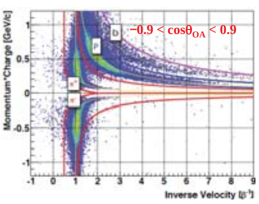

Λ(1116) Decay (cτ =7.89cm)
Λ → pπ⁻ (63.9±0.5 %)
Λ → nπ⁰ (36.1±0.5 %)

Mass squared distribution

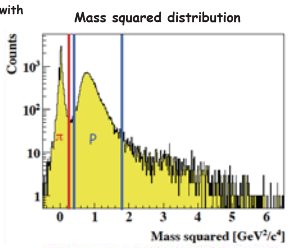

IM accepted: 1.105 -1.1205 [GeV/c2]

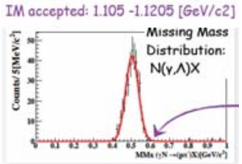

The figure above presents the correspondence particles the between momentum and inverse velocity. The red, blue and magenta line represents the pion, proton and deuteron designated regions.

Λ Event Distribution

Invariant Mass Distribution

Invariant mass distribution of $p\pi^-$. The $p\pi^-$ invariant mass is shown with the missing mass region of region of 0.60 > $MM_{p\pi-}$ >0.40 GeV/c^2 .

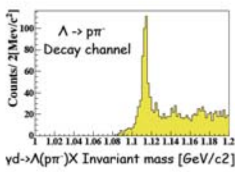

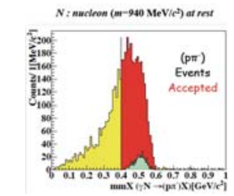

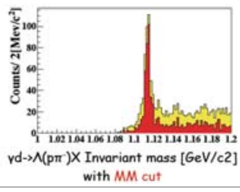

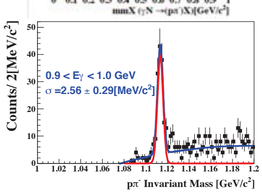

Acceptance

Simulation Condition :
Generated L isotropically in Lab frame,
0 < p_Λ < 1.2 GeV, 0.75 < $\cos\theta_\Lambda^{Lab}$ < 1.0
Use the same analyzer for the experimental data.

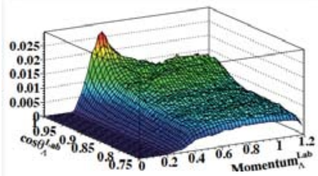

Acceptance = N_{trig}/N_{gen}

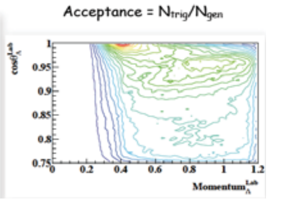

Angular Distribution

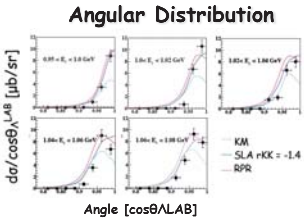

RESULTS

Angular distribution as a function of lab scattering angle.

Photon energy dependent integrated cross

Momentum dependent differential cross section

Integrated Cross Section

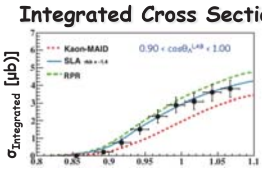

Recoil Polarization

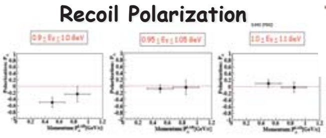

Momentum Distribution

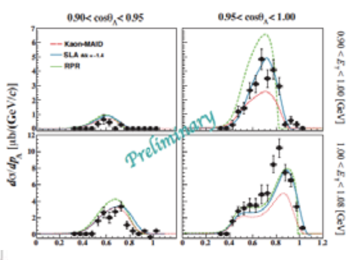

Momentum: P_Λ^{LAB} [GeV/c]

Summary

- Experiment performed with NKS2+ at the ELPH research facility using tagged photon beams on D2 target.
- Λ momentum distribution was obtained for two photon energy region, 0.9 to 1.0 GeV and 1.0 to 1.08 GeV.
- Λ angular distribution for five energy bins
  - First reported data
  - Peaks at small angles
  - NKS2+ can approximately measure total cross sections
- Λ excitation function at forward hyperon angle derived.
  - New data on excitation curves
- Λ polarization for three energy.
  - Recoil polarization is negative at Eg< 1.0
- Theory Comparison
  - Saclay Lyon A rK1Kγ = -(1.4-1.5) and Regge-Plus-Resonace provides a good agreement with data.
  - Kaon-MAID underestimates all data.

Dedicated to the memory of Professor Osamu Hashimoto

Observation of ^{7}Be Solar Neutrinos with KamLAND

The 5th GCOE International Symposium
Takemoto Yasuhiro (Physics, D3, Tohoku University) PN.4, 2013/Mar/05

^{7}Be Solar Neutrino

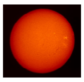

pp-chain neutrinos

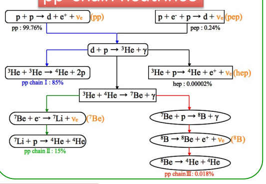

Standard Solar Model (SSM) ν flux prediction

type [cm^{-2}s^{-1}]		Emax [keV]	SSM-GS98	SSM-AGSS09
pp	10^{10}	260	5.98 (±0.6%)	6.03 (± 0.6%)
pep	10^8	1220	1.44 (±1.1%)	1.47 (± 1.2%)
hep	10^3	18,500	8.04 (±30%)	8.31 (± 30%)
^{7}Be	10^9	660	5.00 (± 7%)	4.56 (± 7%)
^{8}B	10^6	15,200	5.58 (± 14%)	4.59 (± 14%)

^{7}Be superiority

- Low, but enough high energy for a clean liquid scintillator detector
- Low energy to test matter effect to neutrino oscillation in combination with ^{8}B solar neutrinos →particle-physics
- High flux to test SSM, especially the new solar problem "solar abundance problem" →astro-physics

matter effect on neutrino oscillation

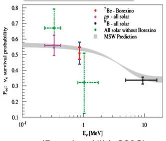

(Borexino, NIM, 2012)

- 3D solar atm.
- non-LTE

solar abundance problem

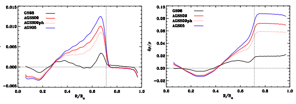

discrepancy on solar sound speed & density btw. helioseismology & SSM

(Serenelli, Astrophys.J. 2009)

KamLAND (Kamioka Liquid scintillator anti-neutrino detector)

The Detector

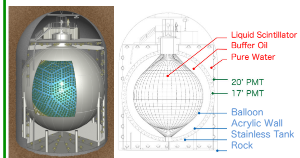

Detection method for solar ν

neutrino-electron elastic scattering

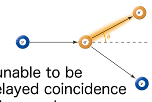

→ any events, unable to be tagged by delayed coincidence could be background

Cleanness

- cosmic rays:
  - < 10^{-5} of that at land surface ◁ 2700 m.w.e depth
- radio activities
  - ^{238}U: 7.3 x 10^{-19} [g/g]
  - ^{232}Th: 1.5 x 10^{-17} [g/g]
  - ^{40}K: < 1.5[uBq/m^3]
  - ◁ water extraction
  - ◁ nitrogen purging
  - ◁ distillation

Statistics

- volume:
  - 1000 ton liquid scintillator

Resolution

- energy:
  - 6.9%/√E(MeV)

Trigger Efficiency

- 100% @ E > 380keV
  - E(^{7}Beν) < 662keV

Purification of KamLAND liquid scintillator

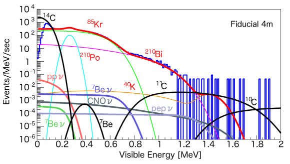

LowE data (before↑ after↓ LS_Distill)

Major Distillation Targets

Target	Reduction Goal
^{210}Pb	10^5~10^4
^{222}Rn	~10^3
^{40}K	10^2~10^1
^{85}Kr	10^6~10^5

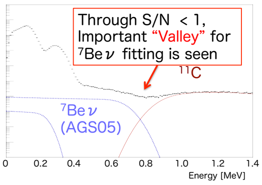

Campaign
1st phase '07/05 ~ '08/06 1,600m^3
2nd phase '08/06 ~ '09/02 3,500m^3

Temporally & Spatially variation of background

Event rate fluctuation inside R < 4.5m, ^{7}Beν energy range

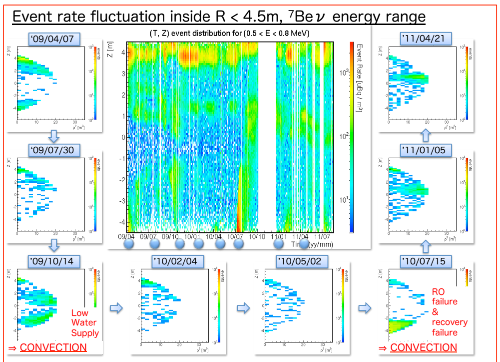

Convection of Liquid Scintillator due to thermal destabilization induces ^{210}Bi (mostly) from balloon edge.

If we fit all data at once?

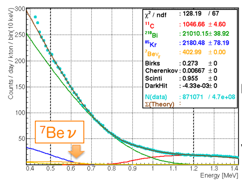

^{210}Bi overwhelms ^{7}Beν
⇓
subtle spectrum difference btw. ^{85}Kr & ^{7}Beν is missed
⇓
obtained finite value is unreliable

Better use of clean region

previous approaches

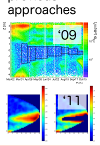

Clean region selection
① Larger volume → stat.
② Smaller surface → event position uncert.
③ Analytical selection → Smaller bias

※selection bias remains → "clean" is defined by own event rate

Fiducial Volume selection

① Larger volume
② Smaller surface
③ Analytical selection
④ Less selection bias

Use all data (clean & dirty), but **emphasize clean data**
- rank time-volume slices
- merge them into multi-data

ranking a slice with event rate in neighboring (X, T) slices

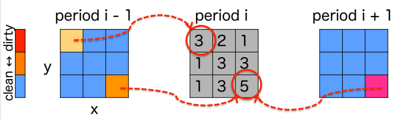

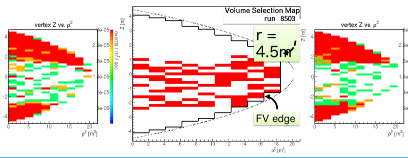

ex.) ranked period

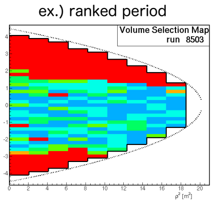

ex.) merged data sets

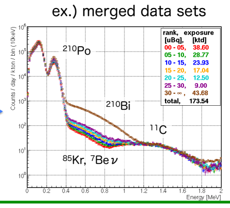

Simultaneous Fitting

Use all data (clean & dirty), but **emphasize clean data**
- simultaneous fitting

^{7}Beν determination superiority of cleaner data is preserved, but dirty data is not discarded

Simultaneous fitting with least χ^2

$$\chi^2[e][d] = \frac{\left\{D[e][d] - \left(\sum Eu[s][e][d] + \sum Ec[s][e]\right)\right\}^2}{De[e][d]^2}$$

$$\chi^2 = \sum_h \sum_b \chi^2[e][d] + \chi^2_{penalty}$$

D : data
De : data error
Eu : $\text{expected}_{uncorrelated}$
Ec : $\text{expected}_{correlated}$
e : energy_bin_{id}
d : data_set_{id}
s : spectrum_{id}

Data Set (ranked by event rate 0.5 ≦ E < 0.8 MeV)	0 - 5 uBq
	5 - 10 uBq
	10 - 15 uBq
	15 - 20 uBq
	25 - 30 uBq
	30 - uBq
Uncorrelated params	^{210}Bi
	^{85}Kr
	^{40}K, ^{238}U-^{234}U
Correlated params	^{7}Beν (free)
	^{11}C (constrained)
Fixed params	^{226}Ra~, ^{232}Th~, Spallation products
Energy Window	0.5 < E < 1.4 MeV

Fit

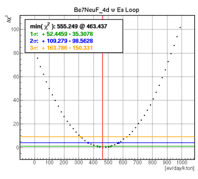

~10% uncertainty on ^{7}Beν flux is achieved so far (cf. ~5% @ Borexino)

Remaining Problems

less understanding of ^{210}Bi spectrum

^{210}Bi β decay : 1st non-unique forbidden
Correction [Allowed → Allowed + Forbidden] decay is based on experiments
Daniel (1965) lens β spectrometer
Carles (2005) LS photon counting
} Each has problem

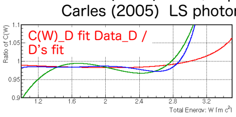

Daniel's fit does not reproduce his paper.

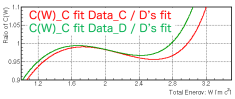

a few % difference btw. Carles' data and Daniel's data

Daniel's method should give finer answer, but not reliable.
Carles' method is better for LS detector, but larger LS detector has different response.
⇒ We need to make own ^{210}Bi spectrum

^{210}Bi spectrum generation and result

Data for ^{210}Bi spectrum
(dirtiest – cleanest) data
Assumption:
no other BG (especially ^{85}Kr) increases as ^{210}Bi increases

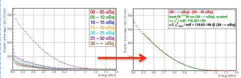

Fit ^{210}Bi spectrum
No forbidden spectrum

$$Corr(E) = (1 + \alpha E + \beta E^2 + \gamma E^3 + \delta E^4)$$

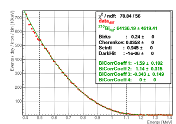

Effect of ^{210}Bi spectrum
Check parameter dependency with fitting each ranked data.
^{7}Beν should be identical by definition
^{85}Kr should be identical by assumption

Effect on ^{85}Kr

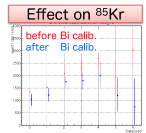

Effect on ^{7}Beν

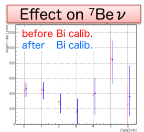

obvious dependency of
- data vs. ^{85}Kr and ^{7}Beν
- ^{85}Kr vs. ^{7}Beν

⇒ improper generation/ assumption

Better ^{210}Bi spectrum generation is required for reliable fitting.
⇒ data extraction from the same volume, different time, free from convection?

Summary

- With long endeavor of KamLAND collaborators, KamLAND equips ultra-low background LS, leading ^{7}Be solar neutrino observation.
- During solar neutrino observation phase, multiple convection induced ^{210}Bi into the center of the detector, which made temporal and spatial variation of background.
- For the better statistical treatment against such overwhelming background, following method was taken.
  - ➢ slicing volume into small pieces
  - ➢ ranking each slices and merging them
  - ➢ fitting all data simultaneously
- ~10% uncertainty of ^{7}Beν flux is achieved.
- With precise understanding of ^{210}Bi spectrum, we will finalize ^{7}Beν result then test SSM and Borexino result.

dedicated to Stuart Freedman, who was one of the great leaders of KamLAND, and who participated and gave a talk in the 1st GCOE symposium.

P-05

"Time-dependent Approach to Two-proton Radioactivity and Di-proton Correlation"

Tomohiro Oishi[A], Kouichi Hagino[A], Hiroyuki Sagawa[B]

[A] Department of Physics, Tohoku University, [B] Center for Mathematical Sciences, University of Aizu

I. Two-proton Radioactivity

✓General properties

- The novel decay-mode of proton-excessive nuclei.
- Two protons are emitted sequentially or simultaneously.
- Famous two-nucleon emitters ; ^{6}Be, ^{16}Ne, ^{45}Fe, ^{54}Zn, ^{16}Be(2n), etc.

Nuclide	^{6}Be(Z=6)	^{16}Ne(Z=10)	^{45}Fe(Z=26)	^{54}Zn(Z=30)	^{16}Be(N=10)
Decay mode	2p (100%)	2p (100%)	2p (70%)	2p (90%)	2n (?)
Q_{2N} [MeV]	1.37	1.40	1.14	1.51	1.35
Decay width [MeV]	0.092	0.11	9.7×10^{-20}	2.1×10^{-19}	?
Lifetime [s]	$\approx 10^{-19}$	$\approx 10^{-19}$	6.8×10^{-3}	3.2×10^{-3}	?

✓^{6}Be nucleus

- The most simple 2p-emitter (alpha + p + p).

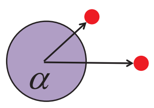

- The sequential decay through (^{5}Li + p) is forbidden.

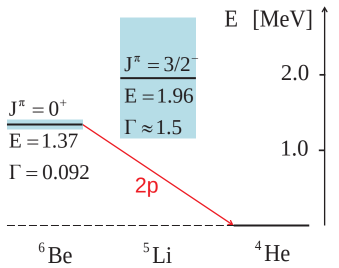

II. Two Important Factors of 2p-decay

✓Final State Interactions (FSIs)

$$H_{3\text{-}body}=h_{\alpha-p1}+h_{\alpha-p2}+\frac{\vec{p}_1\cdot\vec{p}_2}{A_\alpha m}+v_{p1-p2}(\vec{r}_1,\vec{r}_2)$$

$$=\left\{\frac{p_1^2}{2\mu_{\alpha-p}}+\boxed{V_{\alpha-p}(\vec{r}_1)}\right\}+\left\{\frac{p_2^2}{2\mu_{\alpha-p}}+\boxed{V_{\alpha-p}(\vec{r}_2)}\right\}+\frac{\vec{p}_1\cdot\vec{p}_2}{A_\alpha m}+\boxed{v_{p1-p2}(\vec{r}_1,\vec{r}_2)}$$

core-proton interaction
= Woods-Saxon + Coulomb

proton-proton interaction
= Minnesota + Coulomb

✓Initial configuration

- Decay-aspects are dominated not only by interactions but also by how two protons are before the emission.

e.g. with ``Confining Potential'' at t=0,

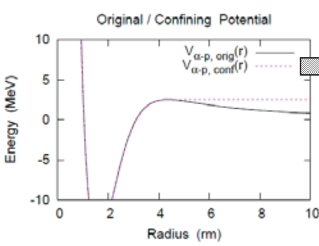

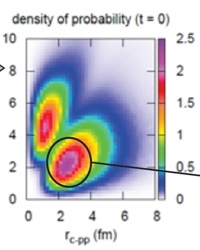

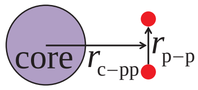

``di-proton correlation''

di-proton or di-neutron correlation (prediction)

It is theoretically expected that there is a strong correlation of two nucleons inside nuclei.

e.g. $^{17}\mathrm{Ne}={}^{15}\mathrm{O}+\mathrm{p}+\mathrm{p}$

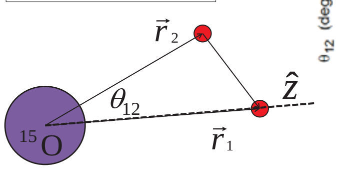

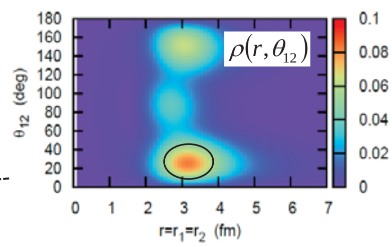

T.Oishi, K.Hagino, and H.Sagawa, PRC82,024315(2010)

III. Time-dependent Approach

✓Formalism

total state ; $|\Psi(t)\rangle=\exp\left(-it\frac{H_{3\text{-}body}}{\hbar}\right)\cdot|\Psi(0)\rangle$

$\Rightarrow$ decay state ; $|\Psi_d(t)\rangle\equiv|\Psi(t)\rangle-\beta(t)\cdot|\Psi(0)\rangle$, $\beta(t)\equiv\langle\Psi(0)|\Psi(t)\rangle$

$\Rightarrow$ decay probability ; $N_d(t)\equiv\langle\Psi_d(t)|\Psi_d(t)\rangle=1-|\langle\Psi(0)|\Psi(t)\rangle|^2$

$\Rightarrow$ decay width ; $\Gamma(t)\equiv-\hbar\frac{d}{dt}\ln[1-N_d(t)]=\frac{\hbar}{1-N_d(t)}\frac{d}{dt}N_d(t)$

✓Advantage of this method

- TD-approach makes it possible to detect the role of the initial configuration and the di-proton correlation in 2p-decay.

IV. Results (2p-decay of ^{6}Be)

✓Decay probability and width

- The calculated $Q_{2p,\mathrm{Thr.}}$ is adjusted to $Q_{2p,\mathrm{Exp.}}$=1.37 (MeV).

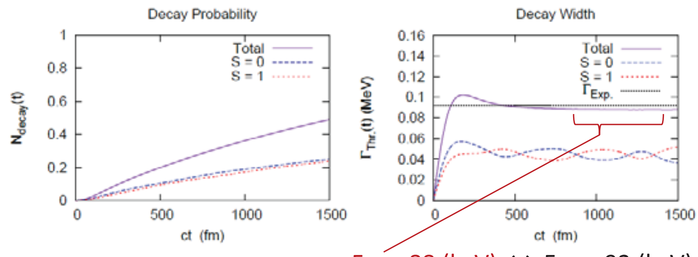

$\Gamma_{\mathrm{Thr.}}$= 88 (keV) ⟷ $\Gamma_{\mathrm{Exp.}}$= 92 (keV)

✓Time-development of density of probability

total ; $|\Psi(t,r_{c-pp},r_{p-p})|^2$ decay ; $|\Psi_d(t,r_{c-pp},r_{p-p})|^2$

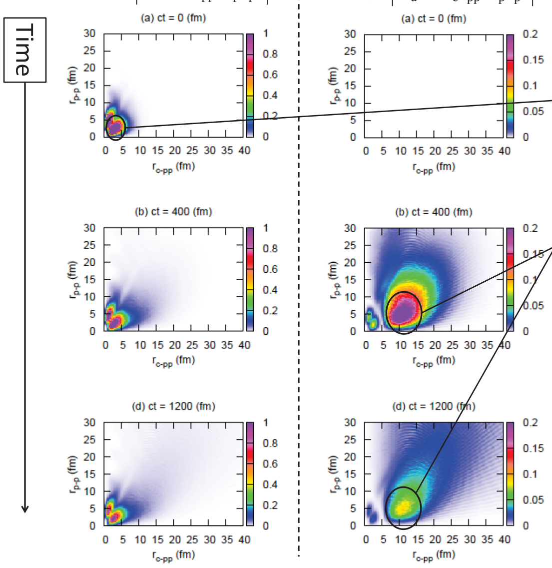

di-proton correlation in the initial configuration.

di-proton correlation by the p-p FSI.

V. Summary

✓ Conclusions

- Decay width ; $\Gamma_{\mathrm{thr.}}$ is in excellent agreement with experiments.
- Di-proton correlation in 2p-decay is apparent, as the result of both p-p FSI and initial configuration.

✓ Future Work

- It is needed to distinguish the effect of initial configuration, which is critical to discuss the intrinsic di-proton correlation inside stable nuclei.

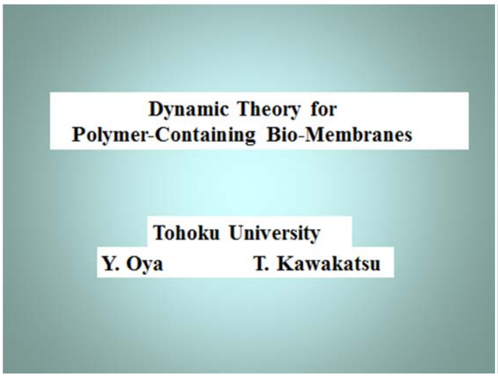
Dynamic Theory for
Polymer-Containing Bio-Membranes
Tohoku University
Y. Oya T. Kawakatsu

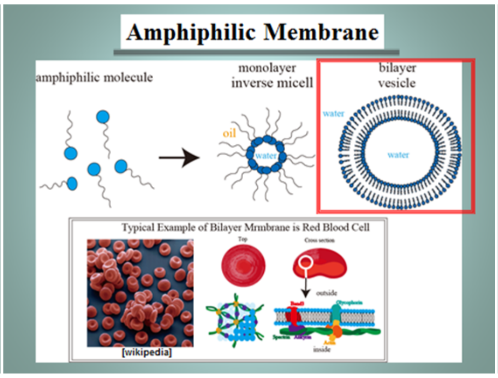
Amphiphilic Membrane
amphiphilic molecule
monolayer inverse micell
bilayer vesicle
oil
water
water
water
Typical Example of Bilayer Mrmbrane is Red Blood Cell
[wikipedia]

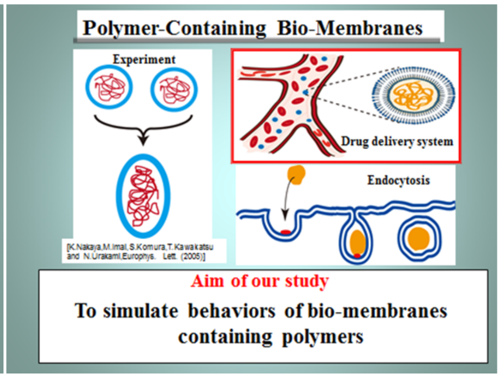
Polymer-Containing Bio-Membranes
Experiment
Drug delivery system
Endocytosis
[K.Nakaya,M.Imai,S.Komura,T.Kawakatsu and N.Urakami,Europhys. Lett. (2005)]
Aim of our study
To simulate behaviors of bio-membranes containing polymers

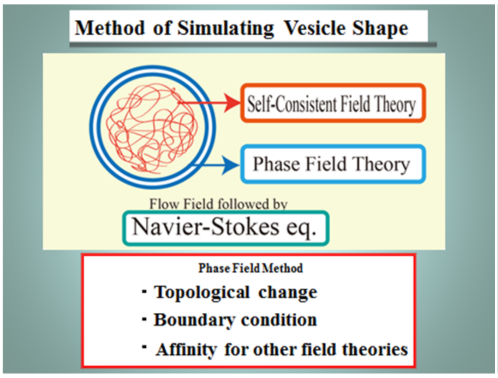
Method of Simulating Vesicle Shape
Self-Consistent Field Theory
Phase Field Theory
Flow Field followed by
Navier-Stokes eq.
Phase Field Method
・Topological change
・Boundary condition
・Affinity for other field theories

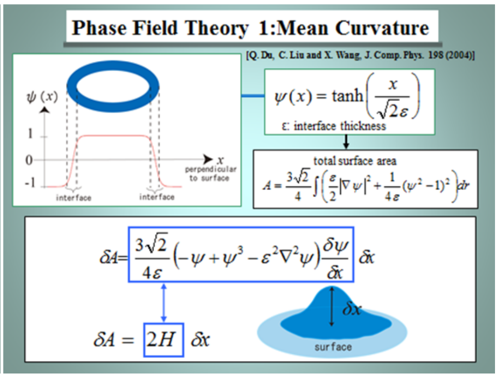
Phase Field Theory 1:Mean Curvature
[Q. Du, C. Liu and X. Wang, J. Comp. Phys. 198 (2004)]
ψ(x) = tanh(x/√2ε)
ε: interface thickness
total surface area
interface
interface
perpendicular to surface
surface

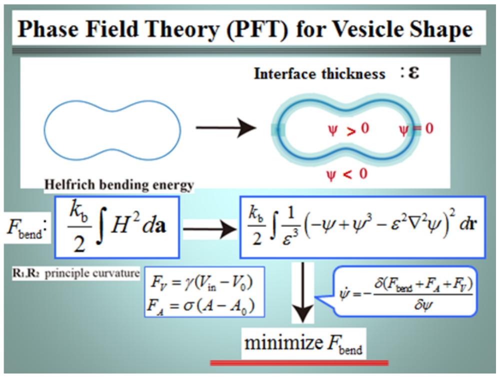
Phase Field Theory (PFT) for Vesicle Shape
Interface thickness :ε
ψ > 0
ψ = 0
ψ < 0
Helfrich bending energy
R1,R2 principle curvature
minimize F_bend

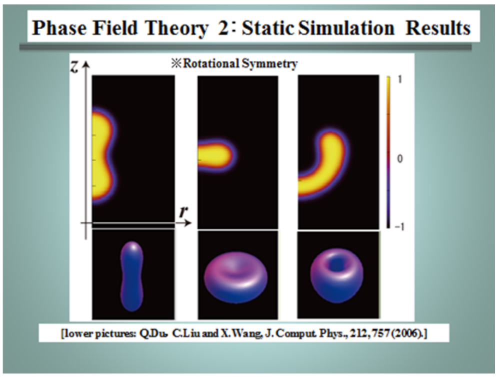
Phase Field Theory 2: Static Simulation Results
※Rotational Symmetry
[lower pictures: Q.Du, C.Liu and X.Wang, J. Comput. Phys., 212, 757(2006).]

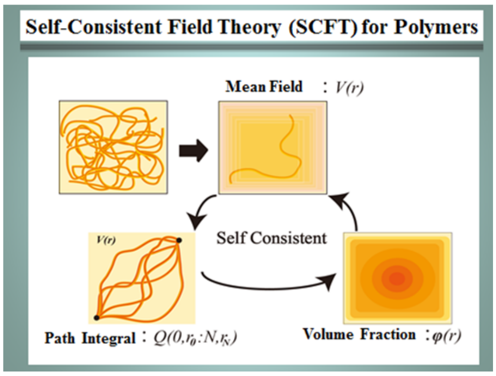
Self-Consistent Field Theory (SCFT) for Polymers
Mean Field : V(r)
Self Consistent
Path Integral : Q(0,r0:N,rN)
Volume Fraction : φ(r)

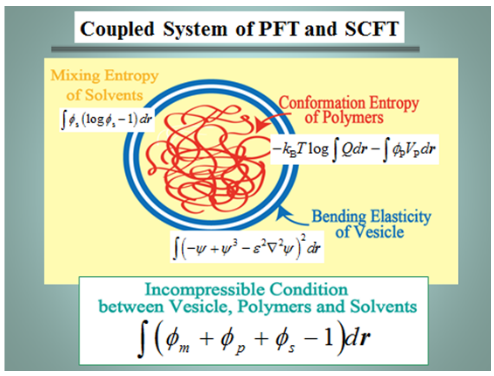
Coupled System of PFT and SCFT
Mixing Entropy of Solvents
Conformation Entropy of Polymers
Bending Elasticity of Vesicle
Incompressible Condition between Vesicle, Polymers and Solvents

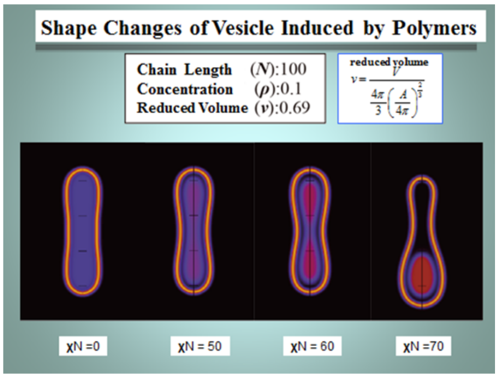
Shape Changes of Vesicle Induced by Polymers
Chain Length (N):100
Concentration (ρ):0.1
Reduced Volume (v):0.69
reduced volume
χN =0
χN = 50
χN = 60
χN =70

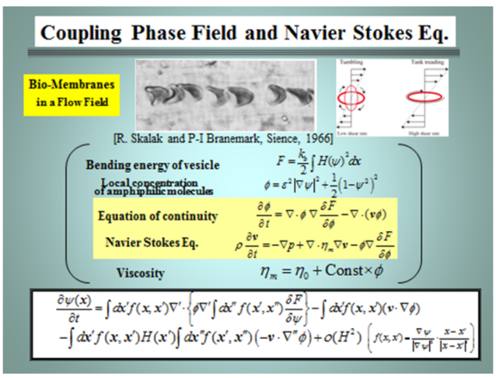
Coupling Phase Field and Navier Stokes Eq.
Bio-Membranes in a Flow Field
[R. Skalak and P-I Branemark, Sience, 1966]
Bending energy of vesicle
Local concentration of amphiphilic molecules
Equation of continuity
Navier Stokes Eq.
Viscosity

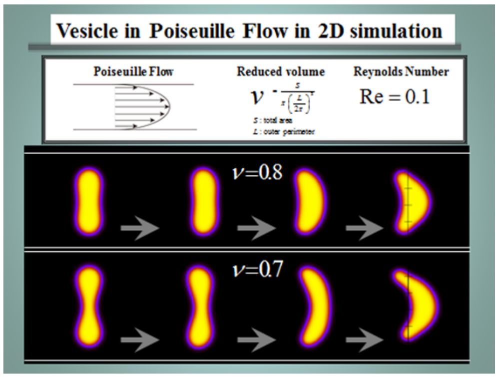
Vesicle in Poiseuille Flow in 2D simulation
Poiseuille Flow
Reduced volume
Reynolds Number
Re = 0.1
ν=0.8
ν=0.7

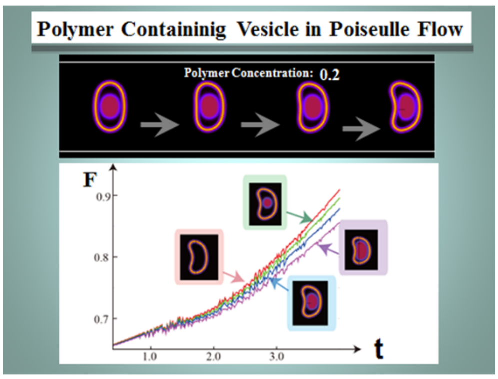
Polymer Containinig Vesicle in Poiseulle Flow
Polymer Concentration: 0.2
F
t

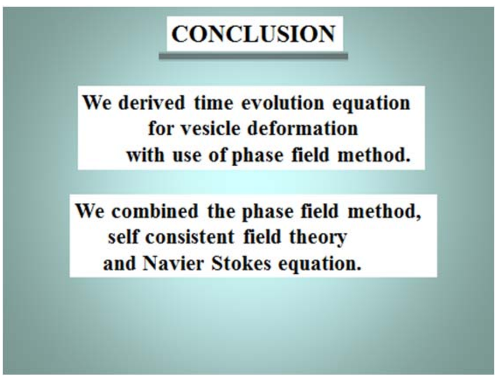
CONCLUSION
We derived time evolution equation for vesicle deformation with use of phase field method.
We combined the phase field method, self consistent field theory and Navier Stokes equation.

The $\gamma d \to \pi^+\pi^- d$ reaction in the energy region of $0.7 \leqq E_\gamma \leqq 1.1$ GeV

Chigusa Kimura for NKS2 Collaboration, Department of Physics, Tohoku University

Introduction

• **Double pion photoproduction**

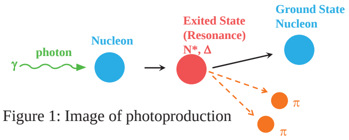

Figure 1: Image of photoproduction

•On nucleon

1. A nucleon absorbs a photon and excites.
2. The nucleon resonance decays, it emits mesons.

• To study emitted pions, we can understand
1, Possible resonance
2, Interaction between photon and nucleon.

•On deuteron

•Above first resonance region (E_γ~400MeV), the photon interacts mainly with each nucleon in the deuteron (quasi-free process).

•However, in the previous study, it was suggested that the contribution of two nucleons excitation (non-quasi-free process) is not small (ref[1]).

•**Non-quasi-free process**

•Double delta production (ref.[1])

•Coherent production (Fig.2)

without deuteron disintegration.

This process mechanism still has not been understand well. There was a few theoretical approach and a few experiments (Fig.3) .

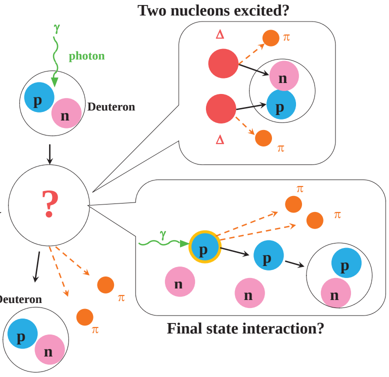

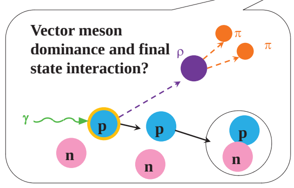

Figure 2: Coherent photoproduction

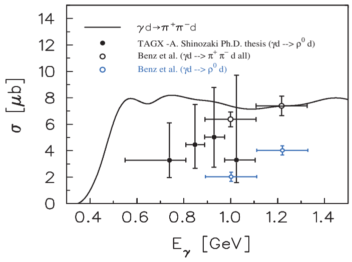

Figure3. Predicted cross section of coherent production and experimental data. (ref.[2])

*Cross section is the effective area which governs the probability of some absorption event.

The objective of this study

• Investigation of the mechanism of coherent double pion photoproduction the role in total photoabsorption.

• Obtaining the cross section and its energy dependence in $0.7 \leqq E_\gamma \leqq 1.1$ GeV.

Experiment

Photon beam

• The experiment was carried out at Research Center for Electron Photon Science (ELPH), using a photon beam.

• A photon beam is created by bremsstrahlung from an electron beam, and tagged by tagging counters.

• The photon energy range : $0.7<E_\gamma<0.9$ GeV (Energy width~5 MeV), $0.8<E_\gamma<1.1$ GeV (Energy width~6 MeV)

Neutral Kaon Spectrometer 2 (Fig. 4)

• The charged particles in the final state were detected using the Neutral Kaon Spectrometer 2 (NKS2)

• Dipole magnet (B ~ 0.42 T at the center)

• Drift chambers :Vertex Drift Chamber (VDC), Cylindrical Drift Chamber (CDC)

• TOF counters : Inner Hodoscope (IH), Outer Hodoscope (OH)

• Electron Veto

•Trigger: Detection of more than two charged particles

• Target: Liquid deuterium :located at the center of NKS2

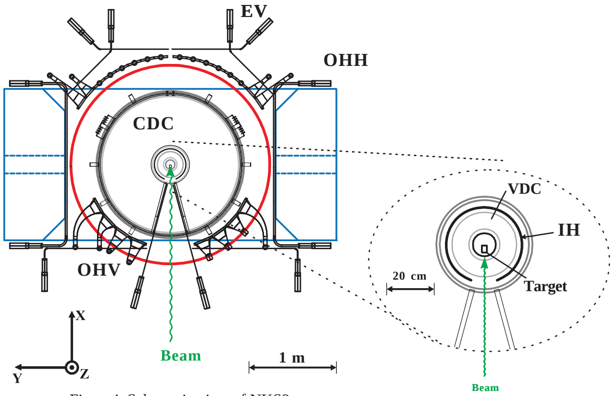

Figure4. Schematic view of NKS2

Analysis

Event Selection

Selecting events which include the three charged particle in the final state.

1. Particle identification (Fig.5)
   • Calculate Mass of particles
     • Drift Chamber: –> Momentum
     • Hodoscope: Time of flight –>Velocity of particles

$$m^2 = (1/\beta^2 - 1)p^2$$

2. Check the momentum conservation between photon energy and total momentum of three particles .
3. Select the $\gamma d \to \pi^+\pi^- d$ reaction

The yields of this reaction is shown in Fig.6.

This yields were normalized by the total photon numbers of the each experiments and the tagging efficiencies .

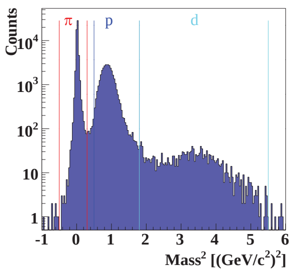

Figure 5: Squared mass distribution.

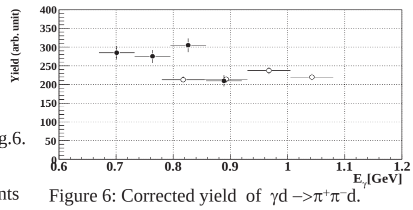

Figure 6: Corrected yield of $\gamma d \to \pi^+\pi^- d$.

Open circle : $0.7<E_\gamma<0.9$ GeV , closed circle : $0.8<E_\gamma<1.1$ GeV .

Reaction Process

Calculate the invariant mass (IM) of 2 pions to check the intermediate state.

$$IM_{\pi\pi}^2 = (E_{\pi+} + E_{\pi-})^2 - (p_{\pi+} + p_{\pi-})^2$$

• Fig. 7 show the invariant mass distribution of π^+ and π^-. Upper is in the photon energy region 0.7-0.9 GeV and lower is in 0.8-1.1GeV.

• The yellow area is 3 body phase space distribution generated by Monte Carlo Simulation.

• The peaks around 0.6 - 0.8 GeV/c² suggest the rho meson production in the intermediate state. (Mρ ~0.77 GeV/c²)

• Now detail simulations are ongoing to determine the intermediate state .

• After determination of reaction processes, the cross section can be obtained.

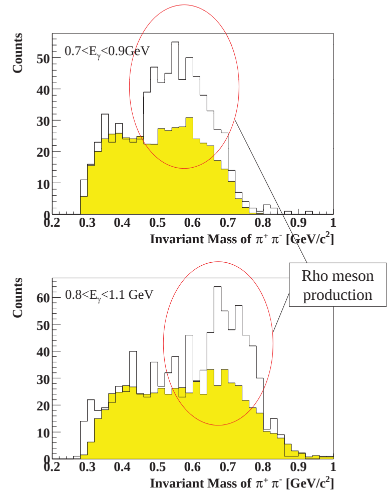

Figure 7: Invariant mass of π^+ and π^-. The yellow distribution is simulation of 3body phase space.

Summary

• The coherent photoproduction on the deuteron is useful for understanding the mechanism of photoabsorption on a bound nucleon in the GeV region.

• The experiments were carried out in the energy range of 0.7-1.1 GeV at ELPH with NKS2.

• The event which include deuteron are detected in our data, and checked these event are $\gamma d \to \pi^+\pi^- d$ event.

•The corrected yield of this event is obtained as a function of photon energy. It seems flat in this energy region.

•Invariant mass distribution of π^+ and π^- shows a peak around rho meson mass. This result shows the rho meson is produced in the intermediate state of this reaction.

Reference

.[1] K. Hirose et al.: Phys. Lett. B674 (2009)

[2] A. Fix and H. Arenhoevel : Eur. Phys.J. A25 115-135(2005)

Zenmei Suzuki (Physics, Tohoku University)

5th Mar. 2013 @ 5th GCOE international symposium

"Study of $B^\pm \to DK^\pm$, $D \to K_S K^\pm \pi^\mp$ for the measurement of CP-violating angle ϕ_3, and $D^{*\pm} \to D\pi^\pm$, $D \to K_S K^\pm \pi^\mp$ for the modeling of $D \to K_S K^\pm \pi^\mp$ Dalitz plane

1.Motivation & Theory

CKM (Cabibbo-Kobayashi-Maskawa) Matrix

$$V = \begin{pmatrix} V_{ud} & V_{us} & V_{ub} \\ V_{cd} & V_{cs} & V_{cb} \\ V_{td} & V_{ts} & V_{tb} \end{pmatrix}$$

Complex terms

$$= \begin{pmatrix} 1-\frac{\lambda^2}{2} & \lambda & A\lambda^3(\rho - i\eta) \\ -\lambda & 1-\frac{\lambda^2}{2} & A\lambda^2 \\ A\lambda^3(1-\rho-i\eta) & -A\lambda^2 & 1 \end{pmatrix} + \mathcal{O}(\lambda^4)$$

$\lambda = \sin\theta_c \sim 0.22$

Unitarity $VV^\dagger = 1$

Unitarity triangle

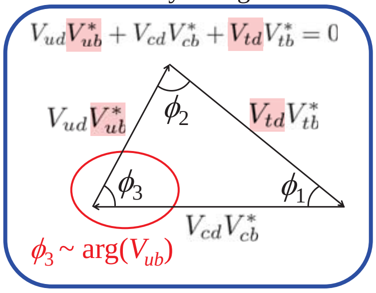

Unitarity triangle is described on complex plane, and represents CP-violation. To understand CP-violation, the angles of this triangle should be measured precisely.

Present limits for each angle

$\phi_1 = 21.15° \,^{+0.90°}_{-0.88°}$

$\phi_2 = 89.0° \,^{+4.4°}_{-4.2°}$

$\boxed{\phi_3 = 68° \,^{+13°}_{-14°}}$

ϕ_3 can be measured by examining the asymmetry between $B^- \to DK^-$ and $B^+ \to DK^+$ decays. Among the various $B^\pm$ decays, $B^\pm$ meson which decays to neutral D meson (D^0 or $\bar{D}^0$) and $K^\pm$ meson is used for ϕ_3 measurement.

The measurement accuracy of ϕ_3 is not so good, and should be improved.

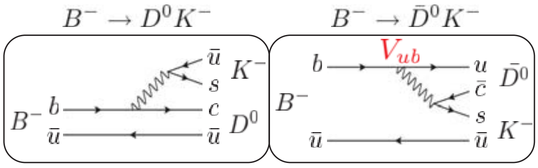

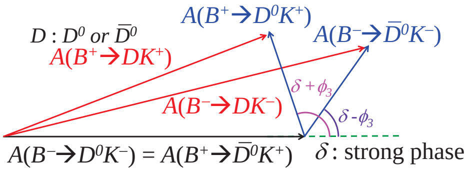

D^0 and $\bar{D}^0$ can decay to the same final states. Therefore $B^- \to D^0K^-$ and $B^- \to \bar{D}^0K^-$ decay amplitudes interfere each other. The interfering between D^0 and $\bar{D}^0$ is used to measure ϕ_3.

2.Facility

KEKB-factory & Belle Detector

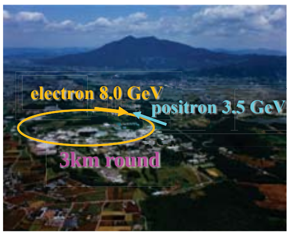

KEK@Tukuba

- KEKB-factory is a facility to make B particles.
- High energy electrons and positrons collide, and annihilate in pairs.
- From the pair annihilation, heavy B mesons are generated.

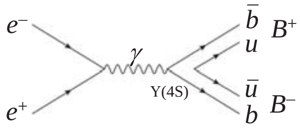

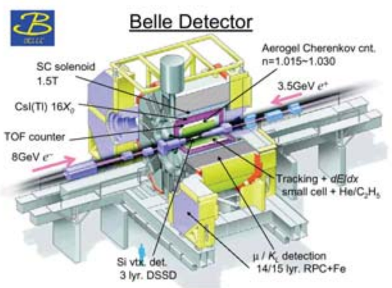

- Belle detector is to search the decays of B particles.
- Belle detector consists of many sub-detectors, and determines the particle type, momentum, charge, and so on.
- The mother particles are reconstructed from detected particles.
- The world largest data of 1014 fb^{-1} had been recorded.

3.Analysis

- Neutral D particles decay to various particles. In this study, $D \to [K_S K^\pm \pi^\mp]$ decay is searched.
- There are 2 modes in $D \to K_S K^\pm \pi^\mp$ decays : $D^0 \to K_S K^- \pi^+$, $D^0 \to K_S K^+ \pi^-$ and their charge conjugate mode, beause both D^0 and $\bar{D}^0$ can decay into $K_S K^- \pi^+$ and $K_S K^+ \pi^-$.
- D decays into $K_S K \pi$ via many intermediate processes (e.g. $D \to [K_S \pi^+]_{K^{*+}} K^-$, $D \to [K^- \pi^+]_{K^{*0}} K_S$, … etc.).
- These processes should be separated because strong phases differ. The Dalitz plot analysis is needed.
- $D^0 \to K_S K^- \pi^+$ cannot be distinguished from $\bar{D}^0 \to K_S K^- \pi^+$ in $B^\pm \to DK^\pm$, however, the information of each Dalitz plot is needed to fit $B^\pm \to DK^\pm$, $D \to K_S K^\pm \pi^\mp$ Dalitz plot.
- Therefore, $D^{*\pm} \to D\pi^\pm$, $D \to K_S K^\pm \pi^\mp$ decay which has large statistics and can be distinguished between D^0 and $\bar{D}^0$ using the charge of $D^{*\pm}$ is studied to model the Dalitz distribution of $D \to K_S K^\pm \pi^\mp$ decay.

$D^{*\pm} \to D\pi^\pm$, $D \to K_S K^\pm \pi^\mp$: Dalitz analysis

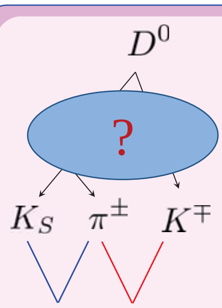

When D decays into 2 particles, and one of them decays furthermore into 2 particles, the reconstructed mass of the correct pair combination yields a mass of a certain particle.

Therefore to verify intermediate states, the plot of combination A versus combination B is used. This is the so called Dalitz plot which is used to extract the value of ϕ_3.

Dalitz plot is fitted as a superposition of some resonances. The fitting strategy has been confirming using Monte Carlo simulation.

Dalitz Plot

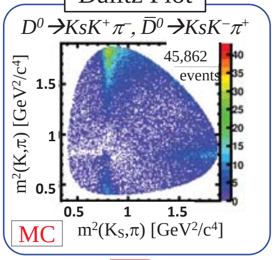

2D fit

- To fit the Dalitz plot, the effects of the background, efficiency, and resolution have been studying.
- Especially, it was understood that the resolution affect the fitting result contrary to expectation.
- The Dalitz plot of $B \to DK$, $D \to K_S K\pi$ is fitted as a superposition of $D^0 \to K_S K^+ \pi^-$ (left figure) and $D^0 \to K_S K^- \pi^+$.

Projection

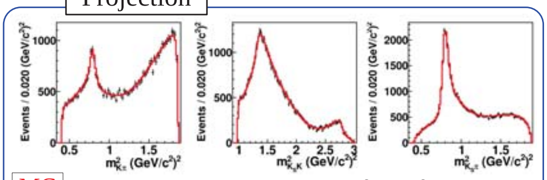

MC Black dots : data , Red line : fitted function

The fitting method is been established, and the fitting using the real data is being prepared.

4.Summary and Plan

- The precise measurement for ϕ_3 is important in terms of verification for CP-violation.
- $B \to DK$ decay is used for the measurement of ϕ_3.
- Among the various D decays, we use $D \to K_S K^\pm \pi^\mp$ with Dalitz plot.
- To make the model of $D \to K_S K^\pm \pi^\mp$ decay, $D^{*\pm} \to D\pi^\pm$, $D \to K_S K^\pm \pi^\mp$ is analyzing. The fitting strategy has been confirming.
- Of course, the final purpose is the measurement of ϕ_3 using $B^\pm \to DK^\pm$, $D \to K_S K^\pm \pi^\mp$.

P-10

Exclusive study of Λ photoproduction in the threshold region

Takao Fujii for the NKS2 Collaboration *Department of physics, Tohoku University*

Introduction

Background

The investigation of strangeness production process is very important for understanding the hadron interactions and their structures. Λ photoproduction in the threshold energy region (around 1.0 GeV) can provide invaluable information by comparing the difference on the proton and on the neutron. The experimental data on the neutron was scarce because of their experimental difficulty, but recently the experimental emphasis has been shifted to the neutron target for the comprehensive description of the reaction processes for all of six isospin channels. Because a free neutron target does not exist, the deuteron can be used as an effective target to provide a loosely bound neutron.

Processes	Photon Energy Threshold
$\gamma + p \to K^+ + \Lambda$	0.9111 GeV
$\gamma + p \to K^+ + \Sigma^0$	1.0462 GeV
$\gamma + p \to K^0 + \Sigma^+$	1.0475 GeV
$\gamma + n \to K^0 + \Lambda$	0.9153 GeV
$\gamma + n \to K^0 + \Sigma^0$	1.0506 GeV
$\gamma + n \to K^+ + \Sigma^-$	1.0521 GeV

Photon energy threshold of six strangeness photoproduction channels

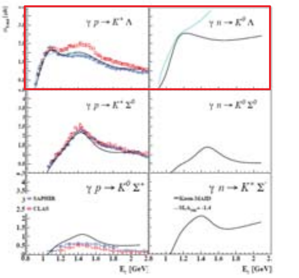

Total cross sections of six strangeness photoproduction channels

Major decay mode of K⁰ and Λ

$K^0 \to K_S^0$ (50%) / K_L^0 (50%)

$K_S^0(c\tau=2.68\,\mathrm{cm})$	$K_L^0(c\tau=1534\,\mathrm{cm})$
$K_S^0 \to \pi^+\pi^-$ (69.2%) $\to \pi^0\pi^0$ (30.7%)	$K_L^0 \to \pi^\pm e^\mp \nu_e$ (40.6%) $\to \pi^\pm \mu^\mp \nu_\mu$ (27.0%) $\to \pi^0\pi^0\pi^0$ (19.5%) $\to \pi^+\pi^-\pi^0$ (12.5%)

$\Lambda \to p\pi^-$ (63.9%) / $n\pi^0$ (35.8%)

KΛ photoproduction

We put emphasis on the KΛ production channels using the deuteron target. It is because the production mechanism of the KΛ photoproduction channels is simpler than the other channels, and the K⁺Λ production on the deuteron can be compared with the results on the free proton. We perform the exclusive study of Λ photoproduction by detecting both of K⁺Λ and K⁰Λ channels.

Neutral Kaon Spectrometer 2 (NKS2)

NKS2

In order to observe the KΛ photoproduction, we built an electromagnetic spectrometer called as the Neutral Kaon Spectrometer 2 (NKS2). The experiment is performed using the real photon beam of the Research Center for Electron Photon Science (ELPH). In the NKS2 experiment, the Λ and the neutral kaon (K^0_S) are detected via their charged decay mode($\Lambda \to p\pi^-$, $K^0 \to \pi^+\pi^-$), and the K^+ is detected directly.

The NKS2 consists of a large dipole magnet, two drift chambers, plastic scintillation hodoscopes and electron veto scintillation counters. Liquid Deuterium are used as the target.

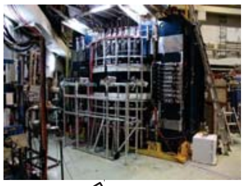

Experiment

The measurement of K^+ / K^0 and Λ photoproduction cross section with NKS2 has been performed at September and October 2010. In this experiment, we used the liquid Deuterium target and tagged photon beams around 1.0 GeV. The number of photons were 2.1×10^{12} for Sep2010 and 6.6×10^{12} for Oct2010 data.

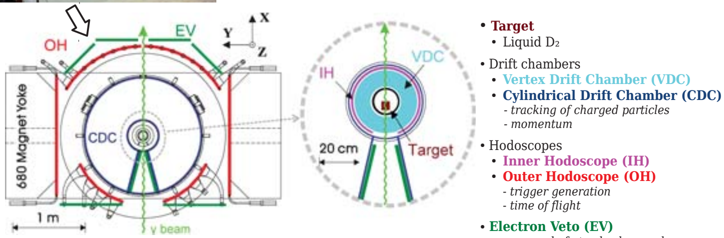

Schematic view of NKS2 & photo from backward of NKS2

Particle Identification (PID)

PID

The particle identification is determined by the mass and the charge of the particle. The mass (m) is calculated by the correlation between the momentum (p) and velocity (β) as follows :

$$m^2 = p^2\left(\frac{1}{\beta^2} - 1\right)$$

The sign of charge is determined by the bending direction in the magnetic field.

- Definition of Pion (mass = 0.1396 GeV)

$$\beta^{-1} > 0.5$$

$$|p| > \frac{0.144}{\beta^{-1} - 0.2} - 0.08 \quad (0.5 \le \beta^{-1} < 2.0)$$

$$-0.5 < m^2 < 0.25 \quad [(\mathrm{GeV}/c^2)^2]$$

- Definition of Proton (mass = 0.9383 GeV)

$$0.5 < m^2 < 1.8 \quad [(\mathrm{GeV}/c^2)^2]$$

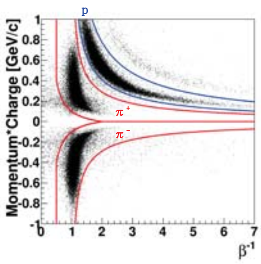

PID distribution

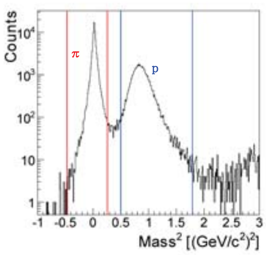

Mass² distribution

K⁺ detection

K⁺ detection

After the Λ particle selects by the invariant mass, the K⁺ is detected by the mass, the charge, and the energy deposit at IH and OH counters. The energy deposit is calculated by the Bethe-Bloch formula,

$$-\frac{dE}{dx} = \frac{Dq^2 n_e}{\beta^2}\left[\ln\left(\frac{2m_e c^2\beta^2\gamma^2}{I}\right) - \beta^2 - \frac{\delta(\gamma)}{2}\right]$$

Where x is the thickness of counters, $D \sim 5.1\times10^{-25}$ MeVcm², q is the charge (±e), n_e is the electron density, m_e is the electron mass, I is the mean ionization potential and δ is a dielectric screening correction (in this case, δ=0). The thickness of IH is 0.5 cm and the thickness of OH is 2.0 cm.

K⁺ definition is as follows,

$0.1 < m^2 < 0.45$ [(GeV/c²)²]

The Λ can be reconstructed by other 2 tracks.

The red points of the right figures are the particles detected as the K⁺. In this analysis, about 100 events are detected as the K⁺Λ reaction event.

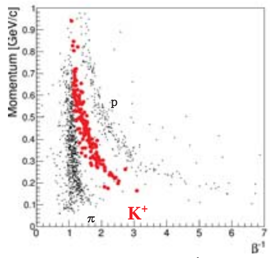

K⁺ in the Momentum vs β⁻¹ plot

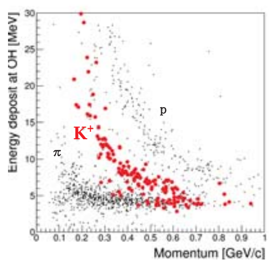

K⁺ in the Energy deposit at OH vs Monetum plot

Λ detection

K⁺Λ analysis

In this analysis, I focused on γd→K⁺Λn reaction. 3 charged tracks and 1 decay vertex are needed for the detection of this reaction. Here shows the decay vertex position around the target. The green region is the position of the target cell, and the black circle means the vacuum chamber. From the lifetime of Λ (cτ=7.89 cm), the red region is determined as the Λ decay region. And in this analysis, only Sep2010 data were used.

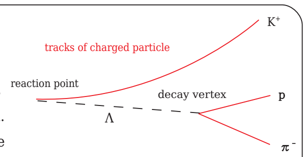

Schematic view of K⁺Λ reaction

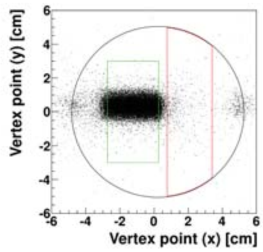

Decay Vertex position around the target

The Λ particle (mass=1.116 GeV) is detected as the peak in the pπ⁻ invariant mass spectrum. The invariant mass of pπ⁻ decay vertex is calculated as follows,

$$m_{p\pi^-}{}^2 = \left(\sqrt{m_p{}^2 + |\boldsymbol{p}_p|^2} + \sqrt{m_{\pi^-}{}^2 + |\boldsymbol{p}_{\pi^-}|^2}\right)^2 - |\boldsymbol{p}_p + \boldsymbol{p}_{\pi^-}|^2$$

Where m_p and m_{π^-} are the masses of the charged pion and proton and p_p and p_{π^-} are the momenta of each particle.

Here shows pπ⁻ decay invariant mass distributions of the simulation data and the experimental data. In the experimental data, the Λ peak can be detected clearly. The peak position is 1.114 GeV/c², and the sigma of the peak is 2.6 MeV.

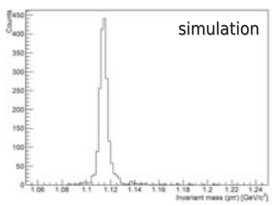

Invariant mass distribution of simulation data

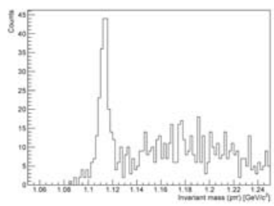

Invariant mass distribution of experimental data

Summary

- Λ photoproduction in the threshold energy region can provide invaluable information for the investigation of hadron interactions and their structure.
- The NKS2 is the electromagnetic spectrometer designed for the measurement of KΛ photoproduction. The experiment has been performed using tagged photon beam around 1.0 GeV and the liquid Deuterium target.
- The particles were identified as the pions, the protons and the kaons by the mass and the charge. The Λ was reconstructed by the pπ⁻ decay invariant mass, and about 100 events were detected as K⁺Λ reaction event in this analysis.
- The analysis for the K⁺Λ photoproduction cross section and the K⁰Λ reaction is being continued.

P-11

Development for Pulse High Field for Neutron Diffraction at J-PARC

T. Morioka, H. Nojiri, Y. Narumi, S. Yoshii, M. Baker, and K. Ohoyama
Magnetism Division, Institute for Materials Research, Tohoku University

Neutron diffraction under high magnetic field

High magnetic field : various novel phase transitions are induced by applying high magnetic fields

For example, in a frustrate system, nontrivial magnetic structure is appeared
Neutron diffraction : direct determination of magnetic structures

Combination with neutron diffraction and high magnetic fields
⇒Powerful method for magnetic materials

We developed neutron diffraction system can be performed measurement at 40 T

How to generate magnetic field

These systems are classified into two; a medium size system and a small portable system
Generate pulsed magnetic field⇒The energy stored in the capacitor is discharged into the coil

	Capacitor (mF)	Energy(kJ)	Size(mm³)	Maximum pulse magnetic field (T)	1/4 cycle (msec)
Small portable system	5.4	24	0.7×0.7×1.4	30	1.9
Medium size system	5	250	1.7×2×3.35	50	3

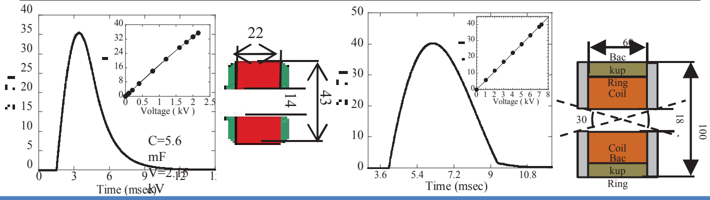

Measurement method

○Relationship between reciprocal space and scan range

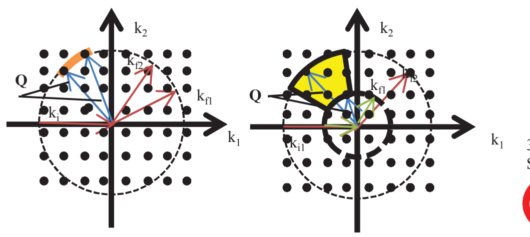

Monochromatic neutron
⇒observed a Bragg peak
Rotation of the sample
⇒scanning along circular arc

White neutron
TOF(Time of flight) method +2D detector
⇒observed wide range reciprocal space
A circular arc drew in the reciprocal space
⇒TOF and magnetic field are constant

○Utilize pulsed neutron source at J-PARC

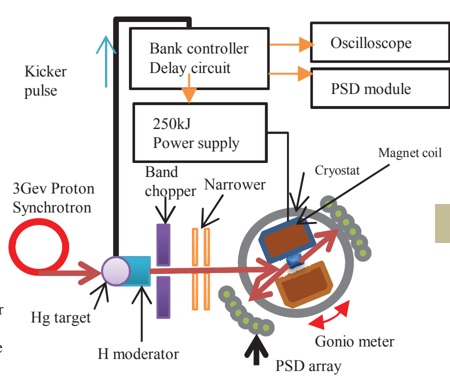

○TOF method

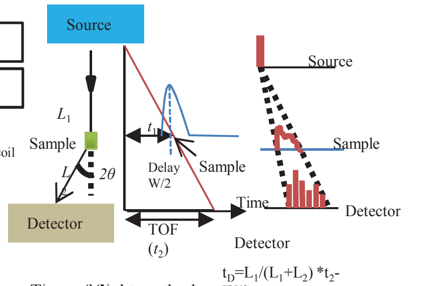

Time of flight method
Observe Bragg peaks in a pulsed magnetic field
⇒ generate a pulsed magnetic field synchronizes with the neutron pulses

Experiment

Sample:TbMnO3(multiferroic material)

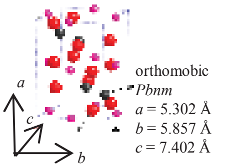

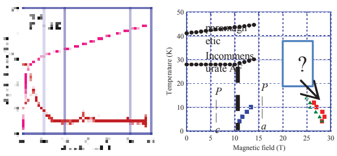

Different magnetic structure ⇒q_{Mn}~0.28 b*, q_{Tb}~0.42b*
Three critical point at zero field⇒T=7K, 28 K,41 K
Anomaly of magnetization around 28 T
⇒ Electric polarization appeared with magnetic structure (B // *a*)
⇒possibility of a new magnetic order
Purpose of our measurement･･･
We perform measurement up to 40 T at J-PARC(BL10 NOBORU)
⇒determine the propagation vector in high magnetic field

Result 1

○Single detector captured multi Bragg peaks along vertical axis

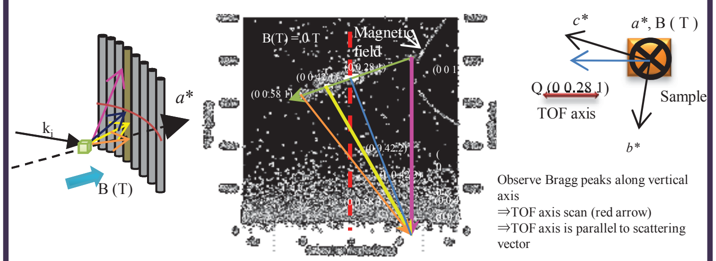

Observe Bragg peaks along vertical axis
⇒TOF axis scan (red arrow)
⇒TOF axis is parallel to scattering vector

○ Bragg peaks are captured along horizontal axis

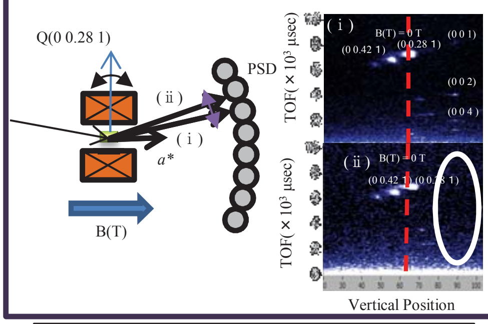

Scanning along 2θ direction
⇒ Bragg peaks of different scattering vector are captured
⇒in this case, scanning around (0 0.28 1) in reciprocal space

Result 2

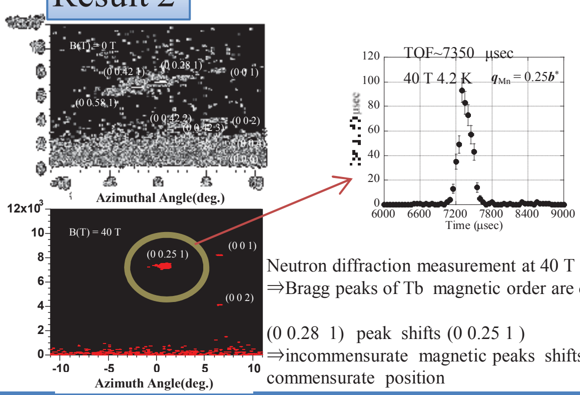

Neutron diffraction measurement at 40 T
⇒Bragg peaks of Tb magnetic order are disappeared

(0 0.28 1) peak shifts (0 0.25 1)
⇒incommensurate magnetic peaks shifts to commensurate position

Discussion and conclusion

- ☐We development of pulse high field for neutron diffraction
- ☐Perform measurement neutron diffraction up to 40 T at J-PARC
- ☐Observed propagation vector change (0 0.28 1) with (0 0.25 1)
- ☐Next step⇒develop this system to perform measurement up to 50 T

P-09

The relationship between various analytical techniques of T-duality

Y.Teshima

In collaboration with T. Asakawa , S. Watamura and U. Carow-Watamura

arXiv:1201.0125v2 [hep-th]

Introduction

String theory

A theory which regards elementary objects as a string

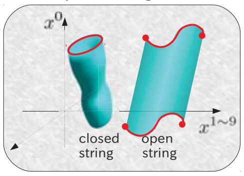

closed string

→ graviton $g_{\mu\nu}$

open string

→ gauge field A_μ

String theory is a candidate of quantum gravity

but defined only perturbatively

→ we want to find the stringy geometry

(cf. general relativity ⟷ Riemannian geometry)

→ This must encode the property of **T-duality**

T-duality

Spectrum of the closed string

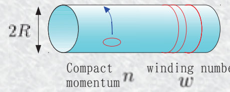

Compact momentum n winding number w

$$m^2 = \frac{n^2}{R^2} + \frac{w^2 R^2}{\alpha'^2} + \frac{2}{\alpha'}(N + \tilde{N} - 2)$$

$$R \to \tilde{R} = \frac{\alpha'}{R}$$

$$m^2 = \frac{w^2}{\tilde{R}^2} + \frac{n^2 \tilde{R}^2}{\alpha'^2} + \frac{2}{\alpha'}(N + \tilde{N} - 2)$$

Compact Momentum w winding nunger n

The theory with radius R
= The theory with radius $\tilde{R}$

→ T-duality

D-brane

the hypersurface where open strings end.

The direction along the D-brane

→ Neumann condition

The direction perpendicular to the D-brane

→ Dirichlet condition

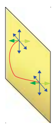

p dimensional D-brane = Dp-brane

The effective theory on N D-branes

= $U(N)$ gauge theory

T-duality and D-brane

Dirichlet and Neumann condition are exchanged under the T-duality

→ T-dual normal to the D-brane $Dp \to D(p+1)$

T-dual along the D-brane $Dp \to D(p-1)$

Bound state of D-branes

Bound state of the D-branes

Correspond to a soliton solution

in the effective theory

※ Topological charge

= the number of D-branes

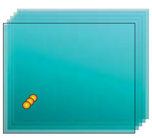

Various approaches to disscuss T-duality

Buscher rule
Nahm transformation
Boundary state analysis
Hori formula

→ We analyzed the compatibility among them.

Nahm transformation

Original Nahm transformation

$U(N)$ Gauge theory k instanton on T^4 ⟶ $U(k)$ Gauge theory N instanton on $\tilde{T}^4$

D-brane interpretation

$N\,D4\,/\,k\,D0$ ⟶ $k\,D4\,/\,N\,D0$

Consistent with T-duality

Generalization of Nahm transformation to 2d

We consider the classical solution on T^2

=constant magnetic flux

$$U(N),\ C_1 = \int \mathrm{tr}\,\frac{F}{2\pi} = k$$

$$\Longrightarrow A_1 = 0\,,\quad A_2 = \frac{k}{2\pi N R_1 R_2} x_1\,,\quad F_{12} = \frac{k}{2\pi N R_1 R_2}$$

There is a freedom to add constants $\tilde{x}_1, \tilde{x}_2$

$$\to A_1 = \tilde{x}_1\,,\quad A_2 = \frac{k}{2\pi N R_1 R_2} x_1 + \tilde{x}_2$$

$$\tilde{x}_\mu \sim \tilde{x}_\mu + 1/R_\mu$$

$\Longrightarrow$ $\tilde{x}_\mu$ is the coordinate on $\tilde{T}^2$

We will construct the gauge field on $\tilde{T}^2$ by Dirac zero mode ($\bar{\mathcal{D}}_{\tilde{x}}\psi = 0$).

$\bar{\mathcal{D}}_{\tilde{x}}$:The Dirac operator on $T^2 \times \tilde{T}^2$

$$\mathcal{D}_{\tilde{x}} = \gamma^\mu D_{\tilde{x}\mu} = \begin{pmatrix} 0 & \mathcal{D}_{\tilde{x}} \\ \bar{\mathcal{D}}_{\tilde{x}} & 0 \end{pmatrix},\quad \begin{aligned} \mathcal{D}_{\tilde{x}} &= -i(\partial_1 - iA_1 - i\tilde{x}_1) - (\partial_2 - iA_2 - i\tilde{x}_2)\,, \\ \bar{\mathcal{D}}_{\tilde{x}} &= -i(\partial_1 - iA_1 - i\tilde{x}_1) + (\partial_2 - iA_2 - i\tilde{x}_2) \end{aligned}$$

$\bar{\mathcal{D}}_{\tilde{x}}\psi = 0$ has k solutions

→ construct $N \times k$ matrix

$$\to \psi = \underbrace{\left(\psi_1 \cdots \psi_k\right)}_{k} \Big\}\, N$$

The gauge field on $\tilde{T}^2$ is

$$\tilde{A}_\mu(\tilde{x}) = i \int_{T^2} d^2x\, \psi^\dagger \tilde{\partial}_\mu \psi$$

$$\longrightarrow \tilde{A}_1 = 0\,,\quad \tilde{A}_2 = -\frac{N}{2\pi k \tilde{R}_1 \tilde{R}_2}\tilde{x}_2\,,\quad \tilde{F}_{12} = -\frac{N}{2\pi k \tilde{R}_1 \tilde{R}_2}$$

$$\to U(k)\,,\ C_1 = -N$$

Atiyah-Singer family index theorem

$$\int_{T^2} \mathrm{ch}(\mathcal{P})\,\mathrm{ch}(E) = \mathrm{ch}(\tilde{E})$$

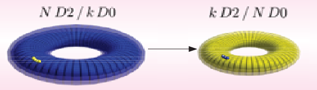

?

Nahm transformation:
$N\,D2\,/\,k\,D0 \to k\,D2\,/\,N\overline{D0}$

Boundary state on the torus

Boundary state

partition function of cylinder

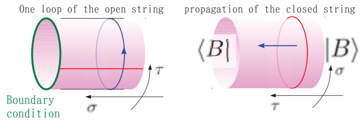

The initial, final state of the closed string associated with

the boundary condition of the open string

‖

D-brane

ex) In case of Dirichlet condition

$$\left.\frac{\partial X^i}{\partial \tau}\right|_{\sigma=0} = 0 \longleftrightarrow \left.\frac{\partial X^i}{\partial \sigma}\right|_{\tau=0} |B\rangle = 0$$

Calculate the boundary state with the flux associated with $(U(N), C_1 = k)$ on T^2

$$\begin{aligned} |B_F\rangle = &\sqrt{(a_1 a_2 N)^2 + k^2}\sum_{\nu\in\mathbb{Z}^2} e^{-i\pi \mathbf{m}^1\mathbf{m}^2 \frac{k}{N}} \\ &\times \left[\prod_{n=1}^\infty \exp\left\{-\frac{1}{n}\frac{1}{a_1^2 a_2^2 N^2 + k^2}(\alpha_n^{1\dagger}\alpha_n^{2\dagger})\begin{pmatrix} a_1^2 a_2^2 N^2 - k^2 & 2a_1 a_2 N k \\ -2a_1 a_2 N k & a_1^2 a_2^2 N^2 - k^2 \end{pmatrix}\begin{pmatrix} \tilde{\alpha}_n^{1\dagger} \\ \tilde{\alpha}_n^{2\dagger} \end{pmatrix}\right\}\right] \\ &\times \left|\begin{pmatrix} -k\nu_2 \\ k\nu_1 \end{pmatrix}, \begin{pmatrix} N\nu_1 \\ N\nu_2 \end{pmatrix}\right\rangle \end{aligned}$$

T-dual transformation $\left\{ \begin{aligned} \mathbf{m}^M &\longleftrightarrow \mathbf{n}^M \\ \alpha_n^M &\longrightarrow \alpha_n^M \\ \tilde{\alpha}_n^M &\longrightarrow -\tilde{\alpha}_n^M \end{aligned} \right.$

$$\begin{aligned} |B_F\rangle_{12} = &\sqrt{N^2 + (\tilde{a}_1 \tilde{a}_2 k)^2}\sum_{\nu\in\mathbb{Z}^2} e^{-i\pi N k \nu^1 \nu^2} \\ &\times \left[\prod_{n=1}^\infty \exp\left\{-\frac{1}{n}\frac{1}{\tilde{a}_1^2 \tilde{a}_2^2 k^2 + N^2}(\alpha_n^{1\dagger}\alpha_n^{2\dagger})\begin{pmatrix} \tilde{a}_1^2 \tilde{a}_2^2 k^2 - N^2 & -2\tilde{a}_1 \tilde{a}_2 N k \\ 2\tilde{a}_1 \tilde{a}_2 N k & \tilde{a}_1^2 \tilde{a}_2^2 k^2 - N^2 \end{pmatrix}\begin{pmatrix} \tilde{\alpha}_n^{1\dagger} \\ \tilde{\alpha}_n^{2\dagger} \end{pmatrix}\right\}\right] \\ &\times \left|\begin{pmatrix} N\nu_2 \\ -N\nu_1 \end{pmatrix}, \begin{pmatrix} k\nu_1 \\ k\nu_2 \end{pmatrix}\right\rangle \end{aligned}$$

$$\to U(k)\,,\ C_1 = -N$$

Consistent with the 2d Nahm transformation

Fermionic Part

NS-NS sector $(\psi_r, \tilde{\psi}_r)$ $\left(r \in \mathbb{Z} + \frac{1}{2}\right)$

R-R sector $(\psi_n, \tilde{\psi}_n)$ $(n \in \mathbb{Z})$

We consider the R-R zeromodes.
(Other modes contribute to the boundary state in the same way to the bosonic sector.)

The state

$$|Dp\rangle = \theta_p^\dagger \theta_{p-1}^\dagger \cdots \theta_0^\dagger\, |[C]\rangle \qquad \theta^\mu = \left(\psi_0^\mu + i\tilde{\psi}_0^\mu\right)/\sqrt{2}\,,\quad \{\theta^\mu, \theta_\nu^\dagger\} = \delta_\mu^\nu$$

$|[C]\rangle$:the vacuum state

satisfies the boundary condition for a Dp brane.

$$\begin{aligned} \theta_\alpha^\dagger\, |Dp\rangle &= 0,\ (\alpha = 0, \cdots, p)\,, \\ \theta_i\, |Dp\rangle &= 0,\ (i = p+1, \cdots, 9) \end{aligned}$$

Then the D2/D0 bound state is

$$\begin{aligned} |D2D0\rangle &= N e^{2\pi\alpha' F_{12}\theta^1\theta^2}\, |D2\rangle \\ &= N(1 + F_{12}\theta^1\theta^2)\, |D2\rangle \\ &= N\, |D2\rangle + k\, |D0\rangle \end{aligned}$$

T-duality transformation is represented by an operator:

$$\mathcal{T}_\alpha = \theta^\alpha - \theta^{\alpha\dagger}$$

Then the T-duality of $|D2D0\rangle$ is

$$|D2D0\rangle' = \mathcal{T}_2\mathcal{T}_1\, |D2D0\rangle = k\, |D2\rangle - N\, |D0\rangle$$
$$(N, k) \to (k, -N)$$

RR-charges of D-branes are measured by the coupling to closed-string states of RR-potentials.

RR-state can be defined as

$$\langle \mathcal{A}| = \langle [C]|\,\mathcal{A} = \langle [C]| \sum A_{\mu_1\cdots\mu_q}\theta^{\mu_1\cdots\mu_q}$$

And the T-duality transformation is

$$\begin{aligned} \langle \mathcal{A}|\, \mathcal{T}_1^\dagger \mathcal{T}_2^\dagger &= \langle [C]| \left(\mathcal{A}^{(0)} + \mathcal{A}_1^{(1)}\theta^1 + \mathcal{A}_2^{(1)}\theta^2 + \mathcal{A}_{12}^{(2)}\theta^1\theta^2\right) \mathcal{T}_1^\dagger \mathcal{T}_2^\dagger \\ &= \langle [C]| \left(\mathcal{A}^{(0)}\theta^1\theta^2 - \mathcal{A}_1^{(1)}\theta^2 + \mathcal{A}_2^{(1)}\theta^1 + \mathcal{A}_{12}^{(2)}\right) \end{aligned}$$

Then the T-duality rule for the RR-potentials is

$$\mathcal{A}'^{(0)} = -\mathcal{A}_{12}^{(2)}\,,\ \mathcal{A}_1'^{(1)} = \mathcal{A}_2^{(1)}\,,\ \mathcal{A}_2'^{(1)} = -\mathcal{A}_1^{(1)}\,,\ \mathcal{A}_{12}'^{(2)} = \mathcal{A}^{(0)}$$

The coupling of RR-potentials to D-brane is given by Chern-Simons term

$$I_{CS} = \langle \mathcal{A}|\, [GSO] c_0 \tilde{c}_0\, |\mathcal{B}\rangle\,.$$

$[GSO]$:GSO projection
$|\mathcal{B}\rangle$:full boundary state
$c_0, \tilde{c}_0$:ghost

We can prove that I_{CS} is invariant under T-duality:

$$\begin{aligned} I_{CS} &= \langle \mathcal{A}|\, [GSO]\mathcal{T}^\dagger\mathcal{T} c_0 \tilde{c}_0\, |\mathcal{B}\rangle \quad (1 = \mathcal{T}^\dagger\mathcal{T}\,,\ \mathcal{T} = \mathcal{T}_2\mathcal{T}_1) \\ &= \langle \mathcal{A}|\, \mathcal{T}^\dagger [GSO] c_0 \tilde{c}_0 \mathcal{T}\, |\mathcal{B}\rangle \quad (\text{Since } \mathcal{T} \text{ commutes with } [GSO].) \\ &= \langle \mathcal{A}'|\, [GSO] c_0 \tilde{c}_0\, |\mathcal{B}'\rangle \end{aligned}$$

I_{CS} is invariant under T-duality transformation.

Hori formula

I_{CS} can be written in terms of differential forms as

$$\begin{aligned} I_{CS} &= \mu_2 \int_M \mathcal{A} \wedge \mathrm{Tr}_N\left(e^{2\pi\alpha' F}\right) \\ &= \mu_2 \int_M \left(\mathcal{A}^{(0)} + \ldots + \mathcal{A}_{12}^{(2)} dx^1 \wedge dx^2\right)\left(N + k dx^1 \wedge dx^2\right) \\ &= N\mu_2 \int_M A_{12}^{(2)} dx^1 \wedge dx^2 + k\mu_0 \int_{\mathbb{R}} A^{(0)} \end{aligned}$$

In terms of differential forms,
T-duality is represented by Hori formula:

$$A' = -\int_{T^2} A e^{dx^i \wedge dy_i}$$

By using this, the Chern-Simons term is transformed as

$$\begin{aligned} &\mu_2 \int_{\tilde{M}} \mathcal{A}' \wedge \mathrm{Tr}_k\left(e^{2\pi\alpha' \tilde{F}}\right) \qquad (\tilde{M} = \mathbb{R} \times \tilde{T}^2) \\ &= \mu_2 \int_{\tilde{M}} \left(\mathcal{A}'^{(0)} + \cdots + \mathcal{A}_{12}'^{(2)} dy^1 \wedge dy^2\right)\left(k - N dy^1 \wedge dy^2\right) \\ &= N\mu_2 \int_{\tilde{M}} A_{12}^{(2)} dy^1 \wedge dy^2 + k\mu_0 \int_{\mathbb{R}} \mathcal{A}^{(0)} \end{aligned}$$

→ invariant under T-duality

Summary and discussion

- Nahm transformation was extended naively to 2d.
- It consistent with T-duality in string theory. $(N, k) \to (k, -N)$
- It indicates $\mathbb{Z}_4$-duality nature of T-duality
  cf. Fourier transformation $(x, p) \to (p, -x) \to (-x, -p)$
- we introduced the T-duality operator which act both on the boundary state and the RR q-form state.
- We clarified the relationship between T-duality rule at the superstring level and that at the low energy effective theory

No.12

Dopant dependence of x-ray induced phase transition In impurity doped layered manganites

Y. Yamaki

Department of physics, Tohoku University

1.Introduction

1-1. Photo induced phase transition

(1)$Pr_{0.7}Ca_{0.3}MnO_3$

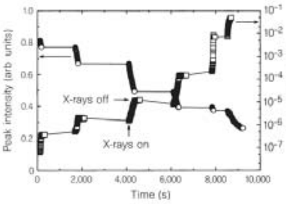

(2)W:VO_2

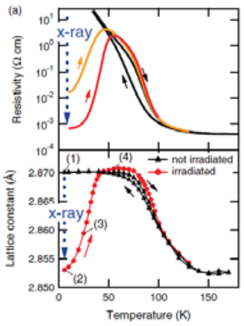

(1) Insulating antiferromagnetic state(charge ordering) → metallic ferromagnetic state
(2)Insulator → metal

1-2. Bicritical phase competition & object material

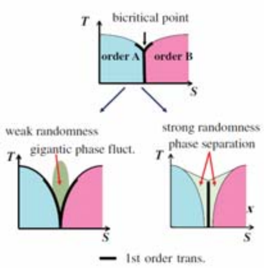

$La_{0.5}Sr_{1.5}MnO_4$

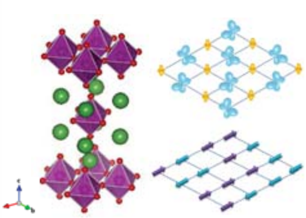

Phase diagram

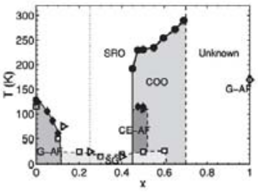

Temperature dependence of order parameter for COO

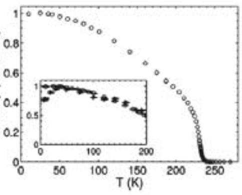

A single layered manganite $La_{0.5}Sr_{1.5}MnO_4$ shows charge-orbital ordering(COO) below T = 240K. We have investigated the impurity effect on COO state in this material and substituted Fe ions for Mn ions. In Fe-doped compound, not only that transition temperature and order parameter of COO decrease but also COO state is strongly suppressed by x-ray irradiation at low temperature. In this paper we report this photo induced phase transition in impurity doped manganite $La_{0.5}Sr_{1.5}Mn_{1-x}Fe_xO_4$.

2.Experiments

Experimental configuration

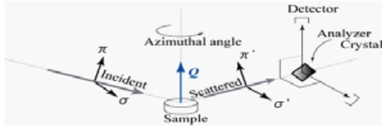

- Resonant and non-resonant x-ray scattering experiment.
- $La_{0.5}Sr_{1.5}Mn_{1-x}Fe_xO_4$ single crystal.
- BL-4C and BL-3A, Photon Factory, KEK.
- Incident x-ray Energy : Mn *K*-edge(~6.55keV) and 6.5keV.
- Polarization analysis : Cu(220).
- Configuration at $E_i//c$ is defined as $\Psi=0$

Spin configurations of impurity ions

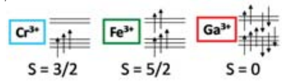

Schematic view of impurity substitution

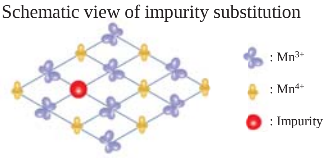

3. Results

3-1. X-ray exposure effect in $La_{0.5}Sr_{1.5}Mn_{0.97}Fe_{0.03}O_4$

(a) X-ray exposure time dependence of the intensity for Q = (1/4 7/4 0)

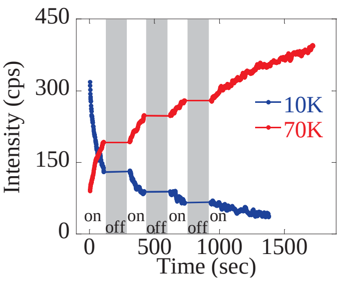

(b) X-ray exposure time dependence of the correlation length of COO

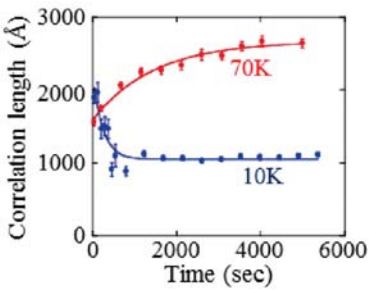

(c) Incident x-ray photon flux dependence of the intensity for Q = (1/4 7/4 0)

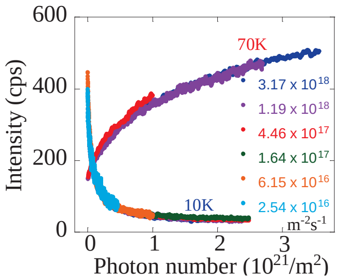

(d) X-ray exposure time dependence of AC-magnetic susceptibility

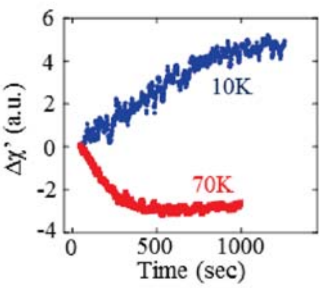

→ **This phenomenon is induced by x-ray exposure.**
X-ray induces phase transition between antiferromagnetic charge-orbital ordered (AFM/COO) and ferromagnetic charge-orbital disordered (FM/DO) states.

3-2. Temperature dependence of x-ray induced phase transition in $La_{0.5}Sr_{1.5}Mn_{0.97}Fe_{0.03}O_4$

(a) Temperature variation of x-ray PIPT

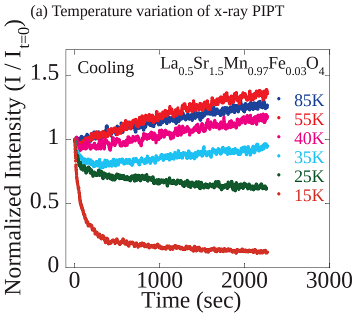

(b) Temperature dependence of I(0) and I(∞)

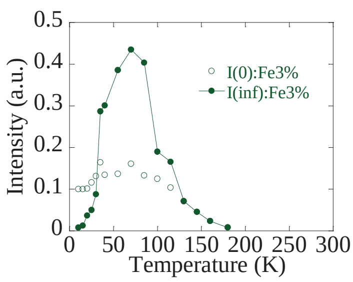

(c) Schematic view of bidirectional x-ray PIPT by double minimum potential model

$T < 35$ K $E_{FM} < E_{CO}$ $40 K < T < 130$ K $E_{FM} > E_{CO}$

3-4. Dopant dependence of x-ray PIPT in $La_{0.5}Sr_{1.5}Mn_{1-x}M_xO_4$ (M = Cr, Fe, Ga)

(a) Dopant dependence of x-ray PIPT

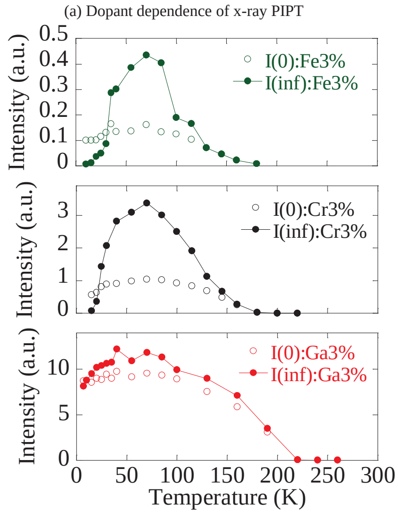

(b) Ga concentration dependence of x-ray PIPT

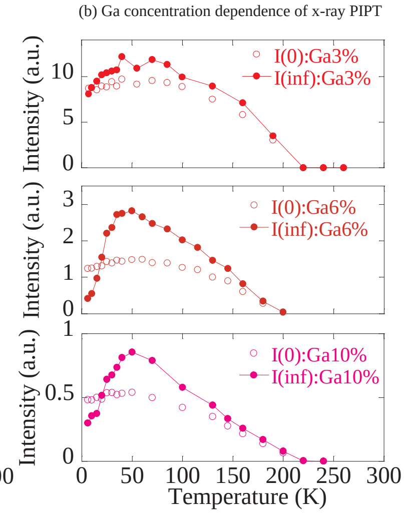

(c) Dopant dependence of x-ray exposure effect on correlation length

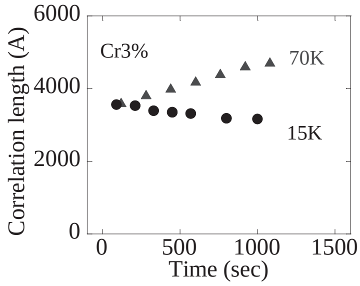

(d) Ga concentration dependence of x-ray exposure effect on correlation length

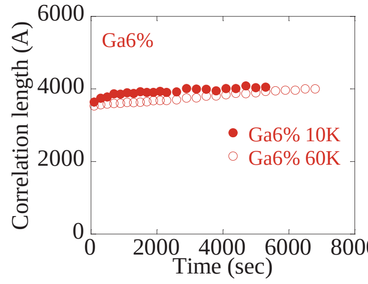

4. Conclusion

In this study we have investigated photo induced phase transition in impurity doped manganites.

1. **Phase-separated state between the charge-orbital ordered and ferromagnetic phases is realized by impurity doping.**
2. **In this phase-separated region, x-ray induced persistent and bidirectional phase transition between charge-orbital ordered and ferromagnetic phases was observed.**
3. **In the present case, impurity doping plays a crucial role in forming the phase-separated state and also in determining the rate of x-ray induced phase transition.**

Reference
- Saioa Cobo, Denis Ostrovskii, Sebastian Bonhommeau, Laure Vendier, Gabor Molnar, Lionel Salmon, Koichiro Tanaka, and Azzedine Bousseksou, J. AM. CHEM. SOC. **130**, 9019 (2008).
- V. Kiryukhin, D. Casa, J. P. Keimer, A. Vigliante, Y. Tomioka, and Y. Tokura, Nature 386, 813 (1997).
- K. Shibuya, D. Okuyama, R. Kumai, Y. Yamasaki, H. Nakao, Y. Murakami, Y. Taguchi, T. Arima, M. Kawasaki, and Y. Tokura, Phys. Rev. B **84**, 165108 (2011)
- S. Larochelle, A. Mehta, L. Lu, P. K. Mang, O. P. Vajk, N. Kaneko, J. W. Lynn, L. Zhou, and M. Greven Phys. Rev. B **71**, 024435 (2005)
- Y. Tokura, JPSJ 75, 011001 (2006)

P-13

Role of noncollective excitations in low-energy heavy-ion reactions

Shusaku Yusa, Kouichi Hagino(Tohoku Univ.), Neil Rowley(IPN Orsay)

1

Introduction heavy-ion reaction

nucleus is composed of protons and neutrons

➡ excitations during the scattering process (channel coupling effect)

⬇

important in reactions near the Coulomb barrier

e.g. large enhancement of fusion cross sections at sub-barrier energies

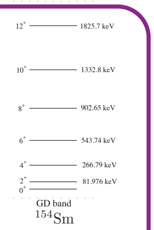

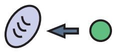

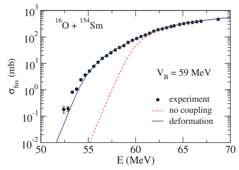

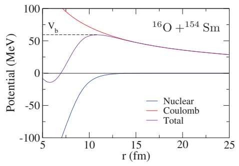

Coupling to collective excitations are taken into account by coupled-channels (c.c.) method

a few states are relevant, coupling is strong

2

Quasi-elastic scattering(elastic+inelastic+transfer) experiment for ^{20}Ne + ^{90,92}Zr

$$D_{\rm qel} = -\frac{d}{dE}\left(\frac{\sigma_{\rm qel}(E,\pi)}{\sigma_R(E,\pi)}\right)$$

A quantity which is sensitive to the excitation effect

Experimental quasi-elastic barrier distributions show **different behavior**

much more smeared distribution for ^{20}Ne + ^{92}Zr system

On the other hand,

C.C. calculation (which includes rotation in ^{20}Ne and vibration in ^{90,92}Zr) yields **similar barrier distributions** between two systems

dominance of the contribution from highly deformed ^{20}Ne

Conventional C.C. calculation (which takes into account only the **collective excitations**) cannot account for the experimental data !

Origin of the difference ?

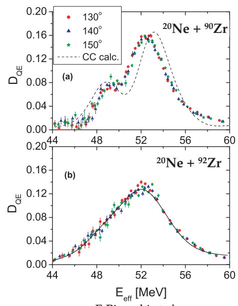

E.Piasecki *et al*., PRC **80**, 054613(2009)

3

Energy spectrum for Zr isotopes

different level density

^{90}Zr : Z=40, N = 50 (shell closure)
^{92}Zr : Z=40, N = 50 + 2

Many **noncollective (single-particle) excited states** appear in ^{92}Zr spectrum

⬇

These noncollective excited states are not taken into account in the conventional c.c. calculations

(red lines : collective excited states taken into account in the analysis)

※ known states

^{90}Zr : 12, ^{92}Zr : 53 up to 4 MeV
^{90}Zr : 35, ^{92}Zr : 87 up to 5 MeV

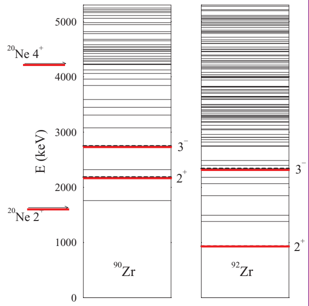

Important role of the noncollective excitations for ^{20}Ne + ^{92}Zr reaction ?

coupling is weak, but there are many states

4

Description of noncollective excitations

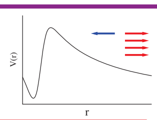

Coupled-channels equations
(in the iso-centrifugal approximation)

$$\left[\frac{d^2}{dr^2}+k^2-\frac{J(J+1)}{r^2}-\frac{2\mu}{\hbar^2}\left(V_{\rm C}(r)+V_{\rm N}(r)+\epsilon_n\right)\right]u_n^J(r)=\sum_m\frac{2\mu}{\hbar^2}V_{nm}(r)u_m^J(r)$$

$k=\sqrt{\frac{2\mu E}{\hbar^2}}$ ϵ_n : excitation energy of the n-th channel

V_{nm} : coupling matrix element → excitations during the scattering process

➡ random matrix theory (RMT) for couplings to noncollective states

$$\overline{V_{nn'}^{II'}(r)}=0$$

D.Agassi, C.M.Ko, H.A.Weidenmüller, Ann. Phys. **107**, 140(1977)

$$\overline{V_{nn'}^{II'}(r)V_{n''n'''}^{I''I'''}(r')}=\{\delta_{nn''}\delta_{n'n'''}\delta_{II''}\delta_{I'I'''}+\delta_{nn'''}\delta_{n'n''}\delta_{II'''}\delta_{I'I''}\}$$
$$\times\sqrt{(2I+1)(2I'+1)}\sum_\lambda\begin{pmatrix}I&\lambda&I'\\0&0&0\end{pmatrix}^2$$
$$\times\frac{w_\lambda}{\sqrt{\rho(n)\rho(n')}}e^{-\frac{(\epsilon_n-\epsilon_{n'})^2}{2\Delta^2}}e^{-\frac{(r-r')^2}{2\sigma^2}}h(r)h(r')$$

$\rho(n)$:level density

5

Coupled-channels calculation for ^{20}Ne + ^{90,92}Zr included channels (model space)

- collective excitations for ^{20}Ne and ^{90,92}Zr

^{20}Ne : 0^+, 2^+, 4^+, 6^+(rotational states), 3^- (octupole phonon state)

Nucleus	ε (MeV)	λ^π	β_λ
^{90}Zr	2.18	2^+	0.089
	2.75	3^-	0.211
^{92}Zr	0.93	2^+	0.144
	2.34	3^-	0.17

- noncollective excitations for ^{90,92}Zr

✓ use experimental data for the excitation energy (ϵ_n) and spin (λ_n)
(RMT determines the coupling strength)

✓ only coupling from the g.s. to the noncollective states are taken into account

^{90}Zr : 45 levels up to 6.7 MeV are included
^{92}Zr : 75 levels up to 5.7 MeV are included

Same parameters in the random matrix model are employed for both ^{20}Ne + ^{90,92}Zr systems

6

Results quasi-elastic scattering for ^{20}Ne + ^{90,92}Zr systems $D_{\rm qel} = -\frac{d}{dE}\left(\frac{\sigma_{\rm qel}(E,\pi)}{\sigma_R(E,\pi)}\right)$

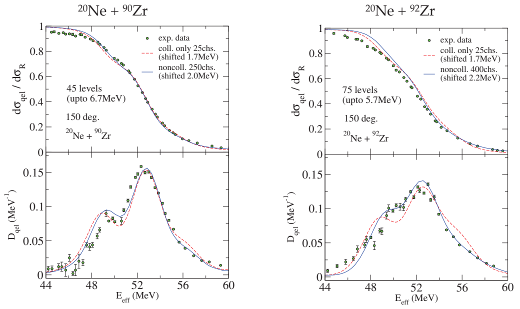

✓ For ^{20}Ne + ^{90}Zr system, the effect of the noncollective excitations is small

✓ For ^{20}Ne + ^{92}Zr system, the barrier distribution is drastically smeared

➡ Difference in the barrier distributions due to the **noncollective excitations**

7

Results Application to ^{24}Mg + ^{90,92}Zr reactions (theoretical prediction)

^{24}Mg : prolate deformation $\varepsilon(2^+) = 1.37$MeV, $\beta_2 = 0.505$

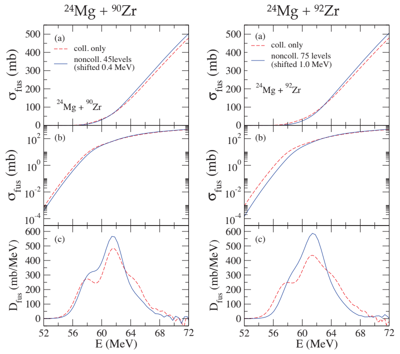

Noncollective effect similar to ^{20}Ne + ^{90,92}Zr reactions

✓ Much smeared barrier distribution for ^{24}Mg + ^{92}Zr system

✓ Smaller noncollective effect for ^{24}Mg + ^{90}Zr system

8

Summary

Role of noncollective excitations in low-energy heavy-ion reaction

✓ Conventional coupled-channels analysis for heavy-ion reactions takes into account only collective excitations

➡ Role of noncollective excitations was not clarified in the previous analyses

✓ The random matrix model for the description of noncollective excitations

✓ Different magnitude of the noncollective effect between ^{20}Ne + ^{90,92}Zr systems

➡ different behavior of the barrier distributions

✓ Similar difference in the barrier distribution can be expected for ^{24}Mg + ^{90,92}Zr reactions

Future perspectives

✓ The effect of multi-nucleon transfer reactions

✓ Application to heavy-ion deep inelastic collision ➡ Quantum mechanical study of friction

Study about frequency response of an AlGaAs/GaAs heterostructured cantilever with optical actuation

Takayuki Watanabe
Department of Physics, Tohoku University

Background

- We have demonstrated that mechanical resonator can be actuated by optical irradiation through optical resonance of AlGaAs/GaAs heterostructure.
- The origin of force induce by the optical irradiation is assumed to be generated through piezoelectric property of GaAs.

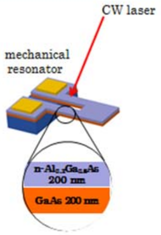

However, the origin of the force is not well verified.

Purpose and method

Purpose

Clarifying features of the force induced in the mechanical resonator which is excited by optical irradiation.

Method

Observing mechanical displacement induced by optical irradiation which the amplitude is modulated at fixed frequency.

Device structure

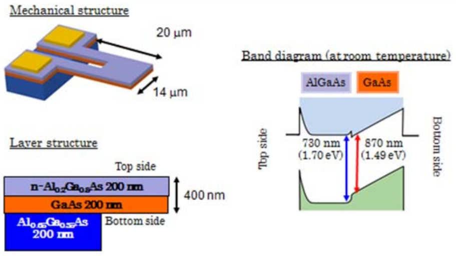

Experimental system

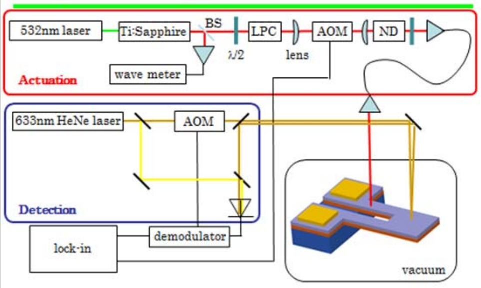

Mechanical displacement actuated by AM optical irradiation

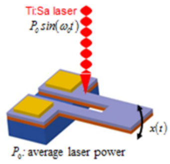

P_0: average laser power
ω_0: angular resonace frequency
$x(t)$: displaceme nt
$\alpha(\lambda)$: absorption coefficien t of GaAs
d_{GaAs}: thickness of GaAs
τ: delay time
γ: dissipation

Equation of motion under AM optical irraditaion

$$\frac{d^2x}{dt^2}+\gamma\frac{dx}{dt}+\omega_0^2 x = F_{ph}$$

$$\left(F_{ph}(t)=CP_0\left(1-e^{-\alpha(\lambda)d_{GaAs}}\right)\frac{\tau}{\sqrt{1+(\omega\tau)^2}}\sin(\omega t+\phi)\right)$$

Apparent displacement of mechanical mode

$$x(t)=\underbrace{C\underset{\text{average laser power}}{\boxed{P_0}}\left(1-e^{-\overset{\text{absorption coefficient}}{\boxed{\alpha(\lambda)}}d_{GaAs}}\right)\overset{\text{delay time}}{\boxed{\frac{\tau}{\sqrt{1+(\omega_0\tau)^2}}}}\frac{1}{\gamma\omega_0}}_{\text{Amplitude } A}\sin\underbrace{\left(\omega_0 t-\frac{\pi}{2}+\boxed{\phi}+\overset{\text{phase delay by circuits}}{\theta_c}\right)}_{\text{Phase}}$$

$(\tan\phi=-\omega\tau)$

Wavelength dependence

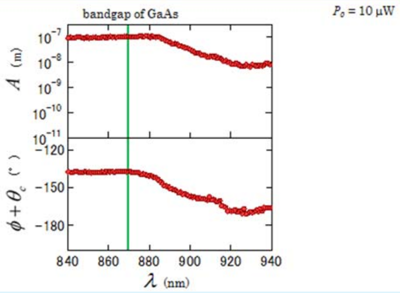

Laser power dependence

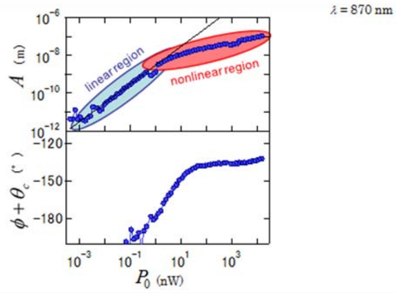

Delay time estimation by phase

Because θ_c is independent to the wave-length and laser power, the dependences observed in the phase are due to the dependences of delay time.

The delay time is calculated from phases observed in the different two mechanical mode .

$$d\Phi_i=\underbrace{\left(\phi_{i,\lambda 1}+\theta_c\right)}_{\text{Phase at } \lambda 1}-\underbrace{\left(\phi_{i,\lambda 2}+\theta_c\right)}_{\text{Phase at } \lambda 2}\ (i=1.2)$$

•Relation between ϕ and τ

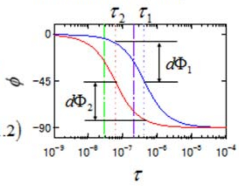

Wavelength dependence of phase at 2 mechanical modes

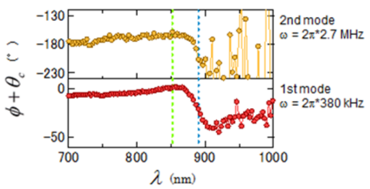

Wavelength dependence of delay time at 2 mechanical modes

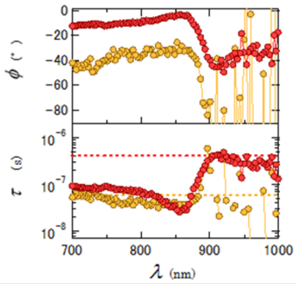

Wavelength dependence of delay time and effective amplitude

Effective temperature

$$A_{eff}=\frac{CP_0\left(1-e^{-\alpha(\lambda)d_{GaAs}}\right)}{\gamma\omega_0}$$

- The delay time depends on wavelength and the absorption coefficient strongly affects it.
- The effective temperature A_{eff} shows more significant wavelength dependence than amplitude A.

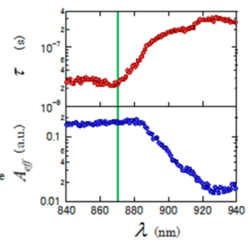

Wavelength dependence of delay time and effective amplitude

- The delay time also depends on laser power.
- A_{eff} shows nonlinear dependence to the laser power. The nonlinearity is well approximated with the following expression.

$$A_{eff,non}\equiv\frac{C\left(1-e^{-\alpha(\lambda)d_{GaAs}}\right)}{\gamma\omega_0}\frac{P_0}{\sqrt{1+P_0/a}}$$

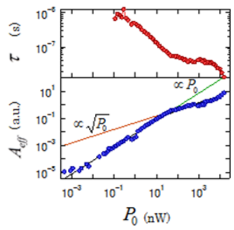

Absorption coefficient calculated from mechanical displacement

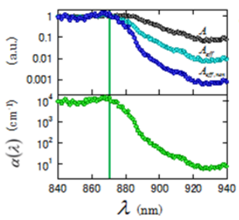

Comparison A, A_{eff} and $A_{eff,non}$

The absorption coefficient calculated from amplitude. It shows good agreement with reported value.

Summary

- The delay time of the force generated by optical irradiation is calculated from forced actuation. It clarified that the delay time strongly depends on optical irradiation condition.
- The absorption coefficient is calculated by treating delay time dependence and laser power nonlinearity of the amplitude.
- The feature of the force generated by optical irradiation is partially clarified.

P-15 # Crystalline electric field study in $Nd_2Ir_2O_7$ with metal-insulator transition

Tohoku Univ., Kyusyu Inst. of Tech.[A], Hokkaido Univ.[B], MLF Division, J-PARC center[C]

M. Watahiki, K. Tomiyasu, K. Iwasa, K. Matsuhira[A], S. Takagi[A], M. Wakeshima[B], Y. Hinatsu[B],

S. Ji[C], and R. Kajimoto[C]

Introduction

Crystal structure of $Nd_2Ir_2O_7$

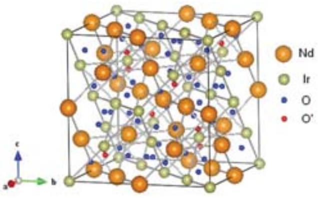

元素	Wyckoff記号	点群
Nd	16*d*	-3m(D_{3d})
Ir	16*c*	-3m(D_{3d})
O	48*f*	mm(C_{2v})
O'	8*b*	-43m(T_d)

・Nd^{3+} (J = 9/2) and Ir^{4+} ($S = J_{eff}$ = 1/2) ions form pyrochlore lattices.

・Local symmetry of rare earth site : $\boldsymbol{D_{3d}}$ (trigonal)

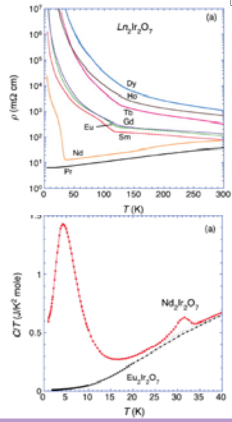

Previous study of $Nd_2Ir_2O_7$

・Metal-insulator (MI) transition at T_{MI} = 33 K [1]

・Magnetic entropy of Nd^{3+} reaches R ln2 at T_{MI} [1].
→ Crystalline electric field (CEF) ground state of Nd^{3+} is doublet.

・Weak ferromagnetism and Schottky anomaly were observed below T_{MI} [1].

[1] K. Matsuhira *et al.*, J. Phys. Soc. Jpn. **80** 094701 (2010).

Purposes

・It is predict that Nd^{3+} feels a static internal magnetic field from Ir^{4+}.

・Determination of CEF level scheme → Investigation of Ir^{4+} electronic state from 5*d*-4*f* interaction

Experiments

・Powder sample of $Nd_2Ir_2O_7$ from K. Matsuhira

・Inelastic powder neutron scattering experiments performed at MLF in J-PARC, Tokai, Japan.

Fermi chopper spectrometer 4SEASONS :

E_i = 24, 27, 39, 47, 76, 97, 205, 309 meV, f = 300 Hz,
5 ≦ T ≦ 295 K (^{4}He closed-cycle refrigerator)

Results

Inelastic scattering intensity distributions in (Q, E) space

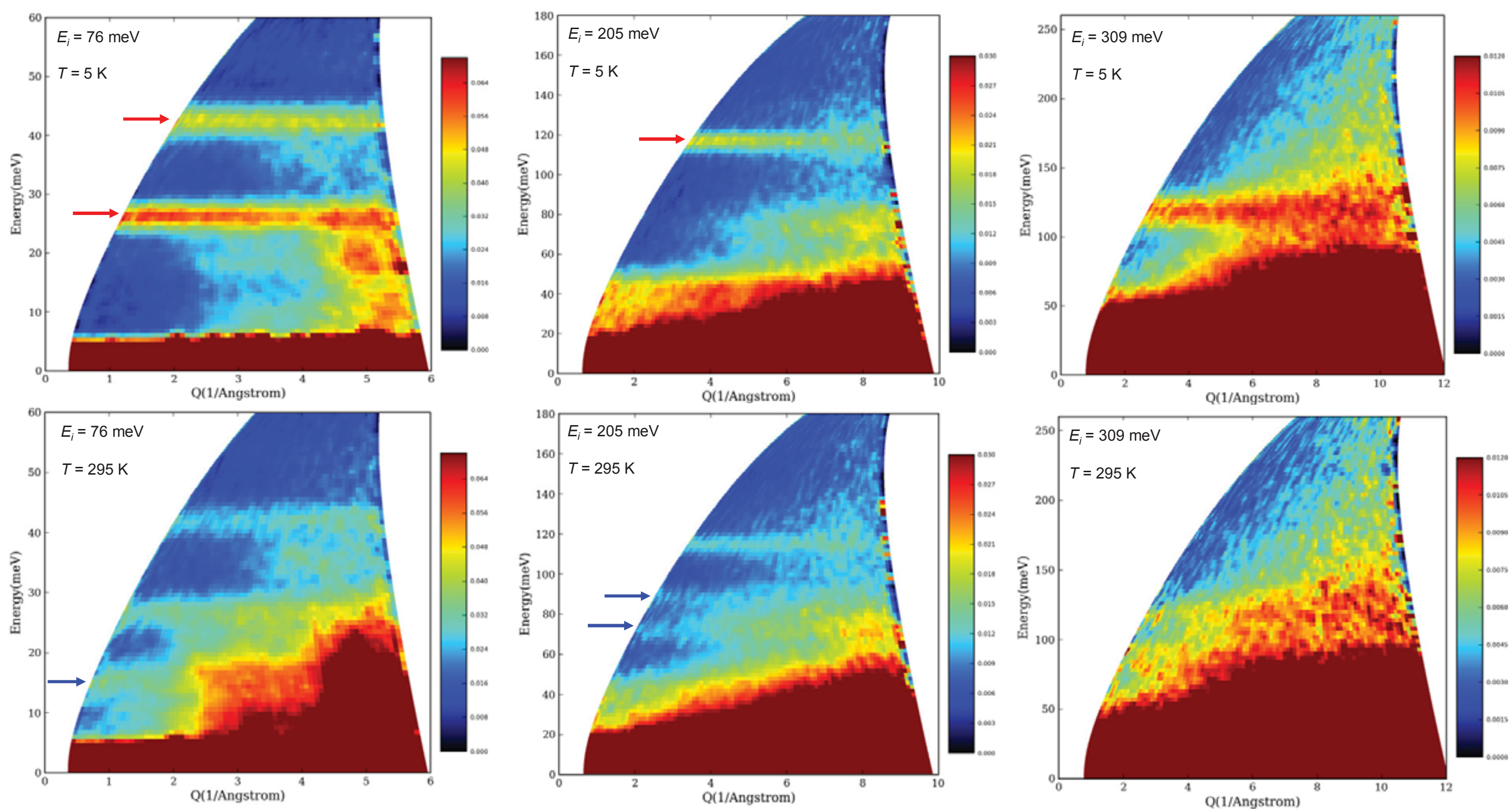

CEF model

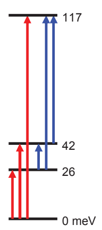

Summary

・At 5 K, three excitation peaks observed at around 26, 42 and 117 meV are interpreted as CEF excitations within five Kramers doublets.

・Fourth excitation peak was not observed below 260 meV.

・Analysis of CEF model is in progress.

Search for a feld-induced quantum critical point in $CeRhSi_3$

H. Iida, T. Sugawara, H. Aoki, and N. Kimura
Dep. Phys., Tohoku University, Sendai 980-8578, Japan

Introduction

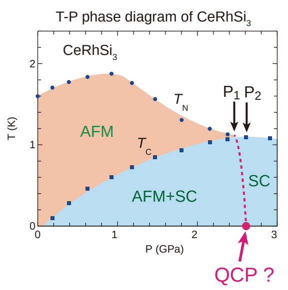

P_1: AFM order vanishes near **2.4GPa**
P_2: T_C maximum at **2.6GPa**

$CeRhSi_3$ is pressure-induced heavy-fermion superconductors [1, 2]. As shown in the T-P phase diagram, the superconducting phase appears below T_N. In zero magnetic fields, magnetic quantum critical point (QCP) is unclear because the superconductivity masks the antiferromagnetic (AFM) transition above P_1. However, the magnetic-filed-induced AFM phase appears above P_1. Therefore, following question arise;

Is there a magnetic field induced QCP in $CeRhSi_3$?

In order to elucidate this problem, we have performed the electrical resistivity measurements under magnetic fields and pressures near P_1.

Experimental

● Sample preparation
・Czochralski pulling method in a tetra-arc furnace

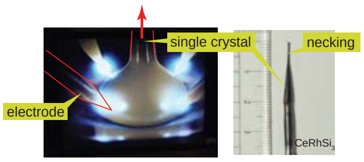

・Residual resistivity ratio (RRR) > 100
・Anneal: 900℃, 2×10^{-6}, 1week

● Hydrostatic pressure system
・Ni-Cr-Al/BeCu Clamped piston cylinder cells
equal mixture of *n*- and *i*-propanol

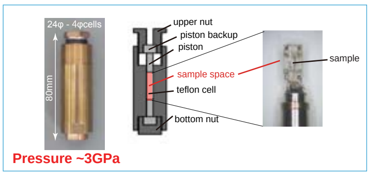

● Resistivity ・Low ac four-terminal method

● $^3He/^4He$ dilution refrigerator with 17T-superconducting magnet

Resisitivity & T-H pase diagrams

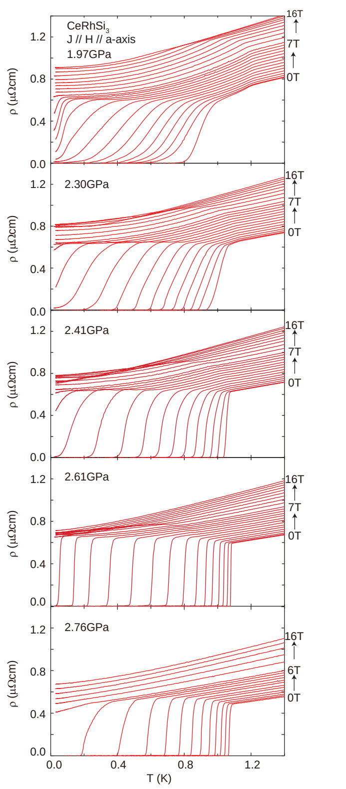

※ρ (T) curves of 1.97-2.61GPa for the magnetic fields every 0.5T from 0T to 7T and every 1T from 7T to 16T each Pressure. ρ (T) curves of 2.71GPa for the magnetic fields every 2T from 6T to 16T.

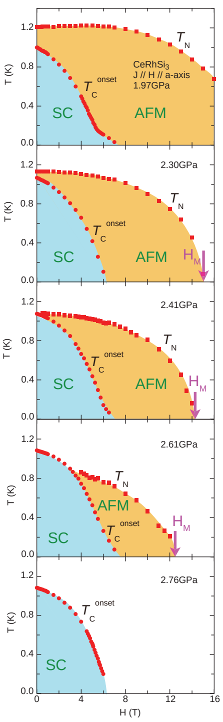

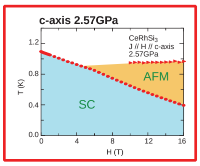

In the paramagnetic state, ρ (T) follows a T-linear dependence for each pressure.
Field induced AFM phase is suppressed by applying pressures.
In contrast a-axis, effect of magnetic field on AFM and SC state seems to be very hard in its c-axis.

2.61GPa, resistivity at visinity of the H_M

● The resistivity plotted against above H_M

Plotted T^n

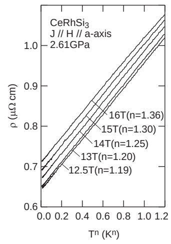

Plotted T^2

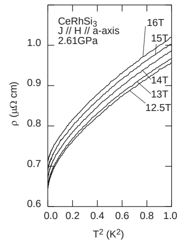

Plotted T^1 at low temp. and T^2 fitting

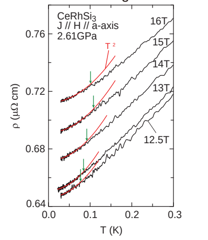

$\rho(T)$ changes in behavior from T^1 to T^n at low temperatures below about 0.8K, with increasing the field, n in $\rho(T) = \rho_0 + A_n T^n$ is slightly increases.

In low temperature, $\rho(T)$ obeys T-square, upper limit of T^2 behaviors slight change.

● Seach for a induced QCP

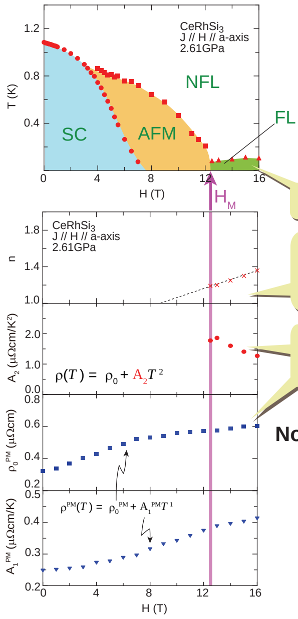

T-linear fitting from paramagnetic state (1.4~1.2K)

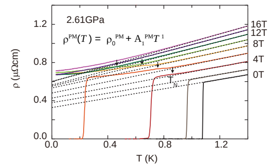

FL state stay constant even at high field.

The exponent increases with increasing field, suggesting a gradual recovery to FL state. However, surprisingly, recovery of the FL state is unlikely to start from H_M.

No enhancement of A_2 and A_1^{PM} at H_M, and no anomaly ρ_0^{PM} at H_M.

Not obtain a clear evidence that H_M is the QCP!!

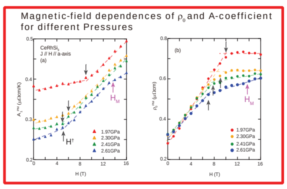

Conclusion

We analyzed $\rho(T)$ under magnetic fields below and above P_1, and we determined the quantum-phase-transition field H_M where the AFM transition temperature drops to zero. Recovery of Fermi liquid state is not clearly observed above H_M, and enhancement of A less obvious in the vicinity of H_M. These results are is in sharp contrast with those of other heavy-fermion compounds. We could not conclude that H_M is the QCP.

References and more information of this study

[1] T. Sugawara, et al., J. Phys. Soc. Jpn. 81 (2012) 054711.
[2] N. Kimura et al., J. Phys. Soc. Jpn. 76 (2007) 051010.
[3] H. Iida, et al., to be published in physical status solidi
"Search for a Quantum Critical point in $CeRhSi_3$ via Electrical Resistivity"

P-18

Reaction Cross Sections of the Deformed Halo Nucleus ^{31}Ne

Y. Urata, K. Hagino, and H. Sagawa, Phys. Rev. C86, 044613 (2012)

Yasuko Urata　　Department of Physics, Tohoku University

① Halo Nuclei

- Large interaction cross section σ_I

e.g. ^{11}Be

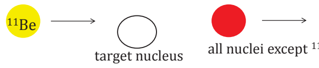

$\sigma_I \sim \pi(R_{projectile} + R_{target})^2$ → **Large radius for ^{11}Be**

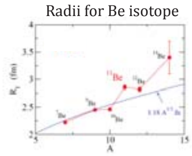

I. Tanihata et al., PRL55(1985)2676; PLB206(1988)592

- Halo structure

Spatially extended density distributions of the weakly bound valence neutron(s)

$\psi(r) \sim e^{-\lambda r}$

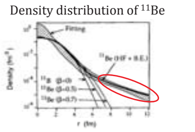

M. Fukuda et al., PLB268, 339 (1991)

✓ reproduce the experimental cross section.

➢ Root-mean-square radii of s- or p- wave states diverge in the weakly bound region.

➢ *s*-wave halo nuclei : ^{11}Be, ^{19}C, ...
p-wave halo nuclei : ^{11}Li, ^{6}He

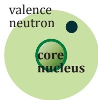

^{31}Ne Nucleus

- Large Coulomb breakup cross section

(T.Nakamura, et al.,PRL103,262501(2009))

- Large interaction cross section

(M.Takechi et al., Phys. Lett. B 707, 357 (2012)

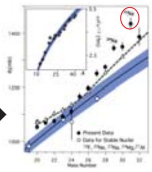

Interaction cross sections

➢ **Halo Structure of ^{31}Ne**

Mean Field Picture

Nucleons are independent particles which move in some average potentials created by all the nucleons in the nucleus.

- Naive spherical shell model

→ $1f_{7/2}$ configuration for the valence neutron of ^{31}Ne

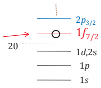

➢ Deformation of ^{31}Ne nucleus

- single particle states in a deformed potential V(r,θ)

➢ $\beta \sim$ 0.2-0.3 : [330 1/2], 0.4-0.6 : [321 3/2]　→ p-wave halo

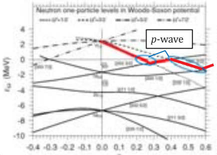

Nilsson diagram

I.Hamamoto, Phy.Rev.C 81, 021304(R) (2010))

Motivations

In the Nilsson model, the rotational excitation energy of the core nucleus is neglected.
In reality, however, ^{30}Ne has the first 2$^+$ excited state at 0.801 MeV.

- Inclusion of the finite excitation energy of the core nucleus with a particle-rotor model
- Calculations of Coulomb breakup cross sections and reaction cross sections

(Y. Urata, K. Hagino, and H. Sagawa Phys. Rev. C 83, 041303(R) (2011))

this work

➢ **The effect of the finite excitation energy**

➢ **Ground state properties of ^{31}Ne**

③ Results

- Probability of each component in the ground state wave function

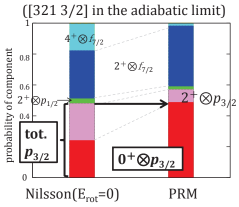

Calculation : S_n= 0.2 MeV
Experimental S_n :
S_n= 0.29 ± 1.64 MeV

✓ In PRM calculations the relevant quantity to the halo structure is the 0^+ component.

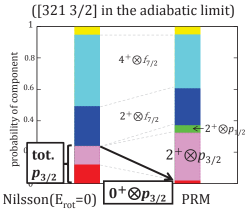

- The reaction cross sections σ_R for ^{30,31}Ne as a function of the one-neutron separation energy S_n
- Comparison to the experimental interaction cross section σ_I

Reaction cross sections σ_R for ^{31}Ne

Root mean square radii for ^{31}Ne

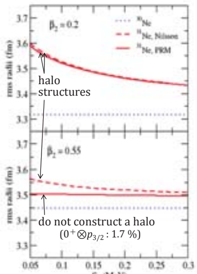

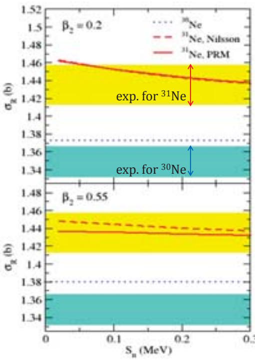

Density distributions for ^{30,31}Ne (in the adiabatic limit)
β_2 = 0.2, S_n=0.2 MeV

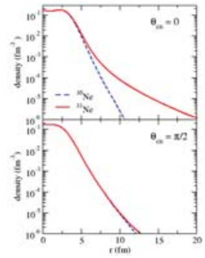

➢ The halo contribution to the reaction cross section for ^{31}Ne is small.

➢ The adiabatic approximation works reasonably well.

Comparison with the experimental data

One-neutron removal cross sections σ_{-1n} for ^{31}Ne

$\sigma_{-1n}(^{31}\mathrm{Ne}) \sim \sigma_R(^{31}\mathrm{Ne}) - \sigma_R(^{30}\mathrm{Ne})$

The increase of the reaction cross sections from ^{31}Ne to ^{30}Ne

(W. Horiuchi et al., Phys. Rev. C81, 024606 (2010))

Experimental $\sigma_{-1n}(^{31}$Ne) : T. Nakamura *et al.*, PRL103, 262501 (2009)

➢ $I^\pi = 3/2^-$ configuration at β_2 = 0.2 well accounts for both σ_R and σ_{-1n} for ^{31}Ne.

One-neutron removal cross sections σ_{-1n} for ^{31}Ne

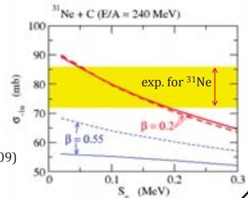

② Particle-Rotor Model

- ^{31}Ne : (deformed core ^{30}Ne) + n
- Axial quadrupole deformation of the core
- The core nucleus has a rotational band.

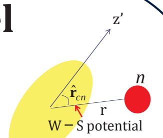

Deformed Woods-Saxon potential :

$$V(r, \hat{\mathbf{r}}_{cn}) = \frac{V_0}{1 + \exp[(r - R_0 - R_0\beta_2 Y_{20}(\hat{\mathbf{r}}_{cn}))/a]}$$

$$\rightarrow H = \underbrace{H_0}_{\text{spherical}} + \underbrace{V_2(r)Y_{20}(\hat{\mathbf{r}}_{cn})}_{\text{deformed}} + \underbrace{\boxed{H_{rot}}}_{\text{rotational}}$$

mixture of angular momenta

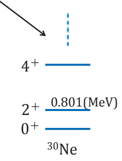

Rotational band

$$\frac{I_c(I_c+1)\hbar^2}{2J}$$

$$\Psi_{IM} = \sum_{I_c jl} \alpha_{jlI_c} \left({}^{31}\mathrm{Ne} \right)^{(IM)} \quad = \text{For example, } 0^+ \, f_{7/2} + 2^+ \, p_{3/2} + 4^+ \, p_{3/2} + \cdots$$

Ground State

$\boxed{H_{rot}(E_{rot}) = 0}$ adiabatic limit → Nilsson diagram (ε_K) : *K* is a good quantum number

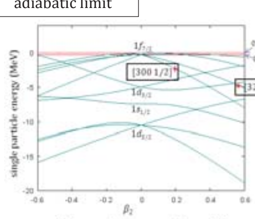

Nilsson diagram (E_{rot} =0)

➢ The non-adiabatic effect of $E_{rot} \neq 0$

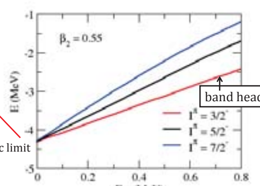

④ Summary

- Ground state properties of the deformed halo nucleus ^{31}Ne
→ particle-rotor model (PRM)
※ the finite rotational excitation energy of the core nucleus
- Reaction cross sections for ^{30,31}Ne on the ^{12}C target → Glauber theory

Results

- **The small non-adiabatic effects** for the reaction cross sections of ^{31}Ne
- The reaction cross section of $\mathbf{I^\pi = 3/2^-}$ **configuration at $\boldsymbol{\beta_2}$ = 0.2**

✓ reproduces the experimental interaction cross section.
✓ leads to a consistent description for the one-neutron removal cross section.

→ **A very promising candidate for the ground state of ^{31}Ne**

※ consistent with the analysis of the Coulomb dissociation cross section of ^{31}Ne with the PRM

(Y. Urata, K. Hagino, and H. Sagawa Phys. Rev. C 83, 041303(R) (2011))

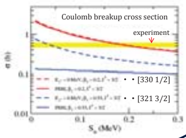

Reaction cross sections

Calculations of reaction cross sections with the Glauber theory which describes high-energy nucleus-nucleus collisions

- Eikonal approximation : scattering in the forward angle
- Adiabatic approximation : neglect the intrinsic excitation energy for the large incident energy

$$\sigma_R = \int d\mathbf{b}\left(1 - \frac{1}{2I+1}\sum_M \left|\langle \Psi_{IM}|S_c \cdot S_n|\Psi_{IM}\rangle\right|^2\right)$$

(P. Batham, I.J. Thompson, and J.A. Tostevin, Phys. Rev. C 71, 064608 (2005))

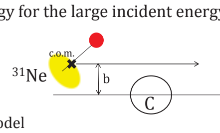

$|\Psi_{IM}\rangle$: initial state wave function (ground state) with particle-rotor model

P-19

Generalized geometric approach to non-geometric spaces

Shuhei Sasa (Physics, D2)

In collaboration with T. Asakawa, S. Watamura

@Tohoku University

The 5th International GCOE Symposium 2013/3/4

Introduction

Superstring Theory :

- a candidate of quantum theory of gravity
- has the possibility to include the standard model of particle theory

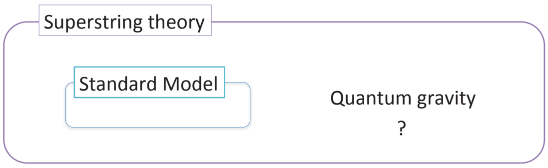

On the other hand,

Gravity = Geometry

What is a geometrical description behind string theory?

Remarkable feature) T-duality

T-duality is a symmetry under which two different compactified spaces with a U(1) isometry are indistinguishable from the viewpoint of string theory.

- Simplest example: S^1 compactification

Radius of S^1 : $R \xrightarrow{\text{T-duality}} \frac{1}{R}$

Kaluza-Klein mode (tangent vector field) $\xleftrightarrow{\text{exchange}}$ Winding mode (one-form)

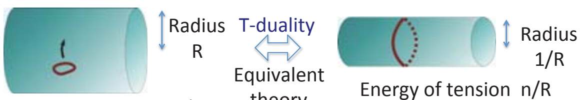

- General background with U(1) isometry:
  for NS-NS flux: a metric g
  a Kalb-Ramond 2-form B (called B-field)
  a dilaton ϕ

→ T-duality in these background is known as Buscher rule.

What is the T-duality invariant formulation in SUGRA?

→ Candidate: Generalized Geometry

- is easier than an analysis of string theory (= conformal field theory)
- makes clear the geometrical meaning of string theory

(There is another candidate; the doubled field theory which is locally same.)

Non-geometric Q-flux spaces:

- appear as T-dual space of geometric space with H-flux.
- are endowed with local coordinates and can be glued with stringy symmetry: Diff., gauge tr., T-duality.
- can be locally described as geometric, but globally non-geometric.

Example) T-fold

Motivations:

String, membrane

(Proposal)

Non-commutative geometry and Non-associative geometry

$$[x^\mu, x^\nu] = \oint Q_\rho{}^{\mu\nu} dx^\rho \quad \text{[Mathai-Rosenberg 2004]}$$

$$[x^\mu, [x^\nu, x^\rho]] + c.p. = R^{\mu\nu\rho} \quad \text{[Lust 2011] [Schupp, Szabo 2012]}$$

Supergravity

Non-geometric flux compactification [Shelton, Taylor, Wecht 2006]

Moduli stabilization [Micu, Palti, Tasinato 2007]

de Sitter vacua [de Carlos, Guarino, Moreno 2009]

10-dim origin of 4-dim non-geometric potential [Patalong 2012]

However the definition of non-geometric space is still obscure.

In this propose, we propose

- a natural definition of non-geometric Q-flux spaces
- an effective theory of non-geometric Q-flux spaces

H-flux : twist in generalized geometry
Q-flux : ?

Example: T-fold [Hull 2004]

- arise as T-duals along y,z-direction for three-dimensional torus with H-flux

$$ds^2 = dx^2 + \frac{1}{1+N^2x^2}(dy^2+dz^2) \qquad B = \frac{Nx}{1+N^2x^2} dy \wedge dz$$

T-fold: $\mathbb{T}^2$ "fiber bundle" over S^1

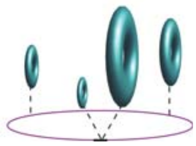

Locally: geometric
Globally: non-geometric
(g, B : ill-defined)

T-duality and B-field gauge tr.
$x \sim x+1$:periodic

New interpretation of T-fols

T-fold
(non-geometric space)

Usual viewpoint | New viewpoint

Non-geometric from the viewpoint of $TM = \text{span}\{\partial_x, \partial_y, \partial_z\}$

Geometry from the viewpoint of $L = \text{span}\{\partial_x, dy, dz\}$
(L :Lie algebroid)

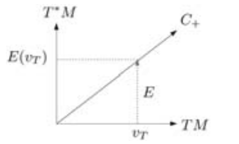

$E = g + B \in \Gamma(T^*M \otimes T^*M)$

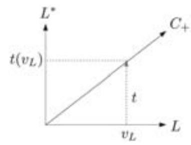

$t \in \Gamma(L^* \otimes L^*)$

L is extended a general Lie algebroid.

Statement

We have analogue discussions of generalized geometry if we replace TM with L .

	Generalized Geometry	New Geometry
	$(TM, [,]_{\text{Lie}})$	$(L, [,]_{\text{Lie}})$
	$TM \oplus T^*M$	$L \oplus L^*$
	H-flux	Q-flux
	Courant algebroid	new algebroid
SUGRA	$\mathcal{R} = R + \frac{1}{12}H^2$	$\tilde{\mathcal{R}} = \tilde{R} + \frac{1}{12}Q^2$

Summary:

- We proposed the definition of non-geometric space.
- We have analogue discussions of generalized geometry if we replace TM with L .

P-20

Continuous Time Quantum Monte Carlo study of strong coupling superconductivity in Holstein-Hubbard model

Satoshi Yamazaki, Shintaro Hoshino, and Yoshio Kuramoto
Department of Physics, Tohoku University, Sendai, Japan

Holstein-Hubbard model

Electron-phonon strongly coupled systems (ex.MgB_2, A_3C_{60} , AOs_2O_6 , etc)

$$\mathcal{H} = \sum_{<i,j>,\sigma} t_{ij}(c^\dagger_{i\sigma}c_{j\sigma} + c^\dagger_{j\sigma}c_{i\sigma}) + \omega_0 \sum_i b^\dagger_i b_i$$
$$+ g\sum_i (b_i + b^\dagger_i)\delta n_i + U\sum_i n_{i\uparrow}n_{i\downarrow} - \mu \sum_{i\sigma} n_{i\sigma} \qquad \delta n_i = \sum_{i\sigma} n_{i\sigma} - 1$$

Effective interaction

$$U_{eff}(\omega) = U + \frac{2g^2\omega_0}{\omega^2 - \omega_0^2} \xrightarrow{\omega_0 \to \infty} U - \lambda\ , \quad \lambda = \frac{2g^2}{\omega_0}$$

- Polaron-Bipolaron transition — W. Koller, *et al.* EPL, **66**, 559 (2004)
- Charge density wave (CDW), Antiferromagnetism — J. Bauer, A. C. Hewson, PRB **81**, 235113 (2010)
- Superconductivity(SC) → Effect of $U,\ \mu$?

J. Bauer, *et al*, PRB **84**, 184531 (2011)

Weak coupling approach — BCS theory, Migdal-Eliashberg theory → Strong coupling region — Breakdown

Purpose

Properties of SC in strong coupling region

Method

Dynamical mean field theory（DMFT+CT-QMC）

E. Gull, *et al.*, Rev. Mod. Phys. **83**, 349 (2011).

- Electron-phonon interaction → Exact solution in infinite dimension
  P. Werner and A. J. Millis, PRL **99**, 146404 (2007).
- Finite temperature

Condition parameter $T,\ \lambda,\ U$

- Lattice vibration $\omega_0 = 1,$ Half band width $D = 2$
- Semi circular type density of states
- Paramagnetic phase + Superconducting phase（No long range order except SC）

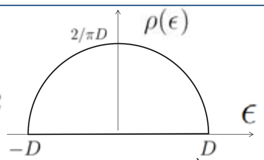

Phase diagram in Holstein model $U = 0$

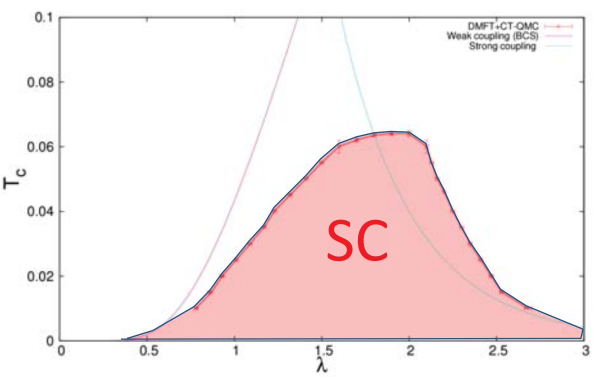

BCS（weak coupling limit）$T_c = \omega_0 \exp(-1/\lambda\rho_F)$

Strong coupling limit $T_c = \frac{D^2}{4\lambda} e^{-2\lambda/\omega_0}\left[1 + \sum_{n=1}^{\infty} \frac{(\lambda/\omega_0)^n}{(1+\lambda/\omega_0)(2+\lambda/\omega_0)\cdots(n+\lambda/\omega_0)}\right]$

J. K. Freericks, *et al*, PRB **48**, 6302 (1993)

- T_c has a maximum $\lambda_{max} \sim 1.9$

cf. Attractive Hubbard model（$\omega_0 \to \infty$）$\lambda^{(\infty)}_{max} \sim 4.0$

A. Koga and P. Werner, PRA **84**, 023638 (2011).

- Strong coupling region $\lambda > \lambda_{max}$ T_c decrease exponentially

Properties of superconductivity

Order parameter & Double occupancy (half filling)

Temperature dependence of order parameter

- Increase monotonically decreasing T
- Saturate in low T

→ Saturate slowly in strong coupling region

→ $\Delta_{T=0}/T_c$ is larger

Temperature dependence of $\langle n_{i\uparrow}n_{i\downarrow}\rangle$

Double occupancy with decreasing T

	$T < T_c$	$T > T_c$
Weak	Increase	Decrease
strong	Decrease	Increase

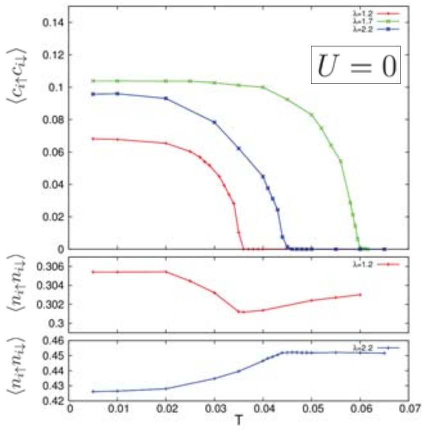

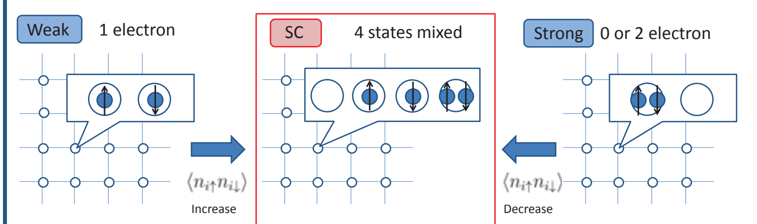

Strong coupling region → Break the local pairs

Coulomb interaction effect in strong region

Coulomb interaction

Induce SC by depairing

Double occupancy decrease

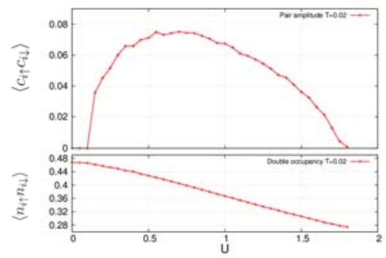

Filling dependence of T_c $U = 0$

$T_{CDW} \geq T_{SC}$ at half filling

Transition temperature with decreasing carrier density

CDW (staggered order)

- Rapidly decrease
- Reentrant behavior away from half filling

Superconductivity

- Decrease monotonically
- Robust at any filling

$T_{SC}(\omega_0 = 1)\ /\ T_{SC}(\omega_0 = \infty) \cong 0.82$

Phase diagram (λ=1.5)

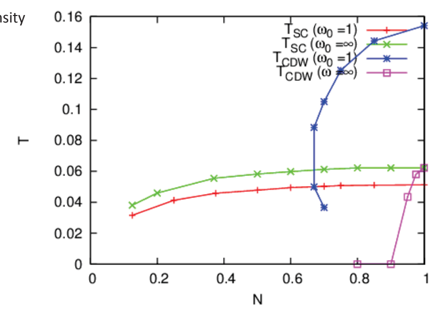

Conclusion

Characteristic properties in strong coupling superconductor

- Retardation effect → Suppress superconductivity
- Double occupancy decrease below T_c

P-21 Study of double delta photoproduction on the deuteron target

Fumiya Yamamoto for the NKS2 collaboration, Department of Physics, Tohoku Univ.

✓Introduction

Nuclear photon absorption

When photon beam impinged on the nucleus,
* nucleus is excited at the photon energy 1 MeV - 150 MeV.
* single nucleon (general term of proton and neutron) is excited at the photon energy 150 MeV -.

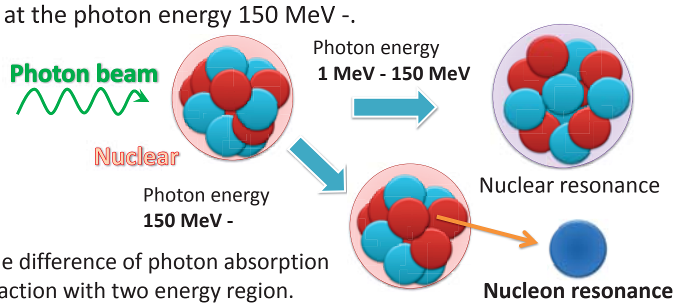

The difference of photon absorption reaction with two energy region.

Nucleon resonance

The nucleon resonances are the excited states of nucleon. These emit mesons (π or η etc.) and decay. Delta particle is one of the nucleon resonances and decay for πN. The life time is very short 10^{-23} s. The mass is 1232 MeV.

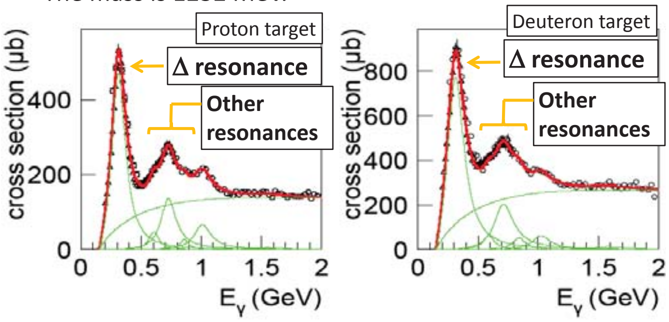

The probability of photon absorption on the proton and deuteron. Single nucleon is excited, and nucleon resonances is generated.

Double delta photoproduction process on the deuteron

Deuteron : The simplest compound nucleus consisting of proton and neutron

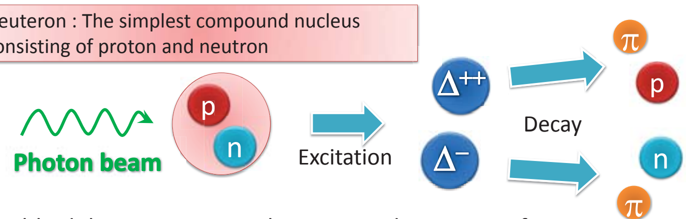

Double delta excitation in the intermediate state of $\pi^+\pi^-$ photoproduction process. Since the wave length for photons is smaller than the average internucleon spacing for deuteron, it is wonderful that two nucleons excite.

Right figure : the reaction probability of double delta photoproduction. The experimental data is poor.

Physics :
- Interaction between nucleon resonances
- Mechanism of double delta process

Aim of study:
-Determination of the reaction probability of double delta process

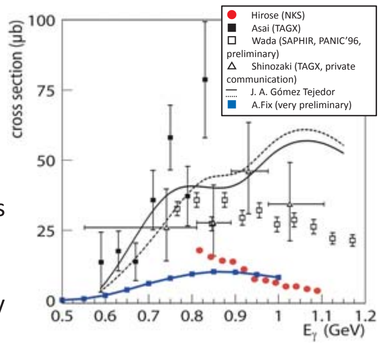

✓Experiment

Neutral Kaon Spectrometer 2 (NKS2)
Measurement of the velocity and momentum of the charged particle
Component :
* Dipole magnet : Momentum analysis
* Hodoscope : Time of flight
* Drift chamber : Detection of track

Right figure : NKS2 seen from the photon beam down stream

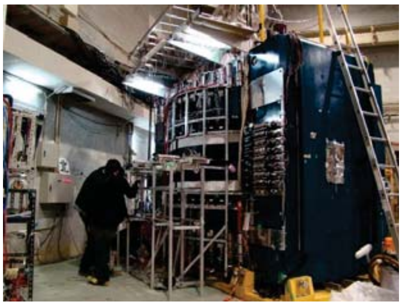

The photon berm at Research Center for Electron Photon Science (ELPH)

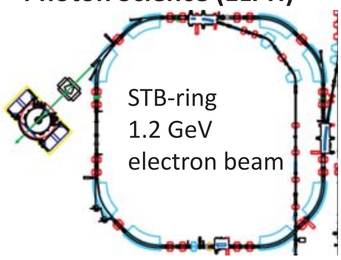

- The photon beam is generated via bremsstrahlung.
- The photon energy is tagged by the detected scattering electron.

✓Analysis

Identification for π^+, π^- and proton
- Using of the velocity β and momentun p of the charged particle, the particle mass is calculated.

$$m^2 = p^2(\beta^{-2} - 1)$$

Mass square distribution

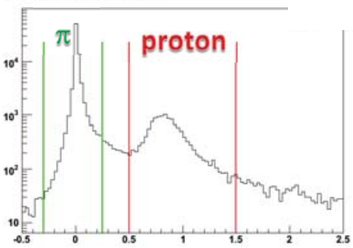

Mass square [(GeV/c²)²]

Selection of $\gamma d \rightarrow \pi^+\pi^- pn$ reaction
- Missing particle : Non detected particle. From energy-momentum conservation, the mass of missing particle is calculated and the neutron is identified.

$$M_X^2 = E_X^2 - P_X^2$$
$$E_X = E_\gamma + M_d - (E_{\pi^+} + E_{\pi^-} + E_p)$$
$$P_X = P_\gamma - (P_{\pi^+} + P_{\pi^-} + P_p)$$

M : Particle mass E : Particle energy
P : Particle momentum

*A lower index expresses the kind of particles.

Missing mass distribution

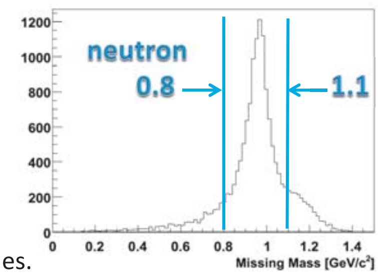

✓Result

Double delta excitation
- Invariant mass : From energy-momentum conservation before and after decay, the mass of particles before decay are calculated. For example, since the delta particles are decayed for π and N,

$$M_\Delta^2 = (E_\pi + E_N)^2 - (P_\pi + P_N)^2$$

- A lower figures are the invariant mass distribution πN.
Left side: 2 dimension of invariant mass π^+p and π^-n.
Right side top : Invariant mass of π^+p.
Right side bottom : Invariant mass of π^-n.
- From left side figure -> double delta excitation.

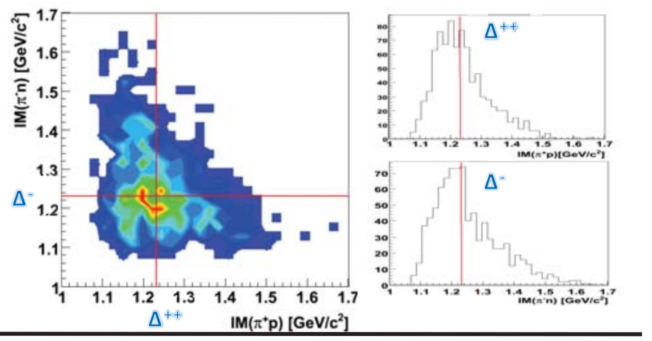

✓Summary

-Double delta photoproduction is the process which excited double delta
in the intermediate state.
- The experiment is carried out at ELPH.
- π^+, π^- and proton were detected using NKS2.
-Neutron was identified using the missing mass.
-Double delta excitation in the intermediate state was shown using the invariant mass distribution π^+p and π^-n.

P-22

Palsed Neutron Scattering Study of Magnetic Excitation in Dilute-Doped Bi2201-Sysyem

Dept of Physics, Tohoku Univ, IMR,Tohoku Univ [A] , Kyusyu Institute of Technology [B] , KEK[C] .
K. Tsutsumi, M. Fujita [A] , M. Enoki [B] , M. Matuura [A] , K. Sato, K. Yamada [C] .

Spin correlation on CuO_2 plane

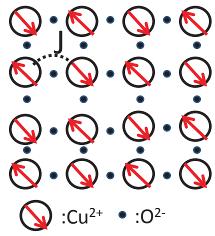

Super exchange constant J is determined by electron hopping parameter t & Coulomb interaction U

insulator ➡ superconductor

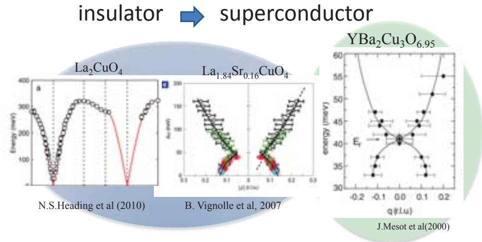

spin wave excitation **Hourglass-shaped excitation**

Magnetic excitation evolves with carrier doping from spin wave to hour glass excitation

Comparison between LSCO with YBCO

	LSCO	YBCO
Hourglass in SC phase	○	○
High-energy excitation	○	Unknown
Collective excitation	○	Unknown

Hourglass excitation has been observed in the two systems, however, the universality is not yet clear due to the different crystal structure

Bi2201-system

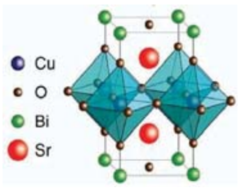

Bi2201 has single CuO_2 layer, like LSCO

Universality could be extracted.

Current research

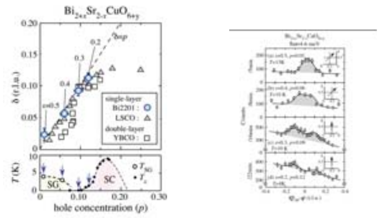

M. Enoki et al. 2013

Doping dependence of low energy is similar with LSCO

Motivation

Comparing with LSCO,
showing universality of
high energy excitation
we prepared dilution doped sample
➡because of clearly magnetic excitatioı
was observed in low energy region

Set up

sample:$Bi_{2.4}Sr_{1.6}CuO_{6+d}$
Volume: about 27g
Temperature: 7K
Ei=40,70,120,240 [meV]
Equipment: ISIS-Merlin
➡ easily observed wide q-w range

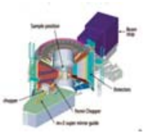

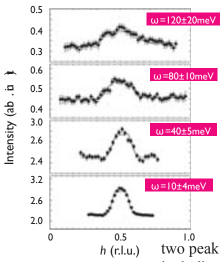

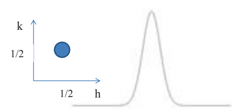

single Gaussian fitting

two peak separation ware not observed including High energy region

2D observation data

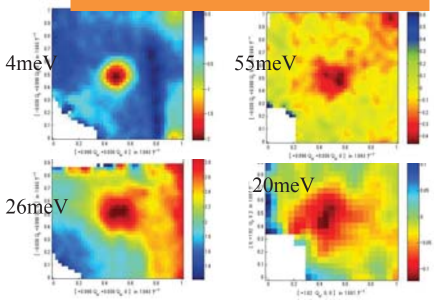

Comparing Dispersion

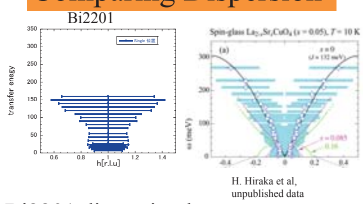

Bi2201 dispersion has extreme spread about high energy region ~100meV

comparison of high energy spectrum

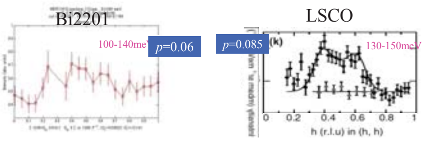

Bi2201 energy spectrum is clearly damped and broadening in high energy region

Summary

Dilution doping Bi2201 , we first observed magnetic excitation ~160meV.
Increasing energy transfer, magnetic peak extreme broadening, and intensity being weak.
This result shows that Bi2201 has large J but not collective excitation.
Mechanism of high-Tc superconductor cuprates might be common with large J of magnetic excitation.

P-23

Double neutral pion photoproduction off the proton

Qinghua HE *for the FOREST Collaboration*

Research Center for Electron Photon Science (ELPH), Tohoku University

Meson Photoproduction

Meson photoproduction off the nucleons is one of a prime tools to study the properties of the strong interaction in the non-perturbative domain of QCD. Single pion photoproduction has been studied intensively to get informations for nucleon resonances especially for the Δ-excitation, while double pion photoproduction gives complementary informations, particularly on resonances that couple weakly to a single pion. Among three channels, the double neutral pion channel ($\gamma p \to \pi^0\pi^0 p$) is the most selective one, which provides interesting details because Born terms are strongly suppressed and ρ meson can not directly decay into two neutral pions. Moreover, interesting physics involving two indistinguishable π^0 system can be investigated through this channel.

Photo Beam

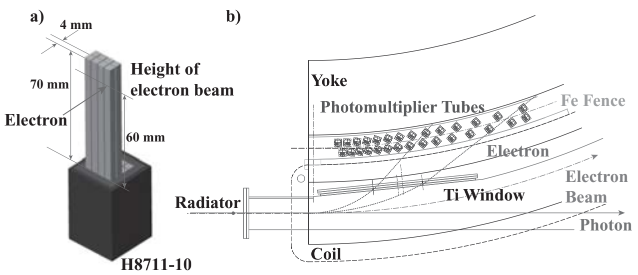

Bremsstrahlung photons are are generated by inserting a carbon fiber to 1.2 GeV circulating electrons in a synchrotron ring. Scattered electrons are bended to Tagger system to determine the energy of bremsstrahlung photons with energy resolution 1-3 MeV.

FOREST Detector System (90% solid angle cover)

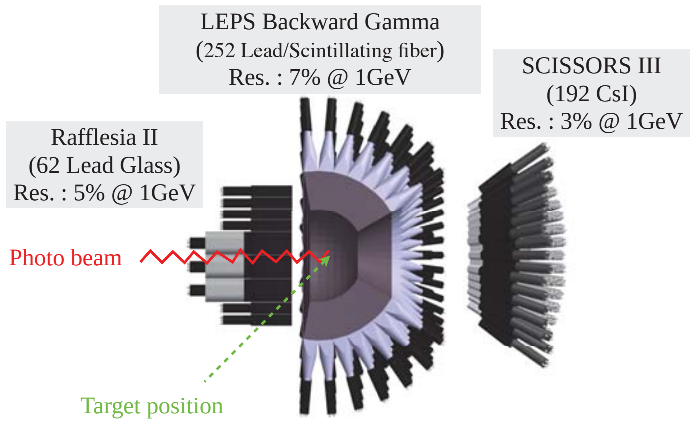

Event Selection

Reaction $\gamma p \to \pi^0\pi^0 p \to 4\gamma p$ is reconstructed by detecting its final state products 4 photons and one proton. Event from FOREST dataset survived after following selection condition will be accepted as true event for $\gamma p \to \pi^0\pi^0 p$:

- Two pairs of photons with time difference within [-1,1] ns.
- One charged cluster in time window [1,10] ns (Figure 1) with respect to the average time of four photons ($t_{4\gamma}$). No other clusters within [1,10] ns.
- Kinematic fitting

All kinematic variables are fitted to the hypothesis of $\gamma p \to \pi^0\pi^0 p$. The fitting result of chi-square(χ^2) probability are used in confidence level (*CL*) cut.

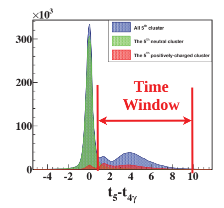

Figure 1. Time difference between the 5th cluster (t_5) and $t_{4\gamma}$.

7 constraints are applied (4 from energy-momentum conservation and other 3 from invariant masses of two pions and one proton). Event with chi-square probability larger than 20% will be accepted(Figure 2).

The error estimation of kinematic variables are checked by PULL distribution (Figure 3). It is sufficiently close to a normal Gaussian distribution N(0,1).

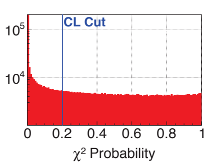

Figure 2. χ^2 probability.

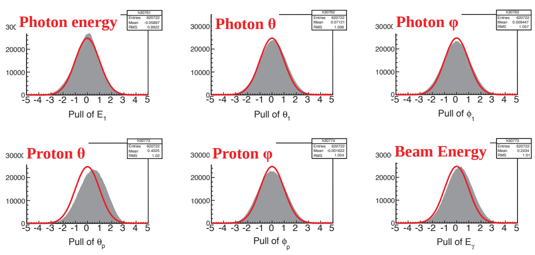

Figure 3 . Pull distribution.

Preliminary Results

- **Invariant mass of two photons and missing mass of $\gamma p \to \pi^0\pi^0 X$**

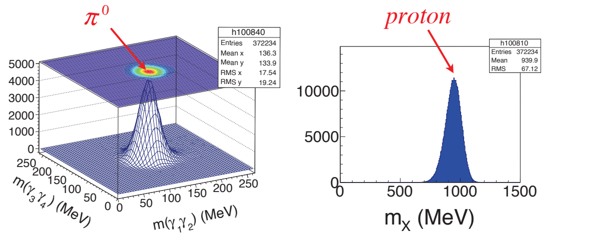

Figure 4. Left: Two photons invariant masses m(γ_1, γ_2) vs. m(γ_3, γ_4). Right: Missing mass (m_X) spectra for $\gamma p \to \pi^0\pi^0 X$. π^0 and proton signal are clearly shown in invariant mass and missing mass spectra.

- **Total cross section of $\gamma p \to \pi^0\pi^0 p$ has been obtained preliminarily and compared with previous data (Figure 5).**

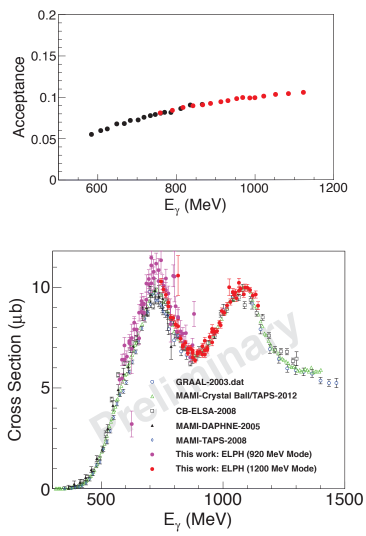

Figure 5. Up:Acceptance. Down: Total cross section for $\gamma p \to \pi^0\pi^0 p$.

Background Events Subtraction

Accidental coincident events between FOREST and Tagging spectrometer have been eliminated by subtraction of scaled distributions of random background events outside the true coincidence time window.

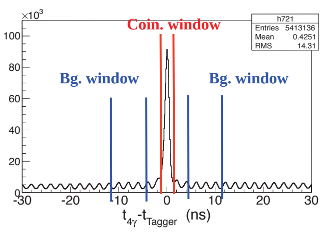

P-24

Beyond the Standard Model :Aspects of Supersymmetry

Wen Yin

Physics,Tohoku University, D1

Introduction

Physics history is the history of **"Unification".**

- Newton unified the motion of a planet and the motion of an apple. (Gravity)
- Maxwell unified electric force and magnetic force.(Electromagnetic force)
- Weinberg and Salam unified weak interaction and electromagnetic interaction. (Weinberg-Salam theory)
- String theory is expected to unify the 4 fundamental forces.

In our nature there are 2 kinds of particles.

Boson: the carrier of interactions **Fermion**: the component of matter

Can we unify these two kinds of particles?

∵Boson has integer spin . Fermion has half integer spin.

∴If we unify these two kinds of particles, we have to do some non trivial things like to **extend the concept of spacetime.**

⇒ **SUperSYmmetry (SUSY)**

On the other hand, the Standard Model (SM) in particle physics has won a lot of success, because SM agrees very much with the experiment. However, there are some theoretical and cosmological problems.

- **The fine tuning of Higgs mass (Fine-tuning problem)**
- **There is no candidate for dark matter.**
- **The accuracy of gauge unification is not so good.**
- **SM can not be combined with gravity naturally. etc.**

If we extend SM to SUSY SM (SSM), we can solve or alleviate these problems.

Also, if we believe in superstring theory in Planck scale, then our nature, which can be described as the effective theory of superstring theory **must have SUSY**.

SUSY Algebra

$$\{Q_\alpha, Q^*_{\dot\beta}\} = \sum_{\mu=0}^{3} P^\mu \sigma_{\mu\alpha\dot\beta}$$

$$\{Q_\alpha, Q_\beta\} = 0$$

$$\sigma_{0\alpha\dot\beta} = \begin{pmatrix}1 & 0\\ 0 & 1\end{pmatrix}, \sigma_{1\alpha\dot\beta} = \begin{pmatrix}0 & 1\\ 1 & 0\end{pmatrix}, \sigma_{2\alpha\dot\beta} = \begin{pmatrix}0 & -i\\ i & 0\end{pmatrix}, \sigma_{3\alpha\dot\beta} = \begin{pmatrix}1 & 0\\ 0 & -1\end{pmatrix},$$

where Q_α *and* $Q^*_{\dot\beta}$ are fermionic. P^μ is the generator of spacetime translational symmetry. With the generator of rotational symmetry of spacetime, P^μ forms the usual Poincaré symmetry which is also called as special relativity.

If we think of the theory with particle masses, Coleman-Mandula theorem says that **the only extension of Poincaré algebra is superPoincaré algebra which is equal to Poincaré algebra + SUSY algebra**.

Taking the expectation value of the first formula on a general momentum eigenstate, we get

$$\left\langle a\middle|\{Q_\alpha, Q^*_{\dot\beta}\}\middle|a\right\rangle = \left\langle a\middle|\sum_{\mu=0}^{3} P^\mu \sigma_{\mu\alpha\dot\beta}\middle|a\right\rangle$$

Tracing the index $\alpha, \dot\beta$, we get

$$|Q_1 a\rangle|^2 + |Q_1^* a\rangle|^2 + |Q_2 a\rangle|^2 + |Q_2^* a\rangle|^2 = \langle a|2P^0|a\rangle$$

∵left hand side ≥ 0,

∴The expectation value of P^0 (energy) is positive or 0.

This formula will hold whether SUSY is broken or not. Let $|a\rangle = |0\rangle$(vacuum state) ,

$$\langle 0|2P^0|0\rangle = 0 \Leftrightarrow |Q_\alpha 0\rangle|^2 = 0 \text{ and } \left|Q^*_{\dot\beta} 0\rangle\right|^2 = 0 \Leftrightarrow \text{SUSY is not broken.}$$

$$\langle 0|2P^0|0\rangle > 0 \Leftrightarrow \left(\textit{one or more of} |Q_\alpha 0\rangle|^2, \left|Q^*_{\dot\beta} 0\rangle\right|^2\right) > 0$$

⇔ SUSY is spontaneously broken.

⇒ **Vacuum energy is the order parameter of whether SUSY is spontaneously broken or not**.

Next, let's think about a massive bosonic state at rest.

The first formula → $\{Q_\alpha, Q^*_{\dot\beta}\}|1,m\rangle = m\begin{pmatrix}1 & 0\\ 0 & 1\end{pmatrix}|1,m\rangle$

∴ Q acts as fermionic version of creation operator in harmonic oscillator.

Assuming $Q^*_{\dot\beta}|1,m\rangle = 0$, there exist other states $Q_1|1,m\rangle$, $Q_2|1,m\rangle$, $Q_1 Q_2|1,m\rangle$.

∵ Q is fermionic

∴ $Q_1|1,m\rangle$, $Q_2|1,m\rangle$, are fermionic. $|1,m\rangle$,$Q_1 Q_2|1,m\rangle$are bosonic.

⇒There are 4 states, 2 are fermionic, 2 are bosonic.

We know

- SUSY is a symmetry that interchanges bosons and fermions.
- In SUSY theory, the number of bosonic particle states is equal to the number of fermionic particle states (for nonzero momentum particles).
- The vacuum energy (cosmological constant) vanishes.
- When we extend SM to SSM, we should add particles. **So some of these can be dark matter candidates.**
- The gauge unification accuracy can increase or decrease since SSM has different particle components from SM. In fact, **the accuracy increases.**

Superspace Formulation

Ordinal field theory: local theory of spacetime coordinate	
P^μ *conjugates to*	$x^\mu \equiv$ spacetime coodinate
Spacetime symmetry	Poincaré symmetry(rotation and translation in spacetime)
⇒Action	$S = \int d^4x L(x)$
Scalar field	$\phi(x)$

∵SuperPoincaré algebra is the extension of Poincaré algebra.

∴We can use the analogy of ordinal field theory to formulate SUSY field theory.

Changing spacetime into superspace, we get the table below.

SUSY field theory: local theory of superspace cordinate	
$\left(P^\mu, Q_\alpha, Q^*_{\dot\beta}\right)$ *conjugates to*	$\left(x^\mu, \theta_\alpha, \theta^*_{\dot\beta}\right) \equiv$ *superspace coodinate*
Superspace symmetry	superPoincaré symmetry(rotation and translation in superspace)
⇒Action	$S = \int d^4x d^2\theta d^2\theta^* K(x,\theta,\theta^*) + \int d^4x d^2\theta W(x,\theta) + h.c$
Chiral superfield	$\Phi(x,\theta) = \phi(x) + \theta_\alpha \psi^\alpha(x) + \theta^2 F(x)$

K is called Kähler potential, and W is called superpotential. **The chiral superfield can be thought as the unification of fermionic fields and bosonic fields.**

W is holomorphic function of chiral superfield. Holomorphic function means W does not contain complex conjugate of $\Phi(x,\theta)$. Holomorphy and ordinary symmetry keep W invariant under perturbative renormalization. This is called non-renormalization theorem.

Thanks to this theorem, there's no more fine-tuning problem. So **SUSY is a major resolution of the fine-tuning problem.**

SUSY Breaking

∵SM is very consistent with the experiment.

∴**SUSY must be broken down spontaneously**. However, if SUSY breaks down classically in the SSM, there would remain a sum rule for particle masses.

$$\Sigma m_{boson} - \Sigma m_{fermion} = 0$$

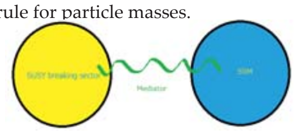

This sum rule contradicts with the experiment.

∴ SUSY can't be broken classically in SSM sector.

⇒three possibilities

1, SUSY is broken classically in the other sector.

2, SUSY is broken non-pertuabatively (i.e. quantumly in this case) in our sector.

3, SUSY is broken non-pertuabatively in the other sector.

∵Non-perturbative breakdown of a symmetry ⇔chiral symmetry breaking (maybe)

If 2, our elementary particles are not all elementary and some are composite which we don't want it to be.(Although there is some work about this type.)

∴We think about 1 and 3.∴**SUSY breaking happens in the other sector.**

∴There should be some fields to mediate the SUSY breaking effect to our sector.

Candidates for the "mediator":①SM gauge field,②gaugino,③gravity etc.

∵ SUSY breaks⇔ $\langle 0|2P^0|0\rangle > 0$

∴Our vacuum has positive energy i.e. the positive cosmological constant.

But the cosmological constant is $\sim 10^{-59} TeV^4$ while $(the$ SUSY breaking scale$)^4$ $\sim 10^4$TeV^4.We have to cancel the positive energy. There is a known mechanism. That is to extend a global SUSY to a local SUSY i.e. SUperGRAvity(SUGRA). SUGRA can produce a negative cosmological constant which cancel the positive cosmological constant produced by SUSY. In this sense **SUSY breaking expects SUGRA.**

My Work

We think that gravity mediates SUSY breaking. So our model belongs to ③. On the other hand, superstring theory predicts a 10-dimensional universe with 6 compact dimensions so that we feel just 4 dimensions. The low energy effective theory of a theory with compact dimensions always has moduli fields. So in our model there are 3 sectors, い: SSM sector ろ: SUSY breaking sector は: moduli sector. い directly interacts with ろ by higher dimensional terms, and は interacts with い,ろ,は by gravity. We assume a general Kähler potential correction generated by the quantum correction for は. The Kähler potential stabilizes the moduli field with negative energy which will cancel the positive energy due to the minimized superpotential in ろ in order to fine-tune the cosmological constant. Assuming squark mass ~ 10TeV(in order to predict Higgs mass 125GeV) we get the spectrum below.

Sparticle (Super partner for SM particle)	Mass
Squark, Slepton	~10TeV
Gaugino	~$3\times10^{-2} - 3\times10^{-1}$TeV
Gravitino	~$3\times10^{2} - 3\times10^{3}$TeV

Reference: The Quantum Theory of Fields 3,S.Weinberg

Supersymmetry and Supergravity ,Wess,Bagger

Study of the Painting Injection including the Space Charge Effect for the High-Intensity Proton Accelerator

Shinichi Kato*A), Kazami YamamotoB), Hiroyuki HaradaB), Kota OkabeB), Michikazu KinshoB)

A) Department of Physics, Tohoku University B) J-PARC Center

*Email : skato@post.j-parc.jp

Abstract

For the hadron accelerator, the beam loss should be minimized because the beam loss causes the activation. In the high-intensity accelerator, the space charge force increases and causes the beam loss. Therefore, the Japan Proton Accelerator Research Complex (J-PARC) 3GeV rapid cycling synchrotron (RCS) is injected the beam with spreading the circulating beam size intentionally. This injection method is called "Painting Injection". In order to optimize this method furthermore, we are studying with considering the optical parameter moderation by the space charge force.

Introduction

J-PARC 3GeV Rapid Cycling Synchrotron (RCS)

Fig : Overview of J-PARC

J-PARC comprises three accelerators and experimental facilities.

The accelerators play a role of source of the "high-intensity" proton beam.

<RCS Parameter>
Bunch : 2
Inj. Energy : 181 (400) MeV
Ext. Energy : 3 GeV
Repetition : 25 Hz
Power : 300 kw (1MW)

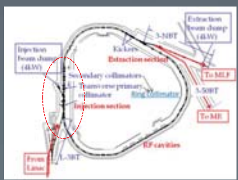

Fig : Overview of RCS

Incoherent tune spread due to the space charge effect

The particles go through while oscillating.

The number of oscillation of one turn ➡ **Betatron Tune (ν_x,ν_y)**

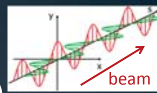

Fig : The schematic drawing of particle oscillation

An accelerator has the tune points where the oscillation amplitude increases immediately. ➡ **Resonance Points (or Lines)**

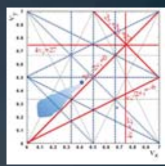

Fig : Tune diagram with the resonance lines of RCS

In the high-intensity accelerator…
A repulsive force due to the charge which each particle has (**Space charge force**) decreases the external convergent force.

The tune of each particle is decreased with each different decrement.

➡ **Incoherent Tune Spread (ν_{incoh} spread)**

we should suppress the ν_{incoh} spread in order to avoid the resonance lines !!

Injection Method of RCS

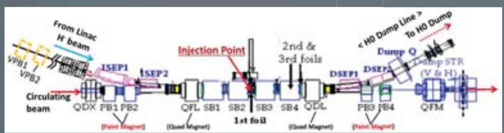

Fig : Injection area of RCS

To achieve "High-Intensity"…
・The beam is injected turn by turn dividing 235 pulses.
・The H- beam is injected and exchanged to proton by charge-exchange foil at Injection point.

➡ **Multi-Turn Charge-Exchange Injection** has been adopted.

Painting Injection

During injection, we change the injection beam position and angle depending on time.

Horizontal

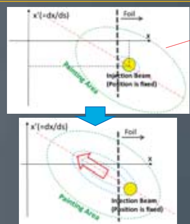

Fig : The schematic drawing of Painting Injection and phase space at 1st Foil

In the accelerator, the particles move along the phase space oval each turn.

If position and angle is moved as follow..

$$x, x' \propto \sqrt{time}$$

The Painting Area is filled with injection beam uniformly.

Vertical

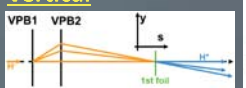

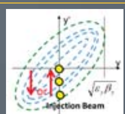

Fig : The schematic drawing of Painting injection and phase space at 1st Foil

↓ : Correlate
↑ : Anti-Correlate

The charge density is reduced and formed uniform.

➡ The ν_{incoh} spread is suppressed !

ε: Beam emittance (phase area size)
β: Twiss parameter (beam width)

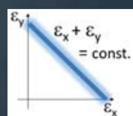

Fig : K-V distribution condition

If the distribution is ideal "**K-V distribution**", all particles receive same space charge force.

➡ **ν_{incoh} doesn't spread (only shift)** and **Anti-Correlate Painting Injection can make the K-V like distribution !!**

Painting Injection Modification

To realize K-V like distribution, 2 manipulations are applied as follow.

1. Applying y' offset

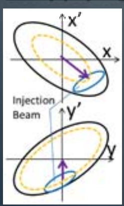

Fig : Anti-Corr. Painting injection for RCS

Painting Injection is performed to let Injection beam tail into same emittance area for Horizontal and Vertical.

But…
Because the slope of injection beam oval is opposite from the Ring, Anti-Correlate Painting run off the ideal K-V condition (present).

➡ **Add offset to y'** (only offset)

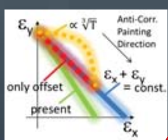

Fig : Anti-Corr. Painting Conditions

2. Time function change

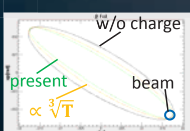

Fig : Horizontal Phase space Oval by Envelope Eq. calculation

When the space charge force is strong…
Injection beam less spread than expected on the Horizontal phase space because the oval become narrow.

To reduce the change of the oval and spread injection beam…
Modify the time function as follow ($\propto \sqrt[3]{T}$) $x, x' \propto \sqrt[3]{time}$

➡ **Tune shift and ν_{incoh} spread is reduced !!**

Optical Parameter Moderation by the space charge force

Transverse motion including space charge force satisfy the **"Envelope equation"** regardless of the distribution approximately as follow…

$$\frac{d\tilde{x}'}{ds} + k(s)\tilde{x} = \frac{\varepsilon_x{}^2}{\tilde{x}^3} + k_{sc}\frac{1}{\tilde{x}+\tilde{y}}$$

$k(s)\tilde{x}$: External convergent force by Magnets; $k_{sc}\frac{1}{\tilde{x}+\tilde{y}}$: Space charge force

$$\varepsilon_{rms} = \sqrt{< x^2 >< p_x{}^2 > - < xp_x >^2}$$

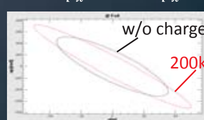

Fig : Horizontal Phase space Oval by Envelope Eq. calculation after Anti-Corr. Injection (ε = 100π mm mrad)

This Equation indicate that…
The β is changed by the space charge force.

➡ **Phase space oval is changed.**

Particular, Horizontal Phase space oval become long and narrow in RCS.

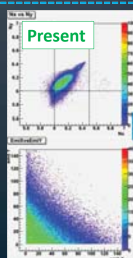

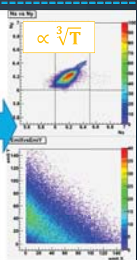

Fig : Tune diagram and emittance distribution after Painting Injection

Summary

We are studying for the Painting Injection including the space charge force in order to reduce the beam loss as possible.

It is expected that the tune shift and the ν_{incoh} spread could be reduced using existing system more than ever before.

PS88 P-26

Anisotropic magnetic response in Kondo lattice with antiferromagnetic order

T. Kikuchi, S. Hoshino, Y. Kuramoto

Department of Physics, Tohoku University

Introduction

Kondo lattice model

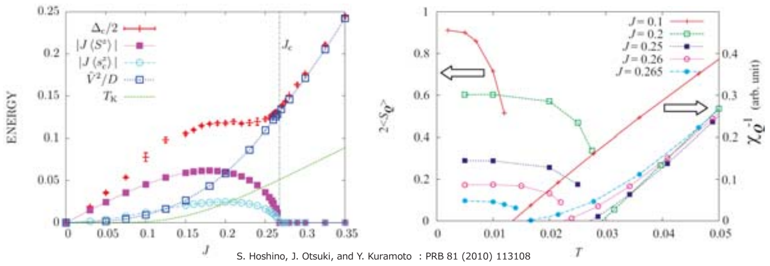

S. Hoshino, J. Otsuki, and Y. Kuramoto : PRB 81 (2010) 113108

① J ≲ 0.10 → Curie-Weiss law → mean field theory in Heisenberg model

② J ≳ 0.27 → Kondo effect is dominant
→ Kondo insulator (no antiferromagnetic order)

0.10 < J < 0.27 → competition between RKKY interaction and Kondo effect

CeT_2Al_{10}

$CeRu_2Al_{10}$ → $CeRu_2Al_{10}$, $CeOs_2Al_{10}$, $CeFe_2Al_{10}$

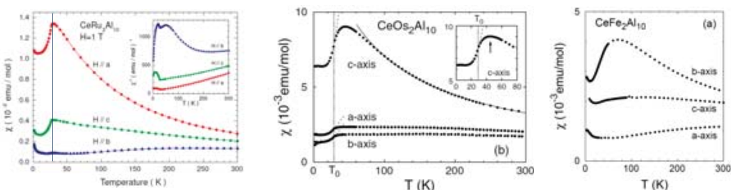

H. Tanida, et al : J. Phys. Soc. Jpn. **79** (2010) 083701 T. Nishida, et. al. : J. Phys. Soc. Jpn 78 (2009) 123705 T. Takesaka, et. al. : Journal of Physics: Conference Series **200** (2010) 012201

- Antiferromagnetic (AF) order in $CeRu_2Al_{10}$, $CeOs_2Al_{10}$ at low temperature
- magnetic susceptibility decreases in all directions below the Ne'el temperature T_N in $CeRu_2Al_{10}$, $CeOs_2Al_{10}$

Purpose

Simple Heisenberg model cannot account for the decrease of susceptibilities in all directions.

↓

We deal with the region (J = 0.1 ~ 0.27) where the AF order occurs under the strong influence of the Kondo effect.

Model

Calculation method for Kondo lattice model

◦ Kondo lattice model

$$\mathcal{H}_{\rm KL} = \sum_{\boldsymbol{k}\sigma} \epsilon_{\boldsymbol{k}\sigma} c^\dagger_{\boldsymbol{k}\sigma} c_{\boldsymbol{k}\sigma} + J \sum_i \boldsymbol{S}_i \cdot \boldsymbol{s}_{c\,i}$$

We solve lattice model with the dynamical mean-field theory combined (DMFT)
→ We have to solve impurity model A. Georges, G. Kotliar, W. Krauth and M.J. Rozenberg, Rev. Mod. Phys. **68** (1996) 13.

$$\mathcal{H}_{\rm Kondo} = \sum_{\boldsymbol{k}\sigma} \epsilon_{\boldsymbol{k}} c^\dagger_{\boldsymbol{k}\sigma} c_{\boldsymbol{k}\sigma} + 2J\boldsymbol{S}\cdot\boldsymbol{s}_c$$

We apply the continuous-time quantum Monte Carlo method (CT-QMC)
E. Gull, et. al., Rev. Mod. Phys. **83** (2011) 349(56)

J expansion for transverse magnetization

◦ Kondo model

$$\mathcal{H}_{\rm Kondo} = \sum_{\boldsymbol{k}\sigma} \epsilon_{\boldsymbol{k}} c^\dagger_{\boldsymbol{k}\sigma} c_{\boldsymbol{k}\sigma} + 2J\boldsymbol{S}\cdot\boldsymbol{s}_c$$

↓

Kondo model plus transverse magnetic field

$$\mathcal{H}_0 = \sum_{\boldsymbol{k}\sigma} \epsilon_{\boldsymbol{k}\sigma} c^\dagger_{\boldsymbol{k}\sigma} c_{\boldsymbol{k}\sigma} - \sum_\sigma \frac{J_{\sigma\sigma}}{2} c^\dagger_\sigma c_\sigma + \underbrace{\sum_{\boldsymbol{k}\sigma} h_{\boldsymbol{k}\sigma\bar\sigma} c^\dagger_{\boldsymbol{k}\sigma} c_{\boldsymbol{k}\bar\sigma}}_{\text{energy for transverse mag}}$$

$$\mathcal{H}_1 = \sum_{\sigma\sigma'} J_{\sigma\sigma'} X_{\sigma\sigma'} (c^\dagger_{\sigma'} c_\sigma - \alpha\delta_{\sigma\sigma'}) + J\alpha$$

Isotropic interaction
$J_{\uparrow\uparrow} = J_{\downarrow\downarrow} = J_{\uparrow\downarrow} = J_{\downarrow\uparrow}$

+ Zeeman term

$$\mathcal{H}_{\rm zeeman} = -\sum_\sigma H_z \sigma^z_{\sigma\sigma} (c^\dagger_\sigma c_\sigma + X_{\sigma\sigma})$$

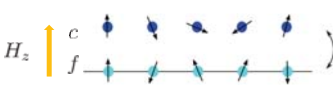

$$\sum_{\boldsymbol{k}\sigma} h_{\boldsymbol{k}\sigma\bar\sigma} c^\dagger_{\boldsymbol{k}\sigma} c_{\boldsymbol{k}\bar\sigma}$$
energy for transverse mag

◦ Initial condition

$h_{\boldsymbol{k}\sigma\bar\sigma} = h_{\rm constant}$

$\sigma\bar\sigma = \uparrow\downarrow$ or $\downarrow\uparrow$

◦ $h_{\boldsymbol{k}\sigma\bar\sigma}$ is determined by DMFT loop

Magnetic susceptibilities

We calculate uniform longitudinal and transverse susceptibilities by applying magnetic field parallel and perpendicular to AF magnetization

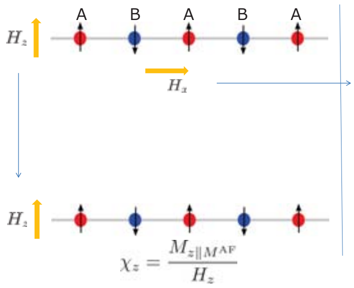

$$\chi_z = \frac{M_{z \parallel M^{\rm AF}}}{H_z}$$

We cannot use segment algorithm because magnetization along z axis is not conserved
→ It is difficult to calculate by present method

◦ Interaction is isotropic

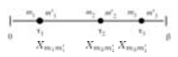

$M_z^{\rm AF}$ in H_x → $M_x^{\rm AF}$ in H_z

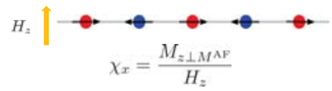

$$\chi_x = \frac{M_{z \perp M^{\rm AF}}}{H_z}$$

Result

◦ Band width
$D = 1$

◦ Filling
$n_c = 1$

◦ Density of states

$$\rho_0(\epsilon) = \frac{2}{\pi D}\sqrt{1-\left(\frac{\epsilon}{D}\right)^2}\,\theta(D-|\epsilon|)$$

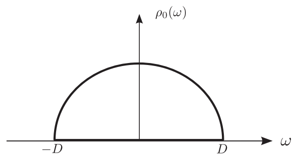

Field dependence of Magnetization

◦ Uniform magnetization ◦ Staggered magnetization

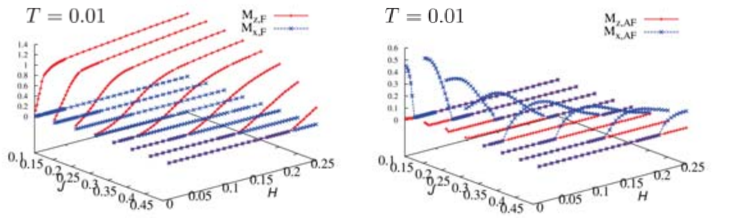

Susceptibilities

◦ $J = 0.10,\ H_z = 0.005$

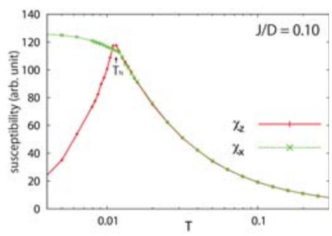

◦ $J = 0.20,\ H_z = 0.01$

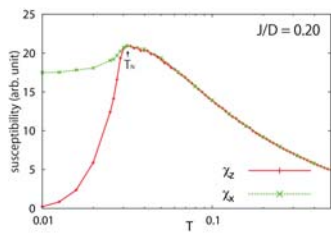

⇔ $CeRu_2Al_{10}$

◦ $J = 0.25,\ H_z = 0.01$

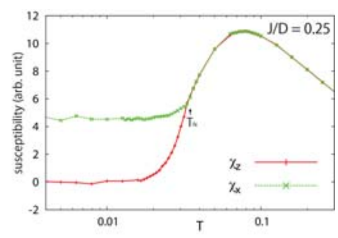

⇔ $CeOs_2Al_{10}$

◦ $J = 0.30,\ H_z = 0.01$

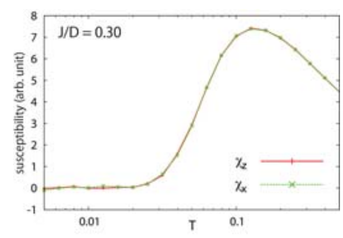

⇔ $CeFe_2Al_{10}$

Summary

Behavior of susceptibilities depend on the value of J

◦ J = 0.10 → mean field theory in Heisenberg model (RKKY interaction)

◦ J = 0.20 → both longitudinal and transverse susceptibilities decease below T_N
→ $CeRu_2Al_{10}$

◦ J = 0.25 → both longitudinal and transverse susceptibilities start to decease above T_N
→ $CeOs_2Al_{10}$

◦ J = 0.30 → Kondo insulator without magnetic order
→ $CeFe_2Al_{10}$

Neutron scattering study on *f* electron states of Pr-based compounds

H. Kobayashi, K. Iwasa, [1]K. Tomiyasu, [2]N. Nagasawa, [2]K. T. Matsumoto, [2]T. Onimaru, [2]T. Takabatake, [3]S. Kawamura, [3]T. Kikuchi, [3]K. Nakajima

Dept. of Phys. Tohoku Univ., [1]Center for the Advancement of Higher Education, Tohoku Univ., [2]AdSM Hiroshima Univ., [3]MLF Division, J-PARC Center, JAEA

Introduction

Strong correlated *f* electron system

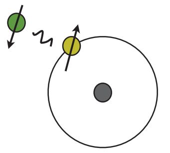

Localized electron

c-f hybridization effect

Itinerant electron

Various electron properties

- Kondo semiconductor
- Valence fluctuation
- Non BCS-type superconductivity
- Heavy electron system
- **Multipolar ordering**

PrT_2Zn$_{20}$ are remarkable compounds because of low-T properties due to degrees of freedom.

Objective

The aim of this study is to investigate the *f* electronic states of PrT_2Zn$_{20}$ (T = Ru, Rh and Ir) by using neutron scattering experiments.

Experiments

Samples (AdSM Hiroshima Univ.)

- PrT_2Zn$_{20}$ polycrystal by zinc self-flux method.

Neutron scattering measurements

- TOPAN 6G, JRR-3, JAEA
- BL-14, J-PARC, JAEA

Properties of PrT_2Zn$_{20}$ (T = Ru, Rh and Ir)

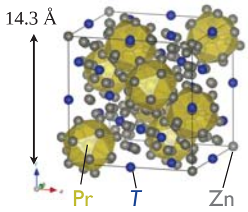

Cubic structure(Fd-$3m$)

local symmetry : T_d

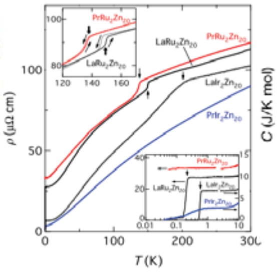

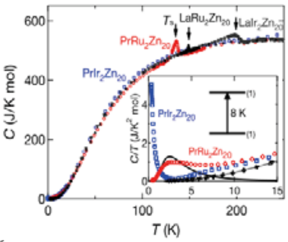

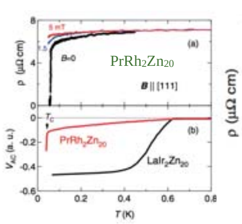

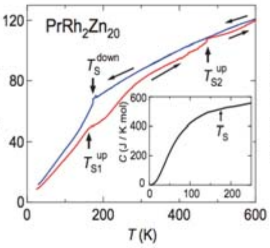

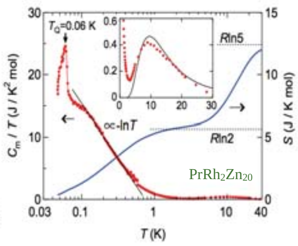

PrIr$_2$Zn$_{20}$: Superconductivity (T_C < 0.05 K), quadrupolar ordering (T_Q = 0.11 K)[1,2]
PrRu$_2$Zn$_{20}$: No anomaly in low temperature. Structural transition (T_s=138 K) [1]
PrRh$_2$Zn$_{20}$: Superconductivity (T_C = 0.06 K), structural transition (T_s=140 K) , quadrupolar ordering (T_Q = 0.06 K), heavy-electron-like behavior[3]

Results & Analysis

PrIr$_2$Zn$_{20}$

Γ$_5$(5.80meV)
Γ$_1$(5.67meV)

Γ$_4$(2.36meV)

Γ$_3$(0)

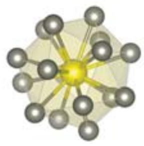

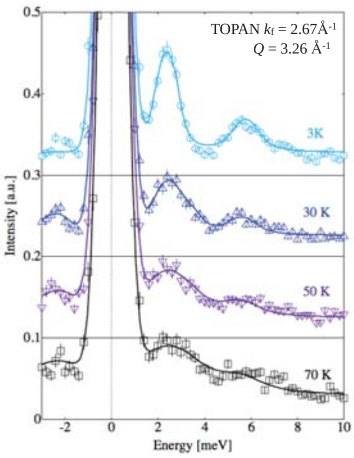

- The spectra composed of sharp peaks → Crystal field (CF) excitation
  The f electrons are well localized.
- CF ground state is Γ$_3$ doublet
  The *f* electrons have a quadrupolar degree of freedom.

PrRh$_2$Zn$_{20}$

Γ$_1$(6.77meV)
Γ$_4^{(2)}$(5.78meV)

Γ$_4^{(1)}$(3.48meV)

Γ$_{23}$(0)

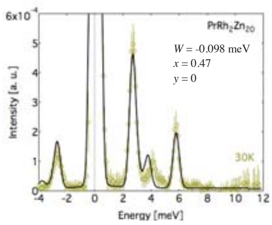

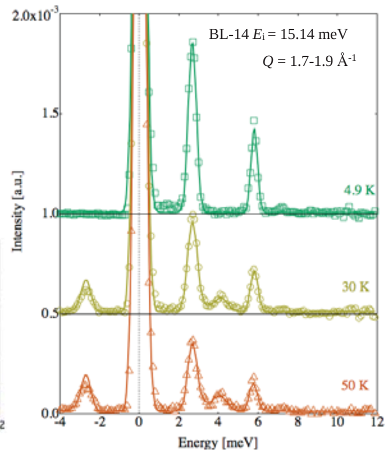

- CF ground state is Γ$_3$ doublet
- Pr-site local symmetry becomes lower on the structural transformation (T_d→T)

PrRu$_2$Zn$_{20}$

Γ$_1$(7.59meV)

Γ$_4$(4.48meV)
Γ$_5$(3.16meV)

Γ$_3$(0)

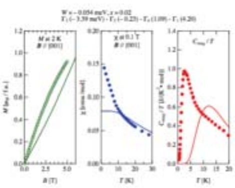

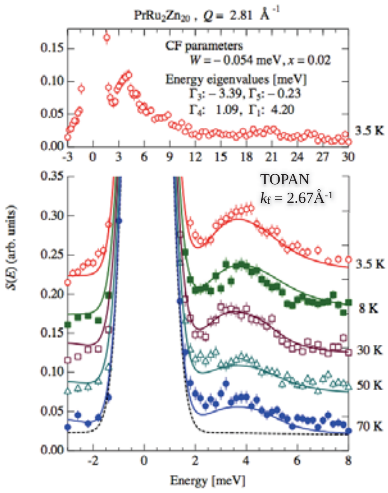

- Well localized *f* electrons
- The spectra seems to be consistent with T_d symmetry, but it does not reproduce M, χ and C/T.

Discussions

- Because PrRu$_2$Zn$_{20}$ undergoes structural transition, the CF model analysis with T_d symmetry is not correct. We need a detailed analysis for whole understanding of the data.
- PrT_2Zn$_{20}$ (T=Ru, Rh, Ir) investigated in this study show clear CF excitations. We did not observe any significant broadening of excitations or quasielastic scattering. PrInAg$_2$, which shows a large Sommerfeld coefficient 6.5 J/(mol.K)^2, was confirmed to exhibit the well-define excitation peaks between CF splitting levels with Γ$_3$ doublet ground state[4]. The strong correlation between *f* and conduction electrons in three compounds does not give renormalization effect on the magnetic excitation spectra, in contrast to the conventional Kondo-effect systems.

Summary

- In this study, we investigated that PrT_2Zn$_{20}$ (T=Ru, Rh and Ir) show clear CF excitations. The ground states are Γ$_3$ doublet which have a quadrupolar degree of freedom.
- The local symmetries of Pr-ion site in the three compounds are different from each other. Details of crystal structures in the low-T phases should be determined.

[1]T. Onimaru *et al.*: J. Phys. Soc. Jpn. **79** (2010) 033704. [2]T. Onimaru *et al.*: J. Phys. Rev. Lett. **106** (2011) 177001.
[3]T. Onimaru *et al.*: Phys. Rev. B **86** (2012) 184426. [4]T. M .Kelly *et al.*:Phys. Rev. B **61** (2000) 1831.

5th GCOE International Symposium, 4-6, March, 2013

Peccei-Quinn invariant extension of the NMSSM with a Higgs mass of 125GeV

Kwang Sik Jeong, Yutaro Shoji, Masahiro Yamaguchi

Department of Physics, Tohoku University

Introduction

The discovery of a new boson

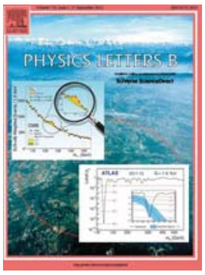

A new boson was discovered at the Large Hadron Collider (LHC) in July 2012; a neutral spin0 (or spin2) boson with a mass around 125GeV. It can be the long-sought last piece of the standard model (SM) of particle physics, the Higgs boson. If it is true, it should be closely tied to a mechanism of generating the masses of the elementary particles, which would be forbidden by the underlying symmetries.
So far the data obtained at the LHC are consistent with the SM Higgs boson.

However, the Higgs field is just a emergency tire for the SM and detailed research in the future may reveal what are really responsible for the mass generation, or the spontaneous symmetry breaking.

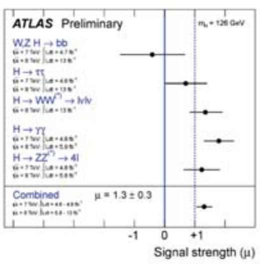

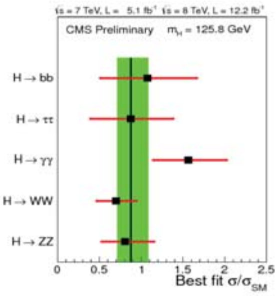

Supersymmetry

Concepts

The supersymmetry is a symmetry relating fermions and bosons. Extending the SM with it enables us to address some mysteries in the SM.

Gauge hierarchy problem

Being a spin0 field, the Higgs field is very sensitive to a more fundamental theory through quantum corrections. This implies that the masses of the gauge bosons would be of the same order as the fundamental scale. However, since the gauge bosons have masses around 100GeV, whereas the gravitational scale is around 10^{18}GeV, the theory seems highly unnatural. This is so-called the gauge hierarchy problem.

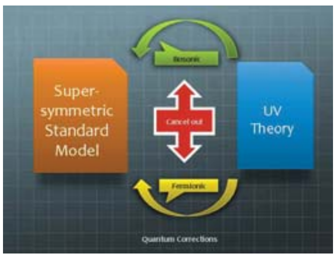

Since quantum corrections from fermions and bosons are the same in magnitude but different in sign, the supersymmetry can make them cancel out and solves the problem.

Dark matter

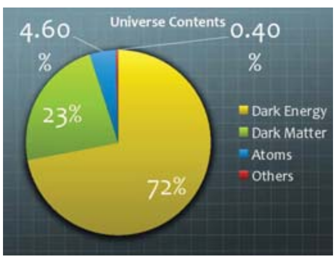

Many astronomical observations such as rotational speeds of galaxies and gravitational lensing effects indicate that there should be a large amount of matter in the universe that cannot be accounted for only by the visible well-known matters.
A supersymmetric SM often contains a stable neutral particle and it has a potential to explain the dark matter.

Gauge unification

The gauge coupling constants of the three fundamental interactions depend on the scale where they are observed. If it is true that these interactions have the same origin, these coupling constants should meet at a certain high scale.In the SM, they fail to though they approach each other.

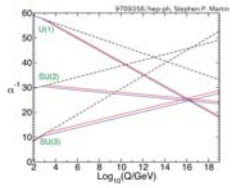

On the other hand, in a supersymmetric SM, the match becomes much more accurate. Thus a grand unified theory prefers the supersymmetry.

Higgs mass

The minimal supersymmetric standard model (MSSM), which is the simplest extension of the SM, predicts the Higgs mass to be around 100GeV. In this sense, the MSSM seems to be favored by the experiment. However, a close investigation reveals that 125GeV is slightly heavy and we need to fine-tune the parameters.

PQ-NMSSM

Philosophy

Higgs mass

A supersymmetric model need not be minimal and can contain another gauge singlet pair. Such a model is called the next-to-MSSM (NMSSM) and is favored also by a theoretical point of view. It has additional contributions to the Higgs mass and alleviates the problem.

Tadpole problem

Since the singlet is not forbidden to couple to heavy fields in a more fundamental theory, it would bring the energy scale of a fundamental theory into the model. This problem, called the tadpole problem, is overcome by imposing a symmetry. One of the most economical way is to assign the singlet a charge of the Peccei-Quinn symmetry, which is originally introduced to solve the strong CP problem.

Constraints

Z boson invisible decay

Since the Peccei-Quinn symmetry forbids the mass term of the singlino, the fermionic component of the singlet, the lightest supersymmetric particle (LSP) becomes very light. This enables the Z boson to decay into a pair of singlinos. However, the Z boson invisible decay is highly constrained by the LEP experiments.

Higgs boson invisible decay

Also the Higgs boson can decay into a pair of singlinos but since we've observed its signal, its decay mode should not dominate.

$\chi_1^0\chi_2^0$ production

The process that the LSP and the next-to-LSP (NLSP) are produced in a e^-e^+ collider and the NLSP decays into the LSP and the Z boson is constrained by the LEP experiments.

Results

We've investigated three possible regions and found the 125GeV mass can be naturally explained in this model evading all the experimental constraints.

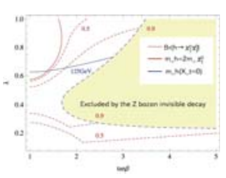

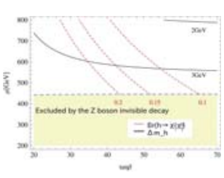

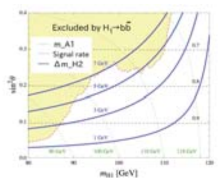

[1] Kwang Sik Jeong, Yutaro Shoji, and Masahiro Yamaguchi, "Peccei-Quinn invariant extension of the NMSSM", JHEP, 1204, 022, 2012

[2] Kwang Sik Jeong, Yutaro Shoji, and Masahiro Yamaguchi, "Singlet-doublet Higgs mixing and its implications on the Higgs mass in the PQ-NMSSM", JHEP, 1209, 007, 2012

P-29 # Electron Correlation Induced Spontaneous Symmetry Breaking in a Strongly Spin-Orbit Coupled System

Akihiko Sekine and Kentaro Nomura, *Institute for Materials Research, Tohoku University*

INTRODUCTION

◆ Three-dimensional (3D) Topological Insulators

= bulk energy gap + gapless surface states

Bi_2Se_3 (most famous 3D TI)
[H. Zhang *et al.*, Nat. Phys. **5** (2009)]

Bulk conduction band

Surface band

Bulk valence band

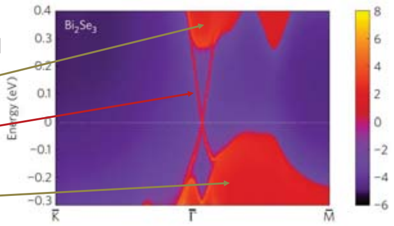

Surface states : two-component massless Dirac fermions

Bulk states : four-component massive Dirac fermions

Strong spin-orbit coupling is the key to realize a topologically nontrivial phase.

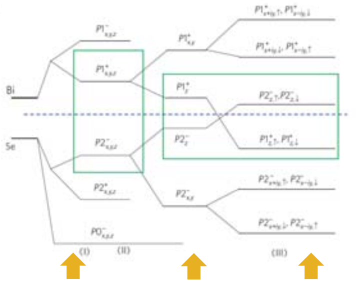

Chemical bonding | Crystal-field splitting | Spin-orbit coupling

◆ Weyl Semimetals (Topological Semimetals)

= Three-dimensional analog of graphene

= predicted in pyrochlore iridates (such as $Y_2Ir_2O_7$)

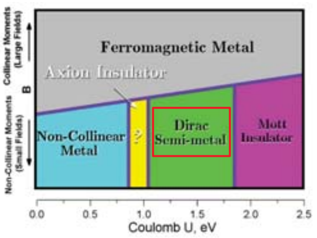

[X. Wan, A. Turner, A. Vishwanath & S. Savrasov, PRB **83** (2011)]

A novel phase induced by the interplay of spin-orbit coupling and electron correlation.

PURPOSE

◆ We investigate the effect of electron correlation in a 3D Dirac fermion system which describes a topological phase.

◆ We search for novel phases induced by the interplay of spin-orbit coupling and electron correlation.

MODEL

◆ Effective Model for 3D Topological Insulators

$$\mathcal{H}_0(\boldsymbol{k}) = \sum_{\mu=1}^{4} R_\mu(\boldsymbol{k})\cdot\alpha_\mu \qquad \begin{cases} R_j(\boldsymbol{k}) = \sin k_j, \\ R_4(\boldsymbol{k}) = m_0 + r\sum_j (1-\cos k_j) \end{cases}$$

$$\alpha_j = \begin{bmatrix} 0 & \sigma_j \\ \sigma_j & 0 \end{bmatrix},\quad \alpha_4 = \begin{bmatrix} 1 & 0 \\ 0 & -1 \end{bmatrix},\quad \alpha_5 = \begin{bmatrix} 0 & -i \\ i & 0 \end{bmatrix}.$$

= *Dirac fermion on a lattice* (called the Wilson fermion)

Z_2 invariant of the system [L. Fu, C. L. Kane & E. J. Mele, PRL **98** (2007)]

$$(-1)^\nu = \prod_{i=1}^{8}\{-\mathrm{sgn}\left[R_4(\Lambda_i)\right]\}$$

topologically nontrivial

$$= \begin{cases} -1 & (0 > m_0 > -2r \text{ or } -4r > m_0 > -6r) \\ +1 & (\text{others}) \end{cases}$$: *trivial*

◆ Coulomb Interaction between the bulk electrons

$$H_{\rm int} = \frac{V}{2N}\sum_{\boldsymbol{k},\boldsymbol{k}',\boldsymbol{q}}\sum_{\alpha,\beta} c^\dagger_{\boldsymbol{k}+\boldsymbol{q}\alpha}c^\dagger_{\boldsymbol{k}'-\boldsymbol{q}\beta}c_{\boldsymbol{k}'\beta}c_{\boldsymbol{k}\alpha}$$

$\alpha,\ \beta = (A,\uparrow),\ (A,\downarrow),\ (B,\uparrow)$ or $(B,\downarrow)$ (a component of spinor)

SUMMARY

◆ Spontaneous time-reversal symmetry and inversion symmetry breaking is induced by electron correlation.

◆ This phase is considered to be the condensed-matter analog of the corresponding phase in the lattice QCD.

RESULTS

◆ Ground State Phase Diagram

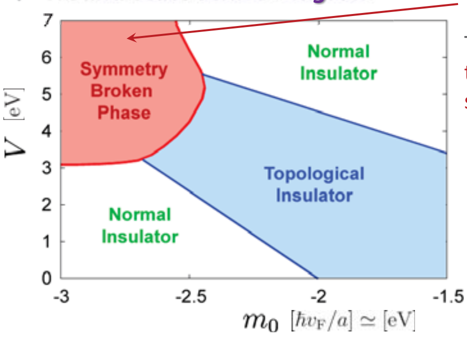

$\Delta_5 \neq 0$

The matrix α_5 breaks both time-reversal and inversion symmetries :

$$\begin{cases} \mathcal{T}\alpha_5\mathcal{T}^{-1} = -\alpha_5, \\ \mathcal{I}\alpha_5\mathcal{I}^{-1} = -\alpha_5 \end{cases}$$

Electron correlation induces spontaneous symmetry breaking.

TI Phase (m_0 = -2.5) | *Symmetry Broken Phase* (m_0 = -2.5)

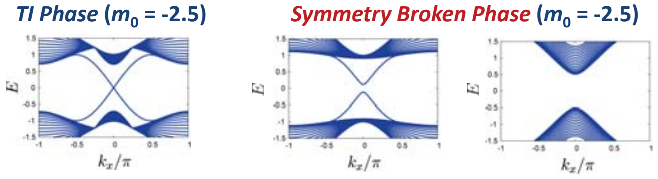

Mean-field approximation

$$H^{\rm MF}_{\rm int} = \frac{V}{2N}\sum_{\boldsymbol{k},\boldsymbol{k}'}\sum_{\alpha,\beta}\left[\langle c^\dagger_{\boldsymbol{k}\alpha}c_{\boldsymbol{k}\beta}\rangle\langle c^\dagger_{\boldsymbol{k}'\beta}c_{\boldsymbol{k}'\alpha}\rangle - 2\langle c^\dagger_{\boldsymbol{k}\alpha}c_{\boldsymbol{k}\beta}\rangle c^\dagger_{\boldsymbol{k}'\beta}c_{\boldsymbol{k}'\alpha}\right]$$ (Fock term)

"Gap Equation"

$$\hat{\Delta}_{\alpha\beta} \equiv \frac{1}{N}\sum_{\boldsymbol{k}}\langle c^\dagger_{\boldsymbol{k}\alpha}c_{\boldsymbol{k}\beta}\rangle = (\Delta_4\alpha_4 + \Delta_5\alpha_5)_{\alpha\beta} \qquad (\{\alpha_\mu, \alpha_\nu\} = 2\delta_{\mu\nu})$$

Δ_4 : Chiral (scalar mode) condensate
Δ_5 : Pion (pseudoscalar mode) condensate

Analogy with lattice QCD

◆ Phase Diagram with a Perturbation Term

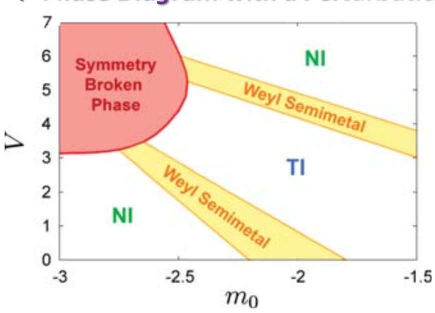

$$\mathcal{H}_{\rm imp}(\boldsymbol{k}) = b\begin{bmatrix} \sigma_z & 0 \\ 0 & \sigma_z \end{bmatrix}$$

[A. Burkov, M. Hook & L. Balents, PRB **84** (2011)]

magnetic impurities (or an external magnetic field along z-axis)

Symmetry broken phase is robust against perturbation.

[m_0 = -0.3]

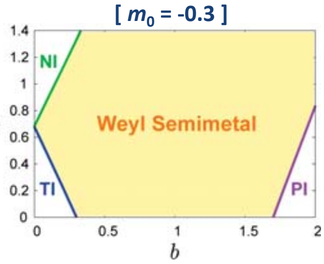

TI Phase | *WSM Phase* | *PI Phase*

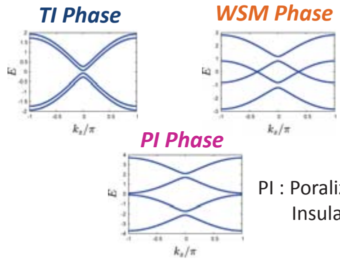

PI : Poralized Insulator

The ground state of the system is obtained as the stationary point of the free energy :

$$\frac{\partial F(\Delta_4,\Delta_5)}{\partial\Delta_4} = \frac{\partial F(\Delta_4,\Delta_5)}{\partial\Delta_5} = 0 \quad \text{where} \quad F(\Delta_4,\Delta_5) = 2V\left(\Delta_4^2+\Delta_5^2\right) - \frac{2}{N}\sum_{\boldsymbol{k}}E_{\boldsymbol{k}}$$

$$E_{\boldsymbol{k}} = \sqrt{\sum_j \sin^2 k_j + \left[m_0 - V\Delta_4 + r\sum_j(1-\cos k_j)\right]^2 + (V\Delta_5)^2}$$

P-30

The roles of excess Fe for magnetic in antiferromagnetic metal $Fe_{1+\delta}Sb$

Phys. Dept. Tohoku Univ.[A], IMR. Tohoku Univ.[B], IMSS KEK[C].
S-C. Choi[A], H. Hiraka[B], K. Ohoyama[B], Y. Yamaguchi[B], S. Nara[A], K. Iwasa[A], K. Yamada[C]

Scientific Background

magnetic excitations with anomalously steep dispersions

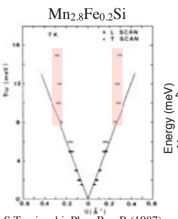

S.Tomiyoshi, Phys.Rev B (1987)

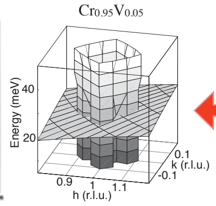

S.M.Hayden, Phys.Rev.Lett (2000)

The typical spin excitation (Fe_3Si)

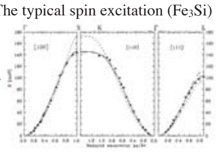
M.Szymanski, J. Phys.Condens. Matter (1991)

$Mn_{3-x}Fe_xSi$

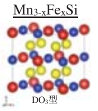

Mn_3Si
Mn-I μ_I=2.43μ_B
Mn-II μ_{II}=0.27μ_B

「Weak」Antiferro Magnetic
→Magnetic moment are small
The importance of Mn site

→ research object
$Mn_{3-x}Fe_xSi$, Cr,
$Fe_{1+\delta}Sb$,,,,

Research purpose

In our research, we aim to clarify the relationship between bulk properties and spin dynamics in itinerant-electron systems. In typical antiferromagnetic 3d metals, Cr, $FeTe_{1-x}Se_x$, $Mn_{3-x}Fe_xSi$, similar magnetic excitations with anomalously steep dispersions are observed. We expect that the anomaly in magnetic excitation must be a common property in antiferromagnetic 3d metals. To confirm the universality, we investigate magnetism of $Fe_{1+\delta}Sb$ as the other target in the antiferromagnetic 3d metals. In this study, we aim at clarifying microscopic magnetic properties in this antiferromagnetic metal $Fe_{1+\delta}Sb$ by neutron diffraction. The purpose of the high-purity sample preparation for this purpose

$Fe_{1+\delta}Sb$

Crystal Structure (Hexagonal)

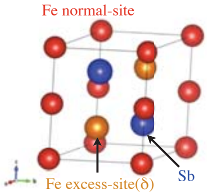

Group space : P63/mmc
a,b: 4.07Å c: 5.13Å

Fe normal-site
μ=0.88±0.05μ_B
T_N=105K ($Fe_{1.30}Sb$)

Neutron diffraction

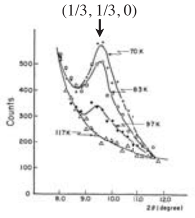

Magnetic peak of (1/3. 1/3. 0)

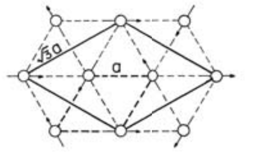
Magnetic structure of spin 120°

T.Yashiro, J. Phys. Soc. Jpn (1973)

Fe-Sb

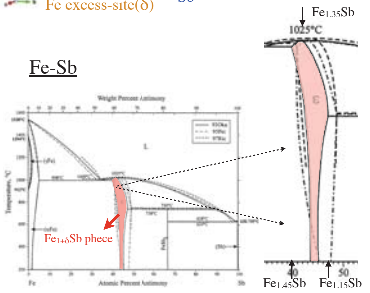

H.Okamoto, J. Phase.Equilibria (1999)

Susceptibility

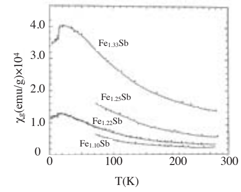

K.Yamaguchi, J. Phys. Soc. Jpn (1972)

Möessbauer

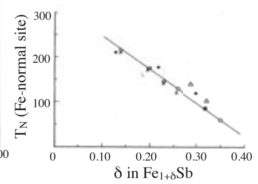

R.Kumar, Phys.Rev. B (1985)

Specimen preparation

Material：Fe(99.9%), Sb(99.9999%)

Encapsulate the Ar-gas to unclarity silica tube

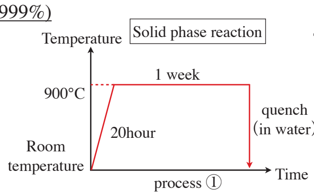

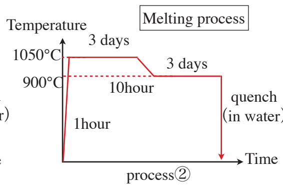

Speed up quench → We expect high purity powder

Sample creation

	Vacuum-encapsulate	Ar-encapsulate
$Fe_{1.40}Sb$	process ①→①	process ①→①
$Fe_{1.35}Sb$	process ①→②	process ①→①
$Fe_{1.30}Sb$	process ①	process ①→①
$Fe_{1.25}Sb$	process ①	
quench-time	few minutes	few seconds


Bridgman furnace photo

Measurement result

X-ray powder diffraction

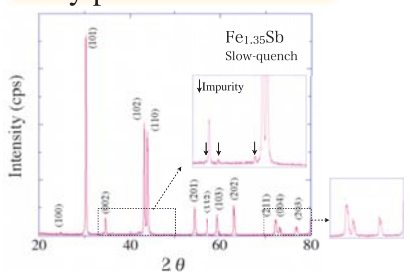

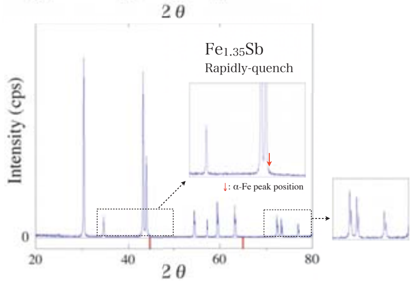

Rietveld analyze

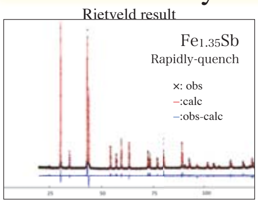

Weighing	excess-Fe occupancy g	Sb occupancy g	a	c
$Fe_{1.30}Sb$	0.22(1)	0.92(1)	4.1316(1)	5.1764(1)
$Fe_{1.35}Sb$	0.19(1)	0.88(1)	4.12586(7)	5.17047(6)
$Fe_{1.40}Sb$	0.33(1)	0.91(1)	4.1336(1)	5.1787(1)

Lattice constant

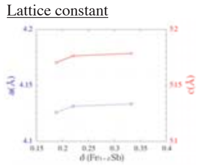
Lattice constant obtained from the Rietveld. (a,c)

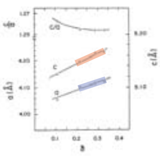
K.Yamaguchi, J. Phys. Soc. Jpn (1972)

Magnetization measurement

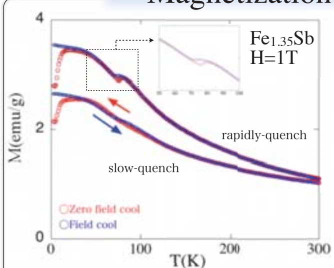

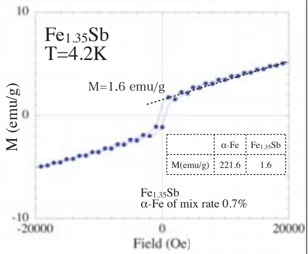

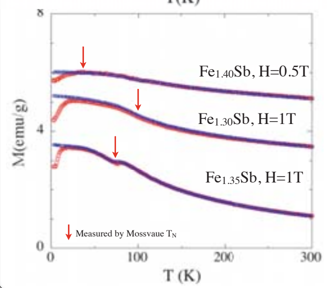

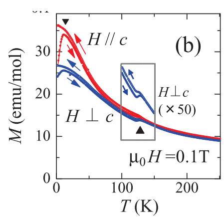

Y.Shiomi, et al, Phys.Rev.Lett (2012)

Summary

・By the rapid quench, we can see a clear anomaly in the vicinity of the T_N, we have succeeded in creating the sample.
・We have successfully fabricated sample to less than 3% of the precipitation Fe
・ We confirmed the shift in the composition, Thus, there is a need for a composition assessment.

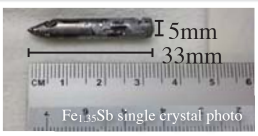

In this presentation has not been said, we have successfully growing up single crystal.

P-31

The $\gamma n \rightarrow K^0\Lambda$ reaction studied with an electromagnetic calorimeter FOREST

Yusuke TSUCHIKAWA for the FOREST Collaboration

Research Center for Electron Photon Science (ELPH), Tohoku University

Baryon spectroscopy

The mass spectra of baryons: an important testing ground for understanding low energy QCD.
A constituent quark model, describing baryons with three valence quarks, well reproduces the properties of the ground state baryons.

Yet...

- Molecule-like structure of $\Lambda(1405)$
- A mass-order-reverse problem (between $N(1535)S_{11}$ and $N(1440)P_{11}$)
- Exotic hadrons: $\Theta^+(1530)$ pentaquark baryon

$\longrightarrow$ A new effective degree of freedom emerges.

Why $K^0\Lambda$?

Recent years, the study of the $\gamma n \rightarrow K^0\Lambda$ reaction has started. Baryon resonances are expected to contribute to the reaction other than those to the $\gamma p \rightarrow K^+\Lambda$. Because both of the 2 particles in the final state are nautral, the kaon exchange and nucleon pole terms are strongly suppressed. Thus, the baryon resonance contribution in the $\gamma n \rightarrow K^0\Lambda$ is relatively much larger.

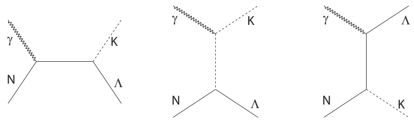

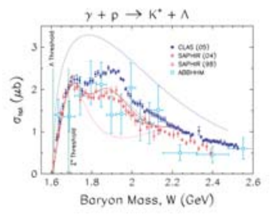

R. Bradford et al., Phys. Rev. C Vol.73, 035202 (2006).

Photon beam

We use bremsstrahlung photons which are generated by inserting a carbon fiber to 1.2 GeV circulating electrons in a synchrotron ring. The energy E_γ of the generated photons are determined by detecting recoil electrons.

E_γ = 750 ~ 1150 MeV for 1.2 GeV electrons
Tagging counter rate: ~ 20 MHz

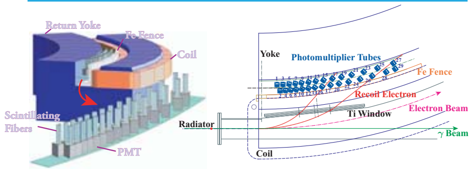

FOREST

FOREST consists of three calorimeters, which cover a solid angle of 90 % in total so as to detect most of particles generated in the final state. A plastic scintillator (PS) hodoscope is placed in front of each calorimeter to identify the charge of detected particles.

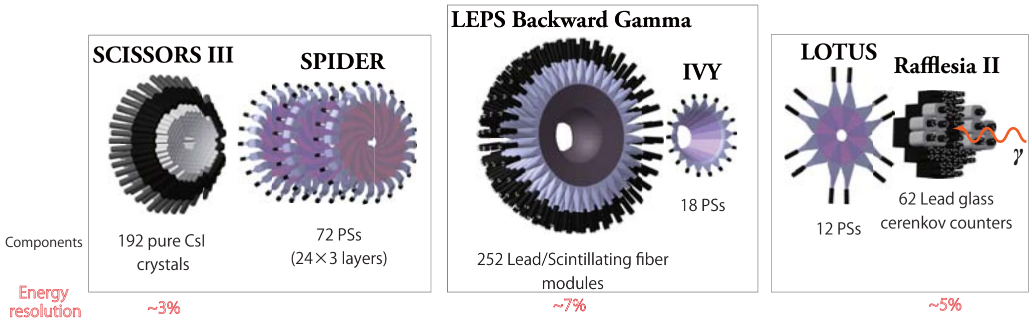

Analysis of the $\gamma n \rightarrow K^0\Lambda$

a) Event selection

The $\gamma n \rightarrow K^0\Lambda \rightarrow \pi^0\pi^0 p\, \pi^- \rightarrow 4\gamma\, p\, \pi^-$ events are selected by the following conditions:

1) 4 neutral clusters are required.

The most probable pair of 2 gammas which have one' s origin in the same π^0, are selected to minimize a following chi square

$$\chi^2 = \frac{(M(\gamma_1,\gamma_2)-m_{\pi^0})^2}{\sigma^2} + \frac{(M(\gamma_3,\gamma_4)-m_{\pi^0})^2}{\sigma^2}$$

Then the timing criterion t_C of each event is set as 4 γ average timing and the timing window is set as [-5, 15) ns from t_C.

2) 2 hits on the PS hodoscopes and no another neutral clusters in the timing window.

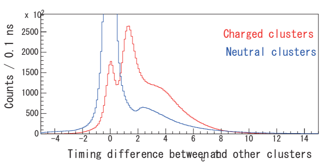

3) Kinematical fitting

The measured values of 4 gammas' are kinematical fitted to satisfy the following conditions:

$$M^2(\gamma_1,\gamma_2) \equiv 2E_1E_2(1-\sin\theta_1\sin\theta_2\cos(\varphi_1-\varphi_2)-\cos\theta_1\cos\theta_2) = m_{\pi^0}^2$$
$$M^2(\gamma_3,\gamma_4) \equiv 2E_3E_4(1-\sin\theta_3\sin\theta_4\cos(\varphi_3-\varphi_4)-\cos\theta_3\cos\theta_4) = m_{\pi^0}^2$$
$$M_X^2(\gamma_1,\gamma_2,\gamma_3,\gamma_4) \equiv E_X^2 - P_X^2 = m_\Lambda^2$$

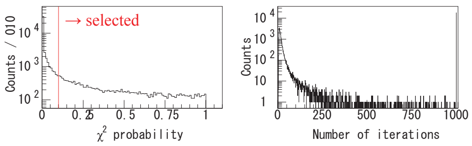

b) Background subtraction

The data include many accidental coincidence events since the tagging rate is high. They are subtracted by using the sideband background events which are indicated in the figure below of the timing difference between 4γ average timing and tagging counters.

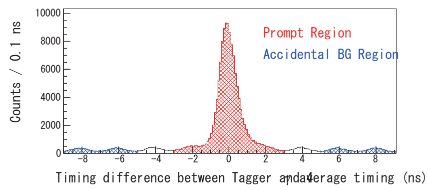

c) Result

The $\pi^0\pi^0$ invariant mass distribution is obtained for 911 < E_γ < 1150 MeV.

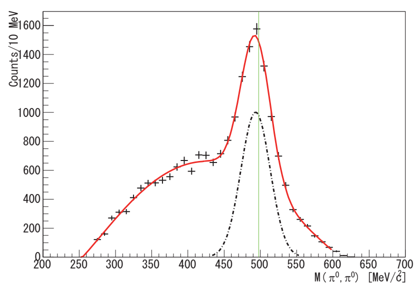

The K^0 peak is clearly observed for E_γ > 911 MeV.
We have about 5,000 K^0 events in this point.

Development of laser-cooled Fr atom source for the electron Electric Dipole Moment search

Tomohiro HAYAMIZU*

Department of Physics, Cyclotron and Radioisotope Center (CYRIC)
Tohoku University, Sendai, Miyagi, Japan
**hayamizu@cyric.tohoku.ac.jp*

(Abstract) A permanent electric dipole moment (EDM) in an elementary particle indicates the violation of the time-reversal (T) symmetry violation, related to the baryon asymmetry in our universe. Since an heavy alkaline atom, Francium (Fr, Z=87) has a large sensitivity to electron EDM, we have developed laser-cooled Fr source which applied laser-cooling and trapping techniques and a nuclear fusion reaction $^{197}Au(^{18}O, xn)^{215-x}Fr$ with an AVF cyclotron in CYRIC. We built an Fr ion beam line and transport and neutralized Fr ions to the end of it. We shows the present status of these Fr source.

Electric Dipole Moment (EDM)

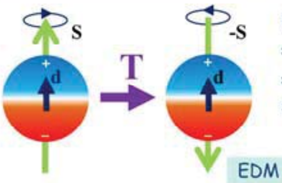

Permanent EDM in an elementary particle
= T violation
= CP violations (via CPT conservation)
⇒ Baryon asymmetry in our universe
(via Sakharov conditions)

EDM and T-violation

Electron EDM d_e in an paramagnetic atom
⇒ enhanced to atomic EDM d_{atom}

Enhancement factor $K = \frac{d_{atom}}{d_e} \propto Z^3\alpha^2$

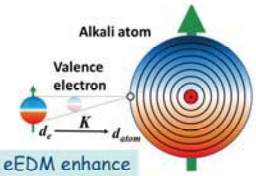

eEDM enhance

Why Francium?
1. Large enhancement factor d_{atom}/d_e
2. Availability of laser-cooling (718 nm)

Atom	Z	Enhance d_e*1
Rb	37	26
Cs	55	121
Tl	81	466
Fr	87	895

*1: Nataraj PRL 101 (08) PRL 106 (11), Mukherjee J. Phys. Chem. A 113 (09)

EDM search: Apply field B and E to atoms and measure its Larmor frequency

EDM Error $\delta d_e = \frac{\hbar F}{e}\cdot\frac{1}{K}\cdot\frac{1}{E}\cdot\frac{1}{\tau}\frac{1}{\sqrt{N\cdot m}}$

For $d_e < 10^{-28}$ ecm (^{210}Fr, Grand state F=13/2)
K : Enhancement d_{atom}/d_e =895 (Fr)
E : External electric field >100 kV/cm
τ : Interaction time ~1 sec (Optical trap)
N : Number of atoms >10^6
m : Measurement time >10^5

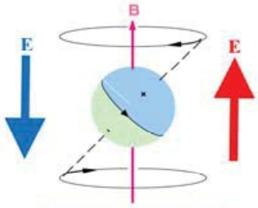

EDM measurement

Francium for EDM

Laser-cooled Fr source for e-EDM @ CYRIC

Challenge
$d_e < 10^{-28}$ ecm
= NEED a high intensity Fr source

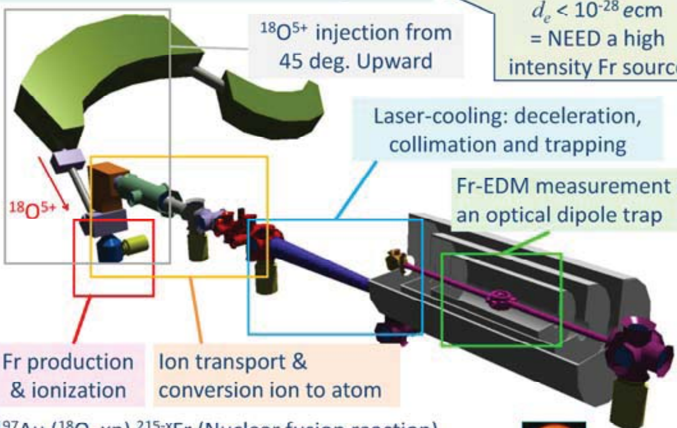

$^{197}Au(^{18}O, xn)^{215-x}Fr$ (Nuclear fusion reaction)
$^{18}O^{5+}$ beam (E_{18O} = 100 MeV) + ϕ12.5mm Au target
$^{210+211}Fr$ production rate : 3.5*10⁷ pps/pμA*2

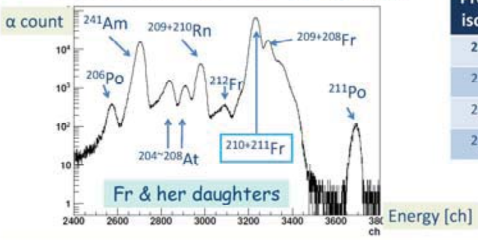

Product isotope	lifetime	Decay-α (MeV)
^{210}Fr	3.18 m	6.545
^{211}Fr	3.10 m	6.437
^{209}Fr	50.1 s	6.646
^{208}Fr	59.1 s	6.636

*2: Calculation using Corradi PRC 71 (05) & SRIM data

Cooled Fr atom source

Cooling & Trapping to Fr atoms

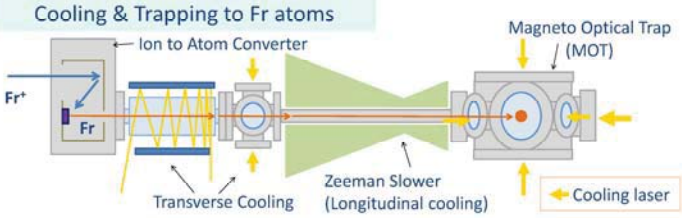

Laser cooling: Cooling by a photon absorption & emission every 20 μs

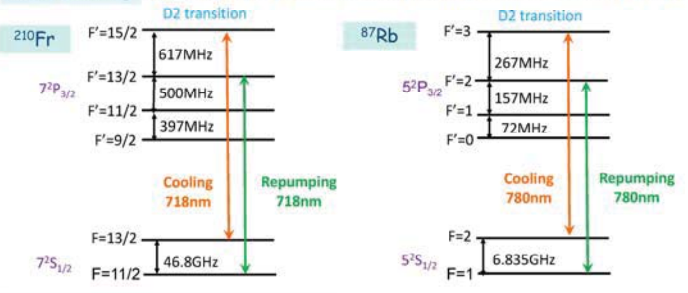

Magneto-optical trap (MOT)

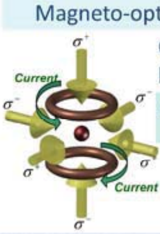

Capture atoms using 6-way cooling laser and anti-Helmholtz coil

Overview of MOT

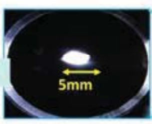

Captured Rb
~10^8 atoms

Double MOT system

Present status

Fr ion production & transport and conversion to atom

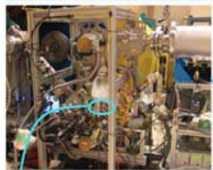

Ion production area

10m

Ion to atom converter

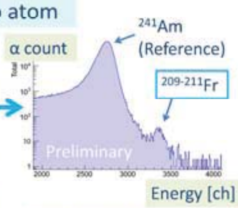

BD1{ Fr: 2.7 × 10^5 pps, Rb: ~40 nA

BD4{ Fr: 1.3 × 10^3 pps, Rb: ~2 nA

Neutral Fr peak (Talk by H. Kawamura)
⇒Observed neutralized Fr

Trapping Rb atom converted from ion

Mini-Laser cooled Rb Factory: for non-accelerator-use experiment

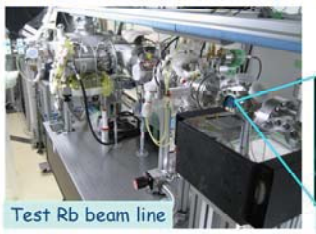

Test Rb beam line

Set up: Rb ion source + The ion to atom converter + MOT

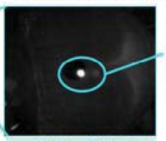

Rb in MOT

Trapped Rb atoms From the converter ~10^6 atoms

(Summary) We have developed laser-cooled Fr source for the electron EDM search. We transported Fr⁺ to the ion to atom converter and observed neutral Fr atoms from it. As next steps, we will improve each apparatuses to confirm Fr trap in the MOT. Also we start to develop of the EDM measurement system in the optical dipole trap.

P-33

Surface phonon dispersion on the hydrogen-terminated Si(110)-(1×1) surface

Stephane Yu Matsushita

Department of Physics, Tohoku University

Introduction

What is the surface phonon?

Coherent vibration of surface atoms.

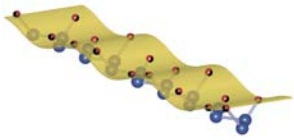

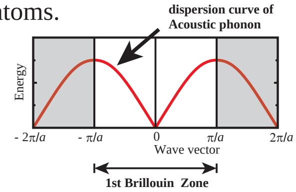

In the reduced zone scheme, it is able to select the wave vector of phonon in "1st Brillouin zone".

Selection rules due to the "glide symmetry operation"

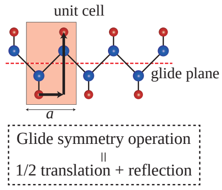

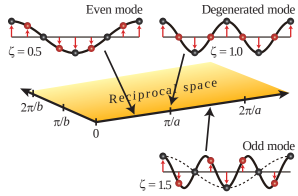

Restrict phonons to the even/odd order zone.

K.C. Prince, J. Electron Spectrosc. Relat. Phenom. **42** (1987) 217.

There is no systematic investigation on the role of the glide plane.

H:Si(110)-(1×1) surface

- Two glide planes
- Stable structure

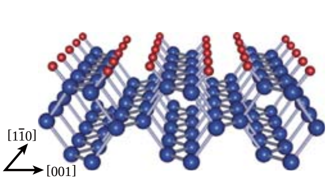

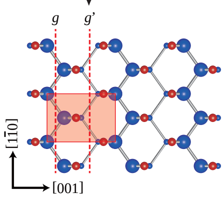

Aim

(a) Prepare a clean, well-ordered H:Si(110)-(1×1) surface.

(b) Measure the surface phonon dispersion.

(c) Clarify the role of the glide plane.

Experimental details

Sample preperation

- Wafer : n-type Si(110)
- Etching solution : NH_4F(40%) + $(NH_4)_2SO_3$(1%)
- Etching time : 10 min.

LEED measurements

- Incident energy : 30 ~ 200 eV

HREELS measurements

- Incident energy : 8 ~ 100 eV
- Resolution : ~7 meV
- Direction : $\bar{\Gamma}$-$\bar{X}$([1$\bar{1}$0]), $\bar{\Gamma}$-$\bar{X}$' ([001])
- Varing the scattering angle

Results & Discussion

(i) *LEED images*

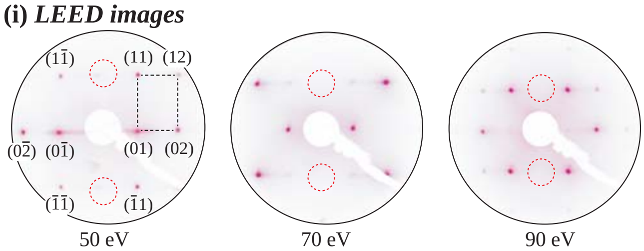

(ii) *HREELS spectra of H:Si(110) surface*

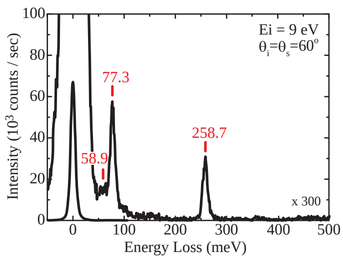

- Vibrational modes of H atoms
  77.3 meV → Si-H bending
  258.7 meV → Si-H stretching
- Vibrational modes of Si atoms
  58.9 meV → Cs
- Vibrational modes of Contaminations
  97.3 meV → Si Oxide
  156, 362 meV → Hydro-Carbon

(iii) *HREELS spectra of surface phonons*

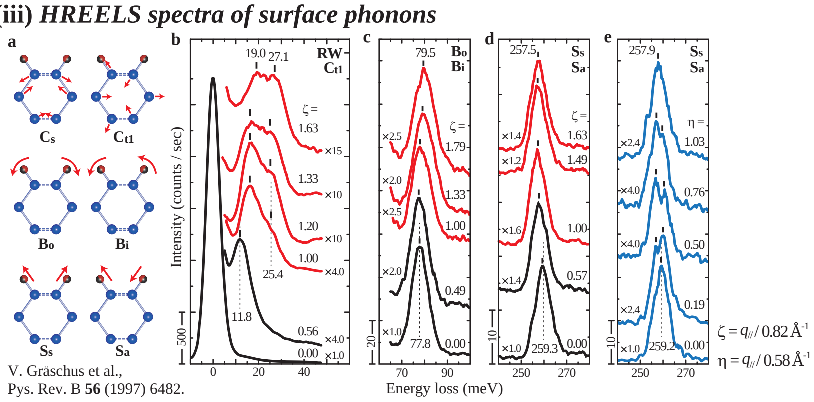

V. Gräschus et al., Pys. Rev. B **56** (1997) 6482.

(iv) *Surface phonon dispersion*

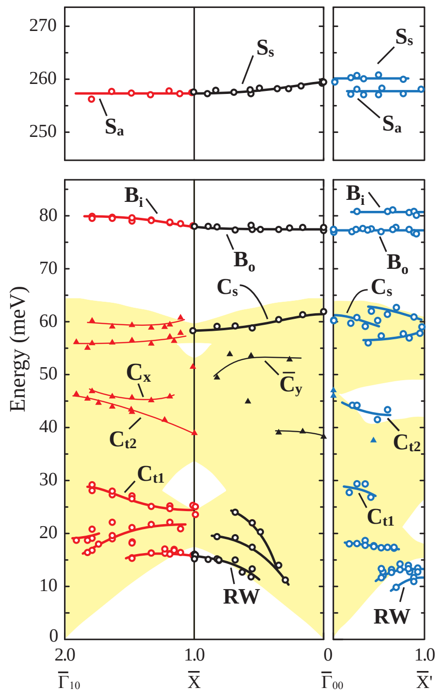

- Onset modes (Cs, Ct1) & Even/Odd shift (Ss, Sa, Bo, Bi, RW) → **Selection rule due to the glide plane.**
- Anisotropic dispersion (Ss, Sa, Bo, Bi) → **Vibrational confinement along the [001] direction.**

Conclusion

- We successfully prepared a well-ordered, ultra-clean H:Si(110)-(1×1) surface.
- Due to the glide plane, the surface modes are restricted to the 1st or 2nd Brillouin zone.
- Between the hydrogen atoms, there is an interaction along the chain, but not accross the chain.

→ **For surfaces which have a glide plane, we need to extend the concept of "Reduced zone scheme" to 2nd Brillouin zone.**

Hopf algebraic symmetry of effective theory of string in H-flux background

Department of Physics, Particle Theory and Cosmology Group, D1 Hisayoshi Muraki

Why string theory?

String theory is a candidate of

- ◆ Quantum theory of Gravity
- ◆ Unified theory, which describes all known interactions

What is string theory?

◆String is Fundamental object

◆The typical length of the string is Planck length $1.6\times 10^{-35}[\mathrm{m}]$

◆Because string is very short, it seems particle for us

STRING 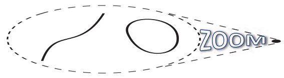 PARTICLE

◆Different Particle corresponds to different Oscillate mode

open string ➡ Gauge field A_μ

closed stirng ➡ Metric $g_{\mu\nu}$

B-filed $B_{\mu\nu}$

Dilation Φ

◆ Dynamics of string in background fields is described by non-linear sigma-model

$$S[X]=\frac{1}{2\pi\alpha'}\int_\Sigma d^2z\partial X^\mu\bar\partial X^\nu(g_{\mu\nu}(X)+\mathcal{F}_{\mu\nu}(X))$$

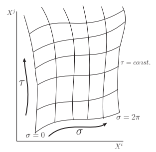

Σ : World-sheet, which is the trajectory of the string's motion

X^μ : Coordinates of the string in the D-dim. space-time

$g_{\mu\nu}$: Metric of the D-dim. space-time

$\mathcal{F}_{\mu\nu}=B_{\mu\nu}+2\pi\alpha' F_{\mu\nu}$: Sum of B-field and field strength

$F_{\mu\nu}=\partial_\mu A_\nu-\partial_\nu A_\mu$: Field strength

◆ Requirement: Theory is Invariant under conformal transformation of the world-sheet

Conformal transformation is the local scale transf. of the parameterization of the world-sheet

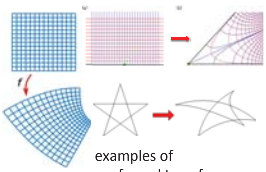

examples of conformal transf.
by Google images

◆This requirement determines dimension of the space-time, backgrounds' equations of motion and etc.

$$\beta^{(A)}_{\mu\nu}=G^{\nu\sigma}\nabla_\sigma\mathcal{F}_{\nu\mu}-\frac{1}{2}\Theta^{\rho\sigma}H_{\rho\sigma\lambda}\mathcal{F}^\lambda{}_\mu=0$$: Maxwell's equation

$$\beta^{(g)}_{\mu\nu}=R_{\mu\nu}-\frac{1}{4}H_{\mu\alpha\beta}H_\nu{}^{\alpha\beta}=0$$: Einstein's equation

$$\beta^{(B)}_{\mu\nu}=-\frac{\alpha'}{2}\nabla^\rho H_{\rho\mu\nu}=0$$: Equation of motion of B-field

Gravity and Geometry

◆Classical theory of Gravity : General relativity

Space-time is physical, formulated by Riemannian geometry

Fundamental object is Particle

◆Quantum theory of Gravity : String theory?

Fundamental object is String

String might see space-time differently from particle

➡ Quantum gravity could change our notion of space-time

Non-commutative space

◆ From the analysis of an opens string in a constant B-field

The Endpoints become non-comutative

$$[X^\mu, X^\nu]=i\Theta^{\mu\nu}$$

Here $\Theta=-(g-\mathcal{F})^{-1}\mathcal{F}(g+\mathcal{F})^{-1}$

◆Reflecting this non-commutativity, the product is replaced with Moyal product, which is non-commutative

$$f*g(x)=\exp\left(\frac{i}{2}\Theta^{\mu\nu}\partial^{(x)}_\mu\partial^{(y)}_\nu\right)f(x)g(y)\Big|_{x=y}$$

e.g. $[x^\alpha, x^\beta]_\star=x^\alpha\star x^\beta-x^\beta\star x^\alpha=i\Theta^{\alpha\beta}$

String in H-flux

◆ Non-commutativity appears in constant B-field

What about non-constant?

◆The non-constantness of the B-filed is described by

H-flux $H_{\mu\nu\rho}=\partial_\mu B_{\nu\rho}+\partial_\nu B_{\rho\mu}+\partial_\rho B_{\mu\nu}$,

which is the field strength of the B-fileld

◆ Taking into account the H-flux in the analysis

Expanding the field in Taylor series,
Regarding the first few terms as interaction,
Calculating the correlation functions perturbatively

➢ The lowest order in approximation is already done

The Moyal product is generalized,

The corresponding star-product becomes non-associative

$$f\circ g=f*g-\frac{1}{12}\Theta^{\mu\rho}\partial_\rho\Theta^{\sigma\nu}(\partial_\mu\partial_\nu f*\partial_\sigma g+\partial_\sigma f*\partial_\mu\partial_\nu g)+\mathcal{O}(\partial^3)$$

This deformation is the same as the result by Kontsevich, which is derived in the context of the deformation quantization of the algebra of functions on the Poisson manifold.

➢ Our research is investigating the geometrical structure suggested by this non-associative star-product

Hopf algebra and Moyal product

- ◆ Hopf algebra $\mathcal{H}$ has some algebraic structure
- ◆ We are mainly focusing on co-product $\Delta:\mathcal{H}\to\mathcal{H}\otimes\mathcal{H}$
- ◆ We take $\mathcal{H}$ to be the enveloping algebra of vector fields, which can act on functions, i.e. fields
- ◆ Moyal product is formulated by twist element $\mathcal{F}$:

$$f\circ g=m\big(\mathcal{F}^{-1}\triangleright(f\otimes g)\big),\quad \mathcal{F}\in\mathcal{H}\otimes\mathcal{H},\ m(f\otimes g):=fg$$

- ◆ Co-product is also twisted: $\Delta\to\Delta_{\mathcal{F}}=\mathcal{F}\cdot\Delta\cdot\mathcal{F}^{-1}$
- ➢ Poincare transformation, i.e. translation, rotation and Lorentz transformation is twisted as well

The notion of Poincare invariance should be changed!

Results and Future works

- ➢ We showed that the star-product can be formulated by quasi-Hopf algebra in similar manner as the Moyal product, which can be formulated by Hopf algebra
- ➢ It needs some generalization on the algebraic structure

  i.e. Hopf algebra ➡ quasi-Hopf algebra
- ➢ We are now investigating its geometrical interpretation

P-35

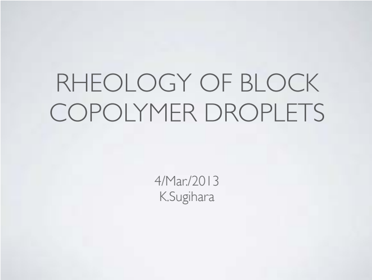
RHEOLOGY OF BLOCK COPOLYMER DROPLETS
4/Mar/2013
K.Sugihara

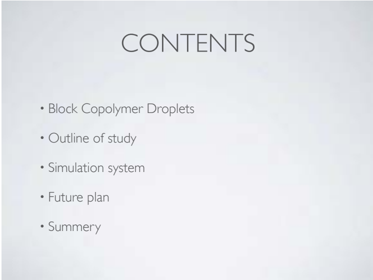
CONTENTS
• Block Copolymer Droplets
• Outline of study
• Simulation system
• Future plan
• Summery

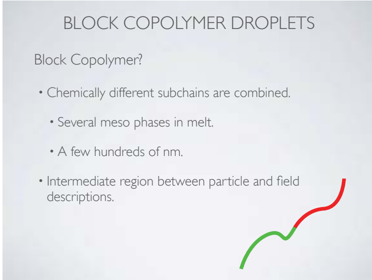
BLOCK COPOLYMER DROPLETS
Block Copolymer?
• Chemically different subchains are combined.
• Several meso phases in melt.
• A few hundreds of nm.
• Intermediate region between particle and field descriptions.

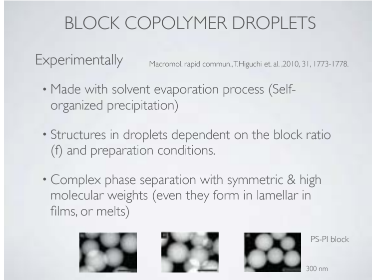
BLOCK COPOLYMER DROPLETS
Experimentally
Macromol. rapid commun., T.Higuchi et al. 2010, 31, 1773-1778.
• Made with solvent evaporation process (Self-organized precipitation)
• Structures in droplets dependent on the block ratio (f) and preparation conditions.
• Complex phase separation with symmetric & high molecular weights (even they form in lamellar in films, or melts)
PS-PI block
300 nm

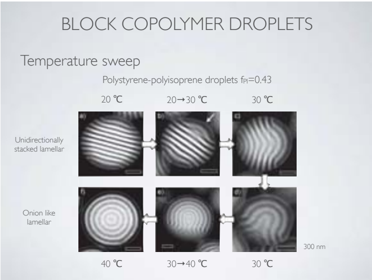
BLOCK COPOLYMER DROPLETS
Temperature sweep
Polystyrene-polyisoprene droplets fPI=0.43
20 ℃
20→30 ℃
30 ℃
Unidirectionally stacked lamellar
Onion like lamellar
40 ℃
30→40 ℃
30 ℃
300 nm

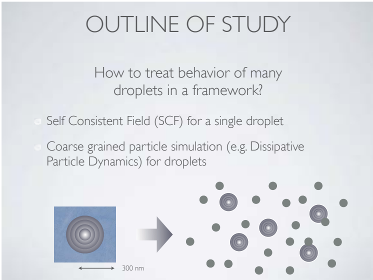
OUTLINE OF STUDY
How to treat behavior of many droplets in a framework?
Self Consistent Field (SCF) for a single droplet
Coarse grained particle simulation (e.g. Dissipative Particle Dynamics) for droplets
300 nm

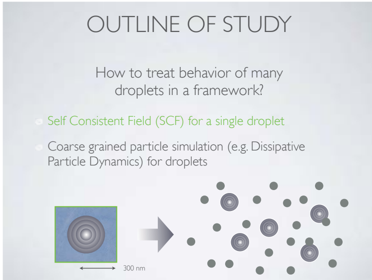
OUTLINE OF STUDY
How to treat behavior of many droplets in a framework?
Self Consistent Field (SCF) for a single droplet
Coarse grained particle simulation (e.g. Dissipative Particle Dynamics) for droplets
300 nm

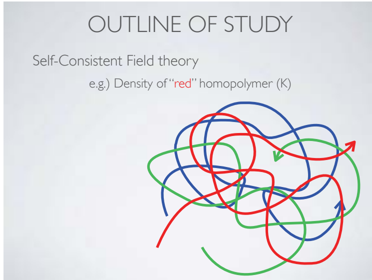
OUTLINE OF STUDY
Self-Consistent Field theory
e.g.) Density of "red" homopolymer (K)

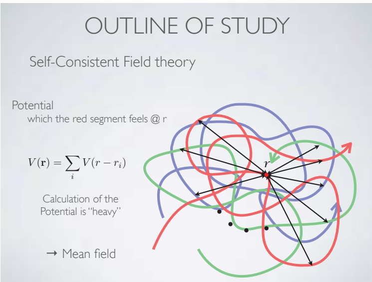
OUTLINE OF STUDY
Self-Consistent Field theory
Potential
which the red segment feels @ r
$V(\mathbf{r}) = \sum_i V(r - r_i)$
Calculation of the Potential is "heavy"
→ Mean field

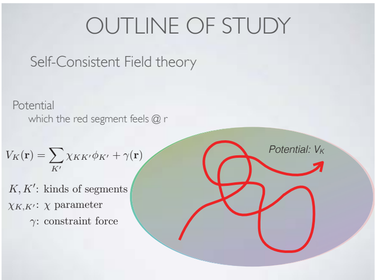
OUTLINE OF STUDY
Self-Consistent Field theory
Potential
which the red segment feels @ r
$V_K(\mathbf{r}) = \sum_{K'} \chi_{KK'}\phi_{K'} + \gamma(\mathbf{r})$
K, K': kinds of segments
$\chi_{K,K'}$: χ parameter
γ: constraint force
Potential: V_K

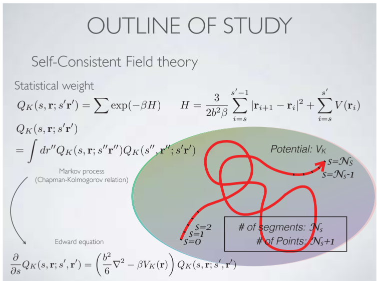
OUTLINE OF STUDY
Self-Consistent Field theory
Statistical weight
$Q_K(s,\mathbf{r};s'\mathbf{r}') = \sum \exp(-\beta H)$
$Q_K(s,\mathbf{r};s'\mathbf{r}')$
$= \int d\mathbf{r}'' Q_K(s,\mathbf{r};s''\mathbf{r}'') Q_K(s'',\mathbf{r}'';s'\mathbf{r}')$
Markov process (Chapman-Kolmogorov relation)
Edward equation
$\frac{\partial}{\partial s} Q_K(s,\mathbf{r};s',\mathbf{r}') = \left(\frac{b^2}{6}\nabla^2 - \beta V_K(\mathbf{r})\right) Q_K(s,\mathbf{r};s',\mathbf{r}')$
Potential: V_K
# of segments: N_s
# of Points: N_s+1

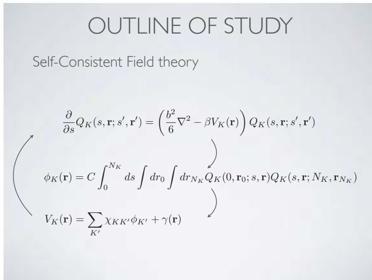
OUTLINE OF STUDY
Self-Consistent Field theory
$\frac{\partial}{\partial s} Q_K(s,\mathbf{r};s',\mathbf{r}') = \left(\frac{b^2}{6}\nabla^2 - \beta V_K(\mathbf{r})\right) Q_K(s,\mathbf{r};s',\mathbf{r}')$
$\phi_K(\mathbf{r}) = C \int_0^{N_K} ds \int d\mathbf{r}_0 \int d\mathbf{r}_{N_K} Q_K(0,\mathbf{r}_0;s,\mathbf{r}) Q_K(s,\mathbf{r};N_K,\mathbf{r}_{N_K})$
$V_K(\mathbf{r}) = \sum_{K'} \chi_{KK'}\phi_{K'} + \gamma(\mathbf{r})$

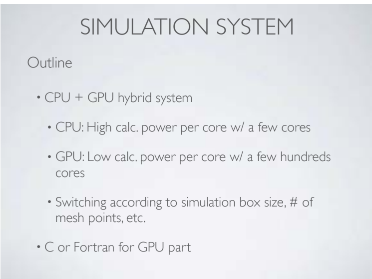
SIMULATION SYSTEM
Outline
• CPU + GPU hybrid system
• CPU: High calc. power per core w/ a few cores
• GPU: Low calc. power per core w/ a few hundreds cores
• Switching according to simulation box size, # of mesh points, etc.
• C or Fortran for GPU part

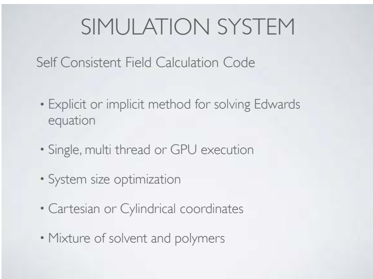
SIMULATION SYSTEM
Self Consistent Field Calculation Code
• Explicit or implicit method for solving Edwards equation
• Single, multi thread or GPU execution
• System size optimization
• Cartesian or Cylindrical coordinates
• Mixture of solvent and polymers

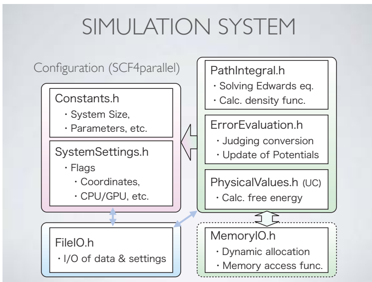
SIMULATION SYSTEM
Configuration (SCF4parallel)
Constants.h
• System Size,
• Parameters, etc.
SystemSettings.h
• Flags
• Coordinates,
• CPU/GPU, etc.
FileIO.h
• I/O of data & settings
PathIntegral.h
• Solving Edwards eq.
• Calc. density func.
ErrorEvaluation.h
• Judging conversion
• Update of Potentials
PhysicalValues.h (UC)
• Calc. free energy
MemoryIO.h
• Dynamic allocation
• Memory access func.

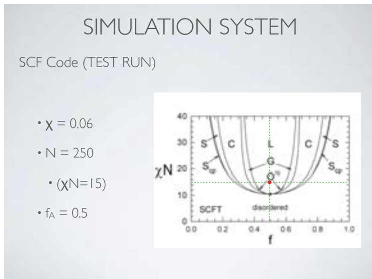
SIMULATION SYSTEM
SCF Code (TEST RUN)
• χ = 0.06
• N = 250
• (χN=15)
• fA = 0.5
χN
f
SCFT
disordered

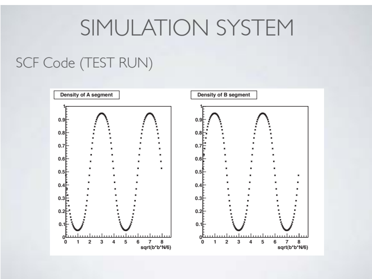
SIMULATION SYSTEM
SCF Code (TEST RUN)
Density of A segment
Density of B segment


FUTURE PLAN
• Simulate the temperature sweep
• On cylindrical coordinate
• Consistency check of theory
• Construction of coarse grained particle system
• Combine behavior of a single droplet into coarse grained particle system

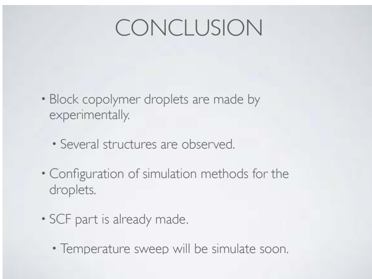
CONCLUSION
• Block copolymer droplets are made by experimentally.
• Several structures are observed.
• Configuration of simulation methods for the droplets.
• SCF part is already made.
• Temperature sweep will be simulate soon.

P-36

Impurity effects on dislocation dynamics in Ge

Y. Murao[1], T. Taishi[2], K. Kutsukake[1], Y. Tokumoto[1], Y. Ohno[1] and I. Yonenaga[1]

[1] Institute for Materials Research, Tohoku University, Sendai, 980-8577, Japan

[2] Faculty of Engineering, Shinshu University, Nagano 380-8533, Japan

Introduction

Germanium

high carrier mobility in comparison with those of Si. (× 2.5~4)

Ge based one chip device

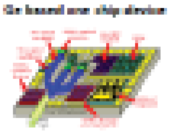

For practical trend

- low resistive materials (to avoid heat generation) → heavily impurities doped Ge
- low density of dislocations → control of dislocation dynamics

To overcome the problems, we should understand interactions of impurities with dislocations in Ge.

Interactions between dislocations and impurities

Dislocation velocity

$v = v_0(\tau/\tau_0)^m \exp(-E/kT)$

v_0, m, E: material constant; τ: shear stress, τ_0 = 1MPa

Locking (immobilization)

Purpose

We investigated impurity effects on dislocation dynamics in Ge heavily doped with impurities O, As and Ga, quantitatively.

Experimental

Stressed specimen

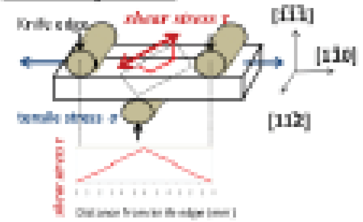

Scratch

→ Source of dislocation generation

Etching

<Chemical Polishing> HF : HNO₃ = 1 : 3
<Selective etching> Billig etchant at 60 °C

Aging for dislocation locking

Diffusion coefficient

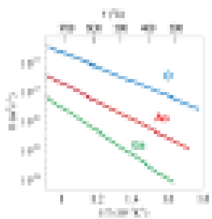

O impurity: high diffusivity

↓

Accumulation on dislocation

↓

locking

Aging is effective ?

Thermal history — Critical stress ?

Aging duration: 0, 0.5, 1, 2, 4 h

Deformation temperature: 375 – 450°C

Dislocation velocity (As and Ga)

Concentration dependence

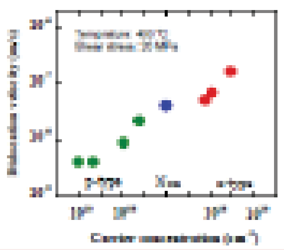

Dislocation velocity is varied dependent on the electrical property of dopants and their concentrations.

→ dependence on the Fermi level

Activation energy

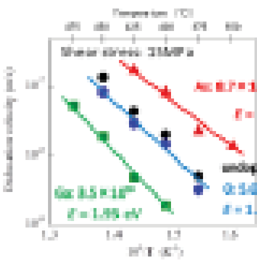

Activation energy E for dislocation motion (in comparison with that in Non-doped)

O doping: no change

As doping: reduction

Ga doping: increase

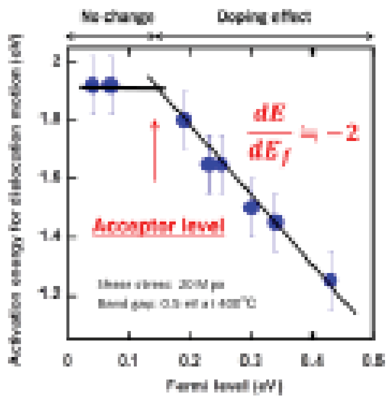

By Hirth and Lothe (1968), the dislocation velocity is proportional to

$$\exp\left[-\frac{2F_k + W_k}{kT}\right]$$

F_k: formation energy of a single kink

W_k: migration energy of a single kink

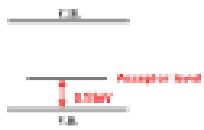

By Hirsch (1979), kink has an acceptor level.

$\frac{dF_k}{dE_f} = 1$

Acceptor level $E_a \sim E_v + 0.15$ eV

Doping effect → kink formation

Dislocation locking (O)

Aging effect for unlocking stress by O impurity

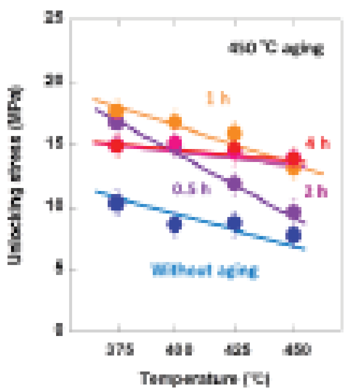

$\tau_{ul} = [E - kT\ln(LN\nu/\Gamma)]N/b^2$

τ_{ul}: unlocking stress

T: temperature

E: interaction energy

N: density of locking particles

L: length of dislocation

ν: frequency of dislocation vibration

Γ: unlocking (release) rate

k: Boltzmann constant

b: magnitude of Burgers vector

E and N were estimated

Variation of interaction energy E and density N

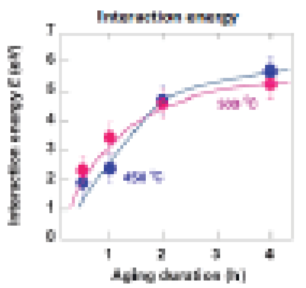

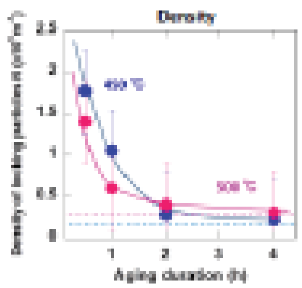

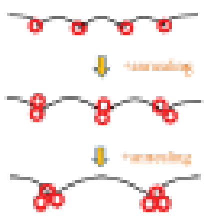

Impurities are gathered along the dislocation and grown up to precipitates with high interaction energy during aging.

Conclusion

We investigated impurity effects on the velocity and locking of dislocations in Ge crystals.

Dislocation veocity

- Impurity concentration dependence of dislocation velocities → Acceptor level $E_a \sim E_v + 0.15$ eV

Doping effect → kink formation

Locking effect

- Aging is effective for dislocation locking by O impurities

Density of locking particles N: decrease

Interaction energy E: increase

→ Dislocations were locked by O precipitates.

M^{2}S - Washington D.C., July 29th - August 3rd 2012

Five-carrier type analysis of transport properties of Ba(FeAs)$_2$

P-37

K. K. Huynh [1], Y. Tanabe [2], T. Urata [1], S. Heguri [1], K. Tanigaki [1,2], T. Kida [3], M. Hagiwara [3]

[1]Department of physics, Graduate school of science, [2] WPI-Advanced Institute for Materials Research (WPI-AIMR)
Tohoku University, Katahira, Aoba-ku, Sendai 980-8577, Japan
[3] Center for Quantum Science and Technology under Extreme Conditions (KYOKUGEN),
Osaka University, Machikaneyama, Toyonaka, Osaka 560-8531, Japan

Viewpoints & Motivations

Ba(FeAs)$_2$ is a multi-band semi-metal with structural and electronic (Spin-Density-Wave) instabilities. A chemical doping or a pressure application brings the system to the superconducting ground state.

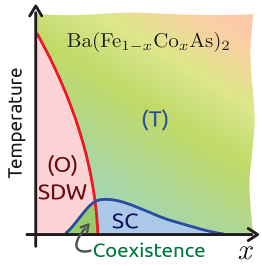

Rich Physics

Complex Fermi surfaces (FS).

Inter-band pairing mechanism of SC.

Tiny Dirac cone with high mobility carriers.

Sensitive to chemical doping.

Experimental Freedom

Eletrical magneto-transport: informative for multi-FS's structure.

Focusing Points

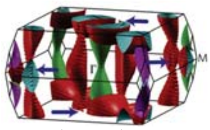

Yin et al., Nat. Phys., 2011

Multi FSs: important to the interband SC.

Each pocket has its own carrier number and mobility, which are very different to those of the others.

Magneto-transport properties are complicated.

Doping effects are difficult and unclear.

1. Parent compound as a starting point.
2. Completely probe all FS's using high magnetic field transport mesurements.

Experiments & Results

High quality Ba(FeAs)$_2$ single crystals were annealed to improve the coductivtity. Transport properties under high magnetic fields (B) were measured.

Sythesis & Measurements

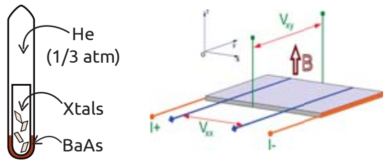

- Single crystal from FeAs flux.
- Annealing: He + BaAs vapor, 850°C, 3 days. (Nakajima et al., PNAS 2011)
- ρ, MR, and R_H were measured using PPMS ($B \leq 9$ T) and ...
- Pulsed magnetic field ($B \leq 50$ T) @ Kyokugen, Osaka Uni.

Transport properties

High RRR

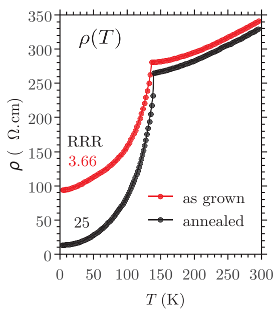

Improved low-T conductivity.

No saturation under $B \leq 50$ T. Complex low-B behaviors.

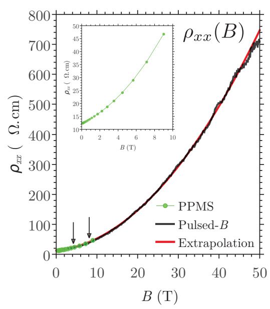

Small $\rho_{yx}(B)$ & slope-turn. Complex low-B behaviors.

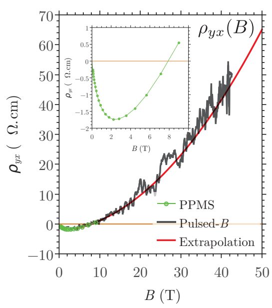

High-B MR and R_H: characteristics of a compensated semimetal.
Low-B behaviors: existence of small pockets of high mobility.

Analysis & Discussions

Conductivity tensor analysis

(J.S. Kim et al., J. Appl. Phys. 73, 8324 (1993)

Effects of different carrier-types can be resovled in conductivity tensor:

$$\mathbf{j} = \tilde{\sigma}\mathbf{E} = (\tilde{\rho})^{-1}\mathbf{E} \quad \text{and} \quad \tilde{\sigma} = \sum \tilde{\sigma}_i$$

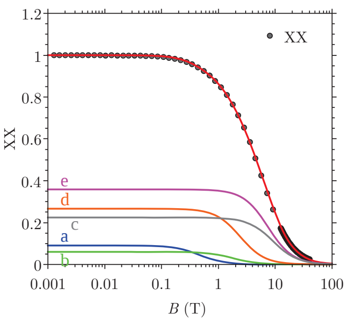

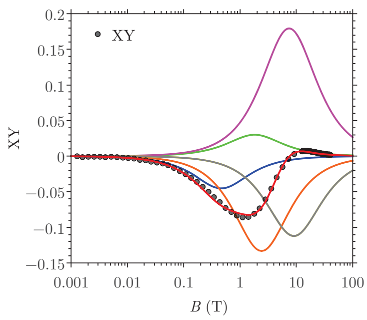

1 Semiclassical 5-band model

$$XX = \frac{\sigma_{xx}(B)}{\sigma_{xx}(0)} = \sum \frac{f_i}{1+(\mu_i B)^2}$$

$$XY = \frac{\sigma_{xy}(B)}{\sigma_{xx}(0)} = \sum \frac{f_i B}{1+(\mu_i B)^2}$$

$$\sigma_{xx}(0) = e\sum N_i \mu_i$$

For holes: $f_i > 0$, for electrons $f_i < 0$

2 In the log-scale:

$$XX = \sum \frac{f_i}{1+e^{2(b-m_i)}}$$ Step-like functions

$$XY = \sum \frac{f_i e^{b-m_i}}{1+e^{2(b-m_i)}}$$ Peak-like functions

$$b = \ln(B) \quad m_i = \ln(\mu_i)$$

Simultaneously least-square fit both $\sigma_{xx}(B)$ and $\sigma_{xy}(B)$ to extract μ_i and n_i.

Interpretations

1. The 5-carrier model fits well to the data. Low-B behaviors sucessfully included.

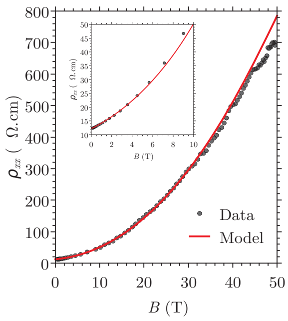

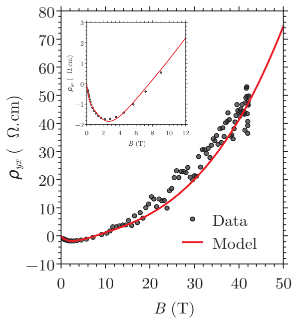

2. 5 carrier types are obtained. Existence of small Dirac cone confirmed.

type	el	el	h	el	h
μ [cm^2(Vs)$^{-1}$]	21,566	4,148	1,343	1,106	5,510
n [cm^{-3}]	2.1e18	3.3e19	1.3e20	1.0e20	5.5e18
	DC	Lagre DC	Parabolic bands		

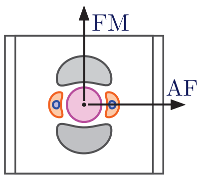

3. Additional "hole-pocket": so far not seen (in band calculations & measurements). Originating from concave segments of the electron-like Fermi pockets (Ong, PRB 43, 1991).

Conclusions

1. All Fermi pockets were successfully detected under $B \leq 50$ T.
2. Four Fermi pockets are necessarry to described the transport properties of Ba(FeAs)2. Non-trivial FS shape is essential.
3. Large asymmetry in relaxation times of Fermi pockets.

Analysis of ^{85}Kr concentration in KamLAND with rollback technique

Benda Xu benda@awa.tohoku.ac.jp
Research Center for Neutrino Science, Department of Physics, Tohoku University

MoGURA Electronics

- $10\mu s$ buffer
- programmable trigger logic

Balance

- trigger efficiency
  - rollback window length (longer is better)
  - trigger threshold (lower is better)
- data flow, grows with efficiency (lower is better)

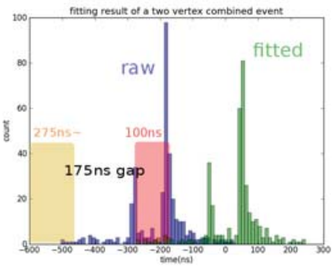

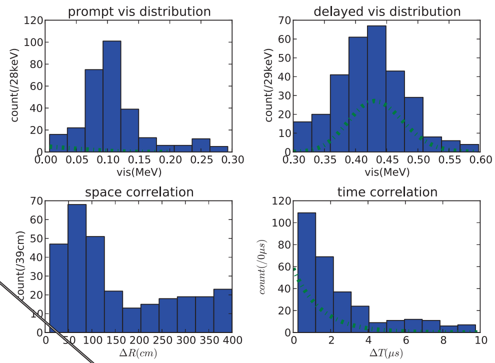

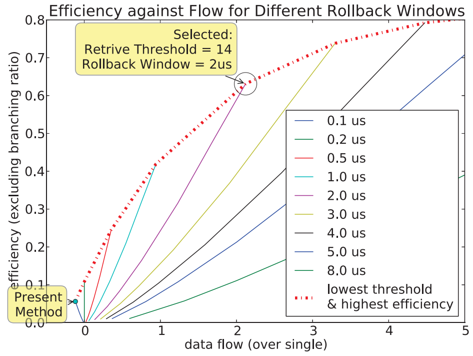

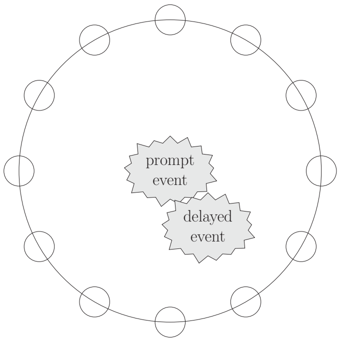

K-means 1D

- applied after a cut based on *median absolute deviation*
- K=2
- $O(n^2)$
- minimizing total *totss*, within-cluster sum of squares

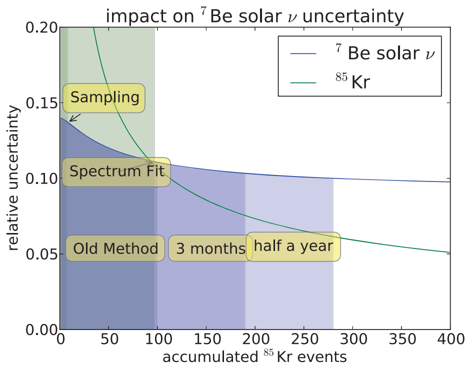

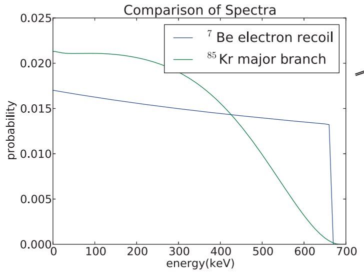

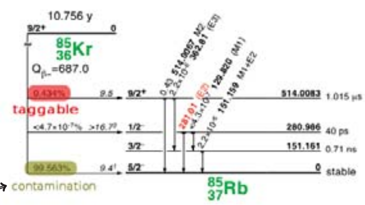

Level diagram for ^{85}Kr

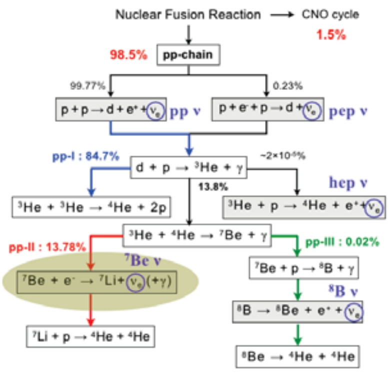

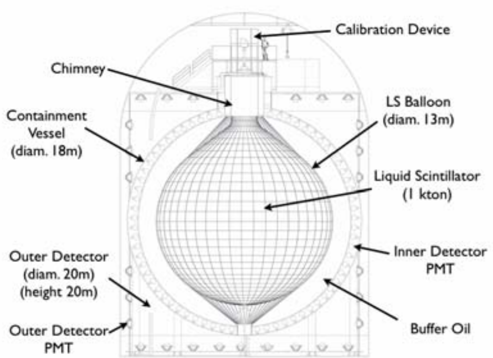

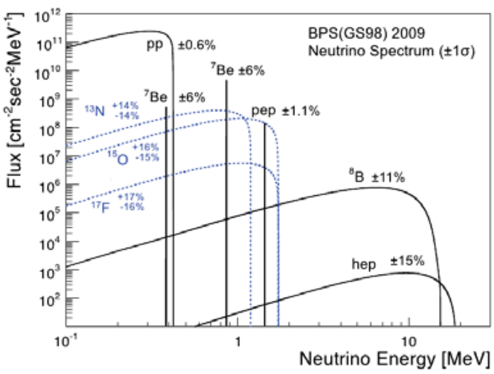

P-39 # Solvent effect on temperature dependence of Terahertz conductivity in conducting polymer PEDOT:PSS thin film

ASI RIKEN[1], Grad. Sch. Sci. Tohoku Univ.[2], IMR Tohoku Univ.[3], Univ. Yamanashi[4]
Yusuke Yamada[1,2], Masatsugu Yamashita[1], Takahiko Sasaki[3], Hidenori Okuzaki[4], Chiko Otani[1,2]

Abstract

Poly(3,4-ethylenedioxythiophene):poly(styrenesulfonate)(PEDOT:PSS) is one of the most successful conducting polymers because of its stable high conductivity and water solubility. However, its mechanism of carrier transport is still poorly understood. We measured DC conductivity and dependence on EG concentration of THz optical conductivity about PH 1000 grade. Moreover the temperature dependence of THz conductivity of PEDOT:PSS PH grade films from 10 K to 300 K by THz time domain spectroscopy and infrared-ultra violet spectroscopy at room temperature to understand the effect of the ethylene glycol (EG) on the carrier transport which improve the crystal structure and morphology of PEDOT:PSS films resulting in the DC conductivity enhancement. The frequency dependences of THz conductivities were well explained by the localization modified Drude (LD) model at higher temperature region which describes the electrical conduction of the weak localized carrier state. On the other hands those at lower temperature deviate from LD model.

PEDOT:PSS {Poly(3,4-ethylenedioxythiophene)/poly(4-styrenesulfonate)}

- **Water soluble**
- **Thermally stable**
- **High conductivity**

It is important to understand how and why we can improve the conductivity

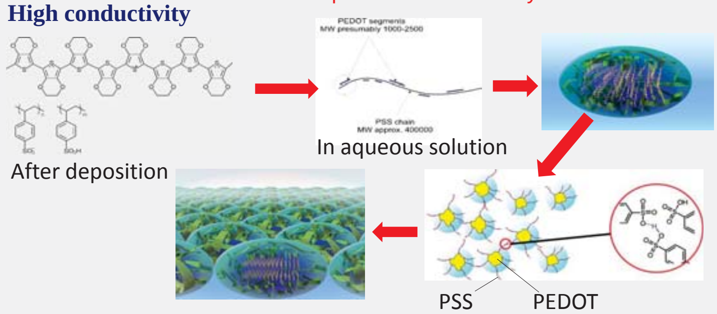

Development toward high conductivity

Application

Mechanism of high conductivity is unknown

<1>: EG concentration dependence of DC and THz conductivity (PH1000 grade)

conductivity → PH1000>>PH

EG concentration and DC conductivity

EG Concentration	0%	5%	10%	15%	20%	25%	50%
Film thickness (nm)	560.5	567.2	573.0	596.8	562.6	522.2	512
Dc Conductivity (S/cm)	1.6	362.0	486.1	464.2	445.5	428.4	383

DC conductivity and THz conductivity

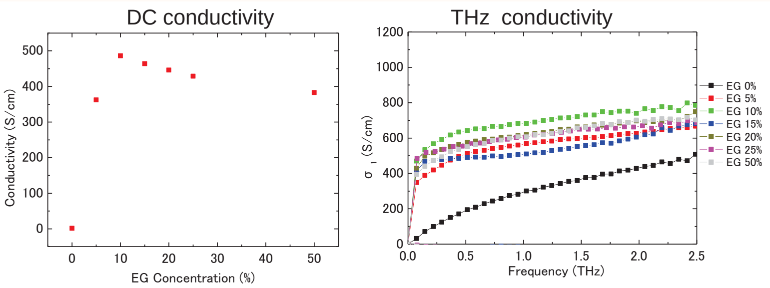

Analysis

Localization-Modified Drude Model (LD model)

Real part of optical conductivity in LD model

$$\sigma_1(\omega) = \frac{\varepsilon_0 \omega_p{}^2 \Gamma}{\omega^2 + \Gamma^2}\left[1 - \frac{C}{(k_F l)^2}\left(1 - \frac{l}{L_\omega}\right)\right]$$

$k_F l$: The ratio of the wavelength of the electron wave scattering length

$k_F l >> 1$ Metal

$k_F l < 1$ Anderson localization

$k_F l \approx 1$ A weakly localized carrier state

K. Lee and A. J. Heeger, Phys. Rev. B 48, 14484 (1993).
M. Yamashta et al., Appl. Phys. Lett. 99, 143307(2011)

L_ω: Diffusion length within a period of the incident radiation
C : ~1
$L_\omega = (D/\omega)^{0.5}$
$D = l^2/\Gamma 3 = v_F{}^2/(3\Gamma)$: Diffusion coefficient

$$\mu = \frac{e}{m^* \Gamma}\left[1 - \frac{C}{(k_F l)^2}\right] \qquad \omega_p = \sqrt{\frac{N_c e^2}{\varepsilon_0 m^*}}$$

$$l = v_F/\Gamma \qquad L_\omega = v_F/\sqrt{\Gamma\omega}$$

Model fitting by LD model

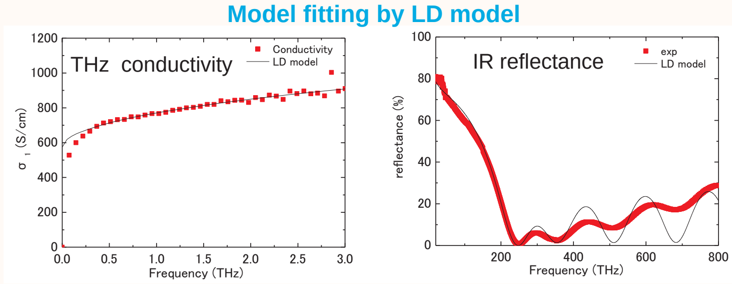

THz conductivity and IR reflectance spectra are well reproduced by LD model

<2>:Temperature dependence of THz-IR Spectroscopy (PH grade)

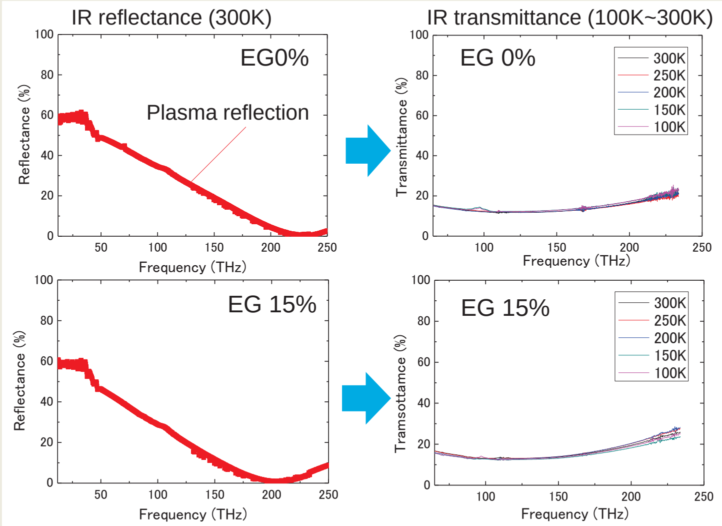

No temperature dependent IR transmittance
No difference in the condition of EG ⇨ **Metallic state in PEDOT chain?**

Temperature dependence of THz conductivity (10K-300K) and fitting of the spectrum by LD model

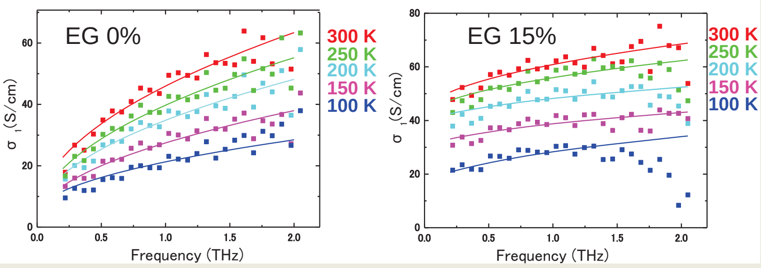

THz conductivity is well reproduced by LD model ⇨ **Weak localized state**

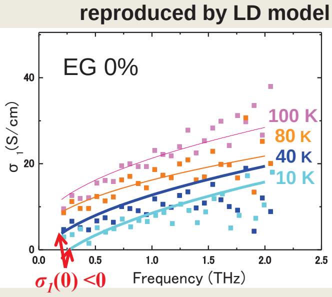

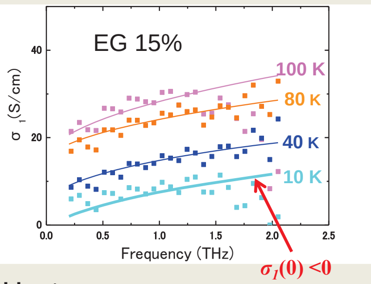

$\sigma_1(0) < 0$
$k_F l = 0.96$ (40K)
$k_F l = 0.98$ (10K)

$\sigma_1(0) < 0$
$k_F l = 0.98$ (10K)

LD model is not suitable at low temperature → **Different from weak localization?**

Spin Pumping in High T_c Superconductor $La_{1.85}Sr_{0.15}CuO_4$ thin films

S.M. Haidar[1] , Y. Kajiwara[1], Y. Shiomi[2] and E. Saitoh[1,2,3,4]

[1] Institute for Materials Research, Tohoku University, Sendai, Japan, [2] WPI-Advanced institute for Materials Research, Tohoku University, Sendai, Japan, [3] CREST, Japan Science and Technology Agency, Tokyo, Japan, [4]Advanced Science Research Center, Japan Atomic Energy Agency ,Tokai, Japan.

Introduction

Spin Current

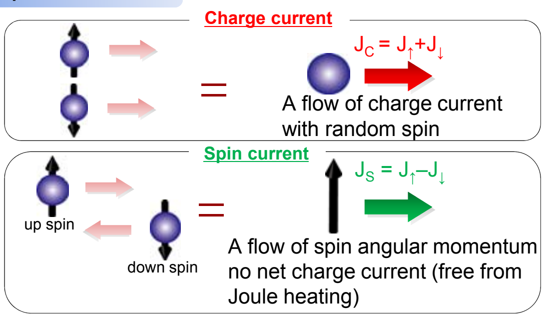

Inverse Spin Hall Effect

Electric current converted from spin current

$$E_{SHE} \propto j_s \times \sigma$$

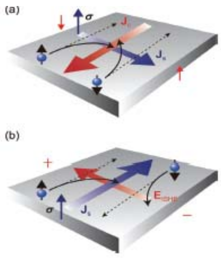

S. O. Valenzuela and M. Tinkham, nature, (2006)

Inverse Spin Hall Effect

Spin current source by processing moment

$$j_s = \frac{\omega}{2\pi}\int_0^{2\pi/\omega} \frac{\hbar}{4\pi} g_r^{\uparrow\downarrow} \frac{1}{{M_S}^2}\left[M(t) \times \frac{dM(t)}{dt}\right]$$

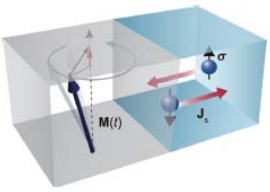

Y. Tserkovnyak, A. Brataas and G. E. Bauer, PRL (2002)
E. Saitoh, M. Ueda, H. Miyajima and G. Tatara, APL (2006)

Method

Sample fabrication

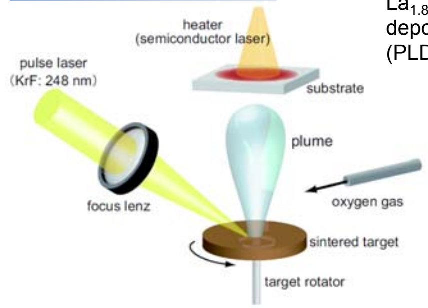

$La_{1.85}Sr_{0.15}CuO_4$ sample has been deposited by Pulse Laser Deposition (PLD) process on $SrLaAlO_4$ substrate.

PLD deposition condition for $La_{1.85}Sr_{0.15}CuO_4$ sample at (001) direction:

Deposition Temperature	:	775℃
Deposition Pressure	:	1.2×10^{-1} Torr
Deposition frequency	:	4Hz
Post deposition annealing	:	60min @ 400℃, 400 Torr

Fabrication for spin pumping:

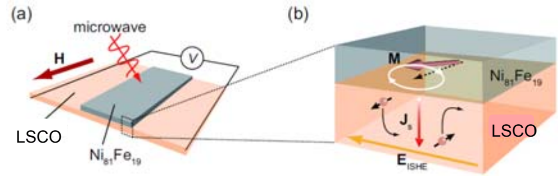

10nm thick Permalloy ($Ni_{81}Fe_{19}$) layer has been deposited on LSCO ($La_{1.85}Sr_{0.15}CuO_4$) by evaporation process.

Result and discussion

Thin film properties

RHEED pattern of $La_{1.85}Sr_{0.15}CuO_4$ at (001)

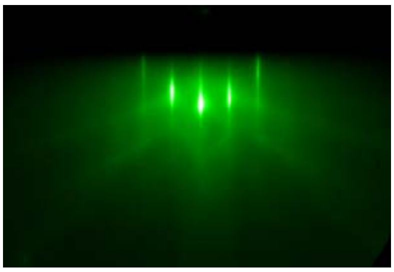

XRD analysis

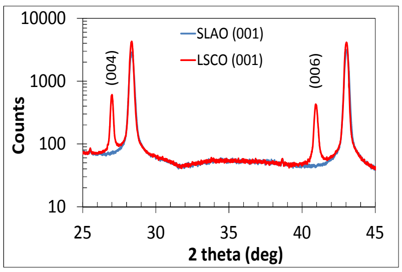

T_c of $La_{1.85}Sr_{0.15}CuO_4$ at (001)

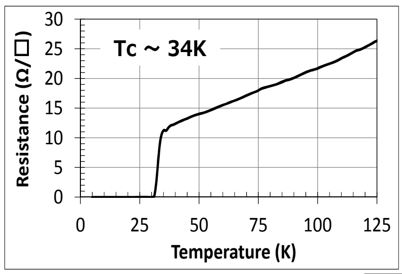

Thin film of $La_{1.85}Sr_{0.15}CuO_4$ single crystal at (001) direction has been fabricated successfully by PLD process.

Spin pumping

FMR signal of Py/LSCO bi-layer

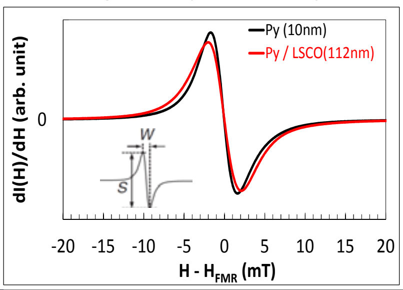

Damping constant vs. thickness

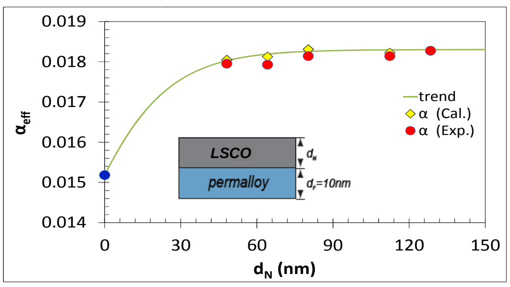

Measurement

$$\alpha_{eff} = \alpha_0 + \Delta\alpha$$

$$\alpha_0 = \frac{\sqrt{3}\gamma}{4\pi f} W_F$$

$$\Delta\alpha = \frac{\sqrt{3}\gamma}{4\pi f}(W_{F/N} - W_N)$$

Calculation

$$\alpha_{eff} = \alpha_0 + \frac{g\mu_B}{4\pi M_S d_F} \times \frac{g^{\uparrow\downarrow}}{1 + \left(2\sqrt{\varepsilon/3}\tanh(d_N/\lambda)\right)^{-1}}$$

H. Nakayama et al., PRB (2012)

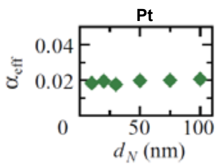

LSCO's damping constant is lower than Pt's

Conclusion

1. **The Gilbert damping Constant α_{eff} for LSCO is ~0.018 which is lower than that of Platinum.**
2. **From calculation, mixing conductance $g^{\uparrow\downarrow}$ and spin diffusion length λ is predicted as ~5×10^{12} (m^{-2}) and ~35nm.**
3. **Experiment on LSCO at lower thickness is necessary to verify the prediction.**

Kentaro Negishi (Physics, Tohoku University)

4^{th} Mar. 2013 @ 2013 GCOE symposium

Study of $B^0 \to DK^{*0}(892)$ for ϕ_3 extraction at Belle

1. Motivation

Lagrangian of charged current weak interaction

$$\mathcal{L}_{int} = -\frac{g}{\sqrt{2}}(\bar{U}_L \gamma_\mu V_{CKM} D_L W_\mu^+) + h.c.$$

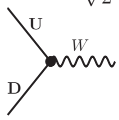

U = (u, c, t)
D = (d, s, b)
U_L, D_L : Left handed

CKM(Cabbibo-Kobayashi-Masukawa) matrix

$$V_{CKM} = \begin{pmatrix} V_{ud} & V_{us} & V_{ub} \\ V_{cd} & V_{cs} & V_{cb} \\ V_{td} & V_{ts} & V_{tb} \end{pmatrix}$$

Unitary condition

$$V_{CKM}V_{CKM}^\dagger = 1 \xrightarrow[\text{1 row, 3 column elements}]{} V_{ud}V_{ub}^* + V_{cd}V_{cb}^* + V_{td}V_{tb}^* = 0$$

Unitary triangle

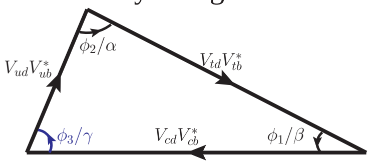

$$\phi_1 = (21.15^{+0.90}_{-0.88})^\circ$$
$$\phi_2 = (89.0^{+4.4}_{-4.2})^\circ$$
$$\phi_3 = (68^{+13}_{-14})^\circ$$

Unitarity triangle is described on complex plane, and represents CP-violation.
To understand CP-violation, the angles of this triangle should be measured precisely.
In the present limits, measurement accuracy of ϕ_3 is not so good.
Need to study more for ϕ_3.

2. Analysis

$$\phi_3 \equiv \arg\left(\frac{V_{ud}V_{ub}^*}{-V_{cd}V_{cb}^*}\right) \sim -\arg(V_{ub})$$

ϕ_3 is measured with the decay include b→u transition.
e.c. $B^\pm \to D^{(*)}K^\pm$
Influence of CP violation is expected to appear due to the interference between the two amplitudes of $\bar{D}^0$ and D^0 decays into a common final state.

Decay $B^\pm \to DK^\pm$

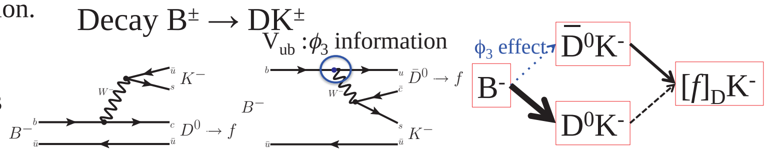

Neutral B Decay $B^0 \to DK^{*0}$

1. More effect of ϕ_3
2. Less signal events → Large backgrounds

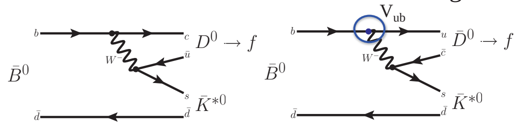

Where, I define $f = K^-\pi^+$.

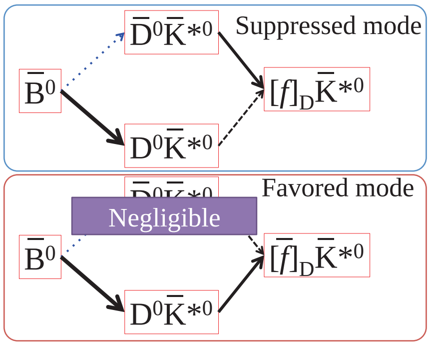

$$R_{DK^*} \cong \frac{\Gamma(B^0 \to [K^+\pi^-]_D K^{*0}) + \Gamma(\bar{B}^0 \to [K^-\pi^+]_D \bar{K}^{*0})}{\Gamma(B^0 \to [K^-\pi^+]_D K^{*0}) + \Gamma(\bar{B}^0 \to [K^+\pi^-]_D \bar{K}^{*0})}$$
$$= r_S^2 + r_D^2 + 2kr_Sr_D\cos(\delta_S + \delta_D)\cos\phi_3$$

Suppressed mode
Favored mode

$D \to K^+\pi^-$ result

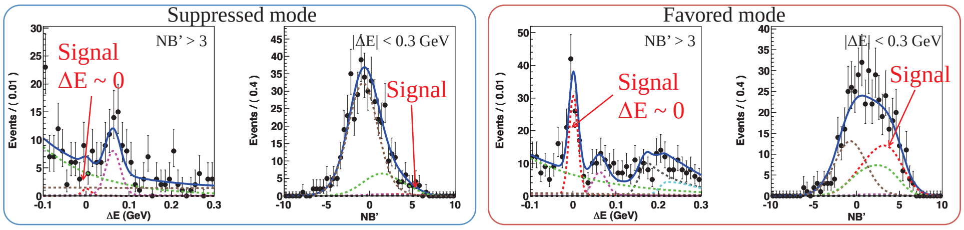

I perform 2D fit for ΔE and NB'.
NB' is one of the parameter for background suppression.
In suppressed mode, there is no signal.
I obtain R_{DK^*} and 95 % C.L. upper limit.

$$R_{DK^*} = (4.1^{+5.6+2.8}_{-5.0-1.8}) \times 10^{-2}$$
$$< 0.16$$

I update R_{DK^*} upper limit world record.

This R_{DK^*} indicates small r_S value.
I'll check r_S value with more sensitive way $D \to K_S\pi\pi$ Dalitz plot analysis.

3. Plan (Dalitz plot analysis)

It was understood that $B \to DK$, $D \to K_S\pi\pi$ can be detected but D decays into $K_S\pi\pi$ via certain intermediate processes.
(e.g. $D \to K^{*+}\pi^- \to [K_S\pi^+]_{K^{*+}}\pi^-$,
$D \to \rho^0 K_S \to [\pi^-\pi^+]_{\rho 0} K_S$ … etc.)
These processes should be divided.

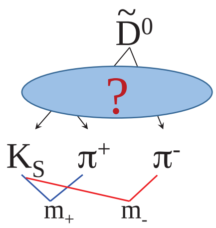

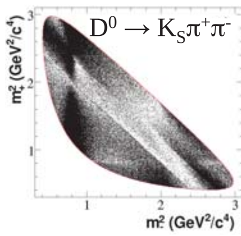

When D decays into 2 particles, and one of them continues to decay furthermore into 2 particles, the reconstructed mass of the correct pair combination yields a mass of a certain particle.

Therefore to verify intermediate states, the plot of combination A versus combination B is used. This is the so called Dalitz plot which is used to extract the value of ϕ_3.

This method of analysis is the first measurement of ϕ_3 using model-independent Dalitz analysis of $D \to K_S\pi^+\pi^-$ from $B^\pm \to DK^\pm$. The data sample used is 710 fb^{-1} Belle collected. In the super-B factory era, ϕ_3 with this method will be dominated by systematic error, esp. Model error.

However, the binned approach allows not only to get rid of the model error, but also to reduce the systematic uncertainties. In my analysis, I try to develop the analysis procedure that minimizes the systematic uncertainties, in view of the future high-precision analyses at the super-B factory where systematics can become a limiting factor.

In model-independent Dalitz analysis(binned method), I take account the signal events number, and obtain CP asymmetry for each bin. Each δ_D for bin is measured, it is equivalent to obtain sixteen A_{DK^*}(= $2r_Sr_D\sin(\delta_S+\delta_D)\sin\phi_3/R_{DK^*}$). corresponding bin δ_D value.

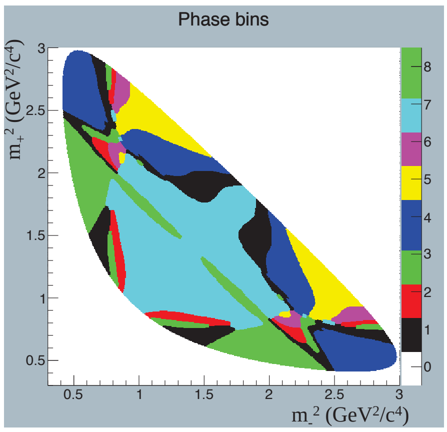

One example of binning on Dalitz plot.

P-42

Polaron Dynamics Properties with Magnetic Impurity in Conjugated Polymers

Wenjing Min[*,†] and Sun Yin[*]

[*] *Department of Physics, Shandong University, Jinan, China*

[†] *Department of Physics, Tohoku University, Sendai, Japan*

(Present supervisor: Sumio Ishihara[†])

Introduction

◆ Background

- Organic Spintronics

Organic Functional Materials
Spintronics
→ Organic Spintronics

- Key issues in Organic Spintronics

Generation、transportation、probe and manipulation of spin signals in organic functional devices

◆ Purpose

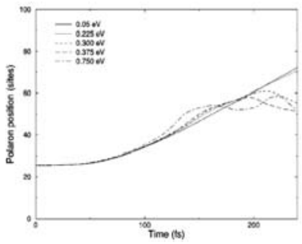

Clebar da Silva et. al., Phys. Rev. B65, 094304 (2002)

charge transport manipulated by *impurity*

No spin signal

Spin transport manipulated by *Magnetic impurity* doped in the polymer chain

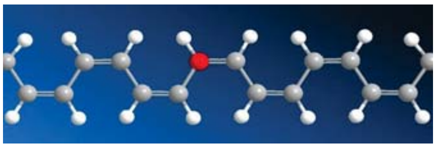

Model & Method

◆ Model

- One-Dimensional extended Hubbard Model

$$H=-\sum_{n,\sigma} t_{n,n+1}\left(e^{-i\gamma A}c^{\dagger}_{n+1,\sigma}c_{n,\sigma}+h.c.\right)+\frac{M}{2}\sum_{n}\dot{u}_n^2+\frac{K}{2}\sum_{n}\left(u_{n+1}-u_n\right)^2$$
$$+U\sum_{n,\sigma}\left(c^{\dagger}_{n,\sigma}c_{n,\sigma}-\frac{1}{2}\right)\left(c^{\dagger}_{n,-\sigma}c_{n,-\sigma}-\frac{1}{2}\right)+V\sum_{n,\sigma,\sigma'}\left(c^{\dagger}_{n,\sigma}c_{n,\sigma}-\frac{1}{2}\right)\left(c^{\dagger}_{n+1,\sigma'}c_{n+1,\sigma'}-\frac{1}{2}\right)$$

t : transfer integral
U : on-site Coulomb interaction
V : neighbouring-site Coulomb interaction

- Magnetic Impurity

$$H_m=\frac{1}{2}\sum_{m,\sigma}\left(V_{m,\sigma}c^{\dagger}_{m,\sigma}c_{m,\sigma}+h.c.\right)$$

m : magnetic impurity location
$\boldsymbol{V_m}$: magnetic impurity potential

◆ Method

time-dependent Hartree-Fock approximation

Results

◆ *Spin-filter Effect* caused by magnetic impurity by adjusting its potential values($V_\uparrow$, $V_\downarrow$)

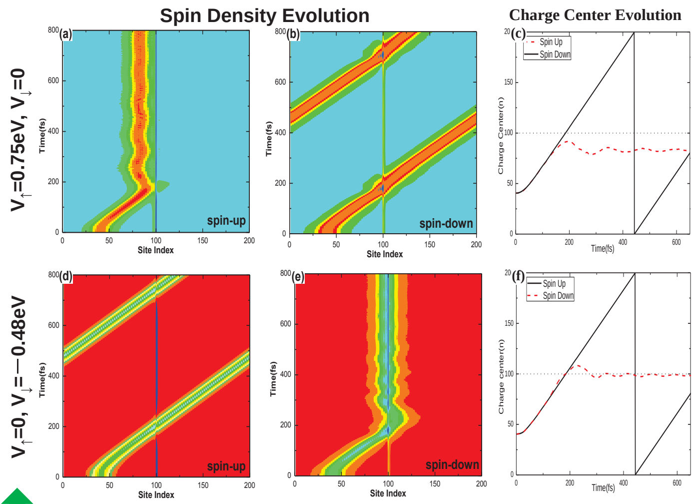

asymmetric values of impurity potential when spin-filter effect happens caused by *strong electron-phonon interaction* in organic polymers

Application

◆ *spin-Organic Light Emitting Diode* theoretical model based on the spin-filter effect caused by *two magnetic impurities*(●●) in a polymer chain

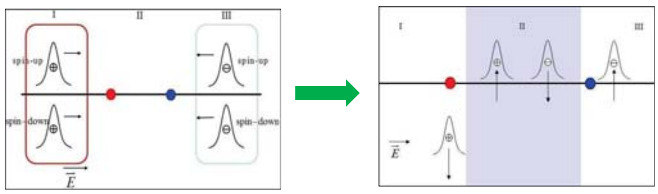

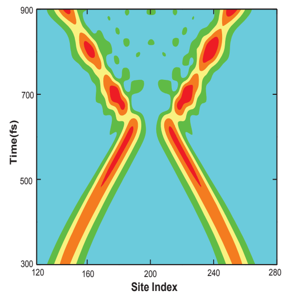

Collsion of negative and positive polaron with antiparallel spin in region II

largest yield of singlet exciton

Summary

- Spin-filter effect occurs with the presence of magnetic impurity
- Yield of singlet exciton is largest in the spin-OLED model

On-going Research

◆ Photo-induced cooperative phenomena in correlated electron system

- Photo-induced *superconductivity* phenomena

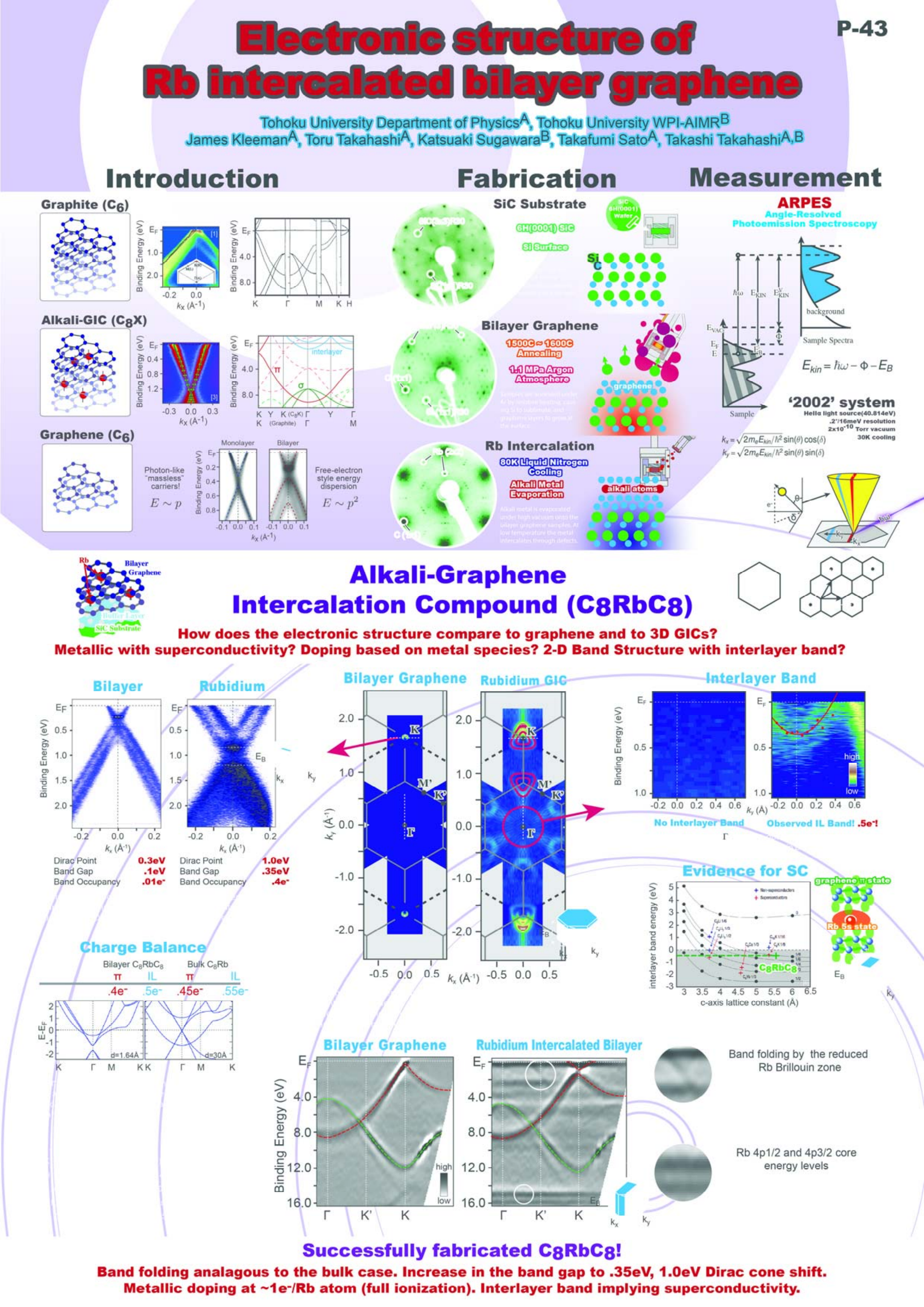
P-43
Electronic structure of
Rb intercalated bilayer graphene
Tohoku University Department of Physics A, Tohoku University WPI-AIMR B
James Kleeman A, Toru Takahashi A, Katsuaki Sugawara B, Takafumi Sato A, Takashi Takahashi A,B
Introduction
Graphite (C6)
Alkali-GIC (C8X)
Graphene (C6)
Monolayer
Bilayer
Photon-like "massless" carriers!
E ~ p
Free-electron style energy dispersion
E ~ p2
Binding Energy (eV)
kx (Å-1)
interlayer
Fabrication
SiC Substrate
6H(0001) SiC
Si Surface
Bilayer Graphene
1500C ~ 1600C Annealing
1.1 MPa Argon Atmosphere
graphene
Rb Intercalation
80K Liquid Nitrogen Cooling
Alkali Metal Evaporation
alkali atoms
Measurement
ARPES
Angle-Resolved Photoemission Spectroscopy
background
Sample Spectra
Sample
Ekin = ħω − Φ − EB
'2002' system
Hella light source(40.814eV)
.2°/16meV resolution
2x10-10 Torr vacuum
30K cooling
Alkali-Graphene
Intercalation Compound (C8RbC8)
Bilayer
Graphene
Buffer Layer
SiC Substrate
How does the electronic structure compare to graphene and to 3D GICs?
Metallic with superconductivity? Doping based on metal species? 2-D Band Structure with interlayer band?
Bilayer
Rubidium
Dirac Point 0.3eV
Band Gap .1eV
Band Occupancy .01e-
Dirac Point 1.0eV
Band Gap .35eV
Band Occupancy .4e-
Bilayer Graphene
Rubidium GIC
Interlayer Band
No Interlayer Band
Observed IL Band! .5e-!
Charge Balance
Bilayer C8RbC8
Bulk C8Rb
π IL π IL
.4e- .5e- .45e- .55e-
Evidence for SC
graphene π state
Rb 5s state
interlayer band energy (eV)
c-axis lattice constant (Å)
Non-superconductors
Superconductors
C8RbC8
Bilayer Graphene
Rubidium Intercalated Bilayer
Binding Energy (eV)
Band folding by the reduced Rb Brillouin zone
Rb 4p1/2 and 4p3/2 core energy levels
Successfully fabricated C8RbC8!
Band folding analagous to the bulk case. Increase in the band gap to .35eV, 1.0eV Dirac cone shift.
Metallic doping at ~1e-/Rb atom (full ionization). Interlayer band implying superconductivity.

P-44

AIMR 2013

TOHOKU UNIVERSITY

wpi

Investigation on Gain Properties of Organic Single Crystals towards Electrically Driven Lasers

Hui Shang[1]*, Susumu Ikeda[2], Kanagasekaran Thangavel[1], Hidekazu Shimotani[1], Kazuaki Oniwa[1], Tienan Jin[2], Naoki Asao[2], Yoshinori Yamamoto[2], Hiroyuki Tamura[2], Ikutaro Hamada[2], Kenta Abe,[1] Masayuki Yoshizawa,[1] Katsumi Tanigaki[1,2]

[1] Department of Science, Tohoku University, Japan

[2] WPI Advanced Institute for Materials Research (WPI-AIMR), Japan

Introduction

Organic Solid Lasers

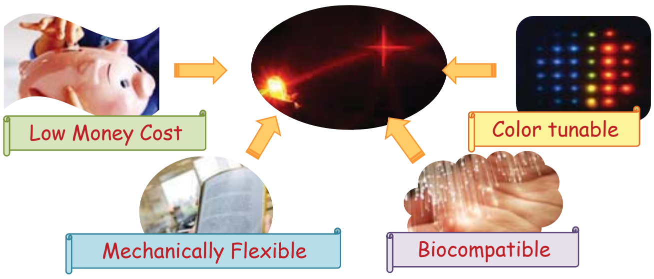

➢ *Electrically driven OLs* *(Still a challenge)*

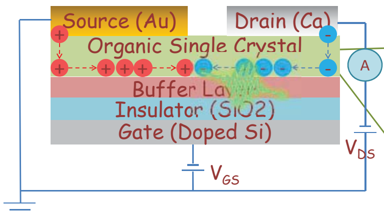

✓High Carrier Mobility

Produce sufficient exciton density

✓High Luminescent Efficiency

Reduce the nonradiative losses

***L**ight-**E**mitting **F**iled **E**ffect **T**ransistor*

➢ *Gain Property* *(Crucial Factor)*

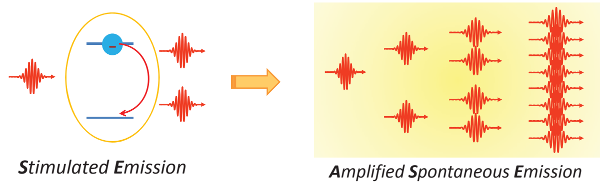

***S**timulated **E**mission* ***A**mplified **S**pontaneous **E**mission*

➢ *ASE Characterization* *(Previous Work)*

Hui Shang, et al., MRS-2012 Spring Meeting, *U. S. A*

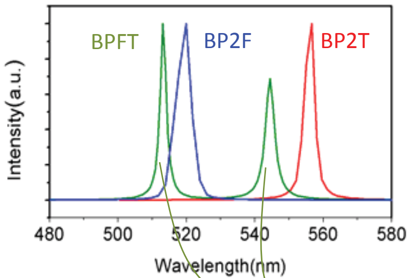

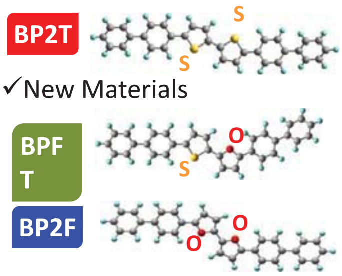

✓New Materials

Research Focus

✓Investigate the reasons of dual gain narrowing peaks

Experimental Processes

➢ *Amplified Spontaneous Emission*

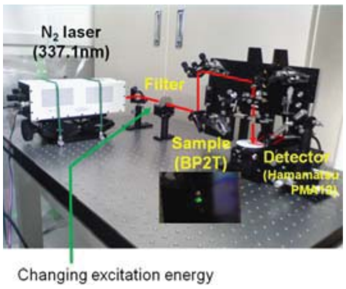

➢ *Transient Absorption*

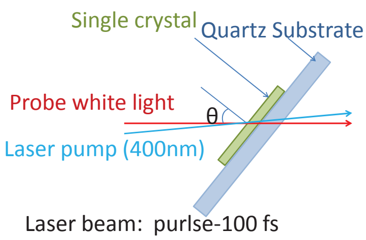

Laser beam: purlse-100 fs

energy density-760 μJ/cm²

Probe light: delay time-0.5 ps

$S_1 + S_1 \rightarrow Sn^* + S_0$

$Sn^* \rightarrow S_1 \rightarrow S_0$ *Non-radiated process*

D. FIchou, et al., *Adv. Mater.*, 1178, **9**, 1997.

✓Singlet-Singlet Annihilation can only explain the saturation behavior of the peak at 544nm.

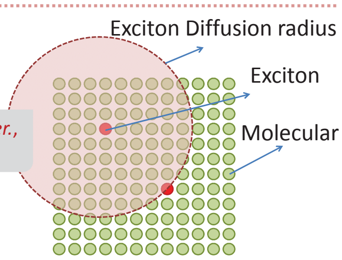

Exciton density at 216μJ/cm² pump laser power

➢ *Self-Absorption*

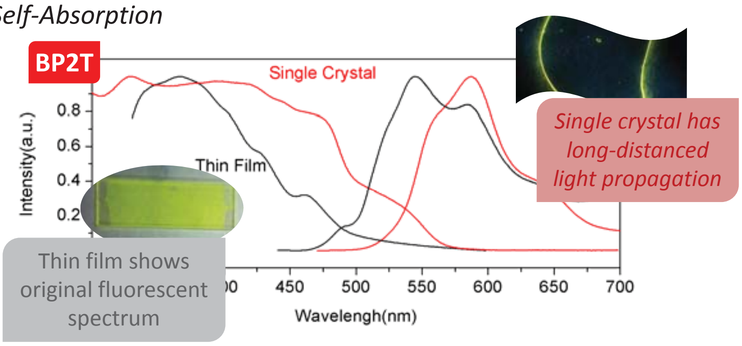

Single crystal has long-distanced light propagation

Thin film shows original fluorescent spectrum

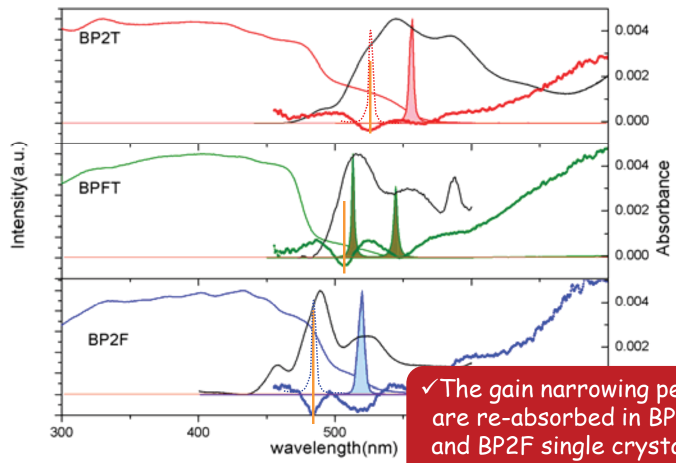

✓The gain narrowing peaks are re-absorbed in BP2T and BP2F single crystals.

Potential Reasons

➢ *Two Parts of Delocalized π-Conjugation of Electrons*

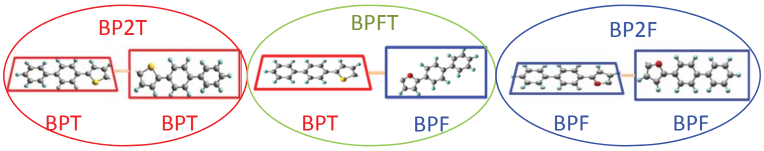

Wavelength** of fluorescent spectrum is determined by **degree of delocalization

✓BPFT spectrum dose not cover those of BP2T and BP2F as expected.

T. J. Dingemans, et al., *Synth. Mater.*, 171, **105**, 1999.

➢ *Singlet-Singlet Annihilation*

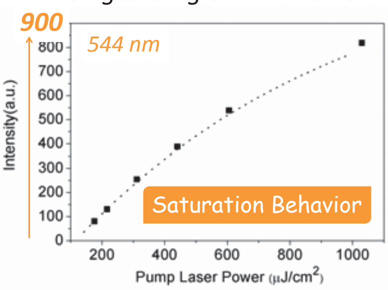

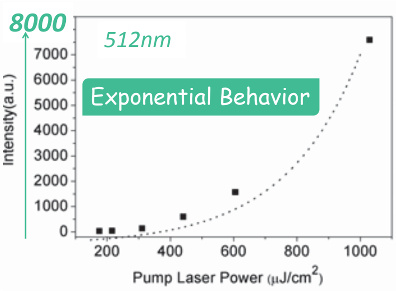

Conclusions

✓The number of gain narrowing peaks are determined by re-absorption.

P-45

The NIR spectroscopy of the galaxies in the SSA22 protoclsuter at z=3.09

２０１3/3/4
Mariko Kubo(D2, Astronomical institute)
Yuka.Uchimoto, Toru Yamada,
Masayuki Akiyama, Tomoki Hayashino(Tohoku university), Yuichi Matsuda(Dahram university), Masaru Kajisawa(Ehime university)

1. The SSA22 protocluster at z=3.09

At z > 2−3, several large scale high density region of the galaxies which are thought to evolve into the present-day clusters have been identified. Among them, the SSA22 protocluster at z=3.09 is known to be one of the most outstanding structure. The number density of the Lyman Break Galaxies(LBGs) and the Lyman Alpha Emitters (LAEs) in the 10' × 10' area is about 6 times the average . The density excess is ~ 15 times of the expected mass fluctuations at that scale. Thus the SSA22 protocluster is well characterized as the significant high density peak at high redshift. Fig.1 is the sly distribution of the LAEs at z=3.09.

The overdensity of ASTE/AzTEC submm sources , extended Lyα nebulae(Lyα Blobs LABs) and the excess hosting rate of Active galactic nuclei (AGNi) among the LBGs, LAEs are also reported . These result suggest that the massive galaxies would be rapidly growing in the high density region.

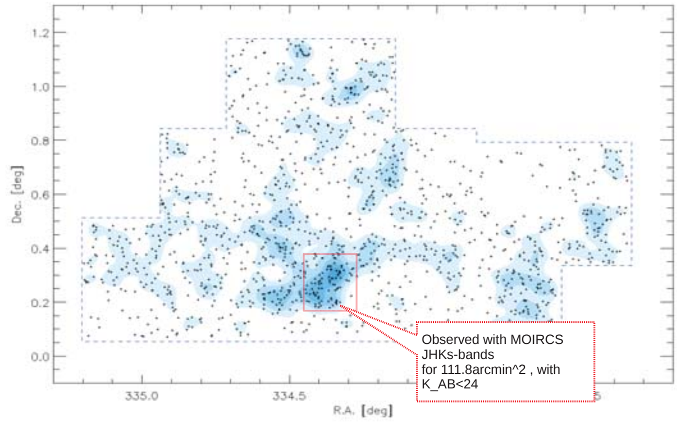

The sky distribution of the LAEs (Yamada et al. 2012). red square region is our survey field.

2. MOIRCS JHK survey in the SSA22 protocluster

In this work, we analysed the galaxies in the protocluster based on the stellar mass. For the purpose, we used the Subaru MOIRCS(Multi Objects InfraRed Camera and Spectroscopy) deep imaging(K<24) at the highest density region in the protocluter. We selected the candidate of the protocluster galaxies with photometric redshift z_{phot} =2.6-3.6 estimated from spectral energy distribution (SED) fitting using UBVRi'zJHK and Spitzer IRAC 3.6, 4.5, 5.8, 8.0 um bands photometries.

Fig.2 is the comparison of photo-z and spec_z of the K-selected galaxies. We obtained good photometric redshifts.. The surface number density of the K-selected galaxies is 1.7 times larger than that in GOODS-North field at same redshift range. While there are uncertainty of the photometric redshifts. we need spectroscopic follow up to confirm them as the protocluster member.

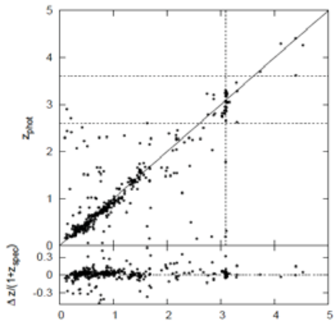

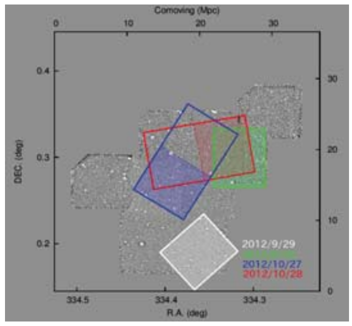

Fig.2 The spectroscopic redshift v.s. photometric redshift we obtained
Fig.3 The target field in this observation

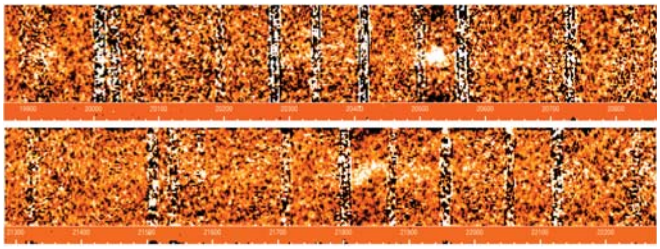

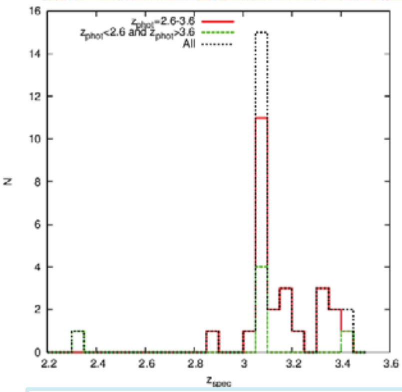

Fig.4 The obtained spectra
OIII line and Hβ line is seen in the top panel
And Hα emission line is detected in bottom panel.
Fig.5 the spectroscopic redshifts distribution of the confirmed objects.
Red: zphot=2.6-3.6
Green:fillar objects.
e.g.,MIPS sources, DRGs
Black dash: All confirmed.

3. The spectroscopic observations

To confirm the redshift of the candidates of the protocluster galaxies, we conducted NIR spectroscopic observations.
The description of the observations are as below.
Targets: K-band selected galaxies with z_phot=2.6-3.6
Date: 2012/9/29-30 (Full), 2012/10/27-28 (half nights)
Instrument: Subaru telescope MOIRCS, Multi-Object Spectroscopy
Using newly developed "VPH-K" grism and HK500 grism. Slit width = 0.7",0.8"
2half and 2 full(4'×7') MOS masks were used.
Seeing: 0.4"~0.7"
Exposure time: Each masks are observed for 3.6-5.5h
Data reduction: MCSRED (Tanaka et al.) was used.
Result; Fig.4 are example of the obtained spectra. Fig. 5 is the spectroscopic redshift distribution. There are cleat spike at z=3.09.
The emission lines are detected for 32/67 objects are confirmed.
(26 / 55 of z_phot=2.6-3.6 &6 /12 of fillar objects)
20/32 are at z_spec~3.09!

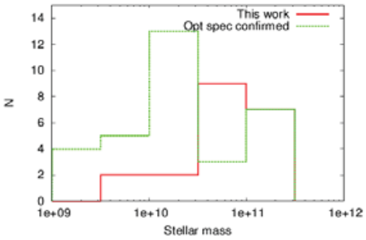

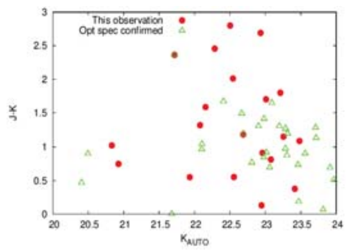

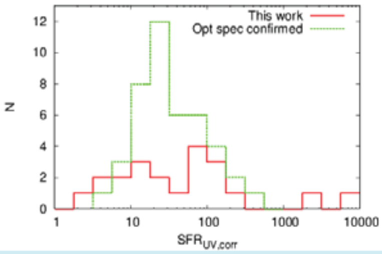

Fig. 6
Top left: Stellar mass (K<24),
Top right: J-K color v.s. K-band mag
Bottom left: SFR_UV.corr,
distributions of the galaxies with z≈3.09 in the SSA22 protocluster from this work (red) and other work (Optically confirmed, green).

4. Discussion

What are the ingredient of the objects we confirmed?
Fig.6 is the stellar mass, J-K color and SFR_UV,corr distributions of the objects we confirmed. They have larger stellar mass, red colors and higher SFR than those of the rest-frame UV selected and confirmed galaxies.
Fig. 7 is one of the very interesting objects in this protocluster. This object is counterpart of the sub-mm source. There are multiple components with z_phot=2.6-3.6 and show extremely red colors (J-K>2.1). We confirmed two of this object. This suggest the multiple merging formation of the massive galaxies occuring in in this protocluster. One of two is the AGN and another one shows very passive stellar population like the local elliptical galaxies.

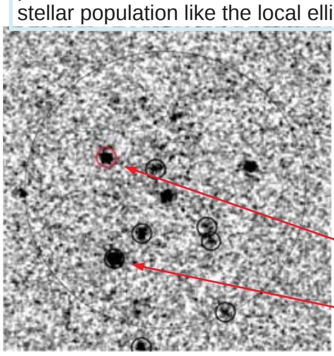

Fig. 7 The counterpart of ASTE/AZTEC submm source.
Black circled objects are those with z_phot=2.6-3.6.
Most of them shows red color J-K>2.1
We confirmed two of the counterparts of this object.

z_spec=3.087

Shwoing 4000Å~3.09

5. Future work and conclution

- We successfully confirmed K-selected galaxies with 2.6<zphot<3.6 to be the members of the SSA22 protocluster.
- We also confirmed the K-band counterparts of LABs and AzTEC sub-mm source.
- <u>This was the first time to confirm such large number of galaxies from [OIII]5007Å at z~3.</u>
- <u>In this observation, we observed 1/6 of our K-selected candidates of the galaxies in the SSA22 protocluster. Further observation is needed to reveal the whole picture of the protocluster.</u>

P-46

On the pulsation modes of OSARGs in the LMC

Masaki Takayama
Department of Astronomy, Tohoku University

Abstract

Wray et al. (2004) and Soszynski et al. (2004) found a number of red giant variables in the Galactic bulge and the LMC/SMC showing relatively small photometric amplitude and irregular (multi-periodic) variability. Such variables ware named "OSARGs (OGLE Small Amplitude Red Giant variables)" after the observation campaign, "OGLE". Three and four ridges ware appear on the Period-luminosity planes of RGB OSARGs and AGB OSARGs , respectively due to their multi-periodic variability.

In this poster, comparing the periods and period ratios of the RGB OSARGs with our theoretical models, we show that their three ridges(b1, b2, b3) on the PL plane correspond to the radial first, second and third overtone, and nonradial dipole P4 and quadrupole P2 mode. As a result of this, we also show to obtain the initial mass range of ~ 0.9 – 1.4Msun. Using the Mass - Luminosity relation, we have found that the scaled optimal frequency, ν_max, for the solar like oscillations goes through roughly the middle of the three ridges on the PL plane. It suggests that the stochastic excitations are likely the case of the pulsations in OSARGs.

1. OSARGs

OSARGs are usually within the period range of ~ 10 – 100 days and feature multi-periodic variability. Typical values of period ratios of RGB OSARGs are ~ 0.5, 0.7, 0.9 and 0.95. The period ratios of ~ 0.5 correspond to the b3/b1 while ~ 0.7 correspond to the b1/b2 and b2/b3. Soszynski et al. (2004, 2007) showed that each of the sequence b2 and b3 has two narrow sub-ridges in addition to the main ridge, and they concluded that the period ratio of ~ 0.9 and 0.95 was consistent with the pair of the main ridge and the sub-ridge.

2. Models

We have obtained linear nonadiabatic radial and nonradial pulsation periods for envelope models along the evolutionary tracks calculated by the MESA code(Paxton et al. 2011) with several initial masses adopting a mixing-length of 1.5 pressure scale height. We have adopted the chemical composition (X, Z)=(0.71, 0.01) for the LMC and used OPAL (Iglesias and Rogers 1996) opacity tables.

3. Data selection

We have obtained the pulsation periods and V- and I- band mean photometric magnitudes of RGB OSARGs (~45,500) of the LMC from OGLE-III. Some OSARGs have Long Secondary Periods(LSPs) that are mysterious long period(~ 500 – 1500 day) unsettled variable phenomenon. We have excepted stars having larger period than log10 P(day) = 2.1 and smaller period ratios then 0.4 then we have obtained non-LSP OSARGs(~8,500).

4-1. Mode identification(radial mode)

Since the pulsation period itself depends on stellar radius and mass, the period ratios are useful for determining pulsation modes, while pulsation periods are used to determine the appropriate luminosity (or mass) ranges.

Fig. 1 shows comparisons with the radial pulsations in the Period - Period Ratio diagram(Petersen diagram) for RGB OSARGs, respectively. From these figures we conclude that radial 1st, 2nd and 3rd overtone correspond to b1, b2 and b3, respectively.

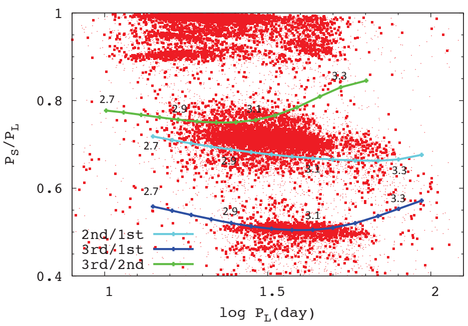

Fig. 1 Petersen diagram of 1.1Msun red giant models are compared with RGB OSARGs. Numbers written along lines indicate log(L/Lsun).

4-2. Mode identification(nonradial mode)

Since period ratios larger than ~ 0.9 ware not explained by radial pulsations, we have considered nonradial pulsations. The presence of such high period ratios indicates that each ridge in PL plane might consist of more than one mode. Figs. 2 and 3 show period ratios obtained between dipole and radial modes, and quadrupole and radial modes, respectively for 1.1Msun RGB models. According to Fig. 1, we have considered only luminosity range of 3.0 < log(L/Lsun) < 3.15 for 1.1Msun models corresponding to RGB OSARGs. Those figures show that the presence of dipole P4 mode in the b3 ridge correspond to a period ratio of ~ 0.9 while the presence of quadrupole P2 mode in the b2 ridge correspond to a period ratio of ~ 0.95. In addition the pair of dipole P4 and radial 2nd overtone and the pairs of quadrupole P2 and each radial 1st and 3rd overtone are consistent with a period ratio of ~ 0.7.

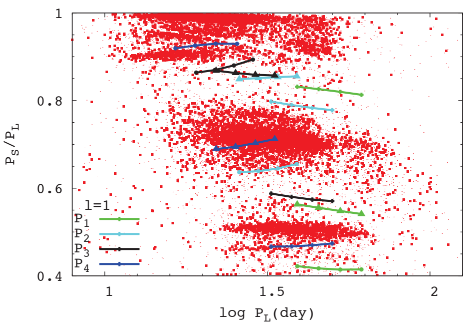

Fig. 2 Period ratios between dipole P1 – P4 and radial modes for 1.1Msun RGB models compare with RGB OSARGs

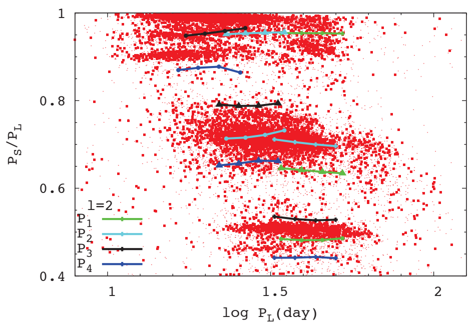

Fig. 3 The same as Fig. 2 but for quadrupole modes

5. Discussion

Even if nonradial pulsations are considered, evolutionary models with an initial mass correspond to only a small part of each ridge on the period – period ratio planes. Therefore we need to consider deferent masses. Fig. 4 shows period luminosity relations of radial 1st – 3rd and nonradial dipole P4 and quadrupole P2 mode for 0.9, 1.1, 1.4Msun RGB models. Each mass models is consistent with three OSARG PL ridges in deferent luminosity range, respectively. We thus have concluded that initial masses of RGB OSARGs should range from 0.9 – 1.4Msun. As a result of this, we have obtained the (initial)mass – luminosity relation:

Log(L/Lsun)=0.91(M/Msun)+2.05 – (1)

The black dashed line in this figure shows the scaled optimal frequency, ν_max, for solar like oscillations computed by using equation (1) and the effective temperature at each evolutionary phase and it goes through roughly the middle of the three ridges. It suggests that the stochastic excitations are likely the cause of the oscillations in OSARGs.

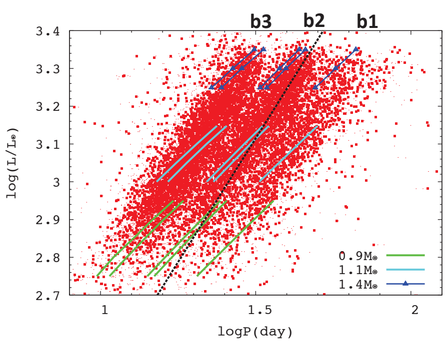

Fig. 4 Period - luminosity diagram of 0.9, 1.1 and 1.4Msun RGB models and the ν_max. The luminosity range for each mass models are determined in 90% of the b3 stars included

6. Conclusion

Comparing the RGB OSARGs in the LMC with linear nonadiabatic radial and nonradial pulsation periods and their period ratios, we have found that radial 1st, 2nd and quadrupole P2, and 3rd and dipole P4 mode for RGB models correspond to the sequence b1, b2 and b3 of RGB OSARGs, respectively. A luminosity range that is consistent with OSARGs PL relations differs by stellar mass. To explain the broad of the ridges or sequences of period – period ratio and period – luminosity relations, we have obtained the (initial)mass range of 0.9 – 1.4Msun. Moreover, we have obtained the (initial)mass – luminosity relation of RGB OSARGs as equation (1) by considering the mean values of the luminosity range of each initial mass. Using equation (1), the scaled optimal frequency, ν_max, for solar like oscillations goes through roughly the middle of the sequence b2 and it suggests that the stochastic excitations are likely the cause of the oscillations of OSARGs. Recently, the evidence of solar like oscillations have been found in a lot of lower luminous red giant variables by CoRoT and Kepler. However, oscillations of Mira variables(the most luminous red giant variables) have been argued to be caused by κ – mechanism (self excitation) for hydrogen in outer layer of the star. OSARGs are much luminous than solar like oscillating red giant variable stars but a little dimmer than Miras. Those things suggest that OSARGs would be the most luminous solar like oscillators along red giant variables and be available to verify a convective theory.

The 5th GCOE International Symposioum on "Weaving Science Web beyound Partice-Matter Hierarchy" SENDAI, JAPAN, 04-06 MARCH 2013

Construction of Global Magnetic Field Structure Model in Spiral Galaxies with Three-dimensional MHD simulations

●S. Nakamura, M. Hattori, T. Morishima (Tohoku Univ.)

Abstract

We carried out global three-dimensional idela magnetohydrodynamic simulations for galactic gaseous disks in the gravitational potential of bulge, disk, halo and spiral arms. We considered radiative cooling energy loss of interstellar medium(ISM).
Synchrotron intensity & polarization observations show magnetic fields in spiral galaxies are along with spiral arms.
Our numerical results indicate that isothermal shocks generate in spiral arms and magnetic fields are amplified due to these shocks.
We expect this results consist with observations.

Introduction & Motivation

In spiral arms, gravitational potential is deeper than disk average about 2-10%. ISM go through these potentials, isothermal shocks generate. Synchrotron radiation intensity & polarization observations suggest that magnetic fields are amplified and concentrate on shock front. We examined effect of spiral gravitational potential on the nonlinear evolution of galactic magnetic fields, we choosed magnetohydrodynamic equilibrium state in axisymmetric potential for initial model in order to investigate physical process of state transition.

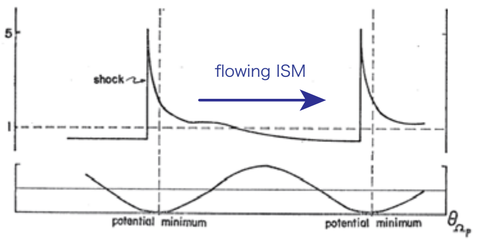

Model for density(upper panel), potential(lower pannel) in spiral potential (Roberts 1969)

contour : total intensity
lines : B vector
(Fletcher et al. 2011)

Simulation Model

Density distribution
Disk : magnetohydrodynamic equilibrium torus
threaded by weak toroidal magnetic fields ($T\sim10^4$K, $\beta\sim100$)
Halo : isothermal hydrostatic equilibrium ($T=10^6$K)
Gravity : Miyamoto-Nagai' s axisymmetric potential including DM
+ spiral arm potential Φ_{sp} (Wada et al. 2011)

$$\Phi_{sp}(r,\varphi,z)=\Phi_{disk}(r,z)\,\epsilon_{sp}\frac{z_0}{\sqrt{z^2+z_0^2}}\cos\left\{m\left(-\varphi-\Omega_{sp}t+\cot i_{sp}\ln\frac{r}{r_0}\right)\right\}$$

$\epsilon_{sp}=0.02$, $z_0=0.3$kpc, $m=2$, $\Omega_{sp}=12.2$km/s/kpc, $i_{sp}=15°$, $r_0=1$kpc are spiral potential strength, scale height、the number of arm、patern angular velocity, pitch angle, scale radius.

Numerical Scheme : MacCormack(time, space 2nd order accuracy)
+ artificial viscousity
Simulation Region : 0kpc<r<56kpc, $0<\phi<2\pi$, 0kpc<z<5kpc
(cylindrical coord., z=0 symmetric bounday)
ISM cooling : Raymond, Cox & Smith 1976 (10^4K<T<10^6K)
0 (otherwise)
applied disk region(white dashed line box)

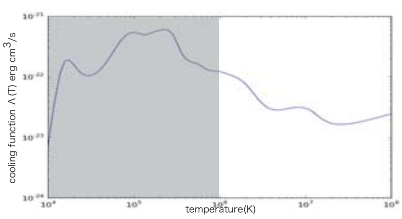

Cooling function. Here $\mu=0.62$ (solar abundance).
We used part of 10^4K<T<10^6K.

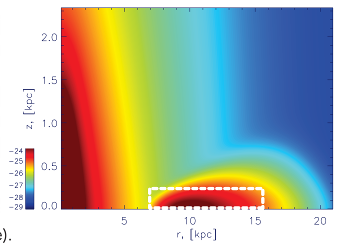

Initial density distribution in r-z plane.

Numerical Result

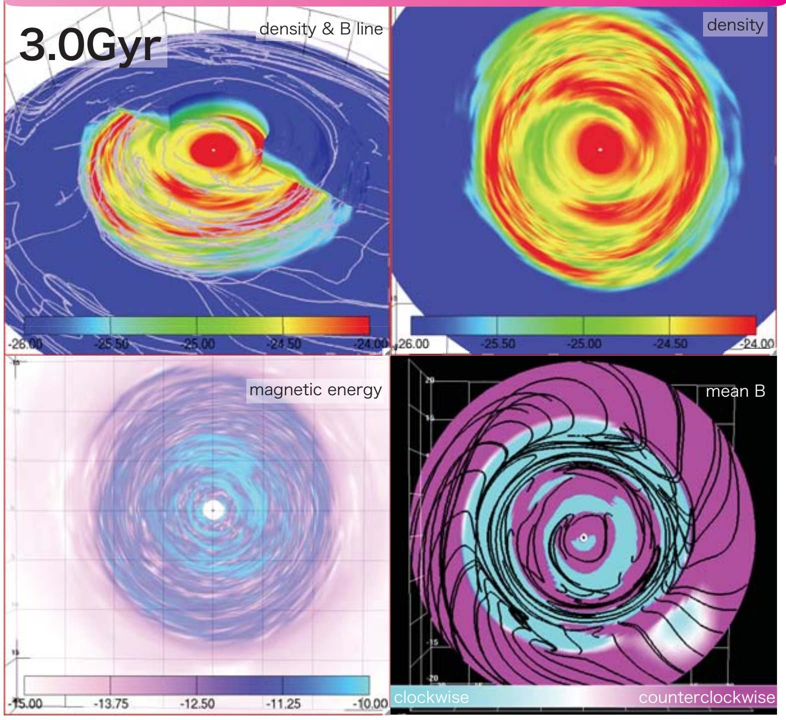

We found that isothermal shocks generate along spiral arms and magnetic field lines concentrate these shock fronts.
We also found magnetic energy is amplified in disk. Plasma β ($=P_{gas}/(B^2/8\pi)$) decreases and stays around ~5.0.
Toroidal magnetic fields reverse in z=0 equatorial plane due to magneto-rotational instability(MRI). Han et al. (2002) pointed out Milky Way galaxy magnetic fields reverse in equatorial plane with rotation measure(RM) observation. After the amplification of magnetic energy saturates, magnetic flux is rise from disk to halo by Parker instability. Nishikori et al. (2006), Machida et al. (2013) carried out global 3D MHD simulation and showed same results.

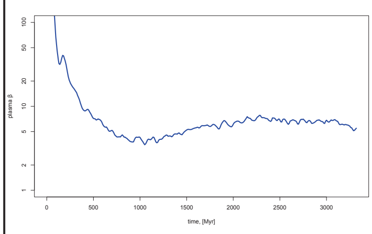

Time evolution of volume-averaged plasma β for 5kpc<r<8kpc, $0<\phi<2\pi$, 0kpc<z<0.15kpc

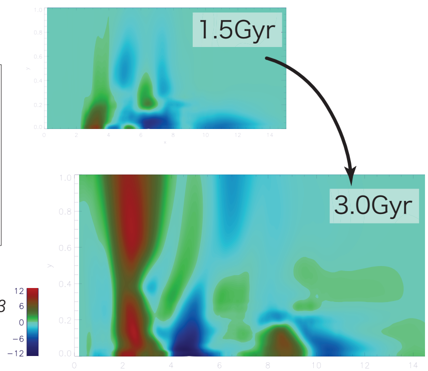

B_ϕ in r-z plane red : positive
blue : negative

Summary & Discussion

We carried out 3D simulations of the time evolution of galactic gaseous disk in non-axisymmetric potential. We maintained galactic shocks over 3Gyr taking into account spiral potential and ISM cooling. Magnetic fields are amplified due to these shocks and β stays aroud 5. Our results are consistent with other numerical simulations.

References

Fletcher et al. 2011, MNRAS, 412, 2396F
Han et al. 2002, ApJ, 570L, 17H
Machida et al. 2013, ApJ, 764, 81M
Nishikori, H., Machida, M., and Matsumoto, R. 2006, ApJ, 641, 862N
Raymond, J. C., Cox, D. P., and Smith, B. W. 1979, ApJ, 204, 290R
Roberts, W. W. 1969, ApJ, 158, 123R
Wada, K., Baba, J., and Saitoh, T. R. 2011, ApJ, 735, 1W

The Prolate dark halo of Andromeda galaxy

P-48

Kohei Hayashi and *Masashi Chiba* — *Tohoku University Astronomical Institute*

The 5th GCOE Symposium 4-6/03/2013

ABSTRACT

In order to obtain more realistic mass distribution of a dark halo in our nearest giant, we adopt axisymmetric mass models constructed by Hayashi & Chiba (2012) and apply these models to latest kinematic data of globular clusters and dwarf spherical galaxies in the halo of M31. Applying our model to Andromeda galaxy, we find that the most plausible cases for Andromeda yield not spherical but prolate shape for its dark halo. This result is profound in understanding internal dynamics of halo tracers in Andromeda, such as orbital evolutions of tidal stellar streams, which play important roles in extracting the abundance of CDM subhalos through their dynamical effects on stream structures.

1.Why Andromeda?

The Milky Way and its nearest neighbor Andromeda provide a unique laboratory to test Lambda-Cold Dark Matter (LCDM) theory of galaxy formation and evolution. In particular, LCDM models, as a current paradigm of structure formation in the Universe, predict universal density distribution for a galaxy-sized halo as well as the presence of numerous subgalactic halos in it, as a consequence of hierarchical assembly process of dark matter. It is thus of importance to derive how dark matter is actually distributed in a galaxy scale like the Milky Way and Andromeda, to get useful insight into the role of dark halos in galactic structure and evolution in the framework of LCDM models.

2.The motive of this study

Until now, most of existing mass models for Andromeda's dark halo have assumed spherical symmetry, for the purpose of simply estimating its total mass. However, LCDM models predict non-spherical virialized dark halos (right figure) in this galaxy scale. We thus need to consider more general models to set more realistic and new limits on global shape and profile of a dark halo.

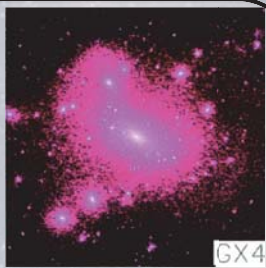

LCDM predicted galaxy-sized dark halo by N-body simulation (Jing & Suto 2000)

3.Model

★Stellar density

$$\Sigma(x,y) \propto \left(x^2 + \frac{y^2}{q'^2}\right)^{-\gamma/2}$$

q' is a projected axial ratio.
γ=3.5 is best-fit power law value.

For axial ratio, q', we apply the inertia tensor method as implemented by Allgood+06. As a result, axial ratio of Andromeda halo's stellar density indicate *q' =1.18*.

★Dark halo

$$\rho(R,z) = \rho_0 \left(\frac{m}{b_{\rm halo}}\right)^{\alpha}\left[1+\left(\frac{m}{b_{\rm halo}}\right)^2\right]^{\delta}$$

$$m^2 = R^2 + \frac{z^2}{Q^2}$$

Q is an axial ratio, $\boldsymbol{b_{halo}}$ is scale length and ρ_0 is a scale density. For ρ_0, We replace it with ***M(<200 kpc)***, which is mass within 200 kpc.
These are free parameters.

For (α,δ): We confine ourselves to plausible density profiles: **SIS with (α,δ)=(-2,0), NFW with (α,δ)(-1,-1) and HYBRID with (α,δ)=(-2,-0.5)**.

4.Data analysis

We use a sample of 91 globular clusters and 15 dwarf galaxies in the halo of Andromeda.
For the kinematic data of GCs and dSphs, we adopt **Revised Bologna Catalogue** of M31 GCs and **Tollerud+ 2012**, respectively.

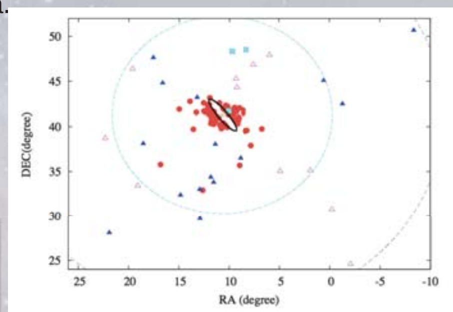

・Maximum likelihood analysis

To obtain halo parameters of our mass models by comparing with observational data, we employ a maximum likelihood method.

$$P(\mathbf{v}_{\rm los}|u,\sigma_t) = \prod_{i=1}^{N} \frac{1}{\sqrt{2\pi\sigma_i^2}} \exp\left[-\frac{1}{2}\frac{(v_{{\rm los},i}-u)^2}{\sigma_i^2}\right]$$

u : systemic velocity of M31

$$\sigma_i^2 = \sigma_{t,i}^2 + \sigma_{m,i}^2 \quad \begin{cases} \sigma_{t,i}^2 : \text{theoretical dispersion} \\ \sigma_{m,i}^2 : \text{measurement uncertainty} \end{cases}$$

5. Prolate dark halo in M31

5-1. Results of Maximum likelihood analysis

$q' = 1.18$	Halo Model	Q	$b_{\rm halo}$ (kpc)	$M_{\le 200{\rm kpc}}$ ($10^{12} \times M_\odot$)
	HYBRID	$2.43^{+0.57}_{-0.73}$	108.4^{+42}_{-21}	$1.21^{+0.29}_{-0.41}$
	SIS	$2.98^{+0.62}_{-1.38}$	$58.6^{+46.4}_{-38.6}$	$2.22^{+0.88}_{-0.92}$
	NFW	$1.62^{+0.44}_{-0.28}$	$46.2^{+13.8}_{-16.2}$	$4.43^{+0.47}_{-2.42}$

We find that the most plausible cases for Andromeda yield not spherical but prolate shape for its dark halo.

5-2. Q vs. M(<200 kpc) and Q vs. b_{halo} with NFW model

Above left and right figures show the likelihood contours Q-M(<200kpc), Q-b_{halo}, respectively.

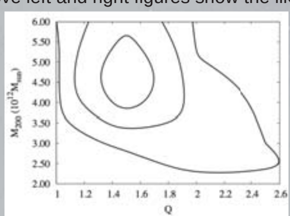

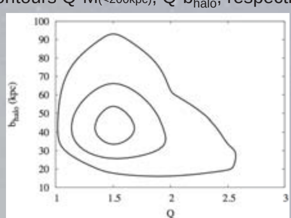

These results suggest that prolate dark halo would be significant results, although it is difficult to determine the shape parameter, Q.

5-3. Comparison with LCDM simulation

Zentner+ 2005

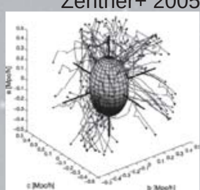

In this work, we find that dark halo in M31 is elongated along the pole of the its disk. This result is consistent with prediction from LCDM based N-body simulation (e.g. Zenter+ 2005).
In particular, Zenter+ 2005 found that subhalos are distributed anisotropically and preferentially located along the major axes of the triaxial their host halos. Therefore, ***our result may contribute valuable evidence for interpreting spatial distribution of dwarf satellites in Andromeda.***

6. Summary

- We adopt axisymmetric models constructed by Hayashi & Chiba (2012) and apply these models to latest kinematic data of globular clusters and dwarf spheroidal galaxies in the halo of Andromeda.
- We find that the best fitting cases for Andromeda's dark halo yield prolate shape and are elongated along perpendicularly to the plane of the its disk.
- This result is profound in understanding internal dynamics of halo tracers in Andromeda, such as orbital evolutions of tidal stellar streams, which play important roles in extracting the abundance of CDM subhalos through their dynamical effects on stream structures.
- In the near future, planned surveys of Andromeda's halo using HSC and PFS will enable us to discover new halo objects (globular clusters, dwarf galaxies and tidal streams) and measure their accurate kinematic data, thereby allowing us to obtain tighter limits on the dark halo distribution in Andromeda.

Solution space of Bianchi type I spacetime in Loop Quantum Cosmology

Kazuya Fujio
Astronomical Institute, Tohoku University

The Bianchi type I spacetime is the most simple model of spacetime with spatial anisotropy. We invetigate behavior of the solutions of quantum Bianchi type I spacetime with a massless scalar field within the frame work of loop quantu cosmology. We construct the solution space of this model by using a new formulation derived by the path integral method.
The 'probability' of having the classical isotropic universe is estimated.

Loop Quantum Cosmology

As is well known, the Universe is expanding now.
Einstein's general theory of relativity describes the dynamics of the Universe very well. However, general relativity breaks down at the very early universe.
Therefore we need the quantum theory of spacetime.
Loop quantum cosmology (LQC) is one of the leading candidates for the quantum theory of the universe, which is based on loop quantum gravity (LQG).
LQC predicts the cosmic bounce to avoid the initial singularity.

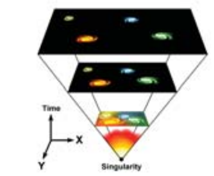

The physical quantities (e.g. the energy density) diverge at the 'beginning' of the universe. It is called initial singularity. GR cannot solve the initial singularity problem.

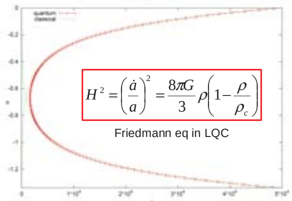

$$H^2=\left(\frac{\dot{a}}{a}\right)^2=\frac{8\pi G}{3}\rho\left(1-\frac{\rho}{\rho_c}\right)$$

Friedmann eq in LQC

LQC replaces the initial singularity with the initial bounce.

Bianchi type I spacetime

The Bianchi type I spacetime is flat, homogeneous but anisotropic model.
In this model, the universe can expand or contract in three directions.
Of course, by the observation, we know that our Universe is very isotropic.
Thus we need to answer the question "Why is our Universe so isotropic ?"

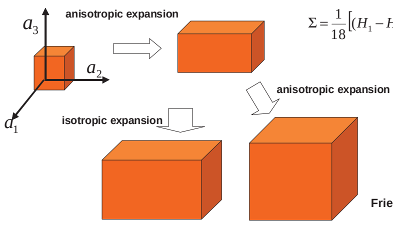

$$\Sigma=\frac{1}{18}\left[(H_1-H_2)^2+(H_2-H_3)^2+(H_3-H_1)^2\right]=\frac{\sigma_{GR}}{a^6}$$

Definition of the anisotropy

$$\boxed{H^2=\frac{8\pi G}{3}\rho+\Sigma}$$

Friedmann eq in classical Bianchi type I model

Note that the 'isotropic' means that three directions have same expansion rate.

Bianchi type I spacetime in LQC

The full equation of Bianchi type I spacetime in LQC is a difference equation.
Therefore effective equations of motion are used to study the dynamics.
We derive the equations by using path integral method and construct a new formulation which is preferable to study the Bianchi type I model.

Hamiltonian constraint $\boxed{C=\left(\frac{p}{\nu}\right)^2+\frac{\pi G}{2l^2}\overline{P}(C_1,C_2,b)=0}$

ν ; The volume of the cell **$\beta\ \lambda$; Constants which denotes anisotropy**

p ; The momentum of the massless scalar field (constant of motion)

$$C_i=\frac{\beta_i\lambda_i}{\nu} \qquad \{\nu,b\}_{Poisson}=-2$$

$$\overline{P}(C_1,C_2,b)=\cos(C_1l+C_2l+2bl)+\cos(C_1l+2bl)+\cos(C_2l+2bl)-\cos(C_1l-C_2l)-\cos(C_1l)-\cos(C_2l)$$

Behavior of solutions in LQC

As well as the isotropic model, the initial singularity is replaced with the initial bounce in our anisotropic model.
Some solutions have very low anisotropy like our observed Universe.
However, on the other hand, some solutions have very large anisotropy.
Therefore we should construct the set of all solutions to estimate the 'probability' to have the classical isotropic universes.

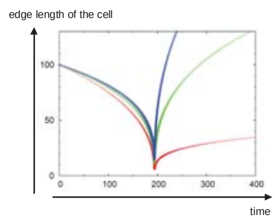

The solution with low anisotropy (case A)

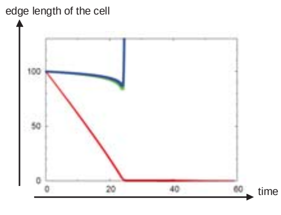

The solution with large anisotropy (case B)

Solution space Analysis

We regard the set of all initial data at the bounce as the solution space.
The solution space of our model is a two-dimensional space.
We found the surprising fact that except the hexagon area at the center, the universe shows cyclic behavior and never becomes sufficiently classical !

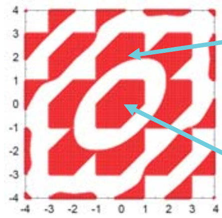

The solution space of our model.

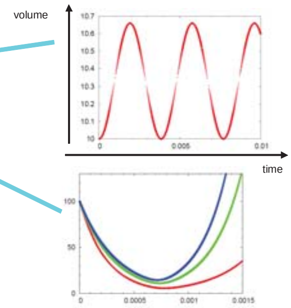

The 'probability' estimation

We define the 'probability' as the normalized area in the solution space where the desired condition is satisfied. We estimate the 'probability' for the anisotropic parameter M<1. The result shows that the isotropic universes are disfavored in LQC. However, if we consider more realistic model, LQC can explain the present isotropy by giving the 'actual' upper limit for M.

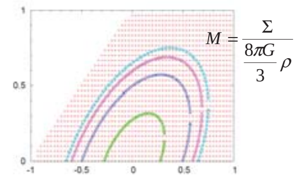

The contours denote, from inside, M=0.1,0.5,1.0,1.5
Note that most of region satisfies M<100.
This is the 'actual' upper limit of M.

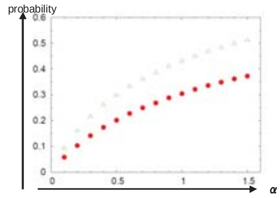

The 'probability' for having M<α
We cannot expect the appearance of the isotropic universes.

Summary

- **We constructed a new formulation of Bianchi type I spacetime in LQC. The formulation extracts the physical degree of freedom. Therefore we can easily construct the set of all physically distinct solutions.**
- **As well as the isotropic model, the initial singularity problem is resolved by replaced with the initial bounce. Although the anisotropy is preserved, the universe is not symmetry across the bounce.**
- **In addition to the universes which evolve into the classical universes, we found the cyclic and the stationary solutions which are dominated by the quantum effect.**
- **The 'probability' for having the isotropic universes are estimated. Although the result is negative, if we consider more realistic stuation, LQC can explain the present isotropy by giving the 'actual' upper limit.**

P-50

The UV-excess Property of LINER/Quiescent Early-type Galaxies

The 5th GCOE International Symposium:
"Weaving Science Web beyond Particle-Matter Hierarchy"
March 4-6, 2013 @Tohoku University

Takayuki Maebayashi, Takashi Murayama.
(Graduate School of Science, Astronomical Institute of Tohoku University)

1. ABSTRACT

Aim: We will focus on UV-excess(UVX) property of 'Active' early-type galaxies(ETGs) particularly to investigate ionizing sources of the 'LINER' population.
Sample: We reconstructed morphologically selected early-type galaxy sample from the SDSS(DR7) optical data and GALEX(GR6) UV data.
Analyses: We examined (1)the emission-line ratio distributions, (2)NUV-r' color vs. stellar mass relation and (3)FUV-NUV color vs. NUV-r' color relation.
Results: We will report three preliminary results: (1)about half of LINERs have NUV-r'≥5.0 mag, (2)most of the bluer(NUV-r'<5.0 mag) half of LINERs show the UV color distribution similar to that of 'Star Formings', (3)the LINERs with a strong UV-upturn feature are rather rare.
Suggestions: (1)The old stars photoionization is promising as a origin of the LINERs with NUV-r'≥5.0 mag, (2)the bluer half of LINERs seems to originate from a combination of young and old stars, (3)the strong UV-upturn activity which are sometimes seen in passive ETGs don't necessarily have a strong connection to the LINER-like emission-line activity.

2. MOTIVATION

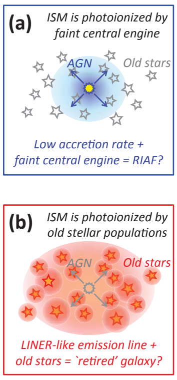

The low-ionization nuclear emission-line region(LINER) has been known as a kind of representative AGN population, which especially dominates in low-luminosity regime. However, LINER has been thought to have several physical origins for now: **LL-AGN**, **fast shock**, **old stars**, **hot ISM/ICM**(Ho 2008). In the AGN context, therefore, it should be noted that many kinds of 'fake AGNs' are included in this population.

Unfortunately, there are no definitive diagnostic schemes for the LINER origins. Some recent SDSS studies noted that most of LINERs may originate from old stars(Cid Fernandes+2011). These models, however, have a big problem: **"Why the 'retired' LINERs are different from the red Quiescent ETGs?"** Therefore, we were motivated to examine some UV properties by utilizing the GALEX database and search unknown ionizing UV sources, the answer to this question and the appropriate diagnostics of LINERs.

Fig.1-(a), (b): Schematic view of two LINER origins.

3. SAMPLE

Data set: SDSS(DR7) 'PhotoObj' & 'SpecObj' joined table,
The MPA-JHU DR7 release of spectrum measurements,
The SDSS(DR7)-GALEX(GR6) matched table('xSDSSDR7').

Early-type galaxy criteria:
0.05 < z < 0.1, modelMag_r' < 16.8 AB mag,
fracDeV_g', r', i' > 0.95, S/N_g', r', i' > 10.0.

GALEX-SDSS (reverse)matching criteria:
S/N_FUV or S/N_NUV ≥ 3.0, NUV ≤ 23.5 AB mag,
(reverse)MultipleMatchCount ≤ 2, (reverse)DistanceRank = 1,
Search radius ≤ 5", Distance between matched sources ≤ 4".

Galactic extinction correction:
R_V=3.1 extinction in Cardelli+(1989) & O'Donnell+(1994),
A/E(B-V) are from Schlegel+(1998) & Wyder+(2007),
E(B-V) are from Schlegel+(1998).

We used only the GALEX 'MIS' & 'DIS' data.

4. ANALYSES & RESULTS

4-1. Classification result

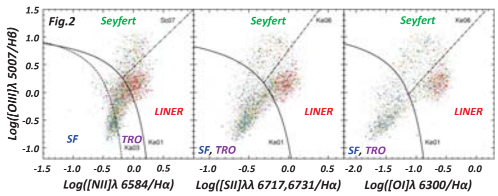

Number of SDSS(DR7)-GALEX(GR6) matched sample: → 4122 total ETGs.
- **Active:** Hβ, [OIII]λ 5007, Hα, [NII]λ 6584 are ≥ 3σ, → **464 Active ETGs**.
- **Semi-Active:** These 1~3 emission lines are ≥ 3σ, → **1487 Semi-Active ETGs**.
- **Quiescent:** Hβ, [OIII]λ 5007, Hα, [NII]λ 6584 are < 3σ, → **2171 Quiescent ETGs**.

Active ETGs → The emission-line diagnostic diagrams(BPT diagrams)
→ **75 Star Forming(SF)**, **123 Transition Region Object(TRO)**, **61 Seyfert**, **205 LINER**.

From Fig.2, we can see a concentrated distribution in each LINER region.
These concentrations are seen in both samples(the cross-matched/SDSS sample).

Color coding in Fig.2: NUV-r'<3.0, 3.0≤NUV-r'<4.0, 4.0≤NUV-r'<5.0, 5.0≤NUV-r'. Gray plots; SDSS early-type sample.

4-2. NUV-r' Color vs. Stellar Mass

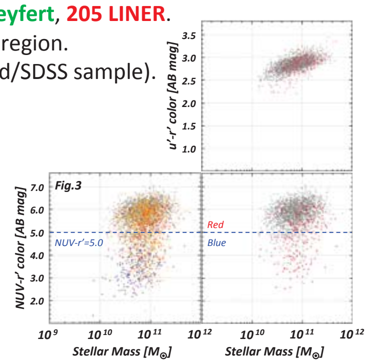

(1) About half of LINERs have NUV-r'≥5.0 mag(Fig.3):
We showed a UV color-mass diagram in Fig.3. In this plot, we adopted the color threshold of NUV-r'=5.0 mag which separates all ETGs into 'blue' or 'red' ETGs. This is because the M89(a strong UV-upturn galaxy) shows NUV-r'=5.0 mag and FUV-NUV=1.0 mag. From Fig.3, we can see about half of LIENRs are red, suggesting that an amount of young OB stars in host galaxy is very small. On the other hand, there are bluer half of LINERs, suggesting that they have some UV sources, i.e., young OB stars and/or LL-AGN.

Color coding in Figs.3-5: SF, TRO, Seyfert, LINER, Semi-Active, Quiescent.

4-3. FUV-NUV Color vs. NUV-r' Color

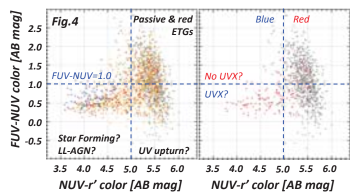

(2) Most of the bluer half of LINERs show the UV color distribution similar to that of SFs(Fig.4):
We showed a UV color-color diagram in Fig.4. In this plot, we adopted the color threshold of FUV-NUV=1.0 mag which separates all ETGs into 'UVX' or 'no UVX' ETGs. Most of the aforementioned 'blue' LINERs distribute in the UVX region and their distribution isn't different from that of SFs. Therefore, we speculated that the origin of 'blue' and 'UVX' LINERs could be more likely to be weak star formation(i.e. young OB stars) than LL-AGN(cf. Salim+2012, Fang +2012). In addition, Fig.5 shows that the luminosity of [OIII]λ 5007 doesn't correlate well with the UV magnitudes, possibly suggesting that LL-AGN isn't a ionizing UV source of LINERs.

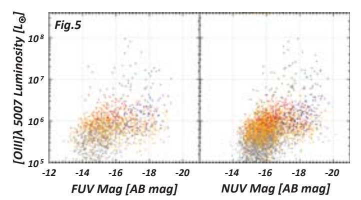

(3) The LINERs with a strong UV-upturn feature are rather rare (Fig.4):
Most of the Quiescents are included in the red subclass and their NUV-r' color is almost constant in Figs.3-4. Their FUV-NUV color, however, does change significantly in Fig.4. This sequence means that they have a wide range of UV-upturn strength(note: bluer FUV-NUV color corresponds to stronger UV-upturn). If the UV-upturn activity links closely to the LINER activity, we would expect that LINERs distribute preferentially around the UV-upturn region. In the case of the aforementioned 'red' LINERs, however, although they showed a wide range of the strength, it seems that they tend to favor the no UVX region(ref. of UV-upturn: Brown+2000, Yi+2011, Ree+2012).

5. DISCUSSION & SUMMARY

(1) Old stars photoionizaion('retired' LINER): Firstly, we presented the 'red' LINERs which show little evidence of young OB stars and/or LL-AGN. If these LINERs don't have a central X-ray source neither, old stars(e.g. Post-AGBs) are promising ionizing sources of the LINERs.

(2) Possible UV contribution from OB stars: Secondly, we presented the 'blue' and 'UVX' LINERs which show clear sign of UV sources. If the sources are OB stars, young-to-total mass fraction is estimated to $F(t_{age};\ t_{age}<1\ \mathrm{Gyr})>10^{-3}$(Kauffmann+2007). Given this mass fraction, OB stars are expected to be stronger ionizing UV sources than old stars(Cid Fernandes+2011). Although the geometry between gas and ionizing source still remains uncertain, we felt it could be necessary to consider a hybrid photoionization model by young and old stars.

(3) UV-upturn and 'retired' LINER: Finally, we presented the 'red' and 'UVX' LINERs which show the UV-upturn feature. We showed that these LINERs are rather minority in the 'red' LINERs, in other words, the UV-upturn activity doesn't tend to induce the LINER activity. Because the UV-upturn activity also has been thought to originate from old stars(i.e. ZAHBs, AGB-Manqués, PE-AGBs, Post-AGBs), this result might suggest that (a)an amount of ionized gas plays a critical role to differentiate between LINERs and Quiescents, or (b)the 'retired' LINERs require some additional ionizing sources other than old stars.

P-51

Search for red K – [3.6] > 2 galaxies in the Spitzer SEDS survey field

K. Mawatari[1,2], J.-S. Huang[2], T. Yamada[1], G. G. Fazio[2], M. L. N. Ashby[2]

[1]Tohoku University, [2]Harvard-Smithsonian Center for Astrophysics

ABSTRACT

We have searched for red galaxies in K – [3.6] color in the UKIDSS Ultra-Deep Survey (UDS) field, and report the preliminary result about these new population galaxies. The Spitzer SEDS survey, where no survey before achieved same depth over such a wide area at mid infrared wavelength, enabled us to detect the hundreds of candidates. There may be three kinds of galaxies among our red galaxy sample that have K-[3.6]>2: (1)passive galaxies at z>5, (2)dusty star forming galaxies at z<2, and (3)emission line galaxies at z~6 ([OIII] and Ha). We also note that the UDS field is potentially unique field to investigate environmental dependency of detected red galaxies at z>5 because the prominent high density regions traced by young star forming galaxies at z = 5.7 (LAEs) are already reported in this field.

I, Introductin

(1)SEDS survey

Spitzer Extended Deep Survey (SEDS) is a very deep infrared survey within five well-known extra-galactic science fields (Ashby et al. 2013). SEDS covers a total area of 1.46 deg^2 to a depth of 26 AB mag (3σ) in both of the warm IRAC bands at 3.6 and 4.5 μm. This wide and deep survey is adequate for investigating high redshift galaxies (z=2-7).

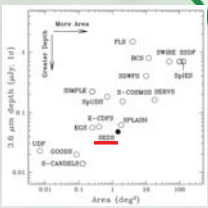

↑SEDS depth and total area, from Ashby et al.(2013)

(2)IRAC selected red galaxies

Passive galaxies at z>3 are difficult to detect because of their red color and lack of emission lines. But some candidates begin to be reported by the combination of very deep Spitzer/IRAC and HST/WFC3 data (Huang et al. 2011, Caputi et al. 2012). Their SEDs are characterized by the Balmer break.

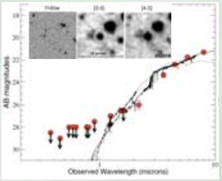

↑z~6 galaxy candidate, from Caputi et al.(2012)

II,Pre-analysis simulation

We expect that **it is possible in principle to locate galaxies at z >5 using K-[3.6] color to detect the Balmer breaks**, where relatively wider area data are available in K band than in HST/WFC3 previous works used.

At first we simulated K-[3.6] color using stellar population synthesis models (GALAXEV). We checked model galaxies' K-[3.6] color changing their

- ✓ redshift
- ✓ star formation history (single burst/constant SF)
- ✓ metallicity
- ✓ dust extinction: E(B-V)
- ✓ formation redshift/age

Finally, we found **passive galaxies at z>5 always have K-[3.6] color larger than 2**, while low-z dusty galaxies also satisfy the same criterion.

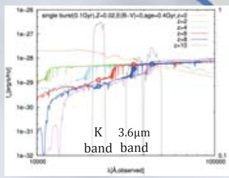

↑Redshifted spectra with single burst model, Their ages are fixed to 0.4 Gyr

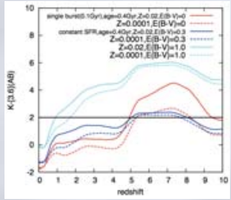

↑K-[3.6] color as function of redshift. Several models are shown, where metallicity and dust extinction are changed.

III, Analysis

1, Data in the UDS field

We searched for objects that have K-[3.6] color redder than 2 in the UKIDSS Ultra-Deep Survey (UDS) field, one of SEDS fields. UDS benefits from rich multi-wavelength ancillary data from X-ray to radio.

	FoV (deg^2)	Depth (3σ,AB, total)	Aperture correction (mag)
SEDS/[3.6]	0.32	26.0	-0.90 (for 2.4" aperture)
UKIDSS/K(DR8)	0.8	25.0	-0.22 (for 2" aperture)

↑Summary of SEDS/[3.6] and UKIDSS/K-band data

2, K-[3.6] color

We used the SEDS and UKIDSS/UDS catalogs to measure K-[3.6], where the empirical aperture corrections are applied to estimate total magnitudes.

As a result, **1049 objects with K-[3.6]>2 are detected**. Note that all of them are redder than the 4 σ photometric error for bluer normal objects.

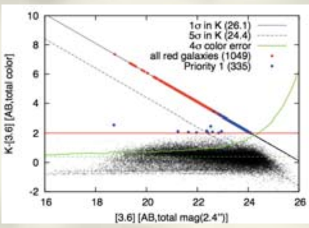

3, Selecting significant sample

There are some possibilities of false detection. As our selection is based on the catalogs, the difference of source extraction is critical. Careful treatment is needed especially for blended sources, where the SEDS catalog identifies objects which suffer source confusion by PSF fitting method (Ashby et al. 2013).

We categorized objects by their blending (see the table below), and **consider the objects which don't suffer source confusion in SEDS and have no or very faint K counterparts as significant sample (Priority 1)**.

suffer source confusion in SEDS	suffer source confusion in UKIDSS/K	have K counterpart	K counterpart is cataloged in the UKIDSS	
No	No	Yes	Yes	→ Priority 1
No	No	Yes	No	→ Priority 4
No	No	No	No	→ Priority 1
Yes	No	Yes	Yes	→ Priority 3
Yes	No	Yes	No	→ Priority 4+
Yes	No	No	No	→ Priority 2
Yes	Yes	No	No	→ Priority 5

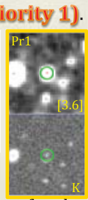

⇒335 Priority1 are found!

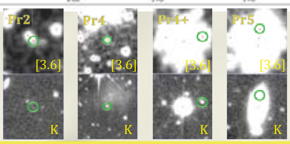

←↑Examples of each priority objects: Green circles shows 2.4″ apertures. Red squares show all SEDS detections. Cyan squares show all DR8 detections.

IV, Early results & Future work

1, What's the nature of K-[3.6]>2 galaxies?

Three kinds of galaxies are expected to satisfy our K-[3.6] color criterion.

(1)Passive red galaxies at z > 5

: They should be most interesting galaxies. Relatively blue [3.6]-[4.5] colors suggest they are not too old or metal rich.

(2) Dusty star-forming galaxies at low-z

: It is difficult to distinguish passive high-z galaxies from dusty low-z galaxies.

(3) Emission line galaxies at z ~ 4.5 or ~ 6

: [OIII] and H α lines of z~6 star-forming galaxies enter [3.6] and [4.5], respectively. H α lines of z~4.5 galaxies also enter [3.6].

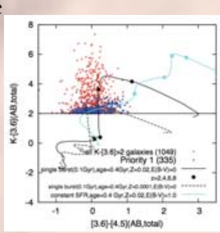

↑The red galaxies in [3.6]-[4.5] vs K-[3.6] two color diagram.

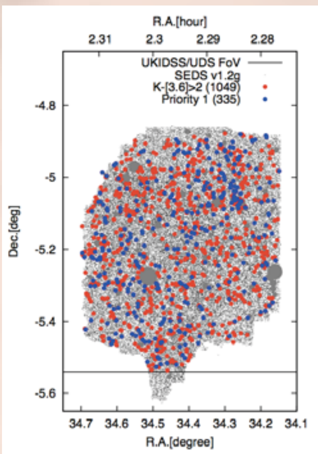

↑Sky distribution of the K-[3.6] red galaxies

high-z passive ?

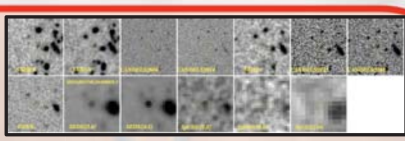

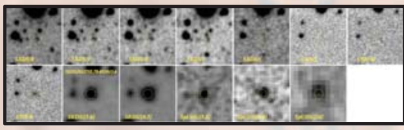

low-z dusty ?

high-z star-forming?

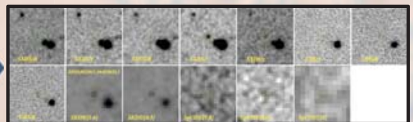

2, Future analysis and observation

- ✓ SED fitting
- ✓ Optical spectroscopy will separate emission line galaxies as they should have Ly α emission lines or Lyman breaks.
- ✓ Comparison with the sky distribution of LAEs at z=5.7 (Ouchi +05), which shows the prominent density peak.

This work is supported by the Brain Circulation Program (R2301) by Japan Society for the Promotion of Science.

http://www.astr.tohoku.ac.jp/~hken/us.tohoku.abce/index.html

P-52

TEST OF SIGNIFICANT SIZE EVOLUTION IN MASSIVE QUIESCENT GALAXIES

MOHAMMAD AKHLAGHI, TAKASHI ICHIKAWA

TOHOKU UNIVERSITY ASTRONOMICAL INSTITUTE

http://www.astr.tohoku.ac.jp/~akhlaghi/

TOHOKU UNIVERSITY

INTRODUCTION

Quiescent galaxies are generally red in the current age of the universe (nearby objects). We associate this color with the assumption that they don't have young stars and thus no large scale star formation. These galaxies also tend to be very spherical and massive. One example can be seen bellow compared to a spiral star forming galaxy.

As we look farther away, the images of the galaxies are not so clear. Take a look at these four red galaxies for example, the light from each departed, from left to right: 7.46, 9.51, 11.26 and 11.69×10^9 years ago. Light from the top galaxy was emitted 3.14×10^9 years ago.

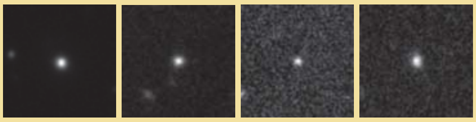

If they have no star formation, then how did they get so massive, concentrated and large? This question has puzzled astronomers for more than 50 years. All aspects of their evolution has been an obstacle for any theory of galaxy evolution. Here we will look at their *size evolution*. Astronomers use the *Sérsic profile* to represent a galaxy's radial light profile:

$$\Sigma(r) = \Sigma_e \exp\left[-b(n)\left(\left(\frac{r}{r_e}\right)^{1/n} - 1\right)\right]$$

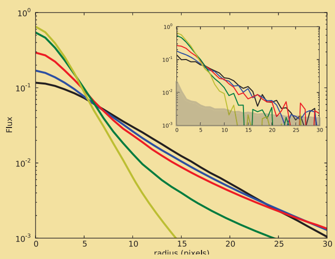

r_e is defined as the radius containing $1/e$ of the total light. n shows the concentration and is known as the Sérsic index. With a similar total light and other observed quantities (eccentricity and etc), these two parameters define the shape of a galaxy light profile.

IN THE LITERATURE

Some authors (e.g. vanDokkum+2010) claim there is a significant size evolution with $r_e \propto (1+z)^{\sim 1.2}$ while others (e.g. Saracco+2011) don't observe such size evolution. Proponents of merging (e.g. vD+2010) associate it with merging and others (e.g. Carollo+2013) to the growth of their possible progenitors.

DIFFERENT PHILOSOPHY

Induction is commonly used by the, generally positivist, astronomers. But here we have used a new logical approach: *Reduction to absurdity*. Instead of placing *positive* faith in fitting results, we will assume the results of the two contesting scenarios on r_e and see how that affects another property of the galaxies: the Sérsic index.

IMAGES & PSFS

In this study we used archival images from the GOODS-N region. For each redshift we used the nearest broadband filter to the restframe V band in that redshift. The ACS Treasury Survey (ATS) i band and z band images were used for $0.16 \leq z < 0.55$ and $0.55 \leq z < 0.88$ respectively. The MODS survey (Deep and Wide) J, H and K band images were used for $0.88 \leq z < 1.5$, $1.5 \leq z < 2.43$ and $2.43 \leq z < 3.5$.

The Point Spread Function (PSF) was fitted for stars separately for the Deep and Wide images of MODS and the whole region for ATS. The final PSF can be seen as the thick black lines of the images bellow.

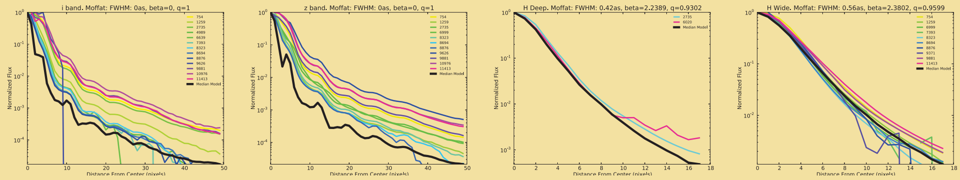

FINDING THE SÉRSIC INDEX (n)

Having assumed r_e and knowing the total magnitude of the galaxy. We can simply find n by creating mock profiles with various ns but similar total magnitude and similar r_e. We measure the flux on all elliptical annuli up to the sky level. Thus a one dimensional profile can be found for each galaxy. The flux value for each radius is divided by the flux of other radii and the various flux ratios for each combination of radii are used compared to those of the models to find the best n.

RESULTS

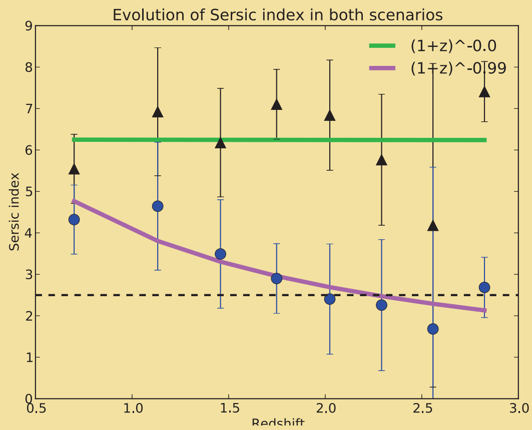

Median Sérsic index of Galaxies placed in bins of equal comoving volume. The purple line shows evolution in n if we assume size evolution and the green line the evolution in n if no size evolution has occurred.

Discussion: Assuming size evolution, results in a significant evolution in n, this suggests a significant evolution in general morphological parameters to simultaneously occur and not just in the size.

REFERENCES

Carollo+2013: arXiv:1302.5115. **Saracco+2011:** doi:10.1111/j.1365-2966.2010.18098.x.
vanDokkum+2010: doi 10.1088/0004-637X/709/2/1018.

An extension of observable diameter

Ryunosuke Ozawa
Mathematical institute Tohoku University (sb0m08@math.tohoku.ac.jp)

Gromov introduced the observable diameter. It measures nearness between a metric measure space and one point measure space in the sence of the observable distance function. We extend the observable diameter to elements of the completion and compactification of the set of metric measure spaces with observable distance function. This is joint research with Takashi Shioya (Tohoku University).

MM-spaces and 1-Lipschitz domination

$X = (X, d_X, \mu_X)$: mm-space $\overset{\text{def}}{\iff}$
(X, d_X) : a complete separable metric space,
μ_X : a Borel probability measure on (X, d_X).

- $\mathcal{X}$: the set of mm-spaces.
- $* := (\{p\}, \delta_p)$: 1-point measure space.

$Y \prec X \overset{\text{def}}{\iff} \exists f : X \to Y$ 1-Lipschitz map s.t. $\mu_X(f^{-1}(A)) = \mu_Y(A)$.

Observable distance [Gromov]

$d_{\mathrm{conc}}(X, Y)$: the observable distance.

- $(\mathcal{X}, d_{\mathrm{conc}})$ is a metric space. This is not complete.
- d_{conc} compares the distance between the sets of 1-Lipschitz functions on X and Y in the sense of measures.
- $(\overline{\mathcal{X}}, d_{\mathrm{conc}})$: the completion of $(\mathcal{X}, d_{\mathrm{conc}})$.
- $\prod_{n=1}^{\infty} S^n \in \overline{\mathcal{X}} \setminus \mathcal{X}$

Observable diameter

Let $X \in \mathcal{X}$, $\kappa > 0$. We define the observable diameter of X by

$$\mathrm{ObsDiam}(X; -\kappa) := \sup_{f:X\to\mathbb{R}\ \text{1-Lip}} \inf\{\ \mathrm{diam} A \mid A \subset \mathbb{R},\ \mu_X(f^{-1}(A)) \geq 1-\kappa\ \},$$

$$\mathrm{ObsDiam}(X) := \inf_{\kappa>0} \max\{\ \mathrm{ObsDiam}(X; -\kappa),\ \kappa\ \}.$$

Some properties of observable diameter

- $d_{\mathrm{conc}}(X, *) \leq \mathrm{ObsDiam}(X) \leq 2 d_{\mathrm{conc}}(X, *)$.
- $Y \prec X \Rightarrow$
  $\mathrm{ObsDiam}(Y; -\kappa) \leq \mathrm{ObsDiam}(X; -\kappa)$.

Theorem [Gromov-Milman]

M : a closed Riemannian manifold,
$\mathrm{Ric}_M > 0$.

$$\Rightarrow\ \mathrm{ObsDiam}(X; -2\kappa) \leq \frac{2}{\sqrt{\kappa \mathrm{Ric}_M}}.$$

S^n, $\mathbb{C}P^n$, $SO(n)$, $SU(n)$, $V_{n,p} \xrightarrow{d_{\mathrm{conc}}} *$.

Pyramid [Gromov]

$\mathcal{P} \subset \mathcal{X}$: pyramid
$\overset{\text{def}}{\iff} X \in \mathcal{P}, Y \prec X \Rightarrow Y \in \mathcal{P}$,
$X, Y \in \mathcal{P} \Rightarrow \exists Z \in \mathcal{P}$ s.t. $X, Y \prec Z$,
$\mathcal{P}$: $\square_1$-closed set.

To understand the topology generated by d_{conc}, Gromov introduced the pyramid.

- $\square_1$: a canonical metric on $\mathcal{X}$.
- Π : the set of pyramids.
- $\mathcal{P}_X := \{Y \in \mathcal{X} | Y \prec X\}$, $\mathcal{X} \in \Pi$.

Theorem [Gromov, Shioya]

- There exists a metirc ρ on Π. (Π, ρ) is a compact metric space.
- $X_n \xrightarrow{d_{\mathrm{conc}}} X \Leftrightarrow \mathcal{P}_{X_n} \xrightarrow{\rho} \mathcal{P}_X$.
- $\{\mathcal{P}_X\}_{X\in\mathcal{X}}$ is dense on (Π, ρ).
- $\rho(\mathcal{P}_X, \mathcal{P}_Y) \leq d_{\mathrm{conc}}(X, Y)$.
- (Π, ρ) is the compactification of $(\mathcal{X}, d_{\mathrm{conc}})$ and $(\overline{\mathcal{X}}, d_{\mathrm{conc}})$.

Proposition [Ozawa-Shioya]

$X, X_n \in \mathcal{X}$, $X_n \xrightarrow{d_{\mathrm{conc}}} X$.

$$\mathrm{ObsDiam}(X; -\kappa) = \lim_{\delta \searrow 0} \lim_{n\to\infty} \mathrm{ObsDiam}(X_n; -(\kappa+\delta)).$$

An extension of observable diameter

Let $\overline{X} \in \overline{\mathcal{X}}$, $X_n \in \mathcal{X}$, $X_n \xrightarrow{d_{\mathrm{conc}}} \overline{X}$, $\mathcal{P} \in \Pi$, $\kappa > 0$. We define the observable diameter of $\overline{X}$ and $\mathcal{P}$ by

$$\mathrm{ObsDiam}(\overline{X}; -\kappa) := \lim_{\delta \searrow 0} \lim_{n\to\infty} \mathrm{ObsDiam}(X_n; -(\kappa+\delta)),$$

$$\mathrm{ObsDiam}(\mathcal{P}; -\kappa) := \lim_{\delta \searrow 0} \sup_{X\in\mathcal{P}} \mathrm{ObsDiam}(X; -(\kappa+\delta)).$$

Proposition [Ozawa-Shioya]

$\overline{X} \in \overline{\mathcal{X}}$.
$\mathrm{ObsDiam}(\overline{X}; -\kappa) = \mathrm{ObsDiam}(\mathcal{P}_{\overline{X}}; -\kappa)$.

- $\mathrm{ObsDiam}(\overline{X}; -\kappa)$ and $\mathrm{ObsDiam}(\mathcal{P}; -\kappa)$ are natural extensions of the observable diameter.

P-54

Elliptic Ding-Iohara Algebra and the Free Field Realization of the Elliptic Macdonald Operator

Yosuke Saito

Mathematical Institute, Tohoku University, Sendai, Japan.

Notations. In this article, we use the following symbols.

The q-infinite product : $(x;q)_\infty := \prod_{n\geq 0}(1-xq^n)$ $(|q|<1)$,

The theta function : $\Theta_p(x) := (p;p)_\infty (x;p)_\infty (px^{-1};p)_\infty$,

The double infinite product : $(x;q,p)_\infty := \prod_{m,n\geq 0}(1-xq^m p^n)$,

The elliptic gamma function : $\Gamma_{q,p}(x) := (qpx^{-1};q,p)_\infty \Big/ (x;q,p)_\infty$.

The Ding-Iohara algebra is a quantum algebra arising from the free field realization (FFR for short) of the Macdonald operator. Starting from the elliptic kernel function as

$$\Pi(q,t,p)(x,y) := \prod_{i,j}\frac{\Gamma_{q,p}(x_i y_j)}{\Gamma_{q,p}(t x_i y_j)} \tag{0.1}$$

introduced by Komori, Noumi and Shiraishi, we can define an elliptic analog of the Ding-Iohara algebra. The free field realization of the elliptic Macdonald operator is also constructed.

$$\begin{array}{ccc}
\begin{array}{c}\text{Elliptic Macdonald operator}\\ H_N(q,t,p)\end{array} & \xrightarrow{\textbf{FFR !}} & \begin{array}{c}\textbf{Elliptic Ding-Iohara algebra}\\ \boldsymbol{\mathcal{U}(q,t,p)}\end{array}\\
\uparrow \text{elliptic deformation} & & \uparrow \textbf{elliptic deformation !}\\
\text{Macdonald operator } H_N(q,t) & \xrightarrow{\text{FFR}} & \text{Ding-Iohara algebra } \mathcal{U}(q,t)
\end{array}$$

1 Main Results

Definition 1.1 (**Elliptic Ding-Iohara algebra** $\mathcal{U}(q,t,p)$). Let us define the structure function $g_p(x)$ by

$$g_p(x) := \frac{\Theta_p(qx)\Theta_p(t^{-1}x)\Theta_p(q^{-1}tx)}{\Theta_p(q^{-1}x)\Theta_p(tx)\Theta_p(qt^{-1}x)}.$$

Here we have used the notation above and assume $|q|<1$, $|p|<1$. We define the elliptic Ding-Iohara algebra $\mathcal{U}(q,t,p)$ to be the associative $\mathbf{C}$-algebra generated by $\{x_n^\pm(p)\}_{n\in\mathbf{Z}}$, $\{\psi_n^\pm(p)\}_{n\in\mathbf{Z}}$ and γ subject to the following relation : we set γ as the central, invertible element and currents to be $x^\pm(p;z) := \sum_{n\in\mathbf{Z}} x_n^\pm(p)z^{-n}$, $\psi^\pm(p;z) := \sum_{n\in\mathbf{Z}}\psi_n^\pm(p)z^{-n}$.

$$[\psi^\pm(p;z),\psi^\pm(p;w)]=0,\quad \psi^+(p;z)\psi^-(p;w)=\frac{g_p(\gamma z/w)}{g_p(\gamma^{-1}z/w)}\psi^-(p;w)\psi^+(p;z),$$
$$\psi^\pm(p;z)x^+(p;w)=g_p\left(\gamma^{\pm\frac12}\frac{z}{w}\right)x^+(p;w)\psi^\pm(p;z),$$
$$\psi^\pm(p;z)x^-(p;w)=g_p\left(\gamma^{\mp\frac12}\frac{z}{w}\right)^{-1}x^-(p;w)\psi^\pm(p;z),$$
$$x^\pm(p;z)x^\pm(p;w)=g_p\left(\frac{z}{w}\right)^{\pm1}x^\pm(p;w)x^\pm(p;z),$$
$$[x^+(p;z),x^-(p;w)] = \frac{\Theta_p(q)\Theta_p(t^{-1})}{(p;p)_\infty^3\Theta_p(qt^{-1})}\left\{\delta\left(\gamma\frac{w}{z}\right)\psi^+(p;\gamma^{1/2}w)-\delta\left(\gamma^{-1}\frac{w}{z}\right)\psi^-(p;\gamma^{-1/2}w)\right\},$$

where we set the delta function $\delta(z) := \sum_{n\in\mathbf{Z}} z^n$.

Theorem 1.2 (**Free field realization of the elliptic Ding-Iohara algebra** $\mathcal{U}(q,t,p)$). *Let us define an algebra $\mathcal{B}_{a,b}$ of bosons : it is generated by $\{a_n\}_{n\in\mathbf{Z}\setminus\{0\}}$, $\{b_n\}_{n\in\mathbf{Z}\setminus\{0\}}$ with the following relations :*

$$[a_m,a_n]=m(1-p^{|m|})\frac{1-q^{|m|}}{1-t^{|m|}}\delta_{m+n,0},\quad [b_m,b_n]=m\frac{1-p^{|m|}}{(qt^{-1}p)^{|m|}}\frac{1-q^{|m|}}{1-t^{|m|}}\delta_{m+n,0},$$
$$[a_m,b_n]=0.$$

Define the boson Fock space $\mathcal{F}$ as the left $\mathcal{B}_{a,b}$ module generated by the vacuum vector $|0\rangle$ which satisfies $a_n|0\rangle = b_n|0\rangle = 0\,(n>0)$: $\mathcal{F} = span\{a_{-\lambda}b_{-\mu}|0\rangle : \lambda,\mu\in\mathcal{P}\}$, where $\mathcal{P}$ denotes the set of partitions and $a_{-\lambda} := a_{-\lambda_1}\cdots a_{-\lambda_{\ell(\lambda)}}$ $(\lambda\in\mathcal{P})$. Set $\gamma := (qt^{-1})^{-1/2}$ and define operators $\eta(p;z)$, $\xi(p;z)$, $\varphi^\pm(p;z) : \mathcal{F}\to\mathcal{F}\otimes\mathbf{C}[[z,z^{-1}]]$ as follows :

$$\eta(p;z) := \boldsymbol{:}\exp\left(-\sum_{n\neq0}\frac{1-t^{-n}}{1-p^{|n|}}p^{|n|}b_n\frac{z^n}{n}\right)\exp\left(-\sum_{n\neq0}\frac{1-t^n}{1-p^{|n|}}a_n\frac{z^{-n}}{n}\right)\boldsymbol{:},$$
$$\xi(p;z) := \boldsymbol{:}\exp\left(\sum_{n\neq0}\frac{1-t^{-n}}{1-p^{|n|}}\gamma^{-|n|}p^{|n|}b_n\frac{z^n}{n}\right)\exp\left(\sum_{n\neq0}\frac{1-t^n}{1-p^{|n|}}\gamma^{|n|}a_n\frac{z^{-n}}{n}\right)\boldsymbol{:},$$
$$\varphi^+(p;z) := \boldsymbol{:}\eta(p;\gamma^{1/2}z)\xi(p;\gamma^{-1/2}z)\boldsymbol{:},\quad \varphi^-(p;z) := \boldsymbol{:}\eta(p;\gamma^{-1/2}z)\xi(p;\gamma^{1/2}z)\boldsymbol{:}.$$

Then the map defined by

$$x^+(p;z)\mapsto\eta(p;z),\quad x^-(p;z)\mapsto\xi(p;z),\quad \psi^\pm(p;z)\mapsto\varphi^\pm(p;z)$$

gives a representation of the elliptic Ding-Iohara algebra $\mathcal{U}(q,t,p)$.

Theorem 1.3 (**Free field realization of the elliptic Macdonald operator**). *The elliptic Macdonald operator $H_N(q,t,p)$ $(N\in\mathbf{Z}_{>0})$ is defined by*

$$H_N(q,t,p) := \sum_{i=1}^N\prod_{j\neq i}\frac{\Theta_p(tx_i/x_j)}{\Theta_p(x_i/x_j)}T_{q,x_i}\quad (T_{q,x}f(x) := f(qx)). \tag{1.1}$$

Let $\phi(p;z) : \mathcal{F}\to\mathcal{F}\otimes\mathbf{C}[[z,z^{-1}]]$ be an operator defined as

$$\phi(p;z) := \exp\left(\sum_{n>0}\frac{(1-t^n)(qt^{-1}p)^n}{(1-q^n)(1-p^n)}b_{-n}\frac{z^{-n}}{n}\right)\exp\left(\sum_{n>0}\frac{1-t^n}{(1-q^n)(1-p^n)}a_{-n}\frac{z^n}{n}\right).$$

Then the operators $\eta(p;z)$, $\xi(p;z)$ reproduce the elliptic Macdonald operator as follows.

$$\begin{aligned}&[\eta(p;z)-t^{-N}(\eta(p;z))_-(\eta(p;p^{-1}z))_+]_1\prod_{j=1}^N\phi(p;x_j)|0\rangle\\
&\qquad=\frac{t^{-N+1}\Theta_p(t^{-1})}{(p;p)_\infty^3}H_N(q,t,p)\prod_{j=1}^N\phi(p;x_j)|0\rangle,\end{aligned} \tag{1.2}$$

$$\begin{aligned}&[\xi(p;z)-t^{N}(\xi(p;z))_-(\xi(p;p^{-1}z))_+]_1\prod_{j=1}^N\phi(p;x_j)|0\rangle\\
&\qquad=\frac{t^{N-1}\Theta_p(t)}{(p;p)_\infty^3}H_N(q^{-1},t^{-1},p)\prod_{j=1}^N\phi(p;x_j)|0\rangle,\end{aligned} \tag{1.3}$$

where $(\eta(p;z))_\pm$ stands for the plus and minus parts of $\eta(p;z)$ respectively as

$$(\eta(p;z))_\pm = \exp\left(-\sum_{\pm n>0}\frac{1-t^{-n}}{1-p^{|n|}}p^{|n|}b_n\frac{z^n}{n}\right)\exp\left(-\sum_{\pm n>0}\frac{1-t^n}{1-p^{|n|}}a_n\frac{z^{-n}}{n}\right)$$

and $(\xi(p;z))_\pm$ is defined in the similar way. The symbol $[f(z)]_1$ denotes the constant term of $f(z)$ in z.

Another forms of the theorem 1.3

Let us introduce the zero mode generators a_0, Q satisfying the following :

$$[a_0,Q]=\frac{1}{\beta},\quad [a_n,a_0]=[b_n,a_0]=0,\quad [a_n,Q]=[b_n,Q]=0\quad (n\in\mathbf{Z}\setminus\{0\}).$$

Here the parameter $\beta\in\mathbf{C}$ is defined by the condition $t=q^\beta$. For a complex number α, we define $|\alpha\rangle := e^{\alpha Q}|0\rangle$. Then we have $\beta a_0|\alpha\rangle = \alpha|\alpha\rangle$.

By using the zero modes, we can reformulate the free field realization of the elliptic Macdonald operator as follows.

Theorem 1.4. *Set operators $\widetilde{\eta}(p;z)$, $\widetilde{\xi}(p;z)$ as $\widetilde{\eta}(p;z) := (\eta(p;z))_-(\eta(p;p^{-1}z))_+$, $\widetilde{\xi}(p;z) := (\xi(p;z))_-(\xi(p;p^{-1}z))_+$. We define operators $E(p;z)$, $F(p;z)$ as follows :*

$$E(p;z) := \eta(p;z)-\widetilde{\eta}(p;z)q^{-\beta a_0},\quad F(p;z) := \xi(p;z)-\widetilde{\xi}(p;z)q^{\beta a_0}. \tag{1.4}$$

Then the elliptic Macdonald operators $H_N(q,t,p)$, $H_N(q^{-1},t^{-1},p)$ are reproduced from the operators $E(p;z)$, $F(p;z)$ as follows :

$$[E(p;z)]_1\prod_{j=1}^N\phi(p;x_j)|N\beta\rangle = \frac{t^{-N+1}\Theta_p(t^{-1})}{(p;p)_\infty^3}H_N(q,t,p)\prod_{j=1}^N\phi(p;x_j)|N\beta\rangle, \tag{1.5}$$

$$[F(p;z)]_1\prod_{j=1}^N\phi(p;x_j)|N\beta\rangle = \frac{t^{N-1}\Theta_p(t)}{(p;p)_\infty^3}H_N(q^{-1},t^{-1},p)\prod_{j=1}^N\phi(p;x_j)|N\beta\rangle. \tag{1.6}$$

2 Related topics

The author is interested in the following materials :

- Relation to the elliptic Feigin-Odesskii algebra, commutative family of the elliptic Macdonald operator.
- An elliptic analog of the q-Virasoro algebra.
- Vertex operator representations of the BC type elliptic q-hypergeometric integrals and superconformal indices.
- Partition functions of six dimensional theories, an elliptic analog of the Nekrasov partition function.

References

[1] Yosuke Saito. *Elliptic Ding-Iohara Algebra and the Free Field Realization of the Elliptic Macdonald Operator.* (2013) arXix:1301.4912.

P-55

Hasse principle for the Chow groups of zero-cycles on quadric fibrations

Kazuki Sato, D1

Department of Mathematics, Tohoku University

1. Introduction

Given a polynomial equation $f(x_1, \ldots, x_n) = 0$ with $\mathbb{Q}$-coefficients, if it has a rational solution $(x_1, \ldots, x_n) \in \mathbb{Q}^n$, then it has a p-adic solution for all primes p and a real solution. If the converse is true, then we say that the Hasse principle holds. For quadratic forms, it is known that the Hasse principle holds, i.e. for $f = a_1x_1^2 + a_2x_2^2 + \cdots + a_nx_n^2$, $f = 0$ has a nontrivial solution over p-adic field $\mathbb{Q}_p$ for all primes p and over the real number field $\mathbb{R}$, then it has a nontrivial solution over the rational number field $\mathbb{Q}$.

Since the reduced norm of $\alpha = x + yi + zj + wk \in A$ is $N_{\mathrm{red}}(\alpha) = x^2 + ay^2 + bz^2 + abw^2$ for a quaternion algebra $A = (-a, -b)_{\mathbb{Q}}$, there exists an isomorphism $A \cong \mathrm{M}_2(\mathbb{Q})$ if and only if $A \otimes_{\mathbb{Q}} \mathbb{Q}_p \cong \mathrm{M}_2(\mathbb{Q}_p)$ for all primes p and $A \otimes_{\mathbb{Q}} \mathbb{R} \cong \mathrm{M}_2(\mathbb{R})$. The same argument holds for any central simple algebras. This is equivalent to say that the global-to-local map for the Brauer groups $\mathrm{Br}(\mathbb{Q}) \to \bigoplus_p \mathrm{Br}(\mathbb{Q}_p) \oplus \mathrm{Br}(\mathbb{R})$ is injective.

2. Chow Group of Zero-cycles on a Quadric Fibration

For an algebraic variety X, a *zero-cycle* on X is a formal finite sum $\Sigma n_P[P]$ of points $P \in X$ with rational integer coefficients $n_P \in \mathbb{Z}$. All zero-cyles on X forms an infinitely generated free abelian group. But it is conjectured that for a smooth projective variety X over a number field, the group $\mathrm{CH}_0(X)$ of zero-cycles modulo rational equivalence on X is a finitely generated abelian group. The group $\mathrm{CH}_0(X)$ is called the *Chow group of zero-cycles on* X.

Let k be a finite extension of $\mathbb{Q}$, and Ω be the set of all places of k. For $v \in \Omega$, k_v denotes the completion of k at v. Let C be a smooth projective geometrically connected curve over k, X be a proper geometrically integral variety over k, and $\pi : X \to C$ be a proper dominant morphism. Then we have the global-to-local map for the Chow groups of zero-cycles:

$$\Phi : \mathrm{CH}_0(X/C) \longrightarrow \prod_{v\in\Omega} \mathrm{CH}_0(X \otimes_k k_v/C \otimes_k k_v),$$

where $\mathrm{CH}_0(X/C)$ is the kernel of the induced map $\pi_* : \mathrm{CH}_0(X) \to \mathrm{CH}_0(C)$.

$\pi : X \to C$ is a *quadric fibration* if the generic fiber of π is a smooth projective quadric hypersurface.

Parimala and Suresh showed that if the generic fiber of a quadric fibration $\pi : X \to C$ is defined by a Pfister neighbour quadratic form of rank ≥ 5 (in this case, $\dim X \geq 4$), then $\operatorname{Ker}\Phi = 0$. Using this result, they showed the Chow group $\mathrm{CH}_0(X)$ on X is a finitely generated abelian group.

Theorem (Hasse principle for the Chow group)

Let $\pi : X \to C$ be a quadric fibration over a number field k. Assume that $\dim X = 2$ or 3, and the generic fiber of π is isomorphic to a quadric defined over k (i.e. there exists a quadric $Q \subset \mathbb{P}^N_k$ such that the generic fiber is isomorphic to $Q \otimes_k k(C)$ over $k(C)$). Then we have $\operatorname{Ker}\Phi = 0$.

- Without the assumption that the generic fiber is defined over k, $\operatorname{Ker}\Phi \neq 0$ in general.
- It is known that $\mathrm{CH}_0(X/C)$ is finite in the above case.

3. Global-to-Local Map Restricted to Real Places

Over a function field with one variable over a p-adic field, any quadratic form of rank ≥ 9 has a nontrivial zero (Parimala-Suresh 2010, D.B. Leep 2012). Therefore, when the generic fiber is Pfister neighbour of rank ≥ 5, Parimala and Suresh's result ($\operatorname{Ker}\Phi = 0$) is equivalent to the injectivity of the following map:

$$\Phi_{\mathrm{real}} : \mathrm{CH}_0(X/C) \longrightarrow \bigoplus_{v:\text{real places}} \mathrm{CH}_0(X \otimes_k k_v/C \otimes_k k_v).$$

Proposition

Let C be the elliptic curve over $\mathbb{Q}$ defined by the affine equation $y^2 = -x(x+2)(x+3)$. Assume that the generic fiber of a quadric fibration $\pi : X \to C$ is defined by the quadratic form $q = x_1^2 - 2x_2^2 + 3x_3^2 - 6x_4^2$. Then $\operatorname{Ker}\Phi_{\mathrm{real}} \neq 0$.

The above form q is a Pfister form, and does not have nontrivial zeros over $\mathbb{Q}_2$ and $\mathbb{Q}_3$. q has a nontrivial zero over $\mathbb{R}$ and $\mathbb{Q}_p$ for all primes p except 2 and 3.

P-56

Local existence and blow-up criterion for the compressible Navier-Stokes-Yukawa equations in Besov spaces

Noboru Chikami (sb0m23@math.tohoku.ac.jp)

Mathematical Institute, Tohoku University

The 5th GCOE International Symposium "Weaving Science Web beyond Particle-Matter Hierarchy"

1 Introduction

We study the compressible Navier-Stokes-Yukawa system:

$$
\text{(NSY)}\quad \begin{cases} \partial_t\rho + \mathrm{div}(\rho u) = 0, & (t,x)\in\mathbb{R}^+\times\mathbb{R}^N,\\ \partial_t(\rho u) + \mathrm{div}(\rho u\otimes u) + \nabla P(\rho) & \\ \quad = \mu\Delta u + (\mu+\lambda)\nabla\mathrm{div}\ u + \rho\nabla\psi, & (t,x)\in\mathbb{R}^+\times\mathbb{R}^N,\\ -\Delta\psi + \psi = \rho - \bar\rho, & (t,x)\in\mathbb{R}^+\times\mathbb{R}^N,\\ u(0,x)=u_0,\ \rho(0,x)=\rho_0, & x\in\mathbb{R}^N, \end{cases}
$$

where $N\geq 2$, describing the motion of a nuclear matter.

$\rho(t,x):\mathbb{R}^+\times\mathbb{R}^N\to\mathbb{R}$: density
$u(t,x):\mathbb{R}^+\times\mathbb{R}^N\to\mathbb{R}^N$: velocity
$\psi(t,x):\mathbb{R}^+\times\mathbb{R}^N\to\mathbb{R}$: Yukawa potential
$P(\rho)=\rho^\alpha,\ \alpha\geq 1$: pressure
$\mu,\ \lambda$: Lamé constant, $\mu>0,\ \lambda+\mu>0$
$\bar\rho>0$: a physical constant

Under assumptions that the density ρ is bounded away from 0 and tends to some positive constant at infinity, the *specific volume* $a = a(t,x)$ is well-defined by $a := \rho^{-1}-1$. Solving the self-consistent third equation for ψ, then the equations for (a,u) is writen as follows:

$$
\begin{cases} \partial_t a + u\cdot\nabla a = (1+a)\mathrm{div}u,\\ \partial_t u + u\cdot\nabla u - (1+a)\mathcal{L}u + \nabla(Q(a)) = -\nabla(Id-\Delta)^{-1}\dfrac{a}{1+a} + f,\\ u(0,x)=u_0,\ a(0,x)=a_0. \end{cases}
$$

Here, we denote $\mathcal{L}=\mu\Delta+(\lambda+\mu)\nabla\mathrm{div}$ and $Q(a) := -\int_0^t \frac{P'((1+z)^{-1})}{(1+z)^2}dz.$

2 Critical argument

The compressible barotropic Navier-Stokes system (CNS in short hereafter), which is simply (NSY) without the potential term, has the following scaling property:

$$
\begin{cases} \rho_\nu(t,x) := \rho(\nu^2 t,\nu x)\\ u_\nu(t,x) := \nu u(\nu^2 t,\nu x), \end{cases}\quad \nu>0.
$$

provided the pressure term has been changed accordingly.

Definition 1 (Critical space of (NSY))**.**

$$
a\in L^\infty(0,T;B^{\frac{N}{p}}_{p,1}),\ u\in L^\infty(0,T;B^{\frac{N}{p}-1}_{p,1}).
$$

Let $\{\Phi,\phi_j\}_{j\geq1}$ be inhomogeneous Littlewood-Paley decomposition.

Definition 2. $s\in\mathbb{R},\ 1\leq p\leq\infty,\ 1\leq\sigma<\infty$.

$$
B^s_{p,\sigma}(\mathbb{R}^N) := \{u\in\mathcal{S}';\ \|u\|_{B^s_{p,\sigma}}<\infty\}
$$
$$
\|u\|_{B^s_{p,\sigma}} := \|\Phi * u\|_{L^p} + (\sum_{j\geq1}2^{js\sigma}\|\phi_j * u\|^\sigma_{L^p})^{\frac{1}{\sigma}},\quad 1\leq\sigma<\infty
$$

3 Known results

(CNS) $N\geq2$, critical Besov space $\dot B^{\frac{N}{2}}_{2,1}\times\dot B^{\frac{N}{2}-1}_{2,1}$, unique local sol., R. Danchin, 2007,
$N\geq2$, critical inhomogeneous Besov space $B^{\frac{N}{p}}_{p,1}\times B^{\frac{N}{p}-1}_{p,1}$, unique local sol., B. Haspot, 2010.

(NSY) The derivation of the hydrodynamical model, B. Ducomet, 2001.

4 Results

Theorem 1. *Let $N\geq2$, $1<p<2N$, and the pressure term P be given by a suitably smooth function of the specific volume a. Assume that the initial data satisfy $a_0\in B^{\frac{N}{p}}_{p,1}$, $u_0\in B^{\frac{N}{p}-1}_{p,1}$ and $f\in L^1_{loc}(\mathbb{R}^+;B^{\frac{N}{p}-1}_{p,1})$ with $1+a_0\geq\underline{a}>0$.*

(1) *Then, there exists a positive time $T>0$ such that system (1) has a solution (ρ,u,ψ) satisfying*

$$
(a,u,\psi)\in C([0,T);B^{\frac{N}{p}}_{p,1})\times\left(L^1(0,T;B^{\frac{N}{p}+1}_{p,1})\cap C([0,T);B^{\frac{N}{p}-1}_{p,1})\right)^N \times C([0,T);B^{\frac{N}{p}+2}_{p,1}).
$$

Furthermore there exists some constant $C(\underline{a})>0$ depending only on $\underline{a}$ such that for all $(t,x)\in[0,T)\times\mathbb{R}^N$, $1+a(t,x)>C(\underline{a})$.

(2) *Moreover if p satisfies*

$$
1<p\leq N \text{ when } N\geq3 \quad \text{or } p=2 \text{ when } N=2,
$$

the solution (a,u,ψ) is unique.

Remark 1. The function space

$$
(\rho-\bar\rho,u)\in C([0,T);B^{\frac{N}{p}}_{p,1})\times\left(L^1(0,T;B^{\frac{N}{p}+1}_{p,1})\cap C([0,T);B^{\frac{N}{p}-1}_{p,1})\right)^N
$$

is scale-critical if one only looks at the high frequency part of the functions. In other words, we need stronger assumptions on the low frequency of the solution to control the potential term .

Theorem 2. *Let $1<p<N$. If the solution of* (1)

$$
(a,u,\psi)\in C([0,T);B^{\frac{N}{p}}_{p,1}\times(B^{\frac{N}{p}-1}_{p,1})^N\times B^{\frac{N}{p}+2}_{p,1})
$$

satisfies

(i) $a\in L^\infty(0,T;B^{\frac{N}{p}}_{p,1})$, $1+a\geq\exists\underline{a}>0$,

(ii) either

(1) $u\in L^{\frac{2}{1-\alpha}}(0,T;\dot B^{-\alpha}_{\infty,\infty})$ $(-1<\alpha<1)$ *or*

(2) $\|\nabla u\|_{\dot B^0_{\infty,\infty}}\log(e+\|\nabla u\|_{\dot B^0_{\infty,\infty}})\in L^1(0,T)$,

then (a,u,ψ) may be continued beyond T.

Remark 2. The condition (3) corresponds to the Beale-Kato-Majda blow-up criterion for the Euler equations.

5 Key estimate

$$
\text{(LPV)}\quad \begin{cases} \partial_t u - (1+a)\mathcal{L}u = -u\cdot\nabla u + h,\\ u(0,x)=u_0(x). \end{cases}
$$

Proposition 3. $N\geq2$, $1<p<\infty$, $\frac{N}{p}\geq s>0$. *Let $a\in L^\infty(0,T;B^{\frac{N}{p}}_{p,1})$ with $1+a\geq\underline{b}$, and u be the solution of* (LPV). $\Rightarrow^\exists$ *some constant C^* (depending on N, s, p, μ, λ, T, $\|u_0\|_{B^s_{p,1}}$, $\|h\|_{L^1(0,T;B^s_{p,1})}$ and $\|u\|_{L^{\frac{2}{1-\alpha}}(0,T;\dot B^{-\alpha}_{\infty,\infty})}$ $(|\alpha|<1)$ or $\int_0^T\|\nabla u\|_{\dot B^0_{\infty,\infty}}\log(e+\|\nabla u\|_{\dot B^0_{\infty,\infty}})dt$) such that we have for all $t\in[0,T]$,*

$$
\|u\|_{\widetilde{L^\infty_t(B^s_{p,1})}}\leq C^*.
$$

P-57

The solution of the Homogeneous Complex Monge-Ampère equation corresponding to a geodesic in the space of Kähler metrics

Kenta Tottori
Department of Mathematics, Tohoku University

0 Introduction

The notion of a geodesic in the space of Kähler metrics was introduced by T. Mabuchi. It is important to study the geodesic because it is related to the existence and uniqueness problem of constant scalar curvature Kähler metrics. For example, X. X. Chen-G. Tian proved the uniqueness by using the geodesic.

1 Preliminaries

M : compact complex manifold of complex dimension m
ω : Kähler form on M
In a local coordinate system $(z^1, \cdots, z^m)$, ω has an expression:

$$\omega = \sqrt{-1}\sum_{\alpha,\beta=1}^{m} g_{\alpha\bar\beta}\, dz^\alpha \wedge d\bar z^\beta.$$

Fix a Kähler form ω.

Lemma 1 ($\partial\bar\partial$-Lemma)
M : compact Kähler manifold
α : exact real (p, p)-form on M
Then there is a real $(p-1, p-1)$-form β such that

$$\alpha = \sqrt{-1}\partial\bar\partial\beta.$$

For any Kähler form $\omega' \in [\omega]$, there exists a smooth real function φ on M such that

$$\omega' = \omega + \sqrt{-1}\partial\bar\partial\varphi$$

- If $\omega + \sqrt{-1}\partial\bar\partial\varphi_1 = \omega + \sqrt{-1}\partial\bar\partial\varphi_2$, then $\varphi_2 = \varphi_1 + c$ for some $c \in \mathbb{R}$

We define a functional I on $C^\infty(M)$ as follows

$$I(\varphi) = \frac{1}{\mathrm{vol}M}\sum_{p=0}^{m}\frac{1}{(p+1)!(m-p)!}\int_M \varphi\omega^{m-p}(\sqrt{-1}\partial\bar\partial\varphi)^p$$

where $\mathrm{vol}M = \int_M \omega^m/m!$.
For any constant c, $I(\varphi + c) = I(\varphi) + c$

Consider the space of Kähler metrics

$$\mathcal{H}_0 = \{\varphi \in C^\infty(M) \mid I(\varphi) = 0,\ \omega_\varphi = \omega + \sqrt{-1}\partial\bar\partial\varphi \text{ is Kähler form}\}$$

For $\omega_\varphi = \sqrt{-1}\sum_{\alpha,\beta=1}^{m} g_{\varphi,\alpha\bar\beta}\, dz^\alpha \wedge d\bar z^\beta$, we set $(g_\varphi^{\alpha\bar\beta}) = (g_{\varphi,\alpha\bar\beta})^{-1}$

Definition 2 (A geodesic in the space of Kähler metrics)
$\varphi_t(x) = \varphi(t, x) \in C^\infty([0,1]\times M)$ such that $\varphi_t \in \mathcal{H}_0$
We say φ_t is a geodesic in $\mathcal{H}_0$ if

$$\varphi_t'' - |\partial\varphi_t'|^2_{\varphi_t} = 0$$

where φ_t', φ_t'' denote the partial derivatives of φ_t with respect to t and

$$|\partial\varphi_t'|^2_{\varphi_t} = \sum_{\alpha,\beta=1}^{m} g_{\varphi_t}^{\alpha\bar\beta}\frac{\partial\varphi_t'}{\partial z^\alpha}\frac{\partial\varphi_t'}{\partial\bar z^\beta}$$

2 HCMA equation associated with a geodesic

$\Sigma = \{\tau \in \mathbb{C} \mid 0 \le \mathrm{Re}\,\tau \le 1\}$
φ_t : a curve in $\mathcal{H}_0$ $(0 \le t \le 1)$
For φ_t, we set

$$\Phi(\tau, x) = \varphi_{\mathrm{Re}\,\tau}(x) \qquad (\tau, x) \in \Sigma \times M$$

Proposition 3

$$\varphi_t \text{ is a geodesic} \iff (p^*\omega + \sqrt{-1}\partial\bar\partial\Phi)^{m+1} = 0 \quad \text{on } \Sigma\times M,$$

where $p : \Sigma \times M \to M$ is a natural projection.

We study the following problem

Problem 4
Suppose given smooth functions $F_k : \mathbb{R}\times M \to \mathbb{R}$ $(k = 0, 1)$ such that $F_k(s, \cdot) \in \mathcal{H}_0$ for all $s \in \mathbb{R}$.
Find a smooth function $\Phi : \Sigma \times M \to \mathbb{R}$ such that

$$(p^*\omega + \sqrt{-1}\partial\bar\partial\Phi)^{m+1} = 0 \quad \text{on } \Sigma\times M$$
$$\Phi(\sqrt{-1}s, \cdot) = F_0(s, \cdot)$$
$$\Phi(1 + \sqrt{-1}s, \cdot) = F_1(s, \cdot)$$
$$\Phi(\tau, \cdot) \in \mathcal{H}_0 \qquad \forall\tau \in \Sigma$$

3 MA foliation

$T^{1,0}(\Sigma\times M)$: holomorphic tangent bundle over $\Sigma \times M$
For a solution Φ of Problem 4,

$$\ker(p^*\omega + \sqrt{-1}\partial\bar\partial\Phi) = \{X \in T^{1,0}(\Sigma\times M) \mid (p^*\omega + \sqrt{-1}\partial\bar\partial\Phi)(X, \cdot) = 0\}$$

defines a foliation $\mathcal{F}_\Phi$ on $\Sigma \times M$.

$\mathcal{F}_\Phi$ is called the Monge-Ampère foliation associated with Φ.

Since $\Phi(\tau, \cdot) \in \mathcal{H}_0$, each leaf of $\mathcal{F}_\Phi$ is a Riemann surface.

4 Complexification of (M, ω)

$\pi : T^{1,0*}M \to M$ holomorphic cotangent bundle over M
For a Kähler form ω, there is a complex structure $\widetilde{J}$ on $T^{1,0*}M$ and closed nondegenerate holomorphic 2-form $\Theta = \Theta_1 + \sqrt{-1}\Theta_2$ such that

- $i_0(M) \subset T^{1,0*}M$ is totally real submanifold where i_0 is the zero section
- For the section $s_\varphi = \partial\varphi : M \to T^{1,0*}M$ defined by $\varphi \in \mathcal{H}_0$,

$$s_\varphi^*(\Theta_1) = 0, \quad s_\varphi^*(\Theta_2) = \omega + \sqrt{-1}\partial\bar\partial\varphi$$

Let $\mathcal{W}_\omega$ denote the complex manifold $T^{1,0*}M$ equipped with $\widetilde{J}$.
$(\mathcal{W}_\omega, \Theta)$ is called the complexification of (M, ω).

5 Main theorem

$\{g_x\}_{x\in M}$: a family of smooth functions from Σ to $\mathcal{W}_\omega$ parametrized by $x \in M$
We define $\gamma_\tau : M \to \mathcal{W}_\omega$ by

$$\gamma_\tau(x) = g_x(\tau)$$

and $H : \Sigma \to \mathbb{R}$ by

$$H(\tau) = \int_M |\gamma_\tau^*(\Theta_1)|^2\omega^m$$

where $|\,|$ is the norm defined by ω.
For each $\varphi \in \mathcal{H}_0$, we denote Λ_φ the image of $s_\varphi : M \to \mathcal{W}_\omega$.

Main theorem
Assume $H^1(M, \mathbb{R}) = 0$. Problem 4 has a solution Φ if and only if there is a family of holomorphic functions $g_x : \Sigma \to \mathcal{W}_\omega$ parametrized by $x \in M$ satisfying following conditions;

1. $\pi(g_x(0)) = x$
2. *For each* $x \in M$
$$g_x(\tau) \in \begin{cases}\Lambda_{F_0(s,\cdot)} & \tau = \sqrt{-1}s\\ \Lambda_{F_1(s,\cdot)} & \tau = 1 + \sqrt{-1}s\end{cases}$$
3. *For each* $\tau \in \Sigma$, *map* $x \mapsto \pi(g_x(\tau))$ *is a diffeomorphism from* M *to* M.
4. *There are positive constants* $C > 0$ *and* $R > 0$ *such that*
   - $e^{\pi\mathrm{Im}\,\tau}H(\tau) < C$ *for any* $\tau \in \Sigma$ *satisfying* $\mathrm{Im}\,\tau > R$
   - $e^{-\pi\mathrm{Im}\,\tau}H(\tau) < C$ *for any* $\tau \in \Sigma$ *satisfying* $\mathrm{Im}\,\tau < -R$

P-58

Ultracontractivity for Markov semigroups and quasi-stationary distributions

Yusuke Miura
Mathematical Institute, Tohoku University
(mail: sb0m32@math.tohoku.ac.jp)

Notation

- E : locally compact separable metric space
- X_t : m-symmetric Hunt process
- $L^p(m) := \{f : \int_E |f|^p \, dm < \infty\}$
- $\{T_t\}$: the transition semigroup of X_t

A probability measure μ is a quasi-stationary distribution (QSD) of X_t

$\overset{\text{def}}{\Longleftrightarrow}$ $\mathbb{P}_\mu(X_t \in B \mid t < \zeta) = \mu(B), \ {}^\forall t > 0$

Assumption

(a) The transition density $p_t(\cdot, \cdot)$ exists,

i.e., $T_t f(x) = \int_E f(y) p_t(x, y) m(dy)$

(b) ${}^\exists \lambda > 0, \ {}^\exists \phi \in L^2(m)$: ground state

i.e., $T_t \phi(x) = e^{-\lambda t} \phi(x)$

X_t : intrinsically ultracontractive (IU)

$\overset{\text{def}}{\Longleftrightarrow}$ ${}^\forall t > 0, \ {}^\exists \alpha_t, \beta_t > 0$ s.t.,

$$\alpha_t \leq \frac{p_t(x, y)}{\phi(x)\phi(y)} \leq \beta_t, \quad x, y \in E$$

Remark $\{T_t\}$: IU $\Rightarrow \phi \in L^1(m)$

Key lemma

Assume $m(E) < \infty$ and $\{T_t\}$: conservative.

Then for ${}^\forall f \in L^1(E; m)$,

$$\lim_{t \to \infty} T_t f(x) = (m(E))^{-1} \int_E f \, dm, \quad m\text{-a.e.}$$

Theorem

$$T_t : \text{IU} \Rightarrow \mu(B) := \frac{\int_B \phi \, dm}{\int_E \phi \, dm} \quad \text{is a QSD of } X_t$$

(proof) $\displaystyle T_t^\phi f(x) := \frac{e^{\lambda t}}{\phi(x)} T_t(\phi f)(x)$

$\Rightarrow \{T_t^\phi\}$: semigroup on $L^2(\phi^2 m)$ satisfying the assumption in Key lemma

$$\lim_{t \to \infty} \frac{\mathbb{P}_x(X_t \in B; t < \zeta)}{\mathbb{P}_x(t < \zeta)} = \lim_{t \to \infty} \frac{T_t^\phi (1_B/\phi)(x)}{T_t^\phi (1/\phi)(x)} \underset{\substack{\uparrow \\ \text{Key lemma}}}{=} \frac{\int_B \phi \, dm}{\int_E \phi \, dm} = \mu(B)$$

$\Rightarrow \mu$ is a QSD.

Example

Logistic model : $dZ_t = \sqrt{Z_t} \, dB_t + r(Z_t - K Z_t^2) \, dt, \quad Z_0 = z > 0$

Set $X_t := 2\sqrt{Z_t} \xrightarrow{\text{Itô's formula}} dX_t = dB_t - q(X_t) \, dt \quad \left(q(u) = \dfrac{1}{2u} - \dfrac{ru}{2} + \dfrac{rKu^3}{8} \right)$

$\rightsquigarrow X_t$: diffusion on $(0, \infty)$ with the *speed measure* m and the *scale function* s

where $dm(x) = e^{-Q(x)} dx, \quad s(x) = \displaystyle\int_1^x e^{Q(u)} \, du \quad \left(Q(x) = 2 \int_1^x q(u) \, du \right)$

$\Downarrow$ classify boundary points

0 : *exit boundary*, ∞ : *entrance boundary* ($\Rightarrow X_t$ satisfies Assumption (a), (b))

$\Downarrow$ check Tomisaki's condition $\cdots$ [a sufficient condition for IU in terms of the speed measure and the scale function]

X_t : IU $\Rightarrow$ A QSD of Z_t exists

Generalized modal dependence logic

Shota Murakami
Mathematical institute (E-mail: sb0m33@math.tohoku.ac.jp)

1. Modal logic

1. syntax
Var := the set of propositional variables
symbols: $\{\vee, \neg, \Box\} \cup$ **Var**
formula: p ($p \in$ **Var**) :: $A \vee B$ :: $\neg A$ :: $\Box A$

2. semantics
assignment : function form **Var** to $\{T, F\}$
Kripke frame (M, R) : M is a set of assignments, R is a binary relation on M
Let (M, R) be a Kripke frame, $s \in M, A$ be a formula.
We define a relation $\mathbf{s} \models \mathbf{A}$ (A is true in s) as usual.
In case of $\Box A$,

$$\mathbf{s} \models \Box\mathbf{A} \text{ iff } \forall s' \in M((s, s') \in R \to s' \models A)$$

Intuitive meaning of Kripke frame

M : a set of worlds
R: accessibility relation
$s \models \Box A$: A is true in all futures of the world s

A is **valid in (M,R)** iff $\forall s \in M$ ($s \models A$)
A is **valid** iff $\forall (M, R)$ (A is valid in (M, R))

Completeness theorem for modal logic(Kripke1959)
For every formula A,

A is valid $\Leftrightarrow$ A is provable.

A logic has **finite model property** iff

[A is valid $\Leftrightarrow$ A is valid in some finite Kripke frame.]

As a corollary of the completeness theorem, we can prove finite model property for modal logic.

Theorem

Modal logic has finite model property.

2. (Generalized) modal dependence logic

1.dependence
Let (M, R) be a Kripke frame, $X \subset M$ and $p, q \in$ **Var**.
we define a new formula **dep**(p, q) as follows.

$$X \models \mathbf{dep}(p, q) \Leftrightarrow \forall s, s' \in X(s(p) = s'(p) \to s(q) = s'(q))$$

(the truth value of q is depend on that of q w.r.t. X)

2. syntax
(1) Modal dependence logic (**MDL**)
symbols: $\{\vee, \neg, \Box\} \cup$ **Var** $\cup \{\mathbf{dep}_n : n \in \omega\}$
formula: modal formulas :: $\mathbf{dep}_n(p_0, ..., p_{n-1}, p_n)$

(2) Generalized modal dependence logic (**GMDL**)
symbols: {symbols of MDL} $\cup \{\sqcup, \sim\}$
formula:MDL-formulas:$\mathbf{dep}_n(A_0, ..., A_{n-1}, A_n)$:$A \sqcup B$:$\sim A$

3. semantics
Let (M, R) be a Kripke frame and $X \subset M$.

$X \models p \Leftrightarrow \forall s \in X(s(p) = T)$
$X \models \neg p \Leftrightarrow \forall s \in X(s(p) = F)$
$X \models A \vee B \Leftrightarrow \exists Y, Z(X = Y \cup Z \wedge Y \models A \wedge Z \models B)$
$X \models \neg(A \vee B) \Leftrightarrow X \models \neg A \wedge X \models \neg B$
$X \models \neg\neg A \Leftrightarrow X \models A$
$X \models \Box A \Leftrightarrow R[X] \models A$
$(R[X] := \{s' \in M : \exists s \in X((s, s') \in R)\})$
$X \models \neg\Box A \Leftrightarrow \exists Y(\forall x \in X \exists y \in Y((x, y) \in R) \wedge Y \models \neg A)$
$X \models \mathbf{dep}_n(A_0, ..., A_{n-1}, A_n) \Leftrightarrow$
$[\forall s, s' \in X(\{s\} \models A_i \Leftrightarrow \{s'\} \models A_i \ (\forall i < n)]$
$\Rightarrow (\{s\} \models A_n \Leftrightarrow \{s'\} \models A_n)$
$X \models A \sqcup B \Leftrightarrow X \models A \vee X \models B$
$X \models \sim A \Leftrightarrow X \not\models A$

4.validity
A is **true in (M, R, X)** iff $X \models A$
A is **valid in (M, R)** iff $\forall X \subset M$(A is true in (M, R, X))
A is **valid** iff $\forall (M, R)$ (A is valid in (M, R))

Theorem

GMDL has finite model property.

3. Open problems

Open problem 1

Are there any good proof systems to prove completeness theorem for MDL (also for GMDL)?

In 2009, Sevenster proved that satisfiability problem of MDL is NEXPTIME-complete.

Open problem 2

What is the comutational complexity of satisfiablity for GMDL?

Open problem 3

What is the computational complexity of validity for MDL (GMDL)?

Asymptotic error distributions of the Crank-Nicholson scheme for SDEs driven by fractional Brownian motion

Nobuaki Naganuma
Mathematical Institute, Tohoku University

1 Introduction

We consider the following 1-dim SDE:

$$\begin{cases} dX_t = \sigma(X_t)\, d^\circ B_t, & t \in (0,1], \\ X_0 = x_0, \end{cases}$$

where B is a 1-dim. fBm on $(\Omega, \mathcal{F}, P)$ with the Hurst parameter $0 < H < 1$. The solution is expressed by $X_t = \phi(x_0, B_t)$.

Remark 1. FBm B is a conti. centered Gaussian proc. with

$$E[B_s B_t] = \frac{1}{2}(s^{2H} + t^{2H} - |s-t|^{2H})$$

for some $0 < H < 1$. Note that

- B is a Bm if $H = 1/2$, else B is NOT a semimartingale.
- B is $(H - \epsilon)$-Hölder continuous.

The Crank-Nicholson scheme $\{\hat{X}^{(m)}\}_{m=1}^{\infty}$ is defined by the solution to the equation:

$$\begin{cases} \hat{X}_0^{(m)} = x_0 \\ \hat{X}_t^{(m)} = \hat{X}_{k2^{-m}}^{(m)} + \dfrac{1}{2}\left(\sigma\left(\hat{X}_t^{(m)}\right) + \sigma\left(\hat{X}_{k2^{-m}}^{(m)}\right)\right)(B_t - B_{k2^{-m}}), \\ \qquad\qquad\qquad t \in (k2^{-m}, (k+1)2^{-m}]. \end{cases}$$

2 Main theorem

Assumption 2. Assume $1/3 < H < 1/2$ and

$$\sigma \in C_{\mathrm{bdd}}^{\infty}(\mathbb{R};\mathbb{R}), \qquad \sup|\sigma'| > 0, \qquad \inf|\sigma| > 0.$$

Theorem 3 (N). *Under Assumption 2, we have*

$$\lim_{m\to\infty}\left(B, 2^{m(3H-1/2)}(\hat{X}^{(m)} - X)\right) = \left(B, \sigma(X_\cdot)\cdot c_{3,H}\int_0^\cdot f_3(X_s)\, dW_s\right)$$

weakly in $\mathcal{D}([0,1];\mathbb{R}^2)$, where $c_{3,H} > 0$, $f_3 = (\sigma^2)''/24$, and W is a standard Brownian motion independent of B.

3 Proof

We have 5 steps in order to prove the main theorem.

3.1 Analysis of the Hermite variations

Let $q \geq 2$ and $f \in C_{\mathrm{poly}}^{2q}(\mathbb{R};\mathbb{R})$. Put

$$G_q^{(m)}(t) = 2^{-m/2}\sum_{k=0}^{\lfloor 2^m t\rfloor - 1}\frac{f(B_{(k+1)2^{-m}}) + f(B_{k2^{-m}})}{2} \times H_q(2^{mH}\triangle B_{k2^{-m}}),$$

where H_q denotes the q-th Hermite polynomial.

Proposition 4 (N). *If $1/2q < H < 1 - 1/2q$, then we have*

$$\lim_{m\to\infty}(B, G_q^{(m)}) = \left(B, c_{q,H}\int_0^\cdot f(B_s)\, dW_s\right)$$

weakly in weakly in $\mathcal{D}([0,1];\mathbb{R}^2)$.

3.2 Expression of the Crank-Nicholson sheme

Proposition 5 ([1]). *Under Assumption 2, $\hat{X}^{(m)}$ satisfies*

$$\begin{aligned}\hat{X}_{k2^{-m}}^{(m)} &= \phi\left(x_0, B_{k2^{-m}} + U_{k2^{-m}}^{(m)}\right) \\ &= X_{k2^{-m}} + \sigma(X_{k2^{-m}})U_{k2^{-m}}^{(m)} + O((U_{k2^{-m}}^{(m)})^2),\end{aligned}$$

where $U^{(m)}$ is defined by $U_0^{(m)} = 0$ and

$$\begin{aligned}U_{(k+1)2^{-m}}^{(m)} = U_{k2^{-m}}^{(m)} &+ f_3\left(\hat{X}_{k2^{-m}}^{(m)}\right)(\triangle B_{k2^{-m}})^3 \\ &+ f_4\left(\hat{X}_{k2^{-m}}^{(m)}\right)(\triangle B_{k2^{-m}})^4 + O\left((\triangle B_{k2^{-m}})^5\right)\end{aligned}$$

where $f_3 = (\sigma^2)''/24$ and $f_4 = \sigma(\sigma^2)'''/48$.

3.3 Decomposition into the main term and the remainders

Proposition 6 (N). *Under Assumption 2, we have the expansion, for every $\alpha \geq 1$,*

$$U^{(m)} = \sum_{\beta=1}^{\alpha}\Phi^{(m,\beta)} + O(2^{m(\alpha+1)}(\triangle B)^{3(\alpha+1)}),$$

where $\Phi^{(m,1)}$ is definde by $\Phi_0^{(m,1)} = 0$ and

$$\begin{aligned}\Phi_{(k+1)2^{-m}}^{(m,1)} = \Phi_{k2^{-m}}^{(m,1)} &+ f_3(X_{k2^{-m}})(\triangle B_{k2^{-m}})^3 \\ &+ f_4(X_{k2^{-m}})(\triangle B_{k2^{-m}})^4,\end{aligned}$$

and, for $\beta \geq 2$, $\Phi^{(m,\beta)}$ is also defined explicitly.

3.4 Convergence of the main term

Proposition 7 (N). *Under Assumption 2, we have*

$$\lim_{m\to\infty}(B, 2^{m(3H-1/2)}\Phi^{(m,1)}) = \left(B, c_{3,H}\int_0^\cdot h(B_s)\, dW_s\right)$$

weakly in $\mathcal{D}([0,1];\mathbb{R}^2)$.

Proof. Put $h(\eta) = f_3(\phi(x_0,\eta))$. Then we have

$$2^{m(3H-1/2)}\Phi^{(m,1)} = 2^{-m/2}\sum_{k=0}^{\lfloor 2^m\cdot\rfloor - 1}\left(h(B_{k2^{-m}}) + \frac{1}{2}h'(B_{k2^{-m}})\right)(2^{mH}\triangle B_{k2^{-m}})^3$$

Using the Taylor formula, $\xi^3 = H_3(\xi) + 3\xi$ and Proposition 4, we have the assertion. □

3.5 Convergence of the remainders

By long calculation, we have $\Phi^{(m,\beta)} \to 0$ for $\beta \geq 2$.

References

[1] I. Nourdin. A simple theory for the study of SDEs driven by a fractional Brownian motion, in dimension one. In *Séminaire de probabilités XLI*, volume 1934 of *Lecture Notes in Math.*, pages 181–197. Springer, Berlin, 2008.

Homothetic Solution to Curve Shortening Flow

Abdullah Kizilay
Mathematical Institute, Tohoku University
sa9m39@math.tohoku.ac.jp

Preliminaries

As a background of studying geometric flows, the simplest one is the curve shortening flow, given by one-parameter family of closed curves in the plane (t is time and σ is curve parameter),

$$\gamma_t(\sigma) : [0,T) \times [0,1] \to \mathbb{R}^2, \text{ such that } \gamma_t(0) = \gamma_t(1)$$

Let N be unit normal vector, and κ is the curvature, then the evolution law $\frac{d\gamma_t(\sigma)}{dt} = \kappa N$ is called the curve shortening flow(CSF).

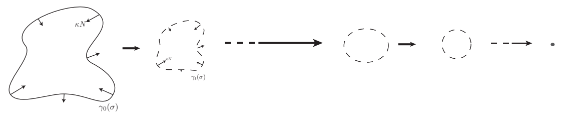

Background of study

Following two results characterize the curve shortening flow(CSF) for embedded, closed initial curves:

- M. Gage and R. Hamilton [1]: Let $\gamma_0(\sigma)$ be a closed, convex curve, then the evolution law preserves convexity and shrinks to a point in a finite time.
- M. Grayson [2] showed that any closed, embedded curves become convex before it shrinks to a point

Aim

According to Abresch and Langer's [3] study, we present curve shortening flow for plane curves which are not necessarily embedded, and these curves evolve by homothety.

Modification of usual curve shortening flow

In [3], the curve shortening flow is modified by adding tangential field hT to kN in the evolution law, with this modification; flow is geometrically unchanged but this helps us to maintain the constant speed

Let M be 2-manifold and let $\gamma_t(\sigma) : [0,T) \times \mathbb{R}/\mathbb{Z} \to M$ be an evolving curve according to

$$\boxed{\frac{\partial \gamma}{\partial t} = hT + kN}$$

where $\sigma \in \mathbb{R}/\mathbb{Z}$ is the curve parameter, and $t \in [0,T)$ is the time parameter, N is the unit normal vector and k is the curvature.

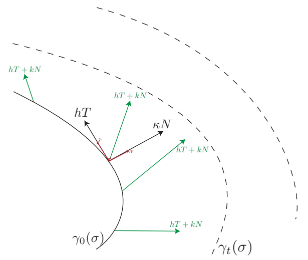

★ Following Proposition shows that the modified CSF has constant speed $\alpha = \left|\frac{\partial \gamma_t}{\partial \sigma}\right|$ along each curves γ_t .

Proposition-1

Let M be 2-manifold, $\gamma_t(\sigma)$ and evolves according to $\partial\gamma/\partial t = hT + kN$, then $\gamma_t(\sigma)$ has constant speed if and only if $\gamma_0(\sigma)$ has constant speed and h satisfies

$$\frac{h'}{\alpha} = k^2 - \int_0^1 k^2 d\sigma \,.$$

Geometry of Normalized Curve Shortening Flow

In terms of new time parameter τ satisfying $\frac{dt}{d\tau} = \alpha^2$, we define the Normalized flow:

$$\frac{\partial \gamma}{\partial \tau} = \alpha^2 (hT + kN)$$

The quantities of interest for us are speed of the curve $\alpha(\tau)$ and evolution equation for the curvature $k(\sigma,\tau)$.

$\alpha(\tau)$ (speed of the curve) evolves:

$$\frac{\partial \alpha}{\partial \tau} = -\alpha^3 \int_0^1 k^2 d\sigma$$

evolution equation for the curvature $k(\sigma,\tau)$;

$$\boxed{\frac{\partial k}{\partial \tau} = \frac{\partial^2 k}{\partial \sigma^2} + \alpha h \frac{\partial k}{\partial \sigma} + \alpha^2 k^3 + \alpha^2 k R|_{\gamma}}$$

Frenet equations take the following form:

$$\left.\begin{aligned} \frac{\partial T}{\partial s} &= kN \\ \frac{\partial N}{\partial s} &= -kT \end{aligned}\right\}$$

where s is arc-lenght parameter which implies

$$\frac{\partial}{\partial s} = \frac{1}{\alpha}\frac{\partial}{\partial \sigma}$$

Moreover, derivative with respect to s and t are related by

$$\frac{\partial}{\partial t}\frac{\partial}{\partial s} = \frac{\partial}{\partial s}\frac{\partial}{\partial t} - \left(\frac{h'}{\alpha} - k^2\right)\frac{\partial}{\partial s} + R\left(T, \frac{\partial \gamma}{\partial t}\right)$$

where R is the curvature operator on M.

Homothetic solution & main result

Contracting a homothetic solution of normalized CSF is a flow in which the shapes of the curves change homothetically and continuously to a point in finite time, which is called also contracting self-similar curve (the circle is a contracting self-similar curve). Moreover, other such curves must have self-intersections. In fact, all closed homothetically evolving curves classified by Abresch and Langer and it is represented in the following:

Proposition-2

A constant speed parametrized closed curve $\gamma : \mathbb{R}/\mathbb{Z} \to \mathbb{E}^2$ represents a homothetic solution of CSF if and only if its normalized curvature function κ (where $\kappa(\sigma,\tau) = \alpha(\tau)k(\sigma,\tau)$) obeys;

$$\frac{\partial \kappa}{\partial \sigma} = \kappa' = -\beta\kappa \quad \text{and} \quad \frac{\partial \beta}{\partial \sigma} = \beta' = \kappa^2 - \lambda^2 \qquad (★)$$

where $\beta(\sigma,\tau)$ is an auxiliary function satisfies $\beta(\sigma,\tau) = \alpha(\tau)h(\sigma,\tau)$, and $0 < \lambda \in \mathbb{R}$.

Reformulation

Using (★) equations, we obtain $\kappa = \lambda e^{-\int \beta}$

$\Downarrow$

rewriting κ as; $\kappa = \lambda e^{P/2}$ with $\beta = -\frac{1}{2}P'$

substituting in (★), we obtain

$$\boxed{\begin{aligned} &P'' + 2\lambda^2(e^P - 1) = 0 \\ &P = 2log\left(\frac{\kappa}{\lambda}\right) \end{aligned}}$$

Theorem (Abresch - Langer)

Let $\gamma : \mathbb{R}/\mathbb{Z} \to \mathbb{E}^2$ be a unit speed closed curve representing a homothetic solution of the curve shortening flow, then γ is an m-covered circle or γ is a member of family of transcendental curves $\{\gamma_{m,n}\}$ having the following description: if m, n are positive integers satisfying $1/2 < m/n < \sqrt{2}/2$, there is a unique unit speed curve $\gamma_{m,n} : \mathbb{R}/\mathbb{Z} \to \mathbb{E}^2$ a solution to the equations

$$P'' + 2\lambda^2(e^P - 1) = 0\,, \qquad P = 2log\left(\frac{\kappa}{\lambda}\right) \qquad \text{for some constant } \lambda \,.$$

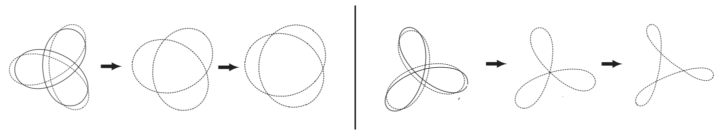

References:

[1] M. Gage and R. Hamilton, The heat equation shrinking of convex plane curves, J. Differential Geometry 23 (1986) 69-96.
[2] M. A. Grayson, The heat equation shrinks embedded plane curves to round points, J. Differential Geom. 26 (1987), no. 2, 285–314.
[3] U. Abresch and J. Langer, The normalized curve shortening flow and homothetic solutions, J. Differential Geometry 23 (1986) 175-196.

P-62

Final state problem for the quadratic nonlinear Schrödinger system with mass resonance

Kota Uriya (sa9m05@math.tohoku.ac.jp)

Mathematical Institute, Tohoku University, Japan

The 5th GCOE international Symposium on "Weaving Science Web beyond Particle-Matter Hierarchy"
March 4 - March 6, 2013.

Introduction

We study the following nonlinear Schrödinger system:

$$\text{(2-NLS)}\quad \begin{cases} i\partial_t u_1 + \dfrac{1}{2m_1}\Delta u_1 = \gamma \overline{u}_1 u_2, \ t \in \mathbb{R},\ x \in \mathbb{R}^2, \\ i\partial_t u_2 + \dfrac{1}{2m_2}\Delta u_2 = u_1^2, \qquad t \in \mathbb{R},\ x \in \mathbb{R}^2, \end{cases}$$

where $u_1(t,x),\ u_2(t,x) : \mathbb{R}\times\mathbb{R}^2 \to \mathbb{C}$; unknown complex valued functions. m_1, m_2 are positive constants, $\gamma = \pm 1$.

L^2-conservation law $(\gamma = 1)$

$$\|u_1(t)\|_{L^2}^2 + \|u_2(t)\|_{L^2}^2 = \textit{constant} \quad \text{for all } t \in \mathbb{R}.$$

Final state condition

We impose a final state condition:

$$\left\|(u_1(t), u_2(t)) - (u_{1a}(t), u_{2a}(t))\right\|_{L^2} \to 0 \text{ as } t \to \infty,$$

where each u_{ja} is defined by a given function $u_{j+} \in H^2$.

Known results

(1) Single nonlinear Schrödinger equation:

$$\text{(NLS)}\qquad i\partial_t u + \frac{1}{2m}\Delta u = |u|^{p-1}u, \quad t \in \mathbb{R},\ x \in \mathbb{R}^2.$$

- $p > 2 : u(t) \sim e^{\frac{it}{2m}\Delta}u_+$ as $t \to \infty$.
- $p \le 2 : u(t) \not\sim e^{\frac{it}{2m}\Delta}u_+$ as $t \to \infty$.
  (Barab ('84), Y. Tsutsumi-Yajima ('84))
- $p = 2 : u(t) \sim e^{\frac{it}{2m}\Delta}e^{iS(t,-i\nabla)}u_+$ as $t \to \infty$.
  $S(t,\xi) := -m|\hat{u}_+(\xi)|\log t$.
  (Ozawa ('91), Ginibre-Ozawa ('93))

(2) (2-NLS) with $2m_1 = m_2$ (mass resonance condition)

Let $\omega(\xi) > 0$ and $\theta(\xi)$ be given real-valued functions.

(i) In the case of $\gamma = 1$:

$$\begin{cases} \varphi_{1\gamma}(t) = \omega(\xi)e^{i\theta(\xi)+\frac{i}{\sqrt{2}}\omega(\xi)\log t}, \\ \varphi_{2\gamma}(t) = -\dfrac{1}{\sqrt{2}}\omega(\xi)e^{2i\theta(\xi)+i\sqrt{2}\omega(\xi)\log t}. \end{cases}$$

(ii) In the case of $\gamma = -1$:

$$\begin{cases} \varphi_{1\gamma}(t) = -\dfrac{i\omega(\xi)e^{i\theta(\xi)}}{1+\omega(\xi)\log t}, \\ \varphi_{2\gamma}(t) = -\dfrac{i\omega(\xi)e^{2i\theta(\xi)}}{1+\omega(\xi)\log t}. \end{cases}$$

Hayashi-Li-Naumkin [1] showed the existence of the solution to (2-NLS) taking each u_{ja} as

$$u_{ja} = -e^{\frac{it}{2m_j}\Delta}\mathcal{F}^{-1}D(m_j)\varphi_{j\gamma} \sim iM_j(t)D(t)\varphi_{j\gamma},$$

where $D(t)\phi := \frac{1}{it}\phi\left(\frac{x}{t}\right)$, $M_j(t)\phi := e^{\frac{im_j|x|^2}{2t}}\phi$.

Main result

Let $\omega(\xi) > 0$ and $\theta(\xi)$ be given real-valued functions.

$$(*)\qquad \begin{cases} \varphi_1(t,\xi) = \operatorname{sech}(\omega(\xi)\log t)\omega(\xi)e^{i\theta(\xi)}, \\ \varphi_2(t,\xi) = -i\tanh(\omega(\xi)\log t)\omega(\xi)e^{2i\theta(\xi)}. \end{cases}$$

Theorem

$2m_1 = m_2$, $\gamma = 1$. *There exist $\varepsilon > 0$ with the following property: Let $\omega(\xi) > 0$ and $\theta(\xi)$ be given real-valued functions which satisfy ω, $\theta \in H^2(\mathbb{R}^2)$, $\|\omega\|_{H^2} \le \varepsilon$. Then (2-NLS) has a unique global solution $(u_1,u_2) \in (C(\mathbb{R};L^2)\cap L^q(\mathbb{R};L^r))^2$ satisfies*

$$\sum_{j=1}^{2}\left\|u_j(t) + e^{\frac{it}{2m_j}\Delta}\mathcal{F}^{-1}D(m_j)\varphi_j\right\|_{L^2} \to 0 \text{ as } t \to \infty$$

where (φ_1,φ_2) is given by $(*)$ and $\frac{2}{q} = \frac{n}{2} - \frac{n}{r}$, $2 \le q \le \infty$, $(q,r) \ne (2,\infty)$.

Remark

(1) For the asymptotic profile of u_1, we have

$$\|u_{1a}(t)\|_{L^2} \to 0 \text{ as } t \to \infty.$$

(2) A similar result was obtained by Katayama-Matoba -Sunagawa [2] for a quadratic nonlinear wave system:

$$\begin{cases} \Box w_1 = -(\partial_t w_1)(\partial_t w_2), & t \in \mathbb{R}, x \in \mathbb{R}^3, \\ \Box w_2 = (\partial_t w_1)^2, & t \in \mathbb{R}, x \in \mathbb{R}^3, \end{cases}$$

where $\Box := \partial_t^2 - \Delta$.

Outline of the Proof of Theorem

Putting $v_j := D\left(\frac{1}{m_j}\right)\mathcal{F}e^{-\frac{it}{2m_j}\Delta}u_j(t)$, (2-NLS) leads to the following approximate nonlinear ODE system :

$$\begin{cases} i\partial_t v_1(t) = \gamma\dfrac{1}{t}\overline{v}_1 v_2 + R_1(t), \\ i\partial_t v_2(t) = \dfrac{1}{t}v_1^2 + R_2(t), \end{cases}$$

where $R_1(t)$ and $R_2(t)$ are errors. Finally, we prove

$$\Phi_1(u_1,u_2)(t) = -e^{\frac{it}{2m_1}\Delta}\mathcal{F}^{-1}D(m_1)\varphi_1 + i\int_t^\infty e^{\frac{i(t-\tau)}{2m_1}\Delta}\left(\overline{u}_1 u_2 + \frac{1}{t}e^{\frac{i\tau}{2m_1}\Delta}\mathcal{F}^{-1}D(m_1)\overline{\varphi_1}\varphi_2\right)d\tau$$

is contraction on

$$X_{\rho,T} := \left\{u \in (C([T,\infty);L^2)\cap L^q(T,\infty;L^r))^2; \|u-u_a\|_X \le \rho\right\}$$

where $u(t) = (u_1,u_2)$,

$$u_a(t) = (u_{1a},u_{2a}) := \left(-e^{\frac{it}{2m_1}\Delta}\mathcal{F}^{-1}D(m_1)\varphi_1, -e^{\frac{it}{2m_2}\Delta}\mathcal{F}^{-1}D(m_2)\varphi_2\right)$$

and

$$\|v\|_X := \sum_{j=1}^{2}\sup_{t\in[T,\infty)} t^\beta\left\{\|v_j\|_{L^\infty(t,\infty;L^2)} + \|v_j\|_{L^q(t,\infty;L^r)}\right\}$$

for $1/2 < \beta < 1$, small $\rho > 0$ and large $T > 0$.

Reference

[1] N. Hayashi, C. Li, P. I. Naumkin, *Modified wave operator for a system of nonlinear Schrödinger equations in 2d*, Comm. Partial Differential equations **37** (2012), 947-968.

[2] S. Katayama, T. Matoba, H. Sunagawa, *A semilinear hyperbolic system violating the null condition*, preprint.

Homogeneous Reinhardt domains containing the origin in the comlex 3-space

Kouichi Kimura

Mathematical Institute,Tohoku University

Algebraic isomorphisms

An analytic automorphism $(z_i) \longmapsto (w_i)$ of $(\mathbb{C}^*)^n$ is called an algebraic automorphism, if whose components are given by Laurent monomials, that is, of the form

$$w_i = \alpha_i \, z_i{}^{a_{i1}} \cdots z_n{}^{a_{in}} \qquad (1 \leq i \leq n)$$

where $(a_{ij}) \in GL(n, \mathbb{Z})$ and $(\alpha_i) \in (\mathbb{C}^*)^n$.

Suppose D_1 and D_2 are domains in $\mathbb{C}^n$ and an analytic isomorphism $\varphi : D_1 \longmapsto D_2$ is induced by an algebraic automorphism. Then the isomorphism φ is said to be an algebraic isomorphism, and two domains D_1, D_2 are called algebraically equivalent. This fact is denoted by $D_1 \overset{alg}{\cong} D_2$.

Bounded Reihardt domains

A domain D in $\mathbb{C}^n$ is called a Reinhardt domain, if it is stable under rtations around the coodinate axis. And D is called homogeneous, if it admits a transitive action of $\mathrm{Aut}(D)$ which is holomorphic automophism groups on D. We interested in the classification of homogeneous Reinhardt domains by algebraic equivalence relation. When D is bounded, by the well-known H.Cartan theorem, $\mathrm{Aut}(D)$ has the structere of a Lie group with respect to compact-open topology. By means of this fact, following result is shown.

Therem 1. Let D be a bounded Reinhardt domain in $\mathbb{C}^n$. If D is homogeneous, then $D \overset{alg}{\cong} B_{n_1} \times \cdots \times B_{n_k}$ where B_{n_i} denotes the unit ball in $\mathbb{C}^{n_i}$.

Homogeneous Reinhardt domains

Unfortunately it is difficult to generalize Theorem 1 in unbounded Reinhardt domains, because in such a case we cannot use the classical Cartan theorem. But the classification is conjectured to be as follows:

Conjecture For a homogeneous Reinhardt domain D in $\mathbb{C}^n$, there exist integers $n_1, \cdots, n_k$ but k may be 0, and non-negative integers l, m with $n_1 + \cdots + n_k + l + m = n$ such that $D \overset{alg}{\cong} B_{n_1} \times \cdots \times B_{n_k} \times \mathbb{C}^l \times (\mathbb{C}^*)^m$.

Wen D is unbounded, this conjecture is still open. The next result in my master's thesis is a partial answer in the unbounded case.

Theorem 2. Let D be a pseudoconvex Reinhardt domain in $(\mathbb{C}^*)^n$. If D is homogeneous, then D is coinside with $(\mathbb{C}^*)^n$.

It is expected that homogeneity implies pseudoconvexity in Reinhardt domains. But it is not proved at this moment.

Current study

Now We reseach on the conjecture under the opposite condition of Theorem 2, that is, D contains the origin. In addition, for the sake of simplicity, let the space dimension be 3. Then we proved the following:

Theorem 3. Let D be a unbounded proper Reinhardt domain containing the origin in $\mathbb{C}^3$. If D is homogeneous , then D is algebraic equivalent to one of three canonical domains so that $B_1 \times \mathbb{C}^2$, $B_1 \times B_1 \times \mathbb{C}$, $B_2 \times \mathbb{C}$.

The notion of Liouville foliation, which was introduced by Shimizu in order to analize unbounded Reinhardt domains, play a key role for the proof of Theorem 3.

Definition Let M be a complex manifold. Let $f_1, \cdots .f_m$ be bounded holomorphic functions on M, and $g_1, \cdots, g_n$ be bounded plurisubharmonic (psh.) functions on M. Then a mapping $\varphi_{m,n} = (f_1, \cdots .f_m, g_1, \cdots, g_n)$ is called a Liouville mapping on M.

A collection $\{\Sigma_\alpha\}_{\alpha \in A}$ of subsets of M is called a Liouville foliation on M if the following conditions are satisfied:

(L1) If $\alpha_1 \neq \alpha_2$, then $\Sigma_{\alpha_1} \cap \Sigma_{\alpha_2} = \phi$;

(L2) $\bigcup_{\alpha \in A} \Sigma_\alpha = M$;

(L3) For each Σ_α, any bounded psh. function on M takes a constant value on Σ_α;

(L4) For every $\alpha_1, \alpha_2 \in A$ with $\alpha_1 \neq \alpha_2$, there exists a pair of integers (m, n) and a Liouville mapping $\varphi_{m,n}$ on M such that the constant values of $\varphi_{m,n}$ on Σ_{α_1} and Σ_{α_2} are different.

The important thing is that following:

First, any complex manifold has at most one structure of Liouville foliation, which may contain singular leaves, and it is invariant under holomorphic isomorphisms.

Secondaly, In most cases, we classified Liouville forliations that are defined on unbounded proper Reinhardt domains containing the origin in $\mathbb{C}^3$.

Theorem 3 follows from the two facts mentioned above.

On some results for covering systems of congruences

Rena Tateda
Mathematical Institute, Tohoku University

March 5th, 2013

1 Definition

Definition 1. A system of congruences

$$a_{i0} + \sum_{j=1}^{k} a_{ij} x_j \equiv 0(\mathrm{mod} m_i) \quad (1 \le i \le n) \tag{1}$$

is called *covering system* if every $\boldsymbol{x} = [x_1, ..., x_k] \in \mathbb{Z}^k$ satisfies one of the congruences of the system. Such a system is called *regular* if it has no proper subsystem which is a covering system.

Definition 2. The set of integers $M = \{m_1, ..., m_n\}$ is *good* if there exist a_{ij}'s $\in \mathbb{Z}$ such that $\{a_{i0} + \sum_{j=1}^{k} a_{ij} x_j \equiv 0(\mathrm{mod} m_i)\}$ is covering system. We say that m_i is *helpful* in M if $M \backslash \{m_i\}$ is bad but M is good.

2 General covering system

Here are principal result concerning covering systems for $\mathbb{Z}^k$.

Theorem 3. (Novak, Znam, Crittenden)

1. M is good $\Rightarrow \sum_{i=1}^{n} 1/m_i \ge 1$.
2. the r-th congruence is essential and $m_r = \prod_{\tau=1}^{s} p_\tau^{\alpha_\tau}$ $\Rightarrow n \ge 1 + \sum_{\tau=1}^{s} \alpha_i (p_\tau - 1)$.
3. If a system of the form (1) covers a k-dim cube $C_k \subset \mathbb{Z}^k$ with the side length 2^n, then it's a covering one.

For the *homogeneous covering system* (i.e. $a_{i0} = 0$ for all i), we shall obtain the stronger form and analogue of Thm3.

Theorem 4. (Analogues for homogeneous covering systems)
For a given prime q dividing $\prod_{i=1}^{n} m_i$ and a given $\gamma > 0$, let $n_\gamma := \#\{i; q^\gamma \,\|\, m_i\}$, $\alpha = \min_{n_\gamma \ne 0} \gamma$, $\beta = \max_{n_\gamma \ne 0} \gamma$.

1. $\sum_{\eta=\alpha}^{\beta} n_\eta / q^\eta \ge 1$.
2. the r-th congruence is essential $\Rightarrow n \ge 1 + \sum_{\tau=1}^{s} \{\alpha_\tau (p_\tau - 1) + 1\}$.
3. ($n \ge 2$) If a homogeneous system covers $C_k \subset \mathbb{Z}^k$ with the side length 2^{n-1} and $\mathbf{0} = [0, ..., 0] \in C_k$, then it's a covering one.
($n \ge 5$) If a homogeneous system covers $C_k \subset \mathbb{Z}^k$ with the side length 2^{n-1}, then it's a covering one.

Remark 5. The following example shows that 2^{n-1} cannnot be replaced by $2^{n-1} - 1$ in Thm4:

$$\begin{aligned} y &\equiv 0 \text{ (mod2)}, \\ x + 2^i y &\equiv 0(\text{mod} 2^{i+1}), \quad 0 \le i \le n-2. \end{aligned}$$

Moreover, for $n \le 4$ the assertion of Thm4 doesnot hold. The following systems cover the segment $< 2 >, < 2, 4 >, < 2, 6 >, < 2, 10 >$ of the length:$1, 3, 5, 9$, respectively.

$$\begin{aligned} x &\equiv 0(\text{mod}2); \\ x &\equiv 0(\text{mod}2), 0(\text{mod}3); \\ x &\equiv 0(\text{mod}2), 0(\text{mod}3), 0(\text{mod}5); \\ x &\equiv 0(\text{mod}2), 0(\text{mod}3), 0(\text{mod}5), 0(\text{mod}7); \end{aligned}$$

(Actually, using the estimate for the Jacobsthal function, we could replace 2^{n-1} by $2, 4, 6$ or 10 for $n = 1, 2, 3, 4$, respectively.)

3 An algorithm for testing a set of integers for goodness

We consider the following decision problem for $k = 1$. For answering this problem, we construct an algorithm for testing for goodness.

Covering system

Instance :A multiset of integers $\{m_1, ..., m_n\}$.

Question :Do there exist integers $a_1, ..., a_n$ such that

$$\{x \equiv a_1(\text{mod} m_1), ..., x \equiv a_n(\text{mod} m_n)\}$$

is a covering system?

Algorithm Moduli
input $M := \{m(1), ..., m(n)\}$;
If $1/m(1) + ... + 1/m(n) < 1$ **then output** "No", **stop**;
compute $L := \mathrm{lcm}\{m(1), ..., m(n)\}$;
compute prime factorization of $L := p(1)\hat{}a(1) * ... * p(s)\hat{}a(s)$;
if $s == 1$ **then output** "Don't know", **stop**;
for $i = 1$ to s
  sum := 0;
for $j = a(i)$ to 1 step -1
    compute sum := sum + $p(i)\hat{}(a(i) - j)|\{m \in M : p(i)\hat{}j \mid m, p(i)\hat{}(j+1) \nmid m\}$
    if sum $< p(i)\hat{}(a - j + 1)$ **then call** Moduli($M \backslash \{m \in M : p(i)\hat{}j \mid m\}$), **stop**;
  end;
end;
for $i := 1$ to s;
  $M0 := \{m \in M : p(i) \nmid m\}$
  $M1 := \{m \in M : p(i) \mid m\}$
  Good_Partition_Found := false;
  for each $p(i)$-partition $M1$: $D(1) \cup ... \cup D(p(i))$ of $M1$
    if Moduli($M0 \cup \{d/p(i) : d \in D(k)\}$) =="Don't know" for all $k \in \{1, ..., p(i)\}$
      then Good_Partition_Found := true;
    end;
  if Good_Partition_Found == false **then output** "No", **stop**;
  end;
  output "Don't know";
end;

The correctness of the algorithm follows from Thm3 and the following theorem.

Theorem 6. Write $M = M_0 \cup M_1$ where the members of M_1 are divisible by p and those of M_0 are not. If M is good, then there exists a partition of $M_1 = D_1 \cup ... \cup D_p$ such that $M_0 \cup \{d/p : d \in D_i\}$ is good for each choice of $i \in \{1, ...p\}$.

Unfortunately this algorithm cannot give a positive answer: its output is either "No" or "Don't know". But considering the sets which returned "Don't know" as output, we could show that no regular and composite covering systems exist with fewer that 20 moduli.

References

1. J. Fabrykowski, *Multidimensional covering systems of congruences*, 1984.

P-65

On the formal groups arising from algebraic varieties

Tomonori Nakayama
Mathematical Institute, Tohoku University

Formal Group Law

Let R be a commutative ring with the identity.
Let $X = (x_1, x_2, ..., x_g)$ and $R[[X]]$ be the ring of formal power series with coefficients in R.

$$F(X,Y) = (F_1(X,Y), ..., F_g(X,Y)),\ F_i(X,Y) \in R[[X,Y]]$$

is a formal group law over R if

$$F(Z,0) = F(0,Z) = Z$$
$$F(F(X,Y),Z) = F(X,F(Y,Z))$$

Examples of (a one-parameter) Formal Group Law

The additive formal group law:

$$\mathbb{G}_a(x,y) = x + y$$

The multiplicative formal group law:

$$\mathbb{G}_m(x,y) = (x+1)(y+1) - 1$$

For $f(x) \in R[[x]]$ such that $f(x) = ex + \cdots$ (e is a unit in R), $F(x,y) = f^{-1}(f(x) + f(y)) \in R[[x,y]]$ is a formal group law over R. $f(x)$ is called the logarithm of $F(X,Y)$.

Elliptic Curve

An elliptic curve E over a field K is a nonsingular projective cubic curve, defined over K, with a K-rational point. $P = (x_1, \cdots, x_n)$ is a K-rational point if $\forall i, x_i \in K$. We write $P \in E(K)$.
An elliptic curve over $\mathbb{Q}$ can be expressed in Weierstrass form $\acute{E}$:

$$\acute{E} : y^2 + a_1xy + a_3y = x^3 + a_2x^2 + a_4x + a_6 (a_i \in \mathbb{Q})$$

and by taking the minimal model of $\acute{E}$, a_i will be in $\mathbb{Z}$.
In general, a line through E meets E at 3 points. By using this fact, we can define an addition on an elliptic curve and the points on E form a group. This addition can be expressed as a formal group law (the method I).

Honda's Theorem(1968)

Let E be an elliptic curve over $\mathbb{Q}$, E_w be the Weierstrass minimal model of E, $E_p = E_w \mod p$ for a prime number p, and $E(x,y)$ be the formal group law(I) given by the group law of E. For each prime number p, L_p is defined as:

$$L_p = \begin{cases} (1 - a_pp^{-s} + p^{1-2s})^{-1} & \text{if } E_p \text{ is of genus one;} \\ (1 - \varepsilon_pp^{-s})^{-1} & \text{if } E_p \text{ has an ordinary double point;} \\ 1 & \text{if } E_p \text{ has a cusp.} \end{cases}$$

where $a_p = p + 1 - \#E(\mathbb{F}_p)$, and $\varepsilon_p = 1$ if the tangents at the double point are rational over $\mathbb{F}_p$ and $\varepsilon_p = -1$ if not. We define

$$\sum_{n=1}^{\infty} a_nn^{-s} = \prod_{p \in S} L_p(s)$$

$$l(x) = \sum_{n=1}^{\infty} n^{-1}a_nx^n$$

$$L(x,y) = l^{-1}(l(x) + l(y)).$$

Let S be any set of prime numbers which does not contain 2 (resp. 3) if E_2 (resp. E_3) has genus one with $a_2 = \pm 2$ (resp. $a_3 = \pm 3$), and $\mathbb{Z}_S = \bigcap_{p \in S}(\mathbb{Z}_p \cap \mathbb{Q})$. Then

$$L(x,y) \text{ is a formal group law(the method II) over } \mathbb{Z}$$

$$L(x,y) \cong E(x,y) \quad \text{over } \mathbb{Z}_S$$

*The restriction about S is removed by his paper in 1970.
In this theorem, there are two ways of the construction of a formal group law, (I) and (II).

Formal Group

For a ring R, let $\mathfrak{Nilalgs}_R$ be the category of nil-R-algebras, i.e. the ideals of nilpotent elements of R-algebras. Formal affine n-space over R is the functor

$$\mathbb{A}^n_R : \mathfrak{Nilalgs}_R \to \mathfrak{Sets}$$

which assigns to a nil-R-algebra A the set A^n and to the morphism f the map $\prod^n f$.
An n-dimensional formal group over R is a functor

$$G : \mathfrak{Nilalgs}_R \to \mathfrak{Ab.groups}$$

such that $F_{or} \circ G \cong \mathbb{A}^n_R$, where F_{or} is the forgetful functor.

(e.g.) If $F(X,Y)$ is a formal group law over a commutative ring R, a commutative nil-R-algebra A inherits a group structure from F by $a +_F b = F(a,b)$ for $a, b \in A$, where $F(a,b)$ is a convergent sum. So this induces a formal group.

Artin-Mazur Functor

Let R be a ring, X a scheme over R, $\mathcal{O}_X$ the structure sheaf on X and $i \in \mathbb{Z}_{\geq 0}$. Then we can construct $\mathbb{G}_{m,\mathcal{O}_X}$ and $H^i(X, \mathbb{G}_{m,\mathcal{O}_X})$ by

$$\begin{tikzcd}
\mathfrak{Nilalgs}_R \arrow[r, "\mathcal{O}_X\otimes_R"] \arrow[dr, "\mathbb{G}_{m,\mathcal{O}_X}(c)"] \arrow[ddr, "H^i(X{,}\mathbb{G}_{m,\mathcal{O}_X})(\text{commutes})"'] & \text{sheaves of nil-}R\text{-algebras on } X \arrow[d, "\mathbb{G}_m"] \\
& \text{sheaves of abelian groups on } X \arrow[d, "H^i"] \\
& \mathfrak{Ab.groups}
\end{tikzcd}$$

where $\mathcal{O}_X\otimes_R$ assigns to a nil-R-algebra A the sheaf $\mathcal{O}_X\otimes_R A$ associated with the presheaf (open U) $\mapsto \Gamma(U, \mathcal{O}_X)\otimes_R A$; $\mathbb{G}_m$ assigns to a sheaf $\mathfrak{A}$ of nil-R-algebras the sheaf of abelian groups $\mathbb{G}_m(\mathfrak{A})$ defined by $\Gamma(U, \mathbb{G}_m(\mathfrak{A})) = \mathbb{G}_m(\Gamma(U, \mathfrak{A}))$ for every open $U \subset X$; H^i is taking i-th cohomology.
We will write $\mathbb{G}_{m,X}$ instead of $\mathbb{G}_{m,\mathcal{O}_X}$. The functors $H^i(X, \mathbb{G}_{m,X})$ are called the Artin-Mazur functors.

Formal Group Law for some A-M Functors (Stienstra 1987)

Let R be a noetherian ring, F be a homogeneous polynomial in $R[T_0, \ldots, T_N]$ of degree $2d > 2N$ and let X be the double covering of $\mathbb{P}^N_R$ defined by $W^2 = F$ (W is a new variable of weight d). Then

$$H^N(X, \mathbb{G}_{m,X}) \text{ is a formal group over } R \text{ of dimension } n = \binom{d-1}{N}.$$

If R is flat over $\mathbb{Z}$, put
$J = \{i = (i_0, \ldots, i_N) \in \mathbb{Z}^{N+1} \mid i_0, \ldots, i_N \geq 1, i_0 + \cdots + i_N = d\}$.
Then there is a formal group law (the method III) for $H^N(X, \mathbb{G}_{m,X})$ with logarithm $l(\tau) = (l_i(\tau_j)_{j \in J})_{i \in J}$ given by

$$l_i(\tau) = \sum_{m \geq 1} \sum_{j \in J} m^{-1} \beta_{m,i,j} \tau_j^m$$

where

$$\beta_{m,i,j} = \begin{cases} 0 & \text{if } m \text{ is even;} \\ \text{the coefficient of } T_0^{mj_0 - i_0} \cdots T_N^{mj_N - i_N} \text{ in } F^{(m-1)/2} & \text{if } m \text{ is odd.} \end{cases}$$

*If $N = 1, d = 2$ and $F = T_0T_1^3 + aT_0^3T_1 + bT_0^4$, this is as same as the Weierstrass model of an elliptic curve $y^2 = x^3 + ax + b$. The logarithm $l(\tau)$ we get from this theorem is actually the logarithm of the standard group structure on the elliptic curve(I).

Perturbation of Dirichlet forms and stability of fundamental solutions

Masaki Wada *

March 4, 2013

1 Notions and Notations

The jump type Markov process on $\mathbb{R}^d$ describes the random motion of particle in the state space $\mathbb{R}^d$. We can characterize this by means of Dirichlet form $\mathscr{E}$ as follows:

$$\mathscr{E}(u,v) = \iint_{\mathbb{R}^d\times\mathbb{R}^d} (u(y)-u(x))(v(y)-v(x))J(x,y)dxdy.$$

Here $J(x,y)$ is a symmetric function and describes the frequency of jump from x to y. In particular, if $J(x,y) \asymp 1/|x-y|^{d+\alpha}$ holds for some $0<\alpha<2$, we call the associated Markov process α-stable-like. If $J(x,y) \asymp \exp(-m|x-y|)/|x-y|^{d+\alpha}$ holds for some $0<\alpha<2$ and $m>0$, we call the associated Markov process relativistic α-stable-like. In the sequel, we deal with these two kinds of jump Markov process.

2 Preceding Results

The transition density function $p(t,x,y)$ is one of the important notions in order to analyze Markov processes. This is the probability with which the particle in x at time 0 exists in y at time t. Moreover it is known that $p(t,x,y)$ coincides with the fundamental solution of $\partial u/\partial t = \mathscr{L}u$, where $\mathscr{L}$ is a non-local operator satisfying

$$\mathscr{E}(u,v) = -\int_{\mathbb{R}^d} \mathscr{L}u(x)v(x)dx.$$

Z. Q. Chen, P. Kim and T. Kumagai showed that $p(t,x,y)$ admits the two-sided estimates as follows:

$$C_1\phi(C_2t, C_3|x-y|) \le p(t,x,y) \le C_4\phi(C_5t, C_6|x-y|),$$

where ϕ is an appropriate function and C_i's are positive constants [1, 2].

3 Problem in Consideration

In the sequel we assume that the Markov process is transient, namely it holds that

$$G(x,y) := \int_0^\infty p(t,x,y) < \infty.$$

First we define some classes of small measure μ.

Definition 1. *(i) A measure μ is said to be in Kato class if it holds that*

$$\lim_{a\to 0} \sup_{x\in\mathbb{R}^d} \int_{|x-y|\le a} G(x,y)\mu(dy) = 0 \tag{1}$$

(ii) A Kato class measure μ is said to be Green tight if it holds that

$$\lim_{r\to\infty} \sup_{x\in\mathbb{R}^d} \int_{|y|>r} G(x,y)\mu(dy) = 0. \tag{2}$$

Here we consider the perturbation of Dirichlet form $\mathscr{E}$ by Green tight measure μ as follows:

$$\mathscr{E}^\mu(u,u) = \mathscr{E}(u,u) - \int_{\mathbb{R}^d} u^2 d\mu. \tag{3}$$

It is known that $\mathscr{E}^\mu$ (or corresponding operator $\mathscr{L}^\mu := \mathscr{L} + \mu$) also admits the fundamental solution $p^\mu(t,x,y)$. We consider the condition on μ under which $p^\mu(t,x,y)$ admits the same two sided estimates as $p(t,x,y)$ up to the choice of positive constants. We call this phenomenon stability of fundamental solution.

4 Main Result

The main result is the necessary and sufficient condition on μ for the stability of fundamental solution. The precise statement is as follows:

Theorem 2. *(W. 2012)*
Assume that the Green tight measure μ satisfies

$$\iint_{\mathbb{R}^d\times\mathbb{R}^d} G(x,y)\mu(dx)\mu(dy) < \infty.$$

Then the stability of fundamental solution holds if and only if

$$\inf\{\mathscr{E}(u,u) \mid u\in\mathscr{F}, \int_{\mathbb{R}^d} u^2 d\mu = 1\} > 1, \tag{4}$$

where $\mathscr{F}$ is the domain of the Dirichlet form $\mathscr{E}$.

Note that the formula (4) describes the smallness of measure μ compared with the initial Dirichlet form $\mathscr{E}$. Furthermore, this result is the same as that in Takeda [3], which deals with the same problem in the framework of transient Brownian motion.

References

[1] Chen, Z.-Q., Kumagai, T.: *Heat kernel estimates for stable-like processes on d-sets*, Stoc. Proc. Appli. 108, 27-62, (2003).

[2] Chen, Z.-Q., Kim, P., Kumagai, T.: *Global heat kernel estimates for symmetric jump processes*, Trans. Amer. Math. Soc. 363, 5021-5055, (2011).

[3] Takeda, M.: *Gaussian bounds of heat kernels for Schrödinger oeprators on Riemannian manifolds*, Bull. London Math. Soc. 39, 85-94, (2007).

*Mathematical Institute, Tohoku University. Mail: sb1d14@math.tohoku.ac.jp

Locator function for concentration points of solutions of a reaction-diffusion equation in heterogeneous media

Hiroko Yamamoto

Mathematical Institute, Tohoku University

1 Introduction

Consider the Neumann problem for a semilinear elliptic equation:

$$(1)\quad \begin{cases} \varepsilon^2 \mathcal{A}u - a(x)u + b(x)u^p + \delta\sigma(x) = 0 \ \&\ u(x) > 0 & \textbf{in} \quad \Omega, \\ \displaystyle\sum_{i,j=1}^{n} a_{ij}(x)\frac{\partial u}{\partial x_j}\nu_i = 0 & \textbf{on} \quad \partial\Omega, \end{cases}$$

where $\Omega \subset\subset \mathbb{R}^n$, $\partial\Omega \in C^\infty$, and ν denotes the unit outward normal to $\partial\Omega$; $\varepsilon > 0$ and $\delta \geq 0$ are sufficiently small; $\mathcal{A}u = \sum_{i,j=1}^n \partial/\partial x_i(a_{ij}(x)(\partial u)/\partial x_j)$ is uniformly and strictly elliptic; a_{ij}, a, b, $\sigma \in C^1(\overline{\Omega})$; $a(x)$ and $b(x)$ are strictly positive on $\overline{\Omega}$; $\sigma \geq 0$, $\|\sigma\|_{L^\infty(\Omega)} = 1$; the exponent p satisfies $1 < p < (n+2)/(n-2)$.

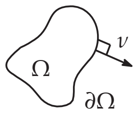

Known Result (Homogeneous Case)

(i.e. $a_{ij}(x) \equiv \delta_{ij}$, $a(x) = b(x) \equiv 1$, $\delta = 0$)

Consider the following single elliptic equation

$$\begin{cases} \varepsilon^2\Delta u - u + u^p = 0 \ \&\ u(x) > 0 & \text{in} \quad \Omega, \\ \partial u/\partial\nu \ = 0 & \text{on} \quad \partial\Omega. \end{cases}$$

$^\exists$ Ground state $u_\varepsilon(x) = w_0\left(\dfrac{x - P_\varepsilon}{\varepsilon}\right) + O(\varepsilon)$,

P_ε : max. pt. of u_ε,

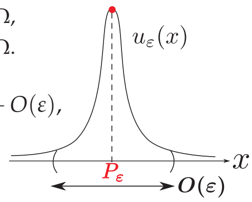

where w_0 is a unique solution of

$$\begin{cases} \Delta w_0 - w_0 + w_0^p = 0 \ \&\ w_0(y) > 0 & \text{in } \mathbb{R}^n, \\ w(0) = \max\limits_{y\in\mathbb{R}^n} w_0(y), \quad w_0(\infty) = 0, \end{cases}$$

and $w_0(y) = w_0(|y|)$ decays exponentially.

$$^\exists P_{\varepsilon_j} \to {}^\exists P_0 \quad (\varepsilon_j \downarrow 0).$$

Then P_0 is the maximum point of the mean curvature of $\partial\Omega$ ([1]). So, geometry of the domain determines the location of P_0.

Our Question: Where is P_0 in the heterogeneous case?

2 Preparations for generalization

First, there exists a **minimal solution** $u_{m,\varepsilon} = u_{m,\varepsilon}(x)$ of (1) obtained as the perturbation from $\delta = 0$ (i.e. $\|u_{m,\varepsilon}\|_{L^\infty(\Omega)} = O(\delta)$).

Definition 1. *An energy functional corresponding to* (1):

$$J_\varepsilon(u) := \frac{1}{2}\int_\Omega \left\{\varepsilon^2 \sum_{i=1}^{n} a_{ij}(x)\frac{\partial u}{\partial x_j}\frac{\partial u}{\partial x_i} + a(x)u(x)^2\right\} dx - \frac{1}{p+1}\int_\Omega b(x)u_+(x)^{p+1}\,dx - \int_\Omega \delta\sigma(x)u(x)\,dx.$$

For $\delta > 0$ we use an energy functional:

$$I_\varepsilon(v) := J_\varepsilon(u_{m,\varepsilon} + v) - J_\varepsilon(u_{m,\varepsilon}),$$

where $u, v \in H^1(\Omega)$, $u_+(x) := \max\{u(x), 0\}$.

By the MPL, $^\exists$a critical point $v_\varepsilon \in H^1(\Omega)$ of I_ε. We call $u_\varepsilon := u_{m,\varepsilon} + v_\varepsilon$ a **ground state solution** of (1).

Definition 2. *For $Q \in \overline{\Omega}$, define* **the primary locator function Φ** *by*

$$\boldsymbol{\Phi(Q) := a(Q)^{1-\frac{n}{2}+\frac{2}{p-1}} b(Q)^{-\frac{2}{p-1}} \left\{\det\left(a_{ij}(Q)\right)\right\}^{\frac{1}{2}}}.$$

Moreover, by calculating the energy I_ε, $^\exists I_0 > 0$: a const. s.t.

$$\lim_{\varepsilon\downarrow 0}\frac{1}{\varepsilon^n}I_\varepsilon(v_\varepsilon) = \min\left\{\frac{1}{2}\min_{Q\in\partial\Omega}\Phi(Q), \min_{Q\in\overline{\Omega}}\Phi(Q)\right\}\{I_0 - O(\delta)\}.$$

3 Main Results

Theorem 1. *Assume $u_{\varepsilon_j}(P_{\varepsilon_j}) = \max_{x\in\overline{\Omega}} u_{\varepsilon_j}(x)$, $P_{\varepsilon_j} \to P_0$ as $\varepsilon_j \downarrow 0$. Then: for sufficiently small δ,*

(i) $\min\limits_{Q\in\overline{\Omega}}\Phi(Q) < 1/2 \min\limits_{Q\in\partial\Omega}\Phi(Q)$

$\Rightarrow$ *$P_0 \in \Omega$. Moreover, $|P_0 - Q_0| = O(\delta)$, where $Q_0 \in \Omega$ is a global min. pt. of $\Phi(Q)$ over $\overline{\Omega}$.*

(ii) $\min\limits_{Q\in\overline{\Omega}}\Phi(Q) > 1/2 \min\limits_{Q\in\partial\Omega}\Phi(Q)$

$\Rightarrow$ *$P_0 \in \partial\Omega$. Moreover, $|P_0 - Q_0| = O(\delta)$, where $Q_0 \in \partial\Omega$ is a min. pt. of $\Phi(Q)$ over $\partial\Omega$.*

4 Examples of a concentration point P_0

Example 1. $n = 1$, $\Omega = (0,1)$, $p = 2$, $a_{ij}(x) \equiv \delta_{ij}$, $\delta = 0$.

$$\begin{cases} a(x) = x + 0.03, \\ b(x) = x + 0.01. \end{cases}$$

$\Rightarrow \Phi(x)^2 = a(x)^5 b(x)^{-4}$, $P_0 = 0.07$.

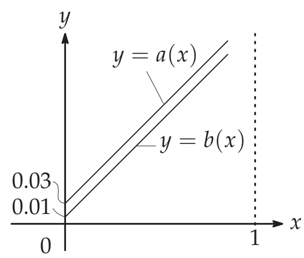

Observation:

For any linear functions $a(x)$, $b(x)$,

- In most cases $P_0 \in \partial\Omega = \{0, 1\}$,
- Even if P_0 is an interior pt. of $(0,1)$, P_0 must be very close to $x = 0$ or $x = 1$.

Example 2. $n = 2$, $\Omega = B_1(0)$, $a_{ij}(x) \equiv \delta_{ij}$, $a(x) \equiv b(x)$, $\delta > 0$.

$$\Rightarrow \Phi(Q) = a(Q)^{1-\frac{2}{2}+\frac{2}{p-1}} b(Q)^{-\frac{2}{p-1}} = a(Q)^{\frac{2}{p-1}} a(Q)^{-\frac{2}{p-1}} \equiv 1.$$

By (ii) of Theorem 1, $P_0 \in \partial B_1(0)$.

Where on the boundary?

We assume the graph of $\sigma(x)/a(x)$ is as in the figure on the right-hand side.

P_0 is in a nbd. of the max. pt. of $\sigma(x)/a(x)$ on $\partial\Omega$.

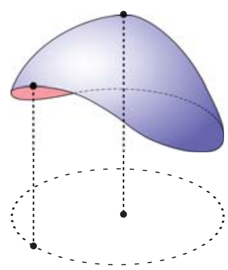

Graph of $\sigma(x)/a(x)$

Reference

[1] W.-M. Ni and I. Takagi, *Locating the peaks of least-energy solutions to a semilinear Neumann problem*, Duke Math. J. **67** (1993), 247–281.

On deformations of singularities of mixed polynomials

Kazumasa Inaba

(Mathematical Institute, Tohoku University, Sendai, Japan)

sb0d02@math.tohoku.ac.jp

Mixed polynomials

Let $f(\mathbf{z},\bar{\mathbf{z}})$ be a polynomial of variables $\mathbf{z}=(z_1,\dots,z_n)$ and $\bar{\mathbf{z}}=(\bar{z}_1,\dots,\bar{z}_n)$

$$f(\mathbf{z},\bar{\mathbf{z}}):=\sum_{\nu,\mu} c_{\nu,\mu}\mathbf{z}^{\nu}\bar{\mathbf{z}}^{\mu},$$

where $\mathbf{z}^{\nu}=z_1^{\nu_1}\cdots z_n^{\nu_n}$ for $\nu=(\nu_1,\dots,\nu_n)$ (resp. $\bar{\mathbf{z}}^{\mu}=\bar{z}_1^{\mu_1}\cdots\bar{z}_n^{\mu_n}$ for $\mu=(\mu_1,\dots,\mu_n)$). of this form is called a *mixed polynomial* [2].

Let $g(\mathbf{x},\mathbf{y})$ and $h(\mathbf{x},\mathbf{y})$ be real polynomials with variables $\mathbf{x}=(x_1,\dots,x_n)$ and $\mathbf{y}=(y_1,\dots,y_n)$. Then the real polynomial map $(g(\mathbf{x},\mathbf{y}),h(\mathbf{x},\mathbf{y})):\mathbb{R}^{2n}\to\mathbb{R}^2$ can be given a mixed polynomial as

$$f(\mathbf{z},\bar{\mathbf{z}}):=g\Big(\frac{\mathbf{z}+\bar{\mathbf{z}}}{2},\frac{\mathbf{z}-\bar{\mathbf{z}}}{2i}\Big)+ih\Big(\frac{\mathbf{z}+\bar{\mathbf{z}}}{2},\frac{\mathbf{z}-\bar{\mathbf{z}}}{2i}\Big),$$

where $z_j=x_j+iy_j$ $(j=1,\dots,n)$. We can regard mixed polynomial maps as smooth maps from $\mathbb{R}^{2n}$ to $\mathbb{R}^2$.

A point $\mathbf{z}\in\mathbb{C}^n$ is a *singularity* of $f(\mathbf{z},\bar{\mathbf{z}})$ if the gradient vectors of $\Re f$ and $\Im f$ are linearly dependent at $\mathbf{z}$.

A *deformation* of f is a polynomial map $f_t:\mathbb{C}^n\times\mathbb{C}\to\mathbb{C}$, $(\mathbf{z},t)\mapsto f_t(\mathbf{z},\bar{\mathbf{z}})$, with $f_0(\mathbf{z},\bar{\mathbf{z}})=f(\mathbf{z})$.

Stable maps

Let $C^{\infty}(\mathbb{R}^{2n},\mathbb{R}^2)$ be the set of differential maps. It is well-known $C^{\infty}(\mathbb{R}^{2n},\mathbb{R}^2)$ is a topological space.

Let $f,g\in C^{\infty}(\mathbb{R}^{2n},\mathbb{R}^2)$. f and g are said to be *right-left equivalent* if there exist diffeomorphisms h_1 and h_2 of $\mathbb{R}^{2n}$ and $\mathbb{R}^2$ respectively such that $h_2\circ f=g\circ h_1$.

A map $f:\mathbb{R}^{2n}\to\mathbb{R}^2$ is called *a stable map* if there exists a neighborhood U_f of f such that for any $g\in U_f$, g is right-left equivalent to f.

If $f:\mathbb{R}^{2n}\to\mathbb{R}^2$ is a stable map, for each singularity of f, one of the following two conditions folds:

1. We can choose coordinates $(u,x_1,\dots,x_{2n-1})$ centered at x such that f has the form:
$$\Big(u,\sum_{j=1}^{2n-1}\pm x_j^2\Big).$$
2. We can choose coordinates $(u,y,x_1,\dots,x_{2n-2})$ centered at x such that f has the form:
$$\Big(u,\sum_{j=1}^{2n-2}\pm x_j^2+yu+y^3\Big).$$

If the singularity x of f satisfies the condition (1), we call x a *fold* singularity, and if it satisfies the condition (2), a *cusp*.

The set of stable maps is open and dense in the space of smooth maps $C^{\infty}(\mathbb{R}^{2n},\mathbb{R}^2)$ topologized with the C^{∞}-topology.

Higher differential d^2f

Let U and V be small neighborhoods of a singularity $x\in\mathbb{R}^{2n}$ and $f(x)\in\mathbb{R}^2$. Choose coordinates $\{\xi_i\}$ in U and $\{\eta_j\}$ in V. Let $E=T_x(U)$ and $F=T_{f(x)}(V)$. Then we can define the following exact sequence

$$0\to L\to E\xrightarrow{df}F\xrightarrow{\pi}G\to 0,$$

where $L=\ker df$, $G=\operatorname{coker} df$ and π is the linear map such that $\operatorname{Im}\pi=\operatorname{coker} df$.

Let $k=\sum_m a_m(\partial/\partial\xi_m)\in E$, $t=\sum_i b_i(\partial/\partial\xi_i)\in L$. We define the map $\varphi^1:E\to L^*\otimes F$ by

$$\varphi^1(k,t)=\sum_{i,j,m}\Big(a_m\frac{\partial^2 f_j}{\partial\xi_i\partial\xi_m}b_i\Big)\frac{\partial}{\partial\eta_j}$$

and then define the map $d^2f:E\to L^*\otimes G$ by

$$d^2f(k)(t)=\pi(\varphi^1(k)(t)).$$

Lemma 1[1]

x is a fold singularity of f $\Longleftrightarrow$ x satisfies the following conditions:

1. the rank of the representation matrix of $d^2f=2n-1$
2. $\ker(d^2f|_L)=\{0\}$

We can show the following theorems.

Theorem 1

Let $f(\mathbf{z})$ be a 2-variable complex polynomial with an isolated singularity at $\mathbf{o}$ and let U be a sufficiently small nbd. of $\mathbf{o}$. Then there exists a deformation $f_t(\mathbf{z})$ of $f(\mathbf{z})$ such that the rank of the representation matrix of $d^2(f_t)$ is equal to 3 in U for any $0<t<<1$.

Theorem 2

Let $f(\mathbf{z})=z_1^p+z_2^q$ and let U be a sufficiently small nbd. of $\mathbf{o}$. Then there exists a deformation $f_t(\mathbf{z})$ of $f(\mathbf{z})$ such that $f_t(\mathbf{z})$ has only fold singularities in U where $0<t<<1$.

The complex Hessian $H_{\mathbb{C}}(f)$ of $f(\mathbf{z})$ is defined by

$$H_{\mathbb{C}}(f):=\Big(\frac{\partial^2 f}{\partial z_j\partial z_k}\Big).$$

Theorem 3

Let $f(\mathbf{z})$ and $g(\mathbf{z})$ be 2-variable complex polynomials with an isolated singularity at $\mathbf{o}$ having no common branches. Then there exists a deformation $f_t\overline{g}_t(\mathbf{z})$ of $f(\mathbf{z})\overline{g}(\mathbf{z})$ such that any singularity of $f_t\overline{g}_t(\mathbf{z})$ in U is either a Morse singularity or the rank of the representation matrix of $d^2(f_t\overline{g}_t)$ is equal to 3 for any $0<t<<1$.

To prove Theorem 1 and 2, we define the following deformation of the complex polynomial $f(\mathbf{z})$:

$$f_t(\mathbf{z}):=f(\mathbf{z})+t\Big(\beta_1z_1+\beta_2z_2+\overline{\Big(\frac{\beta_1}{2\beta_2}\Big)}\bar{z}_1^2+\overline{\Big(\frac{\beta_2}{2\beta_1}\Big)}\bar{z}_2^2+\bar{z}_1\bar{z}_2\Big),$$

where $0\le t<<1$ and $\beta_1,\beta_2\in\mathbb{C}\setminus\{0\}$.

To prove Theorem 3, we define the deformation $f_t(\mathbf{z})\overline{g}_t(\mathbf{z})$ of $f(\mathbf{z})\overline{g}(\mathbf{z})$ as follows:

$$f_t(\mathbf{z})\overline{g}_t(\mathbf{z}):=\Big(f(\mathbf{z})+t(\beta_1z_1+\beta_2z_2)\Big)\overline{\Big(g(\mathbf{z})+t(\gamma_1z_1+\gamma_2z_2)\Big)},$$

where $0\le t<<1$ and $\beta_j,\gamma_j\in\mathbb{C}\setminus\{0\}$ for $j=1,2$.

We can take constants β_j and γ_j such that the deformations satisfy the conditions of theorems.

References

[1] H. Levine, *Elimination of cusps*, Topology, **3** (1965), 263–296.

[2] M. Oka, *Non-degenerate mixed functions*, Kodai Math. J., **33** (2010), 1–62.

On $\mathbb{Z}_p$–orbit spaces of certain prehomogenous vector spaces (Joint work with Pr. Akihiko Yukie (Kyoto University))

Kazuaki Tajima
(Mathmatical Institute, Tohoku University, D4)
sa7m19@math.tohoku.ac.jp

1 PV as moduli space of fields

Let k be a field. Let G be an connected reductive algebraic group defined over k and V a finite vector space over k which acts G rationally. Then, a pair (G,V) said to be a **Prehomonenous vector space (PV)** if there exists a Zariski open orbit. For the rest of this poster, we assume V is an irreducible representation of G for the convinience. A typhical example of PV is the space of quadratic forms:

Example 1.1. Put $G = \mathrm{GL}(1) \times \mathrm{GL}(n)$ and $V = \mathrm{Sym}^2 k^n$ =(the space of n–ary quadratic forms). For $g = (t, g_1) \in G, x = x(v) \in V$, we define $gx = tx(vg_1)$. Then the couple (G,V) is a PV.

Let (G,V) be a PV defined over k. We call (G,V) is **regular PV** if there exists $w \in V_k$ such that G_w is reductive. M.Sato and T.Kimura ware classtified regular PV defined over algbraic closed field with charactaristic 0 for 29 classes (1977, Nagoya J. Math.).

For any regular PV (G,V), it known that there exists the poloynomial $P(x) \in k[V]$ such that $P(gx) = \chi(g)P(x)$ for all $x \in V, g \in G$ and suitable character χ. The poloynomial $P(x)$ is called **rerative invariant polynomial** of (G,V). For example, in the space of quadratic forms, the relative invariant polynomial is equal to the determinant of quadratic forms. Set $V^{\mathrm{ss}} = \{x \in V; P(x) \neq 0\}$.

We consider the following Sato–Kimura type PV's in this section:

Table 1

i	G	V
2	$\mathrm{GL}(1) \times \mathrm{GL}(2)$	$\mathrm{Sym}^2 k^2$
2	$\mathrm{GL}(2) \times \mathrm{GL}(2) \times \mathrm{GL}(2)$	$M(2) \otimes k^2$
3	$\mathrm{GL}(1) \times \mathrm{GL}(3)$	$\mathrm{Sym}^3 k^2$
4	$\mathrm{GL}(3) \times \mathrm{GL}(2)$	$\mathrm{Sym}^2 k^3 \otimes k^2$
5	$\mathrm{GL}(5) \times \mathrm{GL}(4)$	$\wedge^2 k^5 \otimes k^4$

Then $\mathfrak{Ex}_i$ denotes the set of conjugate classes of Galois extension of k whose irreducible polynomial is degree i without multiple roots.

Theorem 1.2 (Wright–Yukie, 1992)**.** *For each $2 \leq i \leq 5$, we consider a pair (G,V) as in table 1.*

(1) We can construct natural map $\alpha_V : G_k \backslash V_k^{\mathrm{ss}} \ni x \mapsto k(x) \in \mathfrak{Ex}_i$, and these maps are always surjective.

(2) For $x \in V_k^{\mathrm{ss}}$, if $k(x) = k' \in \mathfrak{Ex}_i$, there exists correspond homomorphism $\psi_x : \mathrm{Gal}(k'/k) \to \mathfrak{S}_i$. Futhermore, if $x, y \in V_k^{\mathrm{ss}}, k(x) = k(y) = k'$, then

$$x \text{ and } y \text{ are } G_k\text{–equivarent} \Leftrightarrow \exists r \in \mathfrak{S}_i; \psi_x = r\psi_y r^{-1}.$$

Note that ψ_x is the permutation determined form the Galois action for the "Zero set" of x.

2 $\mathbb{Z}_p$–orbits of $\mathrm{Sym}^n \mathbb{Z}_p$

In this section, let (G,V) be as in Ex.1.1.

The following theorem is well–known:

Theorem 2.1 (Jordan decomposition)**.** *Let p be an odd prime. For all $x \in V_{\mathbb{Z}_p}^{\mathrm{ss}}$, there exists $g \in G_{\mathbb{Z}_p}$ such that*

$$gx = \begin{pmatrix} p^{a_1}A_1 & & & \\ & p^{a_2}A_2 & & \\ & & \ddots & \\ & & & p^{a_k}A_k \end{pmatrix},$$

where a_i's and A_j's are satisfy $a_1 < a_2 < \cdots < a_k, a_i \in \mathbb{Z}_{\geq 0}, \det A_j \in \mathbb{Z}_p^\times$.

A.Yukie gaved another simple proof of Theorem 2.1 from the invariant theoritic view.

Proof of Theorem 2.1. We'll denotes $\widetilde{*}$ the reduction modulo p of $*$. Choose an integer $a_1 \in \mathbb{Z}_{\geq 0}$ and a matrix $x^{(1)} \in M(n)_{\mathbb{Z}_p}$ stisfying $x = p^{a_1}x^{(1)}, \widetilde{x}^{(1)} \neq 0$. Then the matrix $\widetilde{x}^{(1)}$ is rank i over $\mathbb{F}_p$ for some $i \leq n$. By choose a lift of $\widetilde{x}^{(1)}$ over $\mathbb{Z}_p$, we can assume $x^{(1)} = \begin{pmatrix} A & pB \\ p\,{}^tB & pC \end{pmatrix}$ with $\det A \in \mathbb{Z}_p^\times$.

Now we claim that $gx^{(1)} = \begin{pmatrix} A & 0 \\ 0 & pC' \end{pmatrix}$ for some $g \in \mathrm{GL}(n), C' \in M(n-i)$. So applying the induction respect to the size of C', finish the proof. Therefore, we have to prove this claim.

If $g = \begin{pmatrix} \alpha & 0 \\ \beta & \gamma \end{pmatrix} \in \mathrm{GL}(n)$, then

$$gx^{(1)} = \begin{pmatrix} \alpha A\,{}^t\alpha & \alpha(A\,{}^t\beta + pB\,{}^t\gamma) \\ (\beta A + p\gamma\,{}^tB)\,{}^t\alpha & \beta A\,{}^t\beta + pC'' \end{pmatrix}.$$

Since A is invertible, we can choose $\alpha = E_i, \beta = -p\,{}^tBA^{-1}$ and $\gamma = E_{n-i}$, as desired. □

In the above proof, note that $\widetilde{x}^{(1)}$ is unstable respect to the projection map $\pi : V_{\mathbb{F}_p} \setminus \{0\} \to \mathbb{P}(V)_{\mathbb{F}_p}$ whenever $i < n$. Also, above simple situation caused from the equivariant–morse–stratification of $\mathrm{Sym}^2 k^n$ exactry determined from the degree of forms (The reason why can be using induction!). But, the equivariant–morse–stratification of the other spaces more difficult.

We currently study the $\mathbb{Z}_p$–orbits of the following space by using the above idea now:

$G = \mathrm{GL}(2) \times \mathrm{GL}(3), V = \mathrm{Sym}^2 k^3 \otimes k^2$.

References

[1] D.J.Wright, A.Yukie, Prehomonenous vector spaces and field extensions, Invent. Math. 110, pp. 283–314 (1992)

A localization of potentials

NISHIMORI Yasuhito
(Mathematical Institute Tohoku University)

Introduction

Let $(\mathcal{E}^{(\alpha)}, \mathcal{D}(\mathcal{E}^{(\alpha)}))$ be a Dirichlet form generated by symmetric α-stable process, where $0 < \alpha < 2$. A function V on $\mathbb{R}^d$ is non-negative and bounded with compact support. If the function V satisfies

$$\lambda_V := \inf\{\mathcal{E}^{(\alpha)}(u,u)\ ;\ u \in \mathcal{D}(\mathcal{E}^{(\alpha)}),\ \int_{\mathbb{R}^d} u^2 V dx = 1\} > 1,$$

V is subcritical. For a subcritical function W and $R \in \mathbb{R}^d$, we set $W_R(x) = W(x+R)$ and $q_R = V + W_R$. For subcritical functions V, W and large $|R|$, we show that $\lambda_{q_R} > 1$. B. Simon shown [2] this for $\alpha = 2$. We extend his fact to symmetric α-stable processes ($\alpha < d$).

1 Preliminaries

$(\{X_t\}, P_x)$ is a symmetric α-stable process, that is, symmetric Markov process generated by $(-\Delta)^{\alpha/2}$. Set

$$A_t^V = \int_0^t V(X_t)dt.$$

We see from [1] that $\lambda_{q_R} > 1$ is equivalent to

$$\sup_{x\in\mathbb{R}^d} E_x[\exp(A_\infty^{q_R})] < \infty. \tag{1}$$

We show (1). Set

$$b_R = \sup_{x\in\mathbb{R}^d} E_x[\exp(A_\infty^V)] \vee \sup_{x\in\mathbb{R}^d} E_x[\exp(A_\infty^{W_R})].$$

By the spatial homogeneity,

$$\sup_{x\in\mathbb{R}^d} E_x[\exp(A_\infty^{W_R})] = \sup_{x\in\mathbb{R}^d} E_x[\exp(A_\infty^{W})].$$

Namely, $b_R = b_0$. Thus we set $b = b_0$. In our proof, the spatial homogeneity plays a most important role. We assume that the supports of V and W are contained by $B := B(0,r)$ and $B_R := B(R,r)$ respectively. Here $B(x,r)$ is a ball centered at x with radius r. τ_1 is the first hitting time to B, i.e., $\tau_1 = \inf\{t > 0\ ;\ X_t \in B\}$. In addition,

$$\sigma_i := \inf\{t > \tau_i\ ;\ X_t \in B_R\}, \quad i \geq 1,$$
$$\tau_i := \inf\{t > \sigma_{i-1}\ ;\ X_t \in B\}, \quad i \geq 2.$$

Then the path space Ω is divided by A_i's, where

$$A_1 = \{\tau_1 = \infty\},\ A_i = \{\tau_i = \infty,\ \tau_{i-1} < \infty\},$$

and so

$$\begin{aligned}\sup_{x\in\mathbb{R}^d} E_x[\exp(A_\infty^{q_R})] &= \sup_{x\in\mathbb{R}^d} \sum_{i\geq 1} E_x[\exp(A_\infty^{q_R}); A_i]\\ \leq &\sup_{x\in\mathbb{R}^d}\Big(E_x[\exp(A_\infty^{q_R}); A_1] + J(2;x)\Big)\\ &+\sum_{i\geq 2}\sup_{x\in\mathbb{R}^d} I(i;x) + \sum_{i\geq 3}\sup_{x\in\mathbb{R}^d} J(i;x).\end{aligned} \tag{2}$$

Here

$$I(i;x) = E_x[\exp(A_\infty^{q_R}); A_i,\ \{\sigma_{i-1} < \infty\}],$$
$$J(i;x) = E_x[\exp(A_\infty^{q_R}); A_i,\ \{\sigma_{i-1} = \infty\}].$$

2 Main theorem

Lemma 2.1. *There exists some non-negative constant $C^V_{B\to B_R}$ and $C^W_{B_R\to B_R}$ such that*

$$\sup_{y\in B} E_y[\exp(A^V_{\sigma_1});\ \{\sigma_1 < \infty\}] \leq C^V_{B\to B_R},$$
$$\sup_{z\in B_R} E_z[\exp(A^{W_R}_{\tau_1});\ \{\tau_1 < \infty\}] \leq C^W_{B_R\to B}.$$

Proof. Because V is subcritical, that is, $\lambda_V > 1$, we can choose $p_V > 1$ such that $p_V < \lambda_V$. This means $\lambda_{p_V V} > 1$, and so $\sup_{x\in\mathbb{R}^d} E_x[\exp(p_V A^V_\infty)] < \infty$. Set $1/q_V = 1 - 1/p_V$.

$$\begin{aligned}&\sup_{y\in B} E_y[\exp(A^V_{\sigma_1});\ \{\sigma_1 < \infty\}]\\ \leq\ &\sup_{y\in B} E_y[\exp(p_V A^V_{\sigma_1})]^{1/p_V}\Big(\sup_{y\in B} P_y(\sigma_1 < \infty)\Big)^{1/q_V}\\ =:\ &C^V_{B\to B_R} < \infty.\end{aligned}$$

By the same manner, we can choose the constant $C^W_{B_R\to B}$. $\square$

For $y \in B$, $P_y(\sigma_1 < \infty) \leq \text{const}(r/|R|)^{d-\alpha}$. From this, we see that $C^V_{B\to B_R}$ converges to 0 as $|R| \to \infty$. In addition, we see that $C^W_{B_R\to B}$ converges to 0 as $|R| \to \infty$.

By the strong Markov property and the spatial homogeneity, we have

$$\sup_{x\in\mathbb{R}^d}(E_x[\exp(A^{q_R}_\infty); A_1] + J(2;x)) \leq b + C_{B\to B_R} + (1+b)C^W_{B_R\to B},$$

and

$$I(i;x) \leq b^i (C^V_{B\to B_R})^{i-1}, \quad \text{for } i \geq 2,$$
$$I(j;x) \leq b^{i-1} C^W_{B_R\to B}(C^V_{B\to B_R})^{i-2}, \quad \text{for } i \geq 3.$$

By (2), we have the following theorem.

Theorem 2.1. *If both $bC^V_{B\to B_R}$ and $bC^W_{B_R\to B}$ are less than 1, then*

$$\begin{aligned}\sup_{x\in\mathbb{R}^d} E_x[\exp(A^{q_R}_\infty)] \leq\ & b + C^V_{B\to B_R}\Big(1 + \frac{b^2}{1 - bC^V_{B\to B_R}}\Big)\\ &+ C^W_{B_R\to B}\Big(1 + b + \frac{b^2 C^V_{B\to B_R}}{1 - bC^V_{B\to B_R}}\Big).\end{aligned}$$

Corollary 2.1. *For $\alpha < d$ and subcritical potentials V, W, the following holds*

$$\lim_{|R|\to\infty}\sup_{x\in\mathbb{R}^d} E_x[\exp(A^{q_R}_\infty)] = b.$$

References

[1] Z.-Q. Chen, Gaugeability and conditional gaugeability, Trans. Amer. Math. Soc., **354**, 4639–4679, 2002.

[2] B. Simon, Brownian motion, L^p properties of Schrödinger operators and the localization of binding, J. Funct. Anal., **35**, 215–229, 1980.

P-72

Penalizations for Generalized Feynman-Kac Functionals

Masakuni MATSUURA[*†]
Mathematical Institute, Tohoku University

March 5, 2013[‡]

1 Feynman-Kac penalization for PCAFs with non-local potentials

Let $X = (\Omega, \mathscr{F}, \mathscr{F}_t, \mathbb{P}_x, X_t)$ be a transient symmetric α-stable process $(0 < \alpha < 2)$ on $\mathbb{R}^n$ and let $A_t^{\mu,F}$ be a positive additive functional ("PAF"):

$$A_t^{\mu,F} := A_t^\mu + \sum_{s \le t} F(X_{s-}, X_s),$$

where A_t^μ is a positive continuous additive functional ("PCAF") with Revuz measure μ and F is a bounded measurable positive symmetric function vanishing on diagonal set. $e^{A_t^{\mu,F}}$ is then decomposed as follows.

$$e^{A_t^\mu + \sum_{s \le t} F(X_{s-}, X_s)} = L_t e^{A_t^{\mu+\mu_{F_1}}}$$

Here,

$$\mu_{F_1}(dx) := \left\{ c \int F_1(x,y) |x-y|^{-n-\alpha} dy \right\} dx, \quad F_1 := e^F - 1,$$

and L_t is an exponential martingale. We give the spectral function

$$\lambda_{\mu+\mu_{F_1}}(\theta) := \inf\{\mathscr{E}^L(f,f) + \theta(f,f); \int f^2 d(\mu+\mu_{F_1}) = 1\} \quad \text{for} \quad \theta \ge 0,$$

where $\mathscr{E}^L$ is the Dirichlet form corresponding to the Girsanov transformed process by L_t, that is, $d\mathbb{P}_x^L := L_t d\mathbb{P}_x$ and $\mathscr{E}^L$ is given by

$$\mathscr{E}^L(f,f) = c \int_{d^c} (f(x) - f(y))^2 e^{F(x,y)} |x-y|^{-n-\alpha} dx dy.$$

We then solve the Feynman-Kac penalization problem in terms of the bottom $\lambda_{\mu+\mu_{F_1}}(0)$ of $\lambda_{\mu+\mu_{F_1}}(\theta)$:

Theorem 1 ([M2012]). *Let $\Lambda \in \mathscr{F}_s$ and assume that $\mu + \mu_{F_1}$ is a Green-tight Kato measure. There exists a limit*

$$\widetilde{\mathbb{P}}_x[\Lambda] = \lim_{t \to \infty} \frac{\mathbb{E}_x[e^{A_t^{\mu,F}} \mathbf{1}_\Lambda]}{\mathbb{E}_x[e^{A_t^{\mu,F}}]}.$$

(a) If $\lambda_{\mu+\mu_{F_1}}(0) > 1$ ($\mu + \mu_{F_1}$ is subcritical), then $\widetilde{\mathbb{P}}_x$ is given by

$$d\widetilde{\mathbb{P}}_x = \frac{e^{A_s^{\mu+\mu_{F_1}}} h(X_s)}{h(x)} L_s d\mathbb{P}_x, \quad h(x) := \mathbb{E}_x^L[e^{A_\infty^{\mu+\mu_{F_1}}}].$$

(b) If $\lambda_{\mu+\mu_{F_1}}(0) < 1$ ($\mu + \mu_{F_1}$ is supercritical), then $\widetilde{\mathbb{P}}_x$ is given by

$$d\widetilde{\mathbb{P}}_x = \frac{e^{-\theta_0 s + A_s^{\mu+\mu_{F_1}}} h(X_s)}{h(x)} L_s d\mathbb{P}_x.$$

Here, $\theta_0 > 0$ satisfies $\lambda_{\mu+\mu_{F_1}}(\theta_0) = 1$ and h is the ground state whose eigenvalue is θ_0.
(c) If $\lambda_{\mu+\mu_{F_1}}(0) = 1$ ($\mu + \mu_{F_1}$ is critical) and $\mu + \mu_{F_1}$ belongs to a restricted Kato class, then $\widetilde{\mathbb{P}}_x$ is given by

$$d\widetilde{\mathbb{P}}_x = \frac{e^{A_s^{\mu+\mu_{F_1}}} h(X_s)}{h(x)} L_s d\mathbb{P}_x.$$

Here, h is the ground state given by the compact embedding of the extended Dirichlet form to $L^2(\mu + \mu_{F_1})$.

*Mail : sa9d10@math.tohoku.ac.jp
†Web : http://www.math.tohoku.ac.jp/~sa9d10/
‡Poster session, Global COE 5th symposium "Weaving Science Web beyond Particle-Matter Hierarchy".

2 Feynman-Kac penalization for non-local PAF with 0-energy parts

Let $(\mathscr{E}, \mathscr{F}_e)$ be the extended Dirichlet space and $U \in \mathscr{F}_e \cap C_b(\mathbb{R}^n_*)$. For AF $U(X_t) - U(X_0)$, Fukushima's decomposition yields the AF N_t^U with unbounded variation:

$$N_t^U = U(X_t) - U(X_0) - M_t^U,$$

where M_t^U is a martingale. N_t^U is said to be a 0-energy part. We give the multiplicative functional ("MF")

$$e^{A_t^{\mu,F,U}} := \exp\left(A_t^{\mu,F} + N_t^U\right)$$

and consider the penalization for the generalized Feynman-Kac multiplicative functional ("FKMF") $e^{A_t^{\mu,F,U}}$.

We employ the Girsanov transform in the sense of Chen and Zhang: The generalized FKMF $e^{A_t^{\mu,F,U}}$ is decomposed as follows.

$$e^{A_t^{\mu,F,U}} = W_t e^{U(X_t) - U(x)} e^{A_t^{\mu+\mu_V}}$$

Here, W_t is the exponential martingale and μ_V is given by

$$\mu_V(dx) = c \left\{ \int \frac{e^{F(x,y) + U(x) - U(y)} - U(x) + U(y) - 1}{|x-y|^{n+\alpha}} \right\} dx.$$

We then define $d\mathbb{P}_x^W := W_t d\mathbb{P}_x$.

Kim and Kuwae give the characterization of the gaugeability of generalized FKMF:

Theorem 2. *Let $g(x) := \mathbb{E}_x[e^{A_\infty^{\mu,F,U}}]$. $||g||_\infty < \infty$ if and only if $\lambda_{\mu+\mu_V}(0) > 0$, where*

$$\lambda_{\mu+\mu_V}(\theta) := \inf\left\{ \mathscr{Q}(f,f) + \theta(f,f); \int f^2 d(\mu + \mu_V) = 1 \right\}$$

and $\mathscr{Q}$ is the quadratic form given by

$$\mathscr{Q}(f,f) = \mathscr{E}(f,f) + \mathscr{E}(U, f^2) - \int f^2 d\mu - \int_{d^c} \frac{c f(x) f(y) F_1(x,y)}{|x-y|^{n+\alpha}} dx dy.$$

We see that

$$\mathscr{Q}(f,f) + \int f^2 d(\mu + \mu_V) = \mathscr{E}^W(f,f)$$

and this gives the last characterization of gaugeability is equivalent to

$$\inf\left\{ \mathscr{E}^W(f,f); \int f^2 d(\mu + \mu_V) = 1 \right\} > 1.$$

We find that the penalization for generalized FKMFs is solved if the Kato potential $\mu + \mu_V$ is subcritical:

$$\begin{aligned}
\frac{\mathbb{E}_x[e^{A_t^{\mu,F,U}} | \mathscr{F}_s]}{\mathbb{E}_x[e^{A_t^{\mu,F,U}}]} &= e^{A_s^{\mu,F,U}} \frac{\mathbb{E}_x[e^{A_{t-s}^{\mu,F,U}} \circ \theta_s | \mathscr{F}_s]}{\mathbb{E}_x[e^{A_t^{\mu,F,U}}]} \\
&= e^{A_s^{\mu,F,U}} \frac{\mathbb{E}_{X_s}[e^{A_{t-s}^{\mu,F,U}}]}{\mathbb{E}_x[e^{A_t^{\mu,F,U}}]} \\
&\to \frac{e^{A_s^{\mu,F,U}} g(X_s)}{g(x)}.
\end{aligned}$$

References

[M2012] Matsuura, M., *Feynman-Kac Penalization Problem for Additive Functionals with Jumping Functions*, J. Math. Soc. Japan, to appear.

P-73

On the analysis of strategies in generalized stochastic reachability games

AHMAD TERMIMI BIN AB GHANI
{ SA9D12 }@MATH.TOHOKU.AC.JP

TOHOKU UNIVERSITY

1. Problems of interest

1. **Determinacy (Values of games)**
   In the sense that from each position, the player has an optimal value.
2. **Optimal strategies**
   Do the players have an optimal strategy? If so, what type of strategy?

2. Games

Definition 1. *A (two-player infinite)* **stochastic game** *is a quadruple* $\mathbb{G} = (S, A_{\mathrm{I}}, A_{\mathrm{II}}, \delta)$, *where*
- S, A_{I} and A_{II} are nonempty finite sets,
- δ is a function from $S \times A_{\mathrm{I}} \times A_{\mathrm{II}}$ into S.
Elements of S are called **states**.
Elements of A_{I} and A_{II} are called **actions** *of Player I and Player II.*
δ is called a **transition function**.

Definition 2 (Mixed strategy). *A (mixed) strategy of Player I in $\mathbb{G}$ is any function $\sigma : \Omega^{\mathrm{fin}} \to \mathcal{D}(A_{\mathrm{I}})$, where $\mathcal{D}(A_{\mathrm{I}})$ be the set of probability distributions on A_{I}. Similarly, a strategy of Player II is any function $\tau : \Omega^{\mathrm{fin}} \to \mathcal{D}(A_{\mathrm{II}})$.*

Definition 3 (Memoryless strategy). *A strategy σ of Player I is called memoryless if $\sigma : S \to \mathcal{D}(A_{\mathrm{I}})$. A memoryless strategy of Player II is defined similarly, i.e., $\tau : S \to \mathcal{D}(A_{\mathrm{II}})$.*

4. Generalized Reachability

Definition 6 (Labeling function). *A function ℓ is called a* **label** *on S if $\mathrm{dom}(\ell) \subset S$ and $\ell(s) \in [0,1]$ for any $s \in \mathrm{dom}(\ell)$.*

Definition 7 (Payoff function). *We define a payoff function $\mathcal{R}^{\mathbb{G},\ell} : \Omega \to [0,1]$ associated to label ℓ by*

$$\mathcal{R}^{\mathbb{G},\ell}(w) = \begin{cases} \ell(w(N_w)) & \text{if } (\exists N \in \mathbb{N})[w(N) \in \mathrm{dom}(\ell)], \\ 0 & \text{otherwise,} \end{cases}$$

where N_w is the least natural number N such that $w(N) \in \mathrm{dom}(\ell)$.

Definition 8. *A game of the form $\mathbb{G}(\mathcal{R}^{\mathbb{G},\ell})$ is called a* **generalized reachability game**.

For a subset T of S, let $\mathcal{R}^{\mathbb{G},T} = \mathcal{R}^{\mathbb{G},\ell_T}$, where $\ell_T : T \to \{1\}$.

Remark 1. *Games of the form $\mathbb{G}(\mathcal{R}^{\mathbb{G},T})$ are called* **reachability games**.

Definition 9 (Limit value). *Let ℓ a label on S. For any $s \in S$ and $n \in \mathbb{N}$, define $V_n^{\mathbb{G},\ell} : S \to [0,1]$ inductively by*

$$V_0^{\mathbb{G},\ell}(s) = \begin{cases} \ell(s) & \text{if } s \in \mathrm{dom}(\ell), \\ 0 & \text{otherwise,} \end{cases}$$

$$V_{n+1}^{\mathbb{G},\ell}(s) = \begin{cases} \ell(s) & \text{if } s \in \mathrm{dom}(\ell), \\ \mathrm{val}_s(V_n^{\mathbb{G},\ell}) & \text{otherwise.} \end{cases}$$

We let $V^{\mathbb{G},\ell}(s) = \lim_{n\to\infty} V_n^{\mathbb{G},\ell}(s)$ for any state s, and we call it the **limit value** *at s.*

3. Backgrounds

Let $\Omega_s = \{w \in \Omega : w(0) = s\}$ and $\Omega_s^{\mathrm{fin}} = \{q \in \Omega^{\mathrm{fin}} : q(0) = s\}$.

Definition 4. *For a pair $(\sigma, \tau) \in \Sigma_{\mathrm{I}} \times \Sigma_{\mathrm{II}}$ of strategies and a state $s \in S$, $P_s^{\sigma,\tau}$ denotes the* **probability measure** *on Ω_s defined by*

$$P_s^{\sigma,\tau}([p]) = \prod_{n \in \{1,|p|-1\}} \sum_{\substack{(a,b) \in A_{\mathrm{I}} \times A_{\mathrm{II}} \\ (p(n-1),a,b) \in \delta^{-1}(p(n))}} \sigma(p \restriction n)(a)\tau(p \restriction n)(b)$$

for any $p \in \Omega_s^{\mathrm{fin}}$, where $[p] = \{w \in \Omega : p \subset w\}$.

In general, for a function $F : \Omega \to [0,1]$ such that $P_s^{\sigma,\tau}(F) = \int_{\Omega_s} F dP_s^{\sigma,\tau}$ exists,

- $P_s^{\sigma,\tau}(F)$ means the **expected value** of an infinite game $\mathbb{G}_s(F)$ when Player I and Player II use the strategies σ and τ, respectively.
- We say that the game $\mathbb{G}_s(F)$ is **determinate** if and only if

$$\sup_{\sigma \in \Sigma_{\mathrm{I}}^{\mathbb{G}}} \inf_{\tau \in \Sigma_{\mathrm{II}}^{\mathbb{G}}} P_s^{\sigma,\tau}(F) = \inf_{\tau \in \Sigma_{\mathrm{II}}^{\mathbb{G}}} \sup_{\sigma \in \Sigma_{\mathrm{I}}^{\mathbb{G}}} P_s^{\sigma,\tau}(F) \text{ holds for any } s \in S. \tag{1}$$

- We write $\mathrm{val}_s^{\mathbb{G}}(F)$ instead of $\sup_{\sigma \in \Sigma_{\mathrm{I}}^{\mathbb{G}}} \inf_{\tau \in \Sigma_{\mathrm{II}}^{\mathbb{G}}} P_s^{\sigma,\tau}(F)$, and call the **value of game** $\mathbb{G}_s(F)$.

Definition 5. *Let $F : \Omega \to [0,1]$ and $\epsilon \in [0,1]$. Suppose that $\mathbb{G}_s(F)$ is determinate. A strategy $\sigma \in \Sigma_{\mathrm{I}}$ of Player I is ϵ-***optimal** *if*

$$\inf_{\tau \in \Sigma_{\mathrm{II}}^{\mathbb{G}}} P_s^{\sigma,\tau}(F) \geq \mathrm{val}_s(F) - \epsilon \text{ holds for any } s \in S.$$

*A strategy $\tau \in \Sigma_{\mathrm{II}}$ of Player II is ϵ-***optimal** *if*

$$\sup_{\sigma \in \Sigma_{\mathrm{I}}^{\mathbb{G}}} P_s^{\sigma,\tau}(F) \leq \mathrm{val}_s(F) + \epsilon \text{ holds for any } s \in S.$$

5. Example

Example 1. *Player I has no optimal strategy in some reachability games.*

Proof. Let $S = \{s_0, s_1, s_2\}$, $A_{\mathrm{I}} = \{x_1, x_2\}$; $A_{\mathrm{II}} = \{y_1, y_2\}$. Define a transition function δ
$\delta(s_0, x_1, y_1) = s_0$; $\delta(s_0, x_2, y_2) = s_2$;
$\delta(s_0, x_1, y_2) = \delta(s_0, x_2, y_1) = s_1$, and
$\delta(s_i, x, y) = s_i$ for any $i \in \{1,2\}$ and $(x,y) \in A_{\mathrm{I}} \times A_{\mathrm{II}}$.

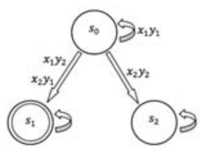

Consider the game $\mathbb{G}(\mathcal{R}^{\mathbb{G},T})$ with $T = \{s_1\}$. One can prove that $\mathrm{val}_{s_0}(\mathcal{R}^{\mathbb{G},\{s_1\}}) = 1$.
Fix a strategy $\sigma \in \Sigma_{\mathrm{I}}$. We construct $\tau \in \Sigma_{\mathrm{II}}$ such that $P_{s_0}^{\sigma,\tau}(\mathcal{R}^{\mathbb{G},\{s_1\}}) < 1$. For $\rho \in \Omega^{\mathrm{fin}}$, define
- $\tau(\rho)(y_1) = 1$ if $\sigma(\rho)(x_1) = 1$, and
- $\tau(\rho)(y_2) = 1$ otherwise.
It is clear that $P_{s_0}^{\sigma,\tau}(\mathcal{R}^{\mathbb{G},\{s_1\}}) < 1$ by definition of $\mathbb{G}$ and τ. □

7. Results

Corollary 2. *Player II has a memoryless optimal strategy in any generalized reachability game.*

Theorem 3. *In every generalized reachability game $\mathbb{G}(\mathcal{R}^{\mathbb{G},\ell})$, there exist an ε-optimal memoryless strategy of Player I for any $\varepsilon > 0$.*

6. Results

Theorem 1 (DETERMINACY). *For any state $s \in S$, the equation $V^{\mathbb{G},\ell}(s) = \mathrm{val}_s(\mathcal{R}^{\mathbb{G},\ell})$ holds.*

Proof. It is enough to show the inequalities

$$\inf_{\tau \in \Sigma_{\mathrm{II}}} \sup_{\sigma \in \Sigma_{\mathrm{I}}} P_s^{\sigma,\tau}(\mathcal{R}^{\mathbb{G},\ell}) \leq V^{\mathbb{G},\ell}(s)$$

$$\leq \sup_{\sigma \in \Sigma_{\mathrm{I}}} \inf_{\tau \in \Sigma_{\mathrm{II}}} P_s^{\sigma,\tau}(\mathcal{R}^{\mathbb{G},\ell}) \text{ hols.}$$

- To show the first inequality, choose an optimal strategy τ^* of Player II in the one-step game $\mathbb{G}(V^{\mathbb{G},\ell})$.
- We show that τ^* satisfies the inequality

$$\sup_{\sigma \in \Sigma_{\mathrm{I}}} P_s^{\sigma,\tau^*}(\mathcal{R}^{\mathbb{G},\ell}) \leq V^{\mathbb{G},\ell}(s) \ \forall s \in S.$$

- It is enough to show that

$$\sup_{\sigma} P_s^{\sigma,\tau^*}(\mathcal{R}_n^{\mathbb{G},\ell}) \leq V^{\mathbb{G},\ell}(s) \ \forall s \in S, n \in \mathbb{N}.$$

  (We show this by induction on n).

For the second inequality, we have

$$P_s^{\sigma,\tau}(\mathcal{R}_n^{\mathbb{G},\ell}) \leq P_s^{\sigma,\tau}(\mathcal{R}^{\mathbb{G},\ell})$$

since $\mathcal{R}_n^{\mathbb{G},\ell}(w) \leq \mathcal{R}^{\mathbb{G},\ell}(w)$ for any $w \in \Omega$. Hence,

$$\sup_{\sigma} \inf_{\tau} P_s^{\sigma,\tau}(\mathcal{R}_n^{\mathbb{G},\ell}) \leq \sup_{\sigma} \inf_{\tau} P_s^{\sigma,\tau}(\mathcal{R}^{\mathbb{G},\ell}) \text{ holds.}$$

Note that any finite game is determinate. So, we have

$$V_n^{\mathbb{G},\ell}(s) = \mathrm{val}_s(\mathcal{R}_n^{\mathbb{G},\ell}) = \sup_{\sigma} \inf_{\tau} P_s^{\sigma,\tau}(\mathcal{R}_n^{\mathbb{G},\ell}) \text{ holds.}$$

Thus, the second inequality holds. □

An application of periodic decompositions of functions holomorphic on convex polygonal domains

Takanao Negishi

In this report, a periodic decomposition of a function f means a representation of f as a finite sum of periodic fnctions. We denote by $[\gamma_1, \gamma_2, \ldots, \gamma_n]$ the n-sided polygon with vertices $A_1(z = \gamma_1), A_2(z = \gamma_2), \ldots, A_n(z = \gamma_n)$ $(\gamma_1, \gamma_2, \ldots, \gamma_n \in \mathbb{C})$ and edges $A_1A_2, A_2A_3, \ldots, A_nA_1$. For convenience, let $\gamma_0 = \gamma_n$ and $\gamma_{n+1} = \gamma_1$. The following theorem is fundamental in this study.

Theorem 1. (*Leont'ev*) *Let D be a convex polygonal domain with vertices $\gamma_1, \gamma_2, \ldots, \gamma_n \in \mathbb{C}$ and let $\gamma_{n+1} = \gamma_1$. For $1 \le k \le n$, let $c_k = \gamma_{k+1} - \gamma_k$ and let D_k be the open half-plane containing D bounded by the line through γ_k and γ_{k+1}. Then, any function f holomorphic in D has a periodic decomposition of the form*

$$f(z) = P_{c_1}(z) + P_{c_2}(z) + \cdots + P_{c_n}(z) \quad (z \in D),$$

where each P_{c_k} is holomorphic and c_k-periodic in D_k.

We can consider some extensions of Theorem 1. We give periodic decompositions of functions holomorphic in some domains that is not necessarily convex polygon. Let D be a domain whose boundary is not empty and $\gamma_1, \gamma_2, \ldots, \gamma_n$ be distinct points on ∂D such that $[\gamma_1\gamma_2\cdots\gamma_n]$ is a convex n-sided polygon. Let E be a convex polygonal domain whose boundary is $[\gamma_1\gamma_2\cdots\gamma_n]$. For $1 \le k \le n$, let $c_k = \gamma_{k+1} - \gamma_k$ and let E_k be the open half-plane containing E bounded by the line through γ_k and γ_{k+1} ($E_0 = E_n$, $E_{n+1} = E_1$). In addition, for $1 \le k \le n$, let $G_k = E_{k-1} \cap E_{k+1} \cap D$. Suppose that the following conditions are satisfied:

(a) $E \subset D$.
(b) $(\mathbb{C} \setminus \overline{E_k}) \cap D \subset G_k$ hold for $1 \le k \le n$.
(c) For each k $(1 \le k \le n)$, the equality $G_k \cap (G_k + c_k) \cap (\mathbb{C} \setminus \overline{E_k}) = \emptyset$ holds.

Then, for each $1 \le k \le n$, the set $D_k = (G_k + c_k\mathbb{Z}) \cup E_k$ is a c_k-periodic domain (i.e. $D_k + c_k = D_k$). In addition, the domain D is one of connected components of $D_1 \cap D_2 \cap \cdots \cap D_n$. Then we call $D = D_1 \cap D_2 \cap \cdots \cap D_n \cap D$ a strictly convex polygonal decomposition of domain D and we call E the base polygonal domain. For example, when D is a disc domain and E is the interior of an inscribed n-sided polygon of D such that the center of D is on $\overline{E}$, then $D = D_1 \cap D_2 \cap \cdots \cap D_n \cap D$ is a strictly convex polygonal decomposition of D.

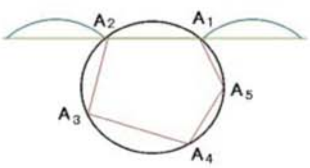

Theorem 2. *Let $D = D_1 \cap D_2 \cap \cdots \cap D_n \cap D$ be a strictly convex polygonal decomposition of domain D with the base polygonal domain E. Then any function f holomorphic in D has a periodic decomposition $f = P_{c_1} + P_{c_2} + \cdots + P_{c_n}$, where each P_{c_k} is holomorphic and c_k-periodic in D_k.*

Next we suppose that the domain D and its boundary points $\gamma_1, \ldots, \gamma_n$ satisfy the conditions (a) and (b). Thus $G_k \cap (G_k + c_k) \cap (\mathbb{C} \setminus \overline{E_k})$ is not necessarily empty, which implies that the function P_{c_k} given by Theorem 2 is not well-defined generally. To overcome this, we adopt the idea of Riemann surface. Let $(\mathbb{C})_{(k,m)}$ $(1 \le k \le n,\ m \in \mathbb{Z})$ be copies of complex plane $\mathbb{C}$. For each k, we consider a domain $E_k \cup \{(E_{k-1} \cap E_{k+1}) + mc_k\}$ in each $(\mathbb{C})_{(k,m)}$, respectively. We write, respectively, a set X and a point z on the complex plane $(\mathbb{C})_{(k,m)}$ as $\langle X \rangle_{(k,m)}$ and $\langle z \rangle_{(k,m)}$ for emphasis. Now if $z \in E_k$, we identify the point $\langle z \rangle_{(k,l)}$ with the point $\langle z \rangle_{(k,m)}$ for $l, m \in \mathbb{Z}$. Meanwhile even if $z \in \{(E_{k-1} \cap E_{k+1}) + lc_k\} \cap \{(E_{k-1} \cap E_{k+1}) + mc_k\} \cap (\mathbb{C} \setminus \overline{E_k})$ and $l \ne m$, we regard $\langle z \rangle_{(k,l)}$ and $\langle z \rangle_{(k,m)}$ as distinct points. Consider the Riemann surface

$$R_k = \bigcup_{m \in \mathbb{Z}} \langle E_k \cup \{(E_{k-1} \cap E_{k+1}) + mc_k\} \rangle_{(k,m)}$$

for $1 \le k \le n$. Then

$$D_k = \bigcup_{m \in \mathbb{Z}} \langle E_k \cup (H_k + mc_k) \rangle_{(k,m)},$$

where $H_k = D \cap E_1 \cap \cdots \cap E_{k-1} \cap E_{k+1} \cap \cdots \cap E_n$, is regarded as a domain in R_k. In addition, if $z \in H_j$, $j \ne k$, and $m \in \mathbb{Z}$, then we identify the point $\langle z \rangle_{(j,0)}$ with the point $\langle z \rangle_{(k,m)}$. Then we call $D = D_1 \cap D_2 \cap \cdots \cap D_n$ a convex polygonal decomposition of domain D and we call E the base polygonal domain.

We introduce the new forward difference operators $\Delta_{\langle c_k \rangle_k}$ as follows: for any function f on R_k and $z \in E_k \cup \{(E_{j-1} \cap E_{j+1}) + mc_k\}$, set

$$\Delta_{\langle c_k \rangle_k} f(\langle z \rangle_{(k,m)}) = f(\langle z + c_k \rangle_{(k,m+1)}) - f(\langle z \rangle_{(k,m)}).$$

Then Theorem 2 can be extended to domains having a convex polygonal decomposition.

Theorem 3. *Let $D = D_1 \cap D_2 \cap \cdots \cap D_n$ be a convex polygonal decomposition of domain D. Then any function f holomorphic in D has a periodic decomposition $f = P_{c_1} + P_{c_2} + \cdots + P_{c_n}$, where each P_{c_k} is holomorphic and $\langle c_k \rangle_k$-periodic (in the sence $\Delta_{\langle c_k \rangle_k} f = 0$) in D_k.*

Example 1. *Let D be a bounded convex domain on $\mathbb{C}$, $[\gamma_1\gamma_2\cdots\gamma_n]$ be an inscribed n-sided polygon of D, and E be the interior of $[\gamma_1\gamma_2\cdots\gamma_n]$. Then $D = D_1 \cap D_2 \cap \cdots \cap D_n$ (the definition of D_k follows Theorem 3) is a convex polygonal decomposition of D.*

Example 2. *Let $D \subset \mathbb{C}$ be a bounded domain and A be its convex hull. Assume that a point $\alpha \in \partial A$ and a positive number $r > 0$ satisfy the following conditions:*
(i) Let $B(\alpha; r) = \{z \in \mathbb{C} |\ |z - \alpha| < r\}$. Then the set $\partial A \cap B(\alpha; r)$ is a curve segment.
(ii) Let δ_1 and δ_2 be the endpoints of $\partial A \cap B(\alpha; r)$ and l be the line through δ_1 and δ_2. Then $\alpha \notin l$.
(iii) Let H be the open half-plane containing α bounded by the line l. Then $A \cap \overline{H} = D \cap \overline{H}$.
Then D has a convex polygonal decomposition.

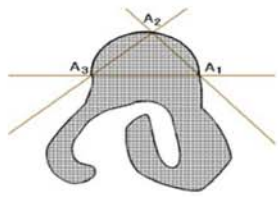

Next we consider an application of a convex polygonal decomposition whose base polygonal domain is a triangle. Let $E \subset \mathbb{C}$ be the interior of a triangle $[\gamma_1\gamma_2\gamma_3]$ and let $\gamma_4 = \gamma_1$. For each $k = 1, 2, 3$, let E_k be the open half-plane containing E bounded by the line through γ_k and γ_{k+1}, and let $H_k = E_{k-1} \cap E_{k+1}$ ($E_0 = E_n$, $E_4 = E_1$). Then the domain $U_1 = H_1 \cup H_2 \cup H_3$ has a convex polygonal decomposition with the base polygonal domain E.

Let $f(z)$ be an entire function on $\mathbb{C}$. Since $f(z)$ is holomorphic on U_1, $f(z)$ has a periodic decomposition $f(z) = P_{c_1}(z) + P_{c_2}(z) + P_{c_3}(z)$ by Theorem 3. We can construct a Riemann surface R by adding some appropriate identifications of points of Riemann surfaces R_k and redefine an appropriate forward difference operators $\Delta_{\langle c_k \rangle_k}$ and backward difference operators $\nabla_{\langle c_k \rangle_k}$. Then R has a natural projection $\pi : R \to \mathbb{C}$ and any function on $\mathbb{C}$ can be regarded as a function on R. Thus we obtain a periodic decomposition $f(\langle z \rangle) = P^{(1)}_{c_1}(\langle z \rangle) + P^{(1)}_{c_2}(\langle z \rangle) + P^{(1)}_{c_3}(\langle z \rangle)$ $(\langle z \rangle \in \langle U_1 \rangle \subset R)$.

Since the domains of $P^{(1)}_{c_k}$ are larger than $\langle E_k \rangle$, we can construct a periodic decomposition $f(\langle z \rangle) = P^{(2)}_{c_1}(\langle z \rangle) + P^{(2)}_{c_2}(\langle z \rangle) + P^{(2)}_{c_3}(\langle z \rangle)$ that holds on a domain $U_2 \subset R$ which satisfies $U_2 \supset U_1$ by repeating the process of the constructing the first decomposition. Furthermore, since the domains of $P^{(2)}_{c_k}$ are larger than that of $P^{(1)}_{c_k}$, we can construct a periodic decomposition of f that holds on a domain $U_3 \subset R$ which satisfies $U_3 \supset U_2$. Repeating this process again and again, we obtain a sequence $\{U_k\}$ of domains in R such that $U_k \subset U_{k+1}$, $\pi(U_k) = \mathbb{C}$ $(k \ge 3)$ and f has a periodic decomposition on U_k.

P-75

Characterization of $\emptyset'$-Schnorr Randomness via Relative Randomness

NingNing Peng

sa8m42@math.tohoku.ac.jp
Mathematical Institute, Tohoku University

Questions

This is a join work with Kojiro Higuchi.

Question 1 *Can we define some randomness notions in terms of another randomness notions?*

Question 2 *How can we define it?*

Let R and S be two randomness notions.

Question 3 $(\exists\Gamma \subset 2^\omega)[\mathrm{R} = \bigcap_{X\in\Gamma} X\text{-S}]$ *or* $(\exists\Gamma \subset 2^\omega)[\mathrm{R} = \bigcup_{X\in\Gamma} X\text{-S}]$?

where X-R and X-S are relativizations of R and S to X, respectively.

Question 4 *What kinds of* Γ *satisfy above relations ?*

Note: Q1 same to Q3, Q2 same to Q4.

Randomness Notions

Definition 1 (Martin-Löf , 1966) (*i*) *A* Martin-Löf *test, or ML-test for short, is a uniformly c.e. sequence* $(G_m)_{m\in\mathbb{N}}$ *of open sets such that* $\forall m \in \mathbb{N}\ \mu(G_m) \le 2^{-m}$.

(*ii*) *A set* $Z \subseteq \mathbb{N}$ fails *the test if* $Z \in \bigcap_m G_m$, *otherwise* Z passes *the test.* Z *is* ML-random *if* Z *passes each ML-test.*

Definition 2 (Kurtz, 1981) *A* generalized ML-test *is a uniformly c.e. sequence* $(G_m)_{m\in\mathbb{N}}$ *of open sets such that* $\mu(\bigcap_m G_m) = 0$. Z *is* weakly 2-random *if it passes every generalized ML-test.*

Definition 3 (Schnorr, 1971) *A* Schnorr test *is a ML-test* $(G_m)_{m\in\mathbb{N}}$ *such that* μG_m *is computable uniformly in* m. *A set* $Z \subseteq \mathbb{N}$ fails *the test if* $Z \in \bigcap_m G_m$, *otherwise* Z passes *the test.* Z *is Schnorr random if* Z *passes each Schnorr test.*

Definition 4 *A* martingale *is a function* $d : 2^{<\mathbb{N}} \to \mathbb{R}_{\ge 0}$ *that satisfies for every* $\sigma \in 2^{<\mathbb{N}}$ *the averaging condition* $d(\sigma) = \frac{d(\sigma 0)+d(\sigma 1)}{2}$. *A martingale* d succeeds *on a set* A *if* $\limsup_{n\to\infty} d(A \upharpoonright n) = \infty$.

Definition 5 *We say that* Z *is* computably random *if no computable martingale succeeds on* Z.

We use ML, W2R, SR, CR to denote the set of 1-random, weakly 2-random, Schnorr random and computably random reals respectively.

References

[1] Liang Yu. Characterizing strong randomness via Martin-Löf randomness. Annals of Pure and Applied Logic, vol. **163**, no. 3, pp. 214-224, 2012.

[2] David Diamondstone. Low upper bounds in the LR degrees. Annals of Pure and Applied Logic, vol. **163**, no.3, pp. 314-320, 2012.

[3] NingNing Peng, Kojiro Higuchi, Takeshi Yamazaki and Kazuyuki Tanaka Relative Randomness for Martin-Lö f random Sets. Lecture Notes in Computer Science, vol.**7318**, pp 581-588, 2012.

Lowness and Highness

Definition 1 *Let* R *and* S *be two randomness notions. We identify these notions with the sets of all random reals in the sense of these notions.*

$$\mathrm{Low(R,S)} = \{X \in 2^\omega : \mathrm{R} \subset X\text{-S}\}$$

$$\mathrm{High(R,S)} = \{X \in 2^\omega : X\text{-R} \subset \mathrm{S}\}$$

where X-R *and* X-S *are relativizations of* R *and* S *to* X, *respectively.*

We can prove Q3 is equivalent to Q5:

Question 5 $\mathrm{R} = \bigcap_{X\in\mathrm{Low(R,S)}} X\text{-S}$ *or* $\bigcup_{X\in\mathrm{High(R,S)}} X\text{-R} = \mathrm{S}$?

Answer a Problem

Theorem 1 (Yu, 2012) *$\emptyset'$-Schnorr randomness* $= \bigcap_{X\in\mathbb{L}} X - MLR$.

where $\mathbb{L}$ is the set of all the low sets.

Problem 1 (Yu, 2012) *Does $\emptyset'$-Schnorr randomness* $= \bigcap_{X\in\mathbb{L}\cap\mathbb{G}} X - MLR$?

where $\mathbb{G}$ is the set of all the 1-generic sets.

Theorem 2 *For any $\emptyset'$-Schnorr test* $\{\mathcal{U}_e\}_{e\in\omega}$, *there exist a low 1-generic real* Z *and a* Z*-Martin-Löf test* $\{\mathcal{V}_e\}_{e\in\omega}$ *with* $\bigcap_{e\in\omega}\mathcal{U}_e \subset \bigcap_{e\in\omega}\mathcal{V}_e$.

Method of proof: A finite injury argument.

Corollary 1 *$\emptyset'$-Schnorr randomness* $= \bigcap_{X\in\mathbb{L}\cap\mathbb{G}} X - MLR$.

This give an affirmative answer to Yu's problem. Recall that a real A is said to be *LR-reducible* to B, abbreviated $A \le_{\mathrm{LR}} B$, if every real Martin-Löf random relative to B is also Martin-Löf random relative to A.

Theorem 3 (Diamondstone, 2012) *For any low real* X, Y, *there exists a low c.e. real* Z *such that* $X, Y \le_{\mathrm{LR}} Z$.

We have the following similar theorem:

Theorem 4 *For any low real* X, Y, *there exists a low 1-generic real* Z *such that* $X, Y \le_{\mathrm{LR}} Z$.

Positive and Negative

Positive Answer to Q1 and Q2:

Theorem 5 (Yu, 2012)
$\bigcup_{X\in\mathrm{High}(\mathrm{MLR},\emptyset'\text{-SR})} X\text{-MLR} = \emptyset'\text{-SR}$

This is a positive answer for Q1' in the uniou part. In fact, Yu also shown that Γ can be $MLR \cap High(ML, \emptyset' - SR)$. This is a interesting answer of Q2.
We give a New Characterization of MLR.

Theorem 6 $\bigcup_{X\in PA} X\text{-CR} = \mathrm{MLR}$.

Negative Answer to Q1 and Q2:

Yu, Merkle's answers:

Theorem 7 (Yu, 2012) $\neg\exists\Gamma \subset 2^\omega$ *such that* $W2R = \bigcap_{x\in\Gamma} X - MLR$.

Theorem 8 (Merkle and Yu, 2013) $\neg\exists\Gamma \subset 2^\omega$ *such that* $W2R = \bigcup_{x\in\Gamma} X - MLR$.

Our answers:

Theorem 9 $\mathrm{SR} = \bigcap_{X\in\mathrm{Low(CR,SR)}} X\text{-SR} \ne \mathrm{CR}$.

Theorem 10 $\emptyset' - SR = \bigcup_{X\in\mathrm{High(SR,CR)}} X\text{-SR} \ne \mathrm{CR}$.

Theorem 11 $\bigcap_{X\in\mathrm{Low(W2R,CR)}} X\text{-CR} \ne \mathrm{W2R}$.

Summary of Results

$\bigcup_{X\in\mathrm{High(R,S)}} X\text{-R} = \mathrm{S}$ $\qquad$ $\bigcap_{X\in\mathrm{Low(R,S)}} X\text{-S} = \mathrm{R}$

R \ S	0'-SR	W2R	MLR	CR	SR
0'-SR		Yes	Yes	?	Yes
W2R	?		No	No	No
MLR	Yes	No		?	?
CR	?	?	Yes		No
SR	Yes	No	No	No	

Deformations of isotropic submanifolds in Kähler manifolds

Satoshi Ueki
(Department of Mathematics, Tohoku University, D2)

Background

(P^{2n}, ω, J, g) : Kähler mfd
$M^k \subset P$: isotropic or Lagrangian submfd

Definition

- M : isotropic $\overset{\text{def}}{\Longleftrightarrow} \omega|_M \equiv 0$
- M : Lagrangian $\overset{\text{def}}{\Longleftrightarrow} \omega|_M \equiv 0,\ k = n$

Hamiltonian volume minimizing problem

Find $M \subset P$ which is Hamiltonian volume minimizing

i.e. $\mathrm{vol}(M) \leq \mathrm{vol}(\phi(M))$ for $^\forall \phi \in \mathrm{Ham}(P, \omega)$

Remark $M \subset P$: Ham vol min
$\Longrightarrow M \subset P$: Hamiltonian stable
$\Longrightarrow M \subset P$: Hamiltonian minimal

Definitions and Properties

$M \subset P$: isotropic submfd
$\Longrightarrow T^\perp M = J(TM) \oplus \nu$
$\iota_t : M \to P$: deformation of M
$\xi_t := \dfrac{d}{dt}\iota_t$: variation vector field
$\alpha_{\xi_t} := \omega(\xi_t, \cdot) \in \Omega^1(M)$

Definition

- ι_t : isotropic deform
  $\overset{\text{def}}{\Longleftrightarrow} \iota_t^* \omega = 0\ (^\forall t)$
  $\Longleftrightarrow d\alpha_{\xi_t} = 0\ (^\forall t)$ ($\because$ Cartan's formula)
- ι_t : exact deform
  $\overset{\text{def}}{\Longleftrightarrow} \alpha_{\xi_t}$: exact
- ι_t : Hamiltonian deform
  $\overset{\text{def}}{\Longleftrightarrow} \iota_t = \phi_h^t$ for some $h_t \in C^\infty(N(M))$

Remark ξ : exact vari, $\xi = \eta + \rho\ (\eta \in J(TM),\ \rho \in \nu)$
$\Longrightarrow \eta$: Ham vari

Definition

- $M \subset P$: isotro(, exact, Ham) minimal
  $\overset{\text{def}}{\Longleftrightarrow} \left.\dfrac{d}{dt}\right|_{t=0} \mathrm{vol}(\iota_t(M)) = 0$
  for $^\forall \iota_t$: isotro(, exact, Ham) deform

Proposition [B. Chen, J-M. Morvan]

- $M \subset P$: exact minimal
  $\Longleftrightarrow d^* \alpha_H = 0$ (H : mean curv vec of $M \subset P$)

Definition

- $M \subset P$: isotro(, exact, Ham) stable
  $\overset{\text{def}}{\Longleftrightarrow} M \subset P$: isotro(, exact, Ham) minimal
  & $\left.\dfrac{d^2}{dt^2}\right|_{t=0} \mathrm{vol}(\iota_t(M)) \geq 0$
  for $^\forall \iota_t$: isotro(, exact, Ham) deform

Main Result

Theorem

P^{2n} : Kähler mfd
$Q^{2k} \subset P^{2n}$: totally geod Kähler submfd
$M^k \subset Q^{2k}$ cpt Lag submfd
($\Longrightarrow M \subset P$: isotro submfd)

(1) $M \subset Q$: Ham minimal
$\Longrightarrow M \subset P$: exact minimal

(2) P : nonposi sec curv, $M \subset Q$: minimal
$M \subset Q$: Ham stable
$\Longrightarrow M \subset P$: exact stable

proof

(1) " m.c.v. of $M \subset Q$ " = " m.c.v. of $M \subset P$ "

(2) ξ : exact vari, $\xi = \eta + \rho\ (\eta \in J(TM),\ \rho \in \nu)$

$$\left.\frac{d^2}{dt^2}\right|_{t=0} \mathrm{vol}(\iota_t(M))$$
$$= \int_M \left(\|\nabla^\perp \xi\|^2 - \|A_\xi\|^2 - \textstyle\sum_{i=1}^k \langle R(e_i, \xi), \xi), e_i \rangle \right)$$
$$= \int_M \Big(\|\nabla^\perp \eta\|^2 - \|A_\eta\|^2 - \textstyle\sum_{i=1}^k \langle R(e_i, \eta), \eta), e_i \rangle + \|\nabla^\perp \rho\|^2 - \textstyle\sum_{i=1}^k \langle R(e_i, \rho), \rho), e_i \rangle \Big)$$
$$\geq 0$$

Quasi-stationary distributions for Markov processes and its applications

Seunghwan, Yang
Department of Mathematics, Tohoku University

Introduction

We study the problem of the existence and uniqueness of quasi-stationary distributions(QSD). The study of quasi-stationary distributions for branching processes began with the work of Russian Mathematician A. M. Yaglom. In [i], P.A.Ferrari et al. study the problem for general continuous Markov Processes and E.A.van Doorn consider the problem for birth and death processes. In particular in [ii] a necessary and sufficient condition for the existence and uniqueness is obtained. By applying this result, we check the existence and uniqueness of quasi-stationary distribution for three typical models, birth and death processes with constant rates, linear birth and death processes and logistic birth and death processes. We consider the application of quasi-stationary distribution on field of demography or biology.

The general theory for QSD

Notations and Assumptions Let $\{X_t : t \le 0\}$ be a continuous time Markov process on a state space E of form $0 \cup \{1, 2, \cdots\}$, where 0 is an absorbing state and $E^* := \{1, 2, \cdots\}$ is a irreducible transient class. Let Q be the corresponding transition rate matrix whose component q_{ij} represents the rate of jumping from i to j. We assume that Q is conservative and honest. Let T_0 be the first hitting time at 0, $T_0 = \inf\{t \ge 0 \ ; \ X_t = 0\}$. We further assume that the expectation of T_0 is finite for any $i \in E^*$.

Definitions

1) $\alpha \in \mathcal{P}(E^*)$: quasi-stationary distribution (QSD)

$$\overset{\text{def}}{\iff} \alpha(A) = \mathbb{P}_\alpha(X_t \in A |\, T_0 > t),\ \forall t \ge 0,\ A \subset E^*$$

2) $\alpha \in \mathcal{P}(E^*)$: quasi-limiting distribution (QLD)

$$\overset{\text{def}}{\iff} \exists\, \nu \in \mathcal{P}(E^*) \text{ s.t. } \alpha(A) = \lim_{t\to\infty} \mathbb{P}_\nu(X_t \in A |\, T_0 > t),\ A \subset E^*$$

3) $\alpha \in \mathcal{P}(E^*)$: Yaglom limit

$$\overset{\text{def}}{\iff} \alpha(A) = \lim_{t\to\infty} \mathbb{P}_x(X_t \in A |\, T_0 > t),\ \forall x \in E^*,\ A \subset E^*$$

$$\text{QSD} \iff \text{QSD} \Longleftarrow \text{Yaglom limit.}$$

The existence of QSD Under the above assumptions and the following condition;

$$\lim_{i\to\infty} \mathbb{P}_i(T_0 < t) = 0 \ \text{ for any } t \ge 0,\ i \in E^*,$$

we see from [i] that the existence of quasi-stationary distribution is equivalent to

$$\mathbb{E}_i[e^{\lambda T_0}] < \infty,$$

for some $\lambda > 0$ and for some $i \in E^*$ (and hence for all i).

In case of birth and death processes

Notations and Assumptions We consider a birth and death process on E with birth coefficients λ_i and death coefficients μ_i, for $i \in E$. We assume that $\lambda_0 = \mu_0 = 0$, $\lambda_i > 0$, $\mu_i > 0$, $i \ge 1$. We further assume that the eventual absorption at 0 is certain. This condition is equivalent to

$$\sum_{i=1}^{\infty} \frac{1}{\lambda_i \pi_i} = \infty \ \text{ where } \pi_1 = 1;\ \pi_i = \frac{\lambda_1\lambda_2\cdots\lambda_{i-1}}{\mu_2\mu_3\cdots\mu_i},\ i = 2, 3, \cdots.$$

In case of birth and death processes, the transition probabilities is given by

$$P_{ij}(t) = \pi_j \int_0^\infty e^{-xt} Q_i(x) Q_j(x) d\psi(x),$$

where ψ is the unique positive probability measure on $[0, \infty)$. Let ξ_1 be the infimum of support of ψ. Then ξ_1 plays a crucial role on the existence of quasi-stationary distribution together with the following sum;

$$S = \sum_{n=1}^{\infty} \frac{1}{\lambda_n \mu_n} \sum_{i=n+1}^{\infty} \pi_i.$$

The existence of QSD

Theorem ([ii]) A necessary and sufficient condition for the existence of QSD is as follows;

1) If the sum S converges, then $\xi_1 > 0$ and there is precisely one QSD.
2) If the sum S diverges and $\xi_1 > 0$, then there is a one-parameter family of QSDs.
3) If the sum S diverges and $\xi_1 = 0$, then there is no QSD.

Examples

1) birth and death processes with constant rates; If $\lambda_i = \lambda$, $\mu_i = \mu$, $i \ge 0$, then the Yaglom limit is $a_j = j(1-\beta)^2\beta^{j-1}$, for $j = 1, 2, \cdots$. If $\mu > \lambda$, then $\xi_1 = (\sqrt{\lambda} - \sqrt{\mu})^2 > 0$ and $S < \infty$. So, there is a unique quasi-stationary distribution. If $\mu = \lambda$, then $\xi_1 = 0$ and there is no quasi-stationary distribution.
2) linear birth and death processes; If $\lambda_i = i\lambda$, $\mu_i = i\mu$, $i \ge 0$, then the Yaglom limit is $a_j = (1 - \frac{\lambda}{\mu})\left(\frac{\lambda}{\mu}\right)^{j-1}$, for $j \ge 1$. So $\xi_1 = \mu - \lambda > 0$, $S = \infty$. Therefore, There are infinitely many QSDs.
3) logistic birth and death processes; If $\lambda_i = \lambda i$, $\mu_i = \mu i + ci(i-1)$, $i \ge 0$, the infinite is a entrance boundary in Feller's sense. This implies that the sum S converges. So, there is a unique QSD.

The application of QSD

In demography or biology, the extinction rate of X starting form μ at time $t \ge 0$ is given by

$$\gamma_\mu(t) = -\frac{\frac{\partial}{\partial t}\mathbb{P}_\mu(T_0 > t)}{\mathbb{P}_\mu(T_0 > t)}.$$

If α is a QLD for X started from a probability measure μ on E^*, then

$$\lim_{t\to\infty} \gamma_\mu(t) = \gamma_\alpha(0).$$

That is, the existence of a QLD for X with initial distribution μ implies the existence of a long term mortality plateau.

References

i) P. A. Ferrari, H. Kesten, S. Martínez and P. Picco, Existence of quasi-stationary distribution. A renewal dynamical approach., *Ann. Probab.*, **23** (1995), 501-521.

ii) E. A. van Doorn , Quasi-stationary distributions and convergence to quasi-stationarity of birth-death processes, *Adv. in Appl. Probab*, **23** (1991), 683-700.

P-78

Optimal stopping and its applications to mathematical finance

Xiaohan Wang

Mathematical Institute, Tohoku University, Japan

Optimal stopping problems often arise when we need to find the best time or the best decision rule to make actions. These kinds of problems often exist in economics and finance, for example, to find the optimal stopping time to exercise an American type option.

In general, an optimal stopping problem has the following descriptions: let $(\Omega, \mathcal{F}, \mathbb{P})$ be a complete probability space with a standard Brownian motion $B = \{B_t; t \geq 0\}$, and consider the diffusion process on state space $I = (a, b) \subseteq \mathbb{R}$ with endpoints $-\infty \leq a < b \leq \infty$ and dynamics

$$dX_t = \mu(X_t)dt + \sigma(X_t)dB_t, \quad X_0 = x,$$

with coefficients μ and σ satisfying certain conditions. Let $h(x)$ be the reward function, Λ_t be the discounting rate functional of X_t. Then the value function is

$$v(x) = \sup_{\tau \in \mathcal{T}} \mathbb{E}_x[e^{-\Lambda_\tau} h(X_\tau)], \quad x \in (a, b)$$

where $\mathcal{T}$ is a set of stopping times.

Objectives of an optimal stopping problem

- characterize the value function by an analytical form (even an explicit form, if possible);
- find the optimal stopping time to maximize the expectation shown in the expression of the value function.

The Big Question

Under the Ito diffusion models, the cases with continuous and bounded reward functions have already been thoroughly researched in the recent decades while the irregular reward function cases, for example, the reward function is discontinuous and/or unbounded, are still not so clear.

Methods

- **Variational Characterization**
  The optimal stopping problem can be formulated as a free boundary value problem by means of variational arguments. This approach is very general and can be extended to multi-dimensional problems, but it requires ellipticity of the diffusion and some regularity of the reward function. This method becomes challenging when the reward function is discontinuous and unbounded. Lamberton and Zervos[2006] constructed the relationship between the variational inequality and optimal stopping problem in the infinite horizon case without the requirement of the continuity and allowing the possibilities that it is unbounded. Lamberton[2009] considered the finite horizon case for very general one-dimensional diffusion only requiring the reward function to be Borel measurable and bounded.
- **Excessive Characterization**
  The value function is excessive with respect to the underlying process. According to Dayanik and Karatzas[2003], by the equivalence between the excessivity and the concavity , the value function of the optimal stopping problem can be characterized as the smallest nonnegative generalized concave majorant of the reward function.

Application

Considering the Down-and-in gap put option, refer to the following figure for the positive payoff area and the reward function.

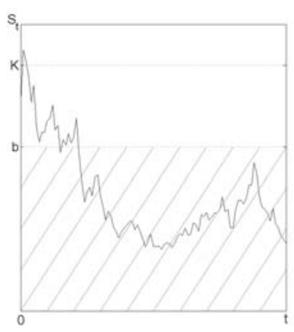

(a) Positive payoff area

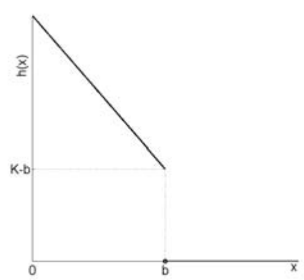

(b) Reward function

Figure: Reward Function

For the basic notations, let K be the strike price, b the barrier line, σ the volatility of the stock price and r the risk free interest rate. Let $(\Omega, \mathcal{F}, \mathbb{P})$ be a complete probability space with a standard Brownian motion B_t. Assume the price of the underlying asset satisfies the SDE:

$$dS_t = S_t(rdt + \sigma dB_t), S_0 = x,$$

with state space $I = (0, \infty)$. Then both boundaries are natural in the sense of Feller's classification. Denote $\{\mathcal{F}_t\}$ the natural filtration of S. Given the reward function $h(x)$, the value function is defined by

$$v(x) = \sup_{\tau \in \mathcal{T}} \mathbb{E}_x[e^{-r\tau} h(S_\tau)], \quad x \in (0, \infty),$$

where $\mathcal{T}$ is the set of finite stopping times.

- **Variational Characterization**
  By the variational arguments, we can obtain the value function if we can construct the corresponding variational inequality and solve it. The following theorem solves such problem.

Theorem [Variational Inequality]

If a number $q \in (0, b]$ and a convex decreasing function u in $C([0, \infty)) \cap C^2((0, \infty) \setminus \{q\})$ satisfy the following variational inequality:

$$\begin{cases} \frac{1}{2}\sigma^2(x)u''(x) + rxu'(x) - ru(x) < 0, & 0 < x < q, \\ \frac{1}{2}\sigma^2(x)u''(x) + rxu'(x) - ru(x) = 0, & q < x < \infty, \\ u(x) = h(x), & 0 < x < q, \\ u(x) > h(x), & q < x < \infty, \end{cases}$$

then $u(x)$ coincides with the value function $v(x)$ of the above optimal stopping problem. Moreover, the stopping time,

$$\tau_{(0,q]} := \inf\{t \geq 0 | S_t \leq q\},$$

is optimal.

This variational inequality can be solved using the smooth-fit principle when $K(1 - 1/\beta) < b$.

- **Excessive Characterization**
  Denote by $\mathcal{L}$ the infinitesimal generator of the above diffusion. Then equation $\mathcal{L}u = ru$ has two linearly independent, positive solutions $\psi(x)$ and $\varphi(x)$: $\psi(x)$ is strictly increasing and $\varphi(x)$ is strictly decreasing. Denote $F(x) = \psi(x)/\varphi(x)$ and $G(x) = -\varphi(x)/\psi(x)$, $x \in [c, d]$, $p(x)$ be the scale function of the above diffusion. The following result will be essential.

Theorem (Dayanik and Karatzas[2003])

The value function is the smallest nonnegative concave majorant of $h(x)$ on (a, b) such that v/φ is F-concave (equivalently, v/ψ is G-concave) on (a, b).

Further according to the relationship between the generalized concave function and the ordinary concave function, we can obtain the explicit form of the value function, which is the same as the former method when $K(1 - 1/\beta) < b$.

Theorem [Value Function]

If $K(1 - 1/\beta) < b$, where $\beta := 1 + 2r/\sigma^2$, then the value function is

$$v(x) = \begin{cases} K - x, & x \in [0, K(1 - 1/\beta)], \\ [K(1 - 1/\beta)]^\beta x^{1-\beta}/(\beta - 1), & x \in (K(1 - 1/\beta), \infty), \end{cases}$$

Moreover, the optimal stopping time is

$$\tau^* = \tau_{(0, K(1-1/\beta)]}.$$

If $K(1 - 1/\beta) \geq b$, then the value function is

$$v(x) = \begin{cases} K - x, & x \in [0, b], \\ (K - b)(x/b)^{1-\beta}, & x \in (b, \infty). \end{cases}$$

Moreover, the optimal stopping time is

$$\tau^* = \tau_{(0,b]}.$$

References

- D. Lamberton, M. Zervos. *On the Problem of Optimally Stopping a One-dimensional Ito Diffusion*, Preprint, 2006.
- D. Lamberton, *Optimal Stopping with Irregular Reward Functions*, Stochastic Process and Their Applications, 2009.
- S. Dayanik, I. Karatzas. *On the Optimal Stopping Problem for One-dimensional Diffusions*, Stochastic Processes and Their Applications, 107(2003), no. 2, pp. 173-212.

Hume's Eclectic Method on Logic

SUGAWARA Hiromichi (Philosophy, D3)
Graduate School of Arts and Letters, Tohoku University

Introduction

In 'Abstract of the Treatise', under the pretense of being a book reviewer of his own work, A Treatise of Human Nature, the 18th century Scottish Philosopher David Hume stated, 'The author has finished what regards logic'. Because it went against the prevailing logic at that time, his logic had a large implication on specific characters. That is, as a matter of form, it inductively pursues the principles of logic into the phenomenological world composed of ideas, rather than deductively in an axiomatic system that holds reasoning as valid from necessary premises. The objects to be treated in his reasoning are only our ideas, and therefore, he studies the mental or moral operations of humans, who are unintentionally engaged in reasoning concerned, as faculties or functions dependent on human nature. It is generally interpreted that he divided reasoning into demonstrative and probable reasoning in the same manner as he divided its objects. He presents, however, the notion in the last section of Book I of Treatise, 'Conclusion of this book', that he could not sincerely devote himself, in his path of life, to only one aspect within the two species of reasoning. On the other hand, he also makes an unanticipated statement in first Enquiry that 'it is, at bottom, erroneous, at least, superficial'. In this presentation, I show his substantial relationship between them.

1. The Role of Hume's Logic

(1) Zabeeh's Insights into Hume's Logic The Sole End of Hume's Logic

Hume stated that 'the sole end of logic is to explain the principles and operations of our reasoning faculty, and the nature of our ideas' (THN intro. xvi). Indeed it might be come down to this one or two points in order to contribute 'the science of man', but he used the term 'logic' in a few manners in his works. F. Zabeeh divided Hume's logic into three parts, which seemingly proper and consistent with each other (Zabeeh 106-107).

① His logic is in part an inquiry into the causal operation of 'our reasoning faculty' (Philosophical Psychology).
② His logic in part consists of rules which an experimental philosophy ought to observe in his search for causal connection (Canons of Induction).
③ His logic in part consists of principles which a philosopher ought to accept if he wants to talk sense and not nonsense (Principle of Meaning).

From these standpoints, he articulated that 'inquiry into the formal relation of terms and propositions (syntactics) is regarded by Hume as trivial and pretended reasoning'. But I think ③ is integrated into ①, whereas ① and ② are rightly classified. So, I will replace ③ with my own view finally.

(2) The Sole End of Hume's Logic

Now, what does logic mean specifically for Hume? I think that to answer the fair-seeming question, we should firstly pay attention to his criticism on existing and prevailing logic that was still taught at schools in those days.

This error consists in the vulgar division of the acts of the understanding, into *conception*, *judgment*, and *reasoning*, and in the definitions we give of them. […] But these distinctions and definitions are faulty in very considerable articles. (THN 1.3.7.n2)

What we may in general affirm concerning these three acts of the understanding is, that taking them in a proper light, they all resolve themselves into the first, and are nothing but particular ways of conceiving our objects. […] <u>the act of the mind exceeds not a simple conception</u>. (ibid.)

This kind of division of them we can easily find in the famous texts of logic in early-modern times (Alnauld & Nicole, Watts, &c.). As opposed to them, he claims that we can naturally conceive *the* proposition composed of only one idea. This claim call a view like that Hume's claim for demonstrative certainty entails needs for 'mere forms or essences' (Anderson 59-63). But I think that demonstrative certainty consists only in setting proportions in arithmetic, not in all the systems of mathematics or algebra.

2. Counterarguments to Hume's Requiring Certainty

(1) Weintraub's Tentative Theory for Justification of Inference

R. Weintraub presented three possible responses in cases of the justification of a form of inference (Weintraub 464). Her points consist in whether a mode of inference itself can be justified or not, and the reasons of those judgments in each cases.

(A) A mode of inference can be *basic* – justified, but not by reference to another.
(B) Its justification might be mediate.
(C) It may be unjustified.

According to her, Hume chose (c) with respect to 'induction'. The reason for ruling out (A) is that induction is not basic (intuitive). And the reason eliminating (B) is that induction can not be justified *inferentially*; because 'it has no deductive justification', though if inductive justifications had some mediate (e.g. the uniformity of nature), only to circular.

On the other hand, she construed Hume as practically picking out (A) in case of 'deduction'. The reason for excluding (B) depends on what Hume said, 'the same principle cannot be both the cause and effect of another' (THN 1.3.6.7). And the reason ruling out (C) derives from his stance not adopting skeptical attitudes towards deduction.

But I disagree with her conclusion in case of deduction. Hume *never* countenance deduction or 'arguments a priori' as being possible to be justified as well as induction. Because they are appreciated in terms of our assurance of reasoning.

(2) Impermanency of Total Skepticism

Hume presented skeptical arguments with our reason in *Treatise* as follows.

'In all demonstrative sciences the rules are certain and fallible; but when we apply them, our fallible and uncertain faculties are very apt to depart from them, and fall into error'. (THN 1.4.1.1)

'Since therefore <u>all knowledge resolves itself into probability</u>, and becomes at last of the same nature with that evidence, which we employ in common life…'. (THN 1.4.1.4)

It is true that when he observe 'all knowledge resolve itself into probability', he does not necessarily assent to that kind of skeptical arguments. Rather he instead implies <u>the influences for us to correct the first or prior judgments from the skeptical perspective of our reason</u>, whereas the claims of total skepticism with regard to our reason or senses remain self-destructive; and also our unreliable faculties may *still* often make mistakes in demonstrative sciences.

For Hume if this kind of skepticism, if ever not so strong as to break up demonstrative sciences, has the role to support us, who are engaged in that sciences or other, then the first or prior judgments, relatively speaking, would practically take the character of probability, which has no certainty therefore requires many corrections up to gaining generalities.

3. Skeptical Arguments against his Dichotomy

Thus, Hume's dichotomy on the issue of our reasoning , or division between argumentation from reason and experience could be open to doubt, especially in that for him each reasoning is always treated as independently in academic or social fields. He observes in first *Enquiry* as follows.

'Though it be allowed, that reason may form very plausible conjectures with regard to the consequences of such a particular conduct in such circumstances; it is still supposed imperfect, without the assistance of <u>experience, which is alone able to give stability and certainty to the maxim, derived from study and reflection</u>'. (EHU 5.1.n1)

'But notwithstanding that this distinction be thus universally received both in the active and speculative scene of life, I shall not scruple to pronounce, <u>that is, at bottom, erroneous, at least superficial</u>'. (ibid.)

But I think these are not problematic views but natural results of his standpoint. Because for Hume reasoning, either inductive or deductive, is irrelevant to their justification. As far as I know, Hume nowhere refers reasoning to be justified in his works.

4. Eclectic Method according as our Ends

To reconcile these seemingly paradoxical circumstances, I should comprehend what he implies in adopting reasoning from reason in our investigations; for example in physics. Of course, we do not always adopt reasoning only from reason, because we assume that what occurs in the phenomenological world can be inquired from the standpoints of causes and effects as ideas.

Mathematics, indeed, are useful in all mechanical operations, and arithmetic in almost every art and profession: But (sic) 'tis not of themselves they have any influence. Mechanics are the art of regulating the motions of body <u>*to some design'd end or purpose*</u>; and the reason why we employ arithmetic in fixing the proportions of numbers, is only that <u>we may discover the proportions of their influence and operation</u>. (THN 2.3.3.2)

We are conscious, that we ourselves, in adopting means to ends, are guided by reason (sic) and design, and that 'tis not ignorantly nor casually we perform those actions, which tend to self-preservation, to the obtaining pleasure, and avoiding pain. (THN 1.3.16.2)

Hume regards judgment from demonstration as useful and helpful as a means to 'matters of fact' which, like natural philosophy, inquires causally. And the ends lie in knowing the nature of what we quest for. This is the point peculiar to Hume's logic that Zabeeh overlooked. And this argument above consistent with his view of 'two kinds of truth' that one is the discovery of the proportions of ideas, the other is 'the conformity of our ideas of objects to their real existence', which, in effects, desired as an exemplary stage.

References

ATHN: Hume, David. [1740], *An Abstract of a Book lately Published; Entitled, A Treatise of Human Nature*, in THN.
EHU: -------- [1748], *An Enquiry concerning Human Understanding*, in *Enquiries concerning Human Understanding and the Principles of Morals*, edited by L.A.Selby-Bigge, revised by P.H.Nidditch.
THN: -------- [1739-40], *A Treatise of Human Nature*, edited by L.A.Selby-Bigge, revised by P.H.Nidditch.
Anderson, R. F., [1966], *Hume's First Principles*.
Arnauld, Antoine. And Nicole, Pierre. [1662], *La Logique ou l'Art de Penser: Contenant, outré les Regles communes, plusieurs observations nouvelles propres à former le iugement*.
Beauchamp, T. L., and Rosenberg, Alexander. [1981], *Hume and the Problem of Causation*.
Beebee, Helen. [2006], *Hume on Causation*.
Broughton, Janet. [1983], 'Hume's Skepticism about Causal Inferences', in Pacific Philosophical Quarterly, Vol.64.
Descartes, René. [1637] *Œvres de Descartes*, Tome V et VI, publiées par C. Adam et P. Tannery.
Gaukroger, Stephen. [1989], *Cartesian Logic: an Essay on Descartes's Conception of Inference*.
Echelbarger, Charles. [1987], 'Hume on Deduction', in Philosophy Research Archives vol.13
-------- [1997], 'Hume and the Logician', in *Hume: General Philosophy*
Freydberg, Bernard. [2012], *David Hume: Platonic Philosopher, Continental Ancestor*.
Harrison, Jonathan. [1976], *Hume's Moral Epistemology*.
Jones, Peter. [1982], *Hume's Sentiments: their Ciceronian and French Context*.
Locke, John. [1689], *An Essay concerning Human Understanding*, edited by P. H. Nidditch.
Jones, Peter. [1982], *Hume's Sentiments: their Ciceronian and French Context*.
Locke, John. [1689], *An Essay concerning Human Understanding*, edited by P. H. Nidditch.
Mackie, J. L. [1979], 'A Defence of Induction', in *Perception and Identity Essays Presented to a A. J. Ayer with his Replies to them*, edited by G. Macdonald (pp.115-116).
Moody, E. A. [1966], 'The Medieval Contribution to Logic', in Studies in Medieval Philosophy, Science, and Logic.
Owen, David. [1999], *Hume's Reason*.
Passmore, J. A. [1952], *Hume's Intentions*.
Serjeantson, R. C. [2005], 'Hume's General Rule and the 'Chief Business of Philosophers'', in *Impressions on Hume*, edited by M. Frasca-Spada and P. J. E. Kail.
Stove, D. C. [1965], 'Hume, Probability, and Induction', in *David Hume: Critical Assessments* Volume 2, edited by Stanley Tweyman.
Tweyman, Stanley. [1974], *Reason and Conduct in Hume and his Predecessors*.
Watts, Isaac. [1726], *Logick: or, The Right Use of Reason*.
Weintraub, Ruth. [1995], 'What was Hume's Contribution to the Problem of Induction?', in Philosophical Quarterly vol.45
-------- [1997], *The Sceptical Challenge*.
Winters, Barbara. [1979], 'Hume on Reason', in *David Hume: Critical Assessments* Volume 1, edited by Stanley Tweyman.
Zabeeh, Farhang. [1960], 'Hume's Scepticism with regard to Deductive Reason', in *David Hume: Critical Assessments* Volume 1, edited by Stanley Tweyman.
-------- [1960], *Hume: Precursor of Modern Empiricism*.

From Heroism to the Politics of Dialogue

Satoshi Nikaido,Department of Philosophy,Tohoku University

Introduction

Maurice Merleau-Ponty, the French phenomenological philosopher, often mentions heroism in his works. However, his meaning of heroism is different from previous types of heroism. Therefore, this poster presentation defines heroism according to Merleau-Ponty.

Heroism (until the Modern Age)

In ***Sens et non-sens***, Merleau-Ponty states that heroism is always present. Yet, according to him, its meaning has been changed by his contemporaries. The following are previous types of heroism, as shown by Merleau-Ponty.

1) Until the Modern Age, the hero was thought to be a representative of the will of God who was present in the world. However, by the time of philosophers such as Hegel and Nietzsche, people were unable to believe in transcendent existence outside of the living world.

2) For Hegel, a hero (under the older definition) was the protector of the world and the hero created (through his actions) new laws and moralities that the following era would recognize as the truth. In other words, this hero did what the history of the world wanted and he sacrificed himself for the future.

However, such an antiquated type of heroism was no longer the belief for Merleau-Ponty and his contemporaries since they no longer believed that there were pre-established harmonies and an ideal direction for future society in the present world.

3)For Nietzsche, the hero did not care about God and the rational flow of history and this type of heroism regarded the ruler. However, it was impossible to dominate absolutely after the hero's death.

Heroism (Merleau-Ponty and his contemporaries)

People do not believe in such antiquated types of heroism, but they still believe in heroism. Merleau-Ponty considers how the meaning of the hero has changed by focusing on the hero as an actual human being. In ***Phénoménologie de la perception***, Merleau-Ponty explains his theory of human nature by presenting humans as existing or ***être au monde***. Such existence in physical form has certain implicit and unachieved meanings about the world, especially in the relationship between the world and the physical body that can move, express, and think. Due to such a link, a human can comprehend others and establish friendships through individual efforts. Ideally, a hero, as a part of this world, assumes his and others' situations, and never betrays his comrades. Such a human is the hero according to Merleau-Ponty and his contemporaries.

Concretely, facing a crisis or even his death, for what hero attempts to fulfill this mission? With a clear goal, it is easy to serve, but if it is not clear, then does he not regard the significance of his own death? The sacrifice,his practice is not for what history wants(Hegel),not for Thanatos(Nietzsche), not for service futile. He sacrificed himself in order to present and prove to himself and others what he and his comrades believe(for example freedom ,equality)are true.

Conclusion

This poster presentation first classified the antiquated types of heroism according to Merleau-Ponty and then defined heroism as presented by Merleau-Ponty and his contemporaries.

In addition, in ***Sens et non-sens***, Merleau-Ponty also often mentions politics. I think that focusing on the relationship between the hero and others is helpful when studying how Merleau-Ponty considered the relationship political between a leader and masses of poeple. In the scene of policy making,to become a hero ,to be trusted by masses of people,a leader has to assume his and others' situations, and he has to continue dialogue with the world and others.Because he as a human is not the representative of the will of God nor the representative of history.

Reference

M.Merleau-Ponty, *Phénomenologie de la perceptio*n(1945),Gallimard,coll.«Tel,"2005

M.Merleau-Ponty,*Sens et non-sens*(1948),Gallimard,1995

P-81

Individuality and historicity of life :
- From Dilthey's middle and late speculations -

Marika Hirama
Department of Philosophy, Tohoku University

1. Introduction : Psychic structure and historicity of individual life

In his late speculation, which is commonly known as "life philosophy," Wilhelm Dilthey shifted his interest from the middle phenomenological and descriptive analysis of the individual mind to the interpretation of the historical world in which we live and act. In this case, the historical world is the spiritual one formed by human beings historically and the one in which we innerly experience and act upon. In addition, this world is clearly distinguished from the mere nature that exists outside of our minds. According to Dilthey, the subject that forms history is always "the mind, which lives, acts, bears the power of forming, and reacts sensitively to all the influences" (Ⅶ, 254). In other words, the fact that the individual grasps, feels the world, and actively works on this world is the key to interpreting the historical world. Dilthey's subject of analysis is the structure of the mind's total ability to become a universal relational form to the world.

Each individual in their process of growth gradually develops the mind's ability of thinking, feeling, and willing, each of which forms the conceptual, self, and practical knowledge in the world. Dilthey referred to the individual mind's total ability as the "psychic acquired nexus" (das erworbene Zusammenhang). This nexus develops purposively in each individual history of growth. However, it is also formed by the common historical context, for example, the social community as family, political or legal organization, culture, and age. These common realms in the historical world always surround and influence the individual beyond their own life and the history of the individual is brought up only under the background of communal or all of humankind's history. Therefore, each individual's psychic acquired nexus "demonstrates both general and more individual characteristics" (Ⅴ, 225–26).

2. Individuality and productive nexus (Wirkungszusammenhang) of the historical world

In his late argument of history, Dilthey focuses his attention much more on the productive nexus in the historical world, which operates beyond the individual. According to Mul, "Although this world is produced by human beings, in its complex nexus it stands opposite the individual as a nexus that precedes him and affects him continuously and deeply" (2004, 261). The social and cultural communities (or the political and economic organizations) are common spiritual realms that consist of the individual and, at the same time, form the purposive nexus independent of the individual mind's purposive nexus. In this case, Dilthey believes that the productive nexus of the communal organization and the purposive nexus of the individual mind is continuous: "It is indeed in this psychic structure that the character of purposiveness is originally given and when we attribute this to an organism or to the world, this concept is only borrowed from the inner lived experience" (Ⅴ, 210).

Furthermore, according to Dilthey, the individual action is, on one hand, dependent on the communal motivation, which is not necessarily awakened by the individual. Each individual, as one unity of life, possesses a complete closed psychic system. However, at the same time, such a system is open for interaction with the common broader unity of life in the historical world (Ⅶ, 154). The passion or feeling that induces individual action works on the historical world and influences the power of forming. However, each of these is also restricted within the individual inner side and the purpose can differ (Ⅶ, 257). The purpose of the individual act can function as the common purpose beyond the individual. Thus, Dilthey finds that the particularity of the productive nexus of the historical world (with regard to the purpose of the self) can become the common historical purpose.

3. Discrepancy between individuality and objectivity of science

. The problem here is that Dilthey overemphasized the continuance between the individual and the community. In addition, he rarely referred to the possible dangers of organizations operating away from the individual such as the oppression of freedom.

As often criticized, Dilthey (under the influence of Georg Wilhelm Friedrich Hegel) aimed at the ideal and harmonious relationship between the individual and the community by using the Hegelian term "objective spirit." According to Dilthey, an individual's meaning of life lies in the historical nexus that works on the world beyond their and the individual's finiteness is regarded as the aspect to overcome to acquire the objective of understanding life. In this regard, the keystone of Dilthey's philosophy, namely that "the history of man should be sought in the individual who weaves the nexus of life as an element," becomes difficult to explain.

The content of Dilthey's term "objectivity" is important to note. According to Mul, the objectivity of human sciences in Dilthey is clearly distinguished from the universal validity in natural sciences.

In this case, Dilthey's "objectivity" is tied with the "inter-subjectively accessible nexus" of the world (Mul, 2004, 261). More specifically, it depends upon the world shared and understood uniformly by an individual and other people surrounding them. In addition, "the more the world an interpretation reveals … the more objective it is" (ibid). Therefore, the interpretation of the historical world becomes more objective when the world in which the interpreter is embedded becomes clarified.

4. Historicity and temporality of individual life: —from Heidegger's perspective—

According to Johach, Dilthey found that "the interest for the individual action which forms the community is always interfered by the ideal and esthetic interest for the objectification" (1974, 162–163). Accordingly, the task of human sciences, namely "becoming the certain foundation for the world of action" (Ⅶ, 261), was not sufficiently accomplished by Dilthey. This is based on the fact that late Dilthey admitted the superiority of the objectivity of the human spirit, and the finiteness or temporality of life was retired from the main argument. In this regard, this author believes that Heidegger's interpretation of the temporality of life helps to resolve Dilthey's aporia of individuality and the objectivity of life since only the viewpoint of the temporality of acting man and the connection between the individual and objective human history can be found.

Heidegger defined human beings as "beings to the end" (Sein zum Ende), which alludes to the possibility of "being toward the future" in which the past can be initially brought to life for each present action. That is to say, the past history can be most effective by becoming the drive to the future. This supremacy of the future is also an important viewpoint for Dilthey in which he stated that, "every understanding of the past should become the power to form the future" (Ⅷ, 204). As mentioned above, the individual is, on one hand, created by the history of the community or all of mankind. On the other hand, the individual continuously works on the world and forms history. Originally, both of these passive and active aspects of the individual were important, but Dilthey places more emphasis on the already formed common social system compared to the individual action that forms the historical world.

5. Action that links individual historicity to human historicity

Although the temporality and finiteness are isolated by Dilthey in his categorical analysis of life, Dilthey fails to connect these characteristics to the historicity of acting man. Action is supported by the common historical foundation of how to act and the individual mind's psychic acquired nexus is utilized in each situation. In this case, the action includes the character of the peculiar event, which occurs only once in an individual's history. Thus, the individual action appears to be regarded as the point of contact between the historicity of the individual and the history of the human past.

Each state of the historical world are formed and altered by their links with the movement of the individual's mind. The world in which we have lived reveals itself each time in concrete individual actions. Therefore, the point of contact between an individual's and humankind's history can be found in finite actions that must remain focused on the future.

References:

Dilthey, W., *Der Aufbau der geschichtlichen Welt in den Geisteswissenschaften* ;
G. S. Ⅶ, Vandenhoeck & Ruprecht,, 1958
… *Die geistige Welt* ; *G.S. Ⅴ*, Vandenhoeck & Ruprecht, 1957
Mul, J., *The tragedy of finitude* ; Yale University Press, 2004
Jung, M., *Dilthey zur Einführung* ; Junius Verlag, 1996
Johach, H., *Handelnder Mensch und objective Geist* ; Verlag Anton Haim, 1974

‘Formal Ontology’ in *Logical Investigations*

Echigo Masatoshi. Tohoku University, Philosophy.

In *Logical Investigations*, Husserl claims abstract notions also exist in another way, and shows how they relate and depend on each other. In this poster session, I would like to call this structure in *Logical Investigations* formal ontology. In this poster session, the whole structure of the ontology that remains implicit, and evaluation of the ontology are focused on.

1. Categorical Intuition and its founded Character

It is necessary to identify categorical intuition and to distinguish it from sensible intuition before taking up formal ontology. Categorical intuition means intuitions that have no element of sensibility in expressions (XIX/2, 659; 661; 667). For example, to intuit what is expressed in expressions like ‘be’, ‘and’, ‘all’, and ‘some’ is categorical intuition.

What is important here is the ‘founded’ character of categorical intuition. X being ‘founded’ by Y means that X could not exist without Y. Categorical intuition is founded by sensible intuition. From this point of view, Husserl characterizes categorical intuition as ‘higher’ act than sensible intuition. When you intuit something categorically, you intuit something (else) sensuously at the same time.

2. Three Kinds of Abstractions

We have to set the following as a premise of the discussion. ‘Categorical intuitions are finally based on sensuous intuitions’ (XIX/2, 712). On top of that, Husserl distinguishes three kinds of abstractions. ‘We call schlicht act of intuition as sensuous act, and founded act which is reduced to sensuous act mediately or immediately, as categorical act. However what is even more important is to distinguish purely categorical act from act of understanding which is mixed up with sensuousness in categorical acts’ (XIX/2, 712).

Husserl says that sensible abstractions that give purely sensible things, for example, give colors and houses, sensible abstractions mixed up with categorical abstractions give some axioms in geometry and the character of having colors, and purely categorical abstractions that give purely categorical forms give collections, relations, concepts and so on (XIX/2, 713).

3. The Model of Founding Relations in *Logical Investigations*

Now that three kinds of abstractions are made clear, it is necessary to make the model of founding relations in *Logical Investigations* explicit. Each kind of the abstractions is in founding relations each other as follows.

Fig. (arrows mean founding)
A. Sensuous Abstraction
↓
B Categorical Abstraction mixed up with Sensuousness
↓
C purely categorical Abstraction

It matters that, at least in *Logical Investigations*, C can be said to be characterized as different abstraction from B. It is sure that when you intuit mathematical-logical thing, that categorical intuition C has to be founded by B. However C does not totally depends on B while C is founded by A through B. This is because B includes some elements of sensibility and the B founded only by sensible intuitions, not by categorical intuitions. According to Haddock (Haddock 1987), I would like to call B like this ‘premoderial’ B. C does not includes that kind of abstraction. It is sure that C is founded by premoderial B, but C itself has nothing to do with A. That is why C can abstract higher, mathematical-logical objects, and intuit them freely from the boundary of sensibility. This so called ‘gap’ between B and C comes from Husserl’s underlying view to categorical forms.

4. Where is the Gap from?

In *Logical Investigations*, Husserl claims that purely categorical objects exist against us(gegenueberstehen) (XIX/1, 51). However details about the ontological entity of the objects are not spoken of. For example, Husserl revisited this theme, and he contemplates the problem over and over again (XX, 364; 369).

Husserl’s position on the purely categorical notions themselves and categorical notions mixed up with sensuousness is still vargue in *Logical Investigations*. This results in making the ‘gap’.

References

E.Husserl. *Logische Untersuchungen.*, Husserliana XIX/1-2, Martinus Nijhoff, 1984.
-. Logische Untersuchungen Ergaenzungsband 2.TeilHusserliana XX, Martinus Nijhoff, 2005.
G.E.R.Haddock."Husserl's epistemology of mathematics and the foundation of platonism in mathematics." in *Husserl Studies* Vol. 4-2, Martinus Nijhoff, 1987.

Comparative study of the concept of organism between Bergson and Kant

Katsuyuki Kuriyama

(Philosophy, Tohoku University)

Introduction

This is a comparative study of the concept of organism between Henri Bergson and Immanuel Kant. They regard organisms as self-creating and self-organizing respectively. Both these determinations contain the sense of not being made by an external cause. Therefore, the two philosophers' conceptions of organism are sometimes equated (cf. F. Dagognet). This study clarifies how Bergson and Kant consider organisms and indicates the differences between their two approaches by referring to *L'évolution créatrice* (*Creative Evolution*) by Bergson and *Kritik der Urteilskraft* (*Critique of Judgment*) by Kant.

Kant: Organisms are self-organizing.
≒ (in the sense that both mean organisms are not what are made by an external cause)
Bergson: Organisms are self-creating.

→ Differences between them?

Background

With regard to the phenomena of organisms, two doctrines often contend with one another: mechanism and teleology. It is certain that organisms are difficult to explain in terms of mechanism since they have finality or purposiveness. However, people hesitate to adopt teleology since it often introduces supernatural and unobservable factors such as external intelligent cause, purpose, and intention. We call such a teleology "anthropomorphic" since its organisms (according to analogy) are much like watches made by watchmakers. In this kind of situation, another mode of explanation is necessary which can become a doctrine that considers organisms to be self-organizing or self-creating.

Mechanism⇔anthropomorphic Teleology
⇕
The third approach
= The theory of self-organization or self-creation

The concept of organism by Kant

Kant defines organisms as natural purpose (Naturzweck), which includes two determinations:1)
its parts reciprocally produce one another to form its whole; and 2)
the idea of its whole is the cognitive ground for estimating the systematic unity of the form and combination of its parts.

According to the first determination, Kant distinguishes organisms as natural purpose from machines which an intelligent being intentionally produces, for, according to Kant, reciprocal production of the parts never occurs in such machines. The whole of an organism is formed through reciprocal production of its parts, not by an external intelligent cause. In this regard, Kant considers that organized beings are self-organizing.

However, the second determination means that entire organism must be regarded as a purpose by human beings. In this case, only intelligent beings can have purposes, and therefore Kant introduces an intelligent cause for the determinations of organisms.

Of course, Kant does not mean that such an intelligent cause should exist objectively, but that it belongs to the subjective principle according to which we must estimate organisms. However, it remains true that an intelligent cause, whether its existence is regarded as objective or subjective, is inseparable from the phenomena (or concept) of organisms. Therefore, according to Kant, organisms must have an aspect of what are made by an external intelligent cause, and they are not thoroughly self-organizing nor self-creating.

The concept of organism by Bergson

Bergson explains organisms as self-creating according to the following procedures: 1)
negation of the reality of material elements that constitute an organism; and 2)
comprehension of organisms by analogy with psychological duration.

Through the first procedure, the common presupposition of mechanism and teleology is denied. Teleology as well as mechanism supposes that organisms consist of a multiplicity of material elements. In other words, just because the reality of material elements is supposed, there should be an intelligent cause that intentionally produces systematic unity such as organisms. Bergson denies the reality of material elements. According to him, the number of elements is relative to the analysis of an observer. In this manner, Bergson attempts to overcome both mechanism and teleology.

Based on the second procedure, Bergson explains organisms through an analogy with psychological duration. Psychological duration is movement as an indivisible continuity, and it potentially contains distinct moments. It is a certain unity, which is dynamic. This dynamic unity is regarded as more than systematic unity, which is static and given by an external cause. Therefore, through such an analogy with psychological duration, organisms are conceived to be what is self-creating. In another words, Bergson denies the absolute reality of the nature described by science, revises the concept of nature, considers organisms that have more than systematic unity, potentially including it, without ceasing being the natural phenomena.

Conclusion

Based on the findings, we can conclude that in Kant, organisms are not completely explained as what are not made by an intelligent being but self-organizing. On the other hand, according to Bergson, they are not what are made by such a being at all. Kant does not completely detach himself from anthropomorphic teleology.

It is also important to note that there is a difference in the overall position between the two philosophers. Kant considers the concept of natural purpose(organisms) or intelligent cause to be a subjective reality while Bergson insists on the objective validity of his theory of organism.

Problems for future discussion

・Is there some possibility that, in Kant, the characteristic of self-organization in organisms will be compatible with the causality of an intelligent being?

・Is Bergson's analogy of organisms with psychological duration valid? More precisely, what enables Bergson to consider in some sense that movement such as psychological duration is more than systematic unity?

References

・Bergson, H., *L'évolution créatrice*, 1907, PUF, coll. « Quadrige. Grands textes », 2007
・Kant, I., *Gesammelte Schriften*, die König Preußische Akademie der Wissenschaften (Hg.), Berlin, 1900-
・Dagognet, F., *Rematérialiser*, Vrin, 1985, translation by Shigeo Ookoda, Hosei University Press, 2010; p. 327
・Mcfarland, J. D., *Kant's Concept of Teleology*, University of Edinburgh Press, 1970

Frege on Unsaturatedness

Tetsuya Yoshida (Department of Philosophy, Tohoku University)

Introduction

Purpose

To elucidate the notion of "unsaturatedness" in Gottlob Frege's works and to focus on the difference between unsaturatedness and the notion of function

Background

The relationship between unsaturatedness and the notion of function is a contentious issue in the construal of Frege's philosophy.

Methods

1. To analyze concepts, predicates, and the sense of predicates through Frege's works.
2. To compare the argument of functions with objects, proper names, and the sense of predicates.

Materials

- … a function by itself must be called incomplete, in need of supplementation, or unsaturated. (FB, 6)
- … a concept is a function whose value is always a truth-value. (FB, 15)
- The second part〔=predicate〕 is unsaturated - it contains an empty place; only when this place is filled up with a proper name, does a complete sense appear. (FB, 17)
- … not all the parts of a thought can be complete; at least one must be unsaturated or predicative … (BG, 205)
- The unsaturated part of the thought we take to be a sense too: it is the sense of the part of the sentence over and above the proper name〔=the sense of the predicate〕. (NS, 209)
- Every individual number is a self-subsistent object. (GLA, § 55)
- … a proper name, which thus has as its *Bedeutung* a definite object … (SB, 27)

Conclusion

Conclusion

1. Unsaturatedness is not intrinsically related to the notion of function.
2. Predicates and the sense of predicates do not have the faculty of mapping. Therefore these are not a type of function.

Future Discussions

Does unsaturatedness have a semantic role? If so, what is the role?

Results & Discussions

1. Concepts are functions that map objects for truth values.

   Concepts require an object that serves as the reference of proper names. When we allocate an object for this concept, we obtain a truth value.

2. In the case of predicates and the sense of predicates, the arguments are not objects.

   Predicates require a proper name, and the sense of predicates requires the sense of proper names. Functions require a number as an argument. Number is an object, but proper names and the sense of proper names are not.

References

Frege, G.

(GLA) *Die Grundlagen der Arithmetik: eine logisch-mathematische Untersuchung über den Begriff der Zahl*, Breslau: W. Koebner, 1884.

(FB) *Funktion und Begriff*, Jena: Hermann Pohle, 1891.

(SB) 'Über Sinn und Bedeutung', in *Zeitschrift für Philosophie und philosophische Kritik*, 100, 1892, 25–50.

(BG) 'Über Begriff und Gegenstand', in *Vierteljahresschrift für wissenschaftliche Philosophie*, 16, 1892, 192–205.

(NS) Hermes, H., Kambartel, F., and Kaulbach, F. (eds.), *Nachgelassene Schriften*, Hamburg: Felix Meiner, 1969.

P-85

Performance Evaluation and Software Development for FPCCD Vertex Detector in ILC

Tohoku University Tatsuya Mori

What is ILC?

ILC (International Linear Collider) is a next generation lepton collider for the high energy frontier physics.

- Basic Characteristics
  - e^+e^- collider
  - total length = 31 km
  - E_{CM} = 250 ~ 500 GeV (upgrade : 1 TeV)
  - peak luminosity = 2 × 10^{34} $cm^{-2}s^{-1}$

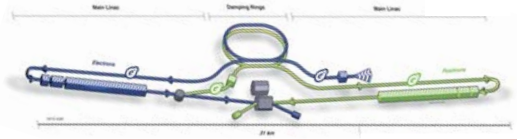

Higgs Study in ILC

One of purposes of ILC is to measure Higgs coupling constant precisely, especially to b-quark and c-quark.

The golden mode of Higgs generation process in ILC is ee -> ZH.

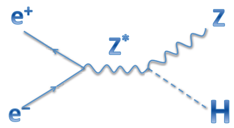

ILC is a lepton collider, so precise measurement of Higgs boson coupling to b-quark and c-quark can be done.

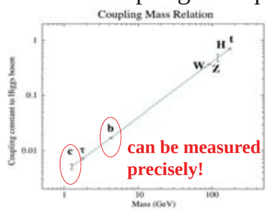

Vertex Detector is required to see measure 100 μm scale and below.

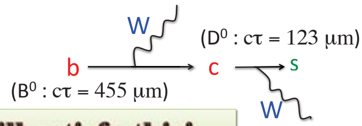

FPCCD Vertex Detector will satisfy this!

FPCCD Vertex Detector

FPCCD (Fine Pixel CCD) Vertex Detector will enable precise flavor tagging.

- Basic Characteristics
  - pixel size : 5μm x 5μm
  - sensor thickness : 50μm
  - number of pixels : ~10^9
  - fully depleted CCD → two-track separation capability : Good
  - three doublet structure
    → background rejection by cluster shape : Good
  - readout par one train
    → completely free from beam-induced RF noise (EMI)

space resolution : Very Good
pixel occupancy of background : Good

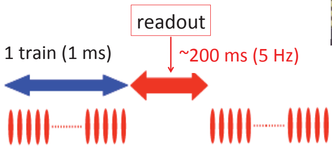

FPCCD prototype : 6μm x 6μm

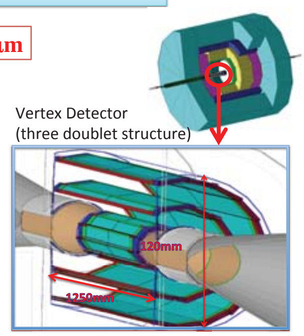

Before building FPCCD Vertex Detector, its performance should be evaluated and optimized.

Performance Evaluation and Software Development for FPCCD

Pixel Occupancy of Background

Main background in VXD is caused by electron-positron beam.

at 500 GeV	
layer No.	occupancy of B.G.(%)
1	2.8
2	1.6
3	0.1
4	0.0
5	0.0
6	0.0

at 1 TeV	
layer No.	occupancy of B.G.(%)
1	19.6
2	10.4
3	0.2
4	0.2
5	0.0
6	0.0

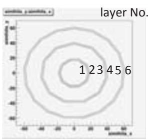

Occupancy must be lower than ~3% in each layer.

Occupancy under 500 GeV is OK!!

Pixel-size configuration has been optimized to reduce power consumption of readout.

If pixel size in the outer 4 layers are 10μm x 10μm, then power consumption of readout is decreased by 70%. If both occupancy and I.P. resolution remain OK, this value is very attractive.

Check! Occupancy: 5μm VS 10μm

at 1 TeV		
	occupancy of B.G.(%)	
layer No.	5 x 5 μm²	10 x 10 μm²
1	19.6	–
2	10.4	–
3	0.2	0.5
4	0.2	0.5
5	0.0	0.1
6	0.0	0.1

Occupancy requirement cleared with 10μm x 10μm pixel configuration!

Check! I.P. resolution: all 5μm VS 5μm in inner 2 layers & 10μm in outer 4 layers

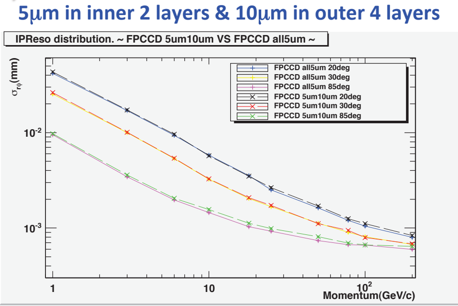

I.P. resolution remains almost same as all 5μm configuration.

From these two results, we can conclude that using 10 x 10 μm² for outer layers is an attractive configuration.

Impact Parameter Resolution (without B.G.)

definition: impact parameter

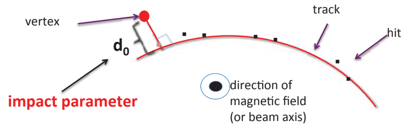

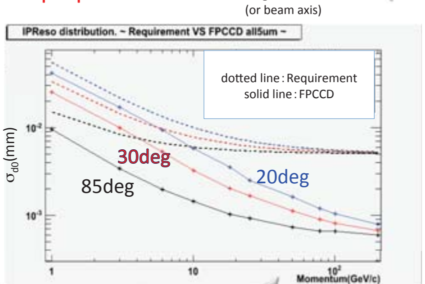

FPCCD provides fantastic I.P. Resolution!!

Currently, tracking efficiency and I.P. resolution with B.G. is being studied. The followings are tentative results.

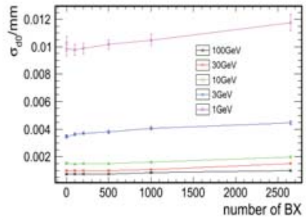

This shows I.P. resolution with background. Even if number of BX increases, it doesn't increase so much.

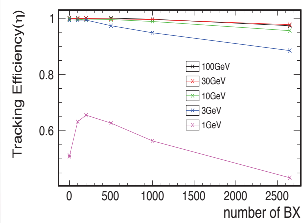

This shows tracking efficiency with background. Definition of the efficiency is whether there are more than 5 hits used in VXD.

Problems about the efficiency:
1. Why is the efficiency at 1GeV with 0BX very low?
2. Why is the efficiency at 1GeV with 100 ~ 1000BX higher than that with 0BX?

→Now the tracking algorithm is being checked.

Summary and Plan

- **If FPCCD is used,**
  → **Occupancy : OK! (under E_{CM} = 500 GeV)**
  → **Impact parameter resolution : Very Good!**
  → **Power consumption can be reduced** with new configuration of pixel size.

- **Plan**

Tracking Algorithm: I'll check and modify it.
Beam Test: June 2013.
I'll prepare analysis code to derive FPCCD's excellent spatial resolution.